A Study on Majorana Zero Modes in Higher-Order Topological Superconductors

by

Majid Kheirkhah

A Thesis Submitted in Partial Fulfillment of the Requirements For the Degree of

Doctor of Philosophy

Department of Physics,
University of Alberta

Abstract

Over the past decade, the interplay between symmetry and topology in condensed matter physics has not only deepened our understanding of matter by prompting a conceptual revolution in classifying all phases of matter, but it has also led to tremendous progress in finding new materials with low energy consumption and new applications such as fault-tolerant topological quantum computing and Weyltronics, to name but few.

This thesis consists of two parts and presents a theoretical study in the field of condensed matter theory with a focus on higher-order topological superconductivity and Majorana zero modes. The first part of this thesis is concerned with high-temperature superconductivity in cuprates, and the last part is dedicated to the high-temperature iron-based superconductors.

In the first part, it will be shown that using a harmonic potential to confine a two dimensional second-order topological superconductor leads to a proliferation of Majorana corner modes. The second-order topological superconductor can be obtained by incorporating a first-order topological insulator in proximity to a high-temperature superconductor. As a consequence, these circumstances result in the formation of Majorana corner flat bands, which have a fundamentally different origin from that of the conventional mechanism. Moreover, we will investigate the superconducting pairing instability of the two-dimensional extended Hubbard model with both Rashba and Dresselhaus spin-orbit coupling within the mean-field level at both zero and finite temperature. We find that both first- and second-order time-reversal symmetry-breaking topological gapped phases can be achieved under appropriate parameters and temperature regimes due to the presence of a favored even-parity $s+id$-wave pairing even in the absence of an external magnetic field or intrinsic magnetism. Our findings suggest new possibilities in interacting spin-orbit coupled systems by unifying both first- and higher-order topological superconductors in a simple but realistic microscopic model.

In the last part of this thesis, the impact of second-order topology on the vortex lines topology in iron-based superconductors in both weak and strong Zeeman field regimes will be investigated. By incorporating a realistic assumption of inhomogeneous superconductivity, our findings can explain the recent experimental observation of the peculiar coexistence and evolution of topologically nontrivial and trivial vortex lines in iron-based superconductors, and hopefully advance our understanding of these materials.

To my loving parents, Fatemeh and Abolghasem,
for their unwavering support and help from the beginning,

to my beloved wife, Maryam,
for her never ending love and encouragement,

and to my dear sons, Sepehr and Sina,
for filling up our lives with lots of joy and happiness.

Acknowledgments

As I am getting ready to leave University of Alberta, I would like to take this opportunity and thank the ones who have helped me a lot during this journey. First of all, I would like to sincerely thank my supervisor, Frank Marsiglio, for his generous support, guidance and patience throughout the past five years. I owe a lot to Frank and his incredible kindness and modest character. He trusted that I would do what needed to be done, and gave me the encouragement and resources to work effectively. Apart from sharing his knowledge on various topics in superconductivity, he granted me much freedom to work on any problem that I found interesting. The door of his office was always open so that I could always stop by to ask a question, share an idea, talk about a project, or even have a casual conversation sometimes in the late evening no matter how busy he was.

I also would like to thank the other two members of my supervisory committee: Joseph Maciejko and Richard Sydora for devoting their valuable time. I have benefited a lot from Joseph's constructive feedbacks and his informal lectures in both Advanced Statistical Mechanics and Linear Response Theory in Condensed Matter Journal Clubs. They have given me a broader knowledge of the field.

I have had a big opportunity to collaborate and discuss about different aspects of topological phases of matter with two brilliant scientists during my PhD studies: Yuki Nagai and Zhongbo Yan. Yuki's expertise in topological superconductivity and a wide range of numerical techniques was just too solid to wear off after finishing my graduate studies. Fortunately, he could visit us in February 2020 for a few days. The later years of my studies was greatly nurtured by a collaboration with Zhongbo. He had an excellent intuition about topological superconductivity especially higher-order ones. His qualifications perfectly complemented my understanding of topological invariants. We all spent countless hours of fruitful online discussions together, which eventually culminated in our publications. Thank you very much for answering all my naive questions and your encouragements.

Furthermore, my research at various stages also significantly benefited from discussions with the postdocs in the condensed matter theory division especially Shu-Ping Lee, Chun Chen, and Rufus Boyak. My officemate, Mason Protter, helped me a lot whenever I stuck with a problem in Julia. I would like to thank all of them for what they have done for me.

Further words of gratitude belong to my master's supervisor, Seyyed Mir Abolhassan

Vaezi, from whom I have heard "topological insulators" for the first time before starting my master thesis at Sharif University of Technology. He was teaching me the basic language of topology in condensed matter physics and introduced me to the beautiful world of condensed matter physics. I also would like to thank him for several delightful conversations during the past few years.

My words will always fall short in acknowledging my loving parents, Fatemeh and Abolghasem, for all of their unconditional support and encouragement throughout my entire life. Thank you both for giving me strength to chase my dreams. I also would like to thank my sister, Zahra, for her constant encouragement. You all have always filled me with joy and kept me going by your Skype calls. I am indebted to all of you.

Most importantly, I send my greatest thanks to my wife, Maryam. She has never stopped supporting my curiosity about physics even when it led me to spend long nights at work. Maryam, you have played the most important role of all. I will be forever grateful for your love, endless understanding, and encouragement. I also would like to extend my thanks to my dear sons, Sepehr and Sina, for filling up our time with lots of joys, happiness, and fun. You all have been inspiring me for many years.

My work herein was supported mainly by Department of Physics, the Natural Sciences and Engineering Research Council of Canada (NSERC), and Major Innovation Fund (MIF) grant from the Province of Alberta, Canada.

Majid Kheirkhah,
Edmonton,
March 2021

Contents

List of Figures

List of Tables

Chapter 1

Introduction

1.1 Overview

Classifying different states of matter and the transitions between them has attracted lots of attention in the past century. In the middle of the twentieth century, Ginzburg-Landau theory had a great success in understanding the phase transitions in terms of symmetry groups, as well as classifying them according to different universality classes. This theory relies on the concept of a local order parameter and a closely related notion of spontaneous symmetry breaking. According to Ginzburg-Landau theory, the transition from one phase to another occurs at a critical point either as a function of temperature (classical phase transition), or as a function of a different parameter inside the Hamiltonian at zero temperature (quantum phase transition). These two phases have to be distinct according to their describing symmetries. One of the phases is then called the ordered phase and the other one the disordered phase. The order parameter, which must vanish in the disordered phase and acquires a finite value in the ordered regime, quantifies the amount of such symmetry breaking. Although the physical origin of classical and quantum phase transitions is different, the same phenomenological approach could be used to understand the phase transition in both cases. In the former case, the macroscopic order is destroyed by thermal fluctuations. However, in the later case, the order is destroyed solely by quantum fluctuations originating from the Heisenberg uncertainty principle. In fact, even though the order parameter is zero in the disordered phase, its fluctuations can be non-zero. When approaching the critical point, the correlation length of such fluctuations diverges, which implies the scale invariance of the system and can be described by universal parameters know as critical exponents. This behavior describes the critical properties of the system. Remarkably, the critical behavior is determined only by the symmetries of the order parameter and the space dimension of the system, which defines the so-called universality classes.

During the last few decades, theoretical investigations and experimental developments

have shown that some phase transitions are not straightforwardly related to symmetries, and are hence situated beyond the Ginzburg-Landau paradigm. In order to understand these phase transitions, one needs to explore the topology of the system, so the associated phase transitions are called *topological phase transitions.*

In 1972, the first theoretical results indicating that the physical properties of some systems cannot be described by the spontaneous symmetry breaking paradigm were found in the seminal independent works by Berezinskii [1, 2], and Kosterlitz and Thouless [3] by studying the two-dimensional XY model.

In 1879, eighteen years prior to the discovery of the electron and long before the discovery of its spin, Edwin Hall conducted an experiment bearing his name nowadays known as *the classical Hall effect.* He considered a metallic two-dimensional sample subject to an in-plane current or electric field and a perpendicular magnetic field. The Lorentz force leads to the displacement of moving charge carriers and hence a new in-plane electric field perpendicular to the first one. By measuring the transversal or Hall resistivity (ρ_{xy}) of the sample, he found that this value is directly proportional to the magnetic field.

In 1980, one hundred years after Edwin Hall's experiment, the *integer quantum Hall effect* was discovered by von Klitzing and collaborators, where a two-dimensional weakly disordered metallic sample is subjected to a strong magnetic field at low temperature [4]. Surprisingly, they found that ρ_{xy} is no longer proportional to the magnetic field in sharp contrast to the classical Hall effect! Instead, there were lots of plateaus at which the longitudinal resistivity (ρ_{xx}) is zero while between two adjacent plateaus its value is finite (see Fig. 1.1). A question immediately arose: is this zero longitudinal resistivity at plateaus a superconductor or a perfect conductor? Surprisingly, the answer is no, it is not even a conductor! It is actually an insulator! The reason is that $\sigma = 1/\rho$ requires a very important assumption which is the following: in general ρ is a tensor and only when it is proportional to the unity matrix, can it be treated as a scalar.

In the quantum Hall system and at plateaus, resistivity is a two by two off-diagonal matrix since the diagonal components are zero *i.e.* $\rho_{xx} = \rho_{yy} = 0$, so here it cannot be treated as a scalar. By inverting this matrix, it turns out that $\sigma_{xx} = \sigma_{yy} = 0$ not infinity, which means that on a plateau there is zero conductivity, so the sample is actually an insulator as already mentioned. By the same procedure, it can be readily found that $\sigma_{xx} = \sigma_{yy} \neq 0$ between two adjacent plateaus since $\rho_{xx} = \rho_{yy} \neq 0$, so the sample is a metal in those regions. In other words, the system turns from one insulator to a metal, then from another insulator and a metal and so on as the magnitude of the external magnetic field is increased. These insulators are not the same as each other topologically. The transport coefficients for the metallic states are non-universal. However, the insulating states are very universal and independent of the sample quality.

Because of the effect of the magnetic field, the energy of the electron is quantized, which leads to the formation of highly degenerate Landau levels at energy $E_n = \hbar\omega_c(n + 1/2)$ for $n = 0, 1, 2, ...$ Here, $\omega_c = eB/m$ is the cyclotron frequency, B represents the magnitude of the

external magnetic field, and e and m are the magnitude of the charge and mass of the electron, respectively. Two things should be noted here: First, such quantized effects are noticeable at low temperatures when the quantum effects are dominant and the thermal energy is much smaller than the spacing between different Landau levels. Second, each Landau level has a finite width due to the presence of disorder in a real experimental sample.

The number of states N_s in each Landau level is given by Φ/Φ_0 which is equal to the ratio of the total magnetic flux piercing the sample to the flux quantum $\Phi_0 = h/e$ (h is the Planck constant). Therefore, N_s is the total number of flux quanta in the system. One expects that such a system is either an insulator, when the chemical potential lies between two Landau levels, or a metal, when the chemical potential crosses with one band. In experiments, the value of magnetic field is usually tuned for a given value of chemical potential. As the energy of all bands increases by increasing B, the chemical potential may be either inside the gap or cross a band as was already mentioned. The Hall conductivity displays plateaus whose value is quantized perfectly with an extremely high precision to

$$\sigma_{xy} = \frac{1}{\rho_{xy}} = \nu \frac{e^2}{h} \tag{1.1}$$

where $\nu = N/N_s$ is *the filling factor* or *the filling fraction*, and N is the number of electrons. The filling factor can take either integer or fractional values. In the first case, an integer number of Landau levels is occupied and the observed effect corresponds to the integer quantum Hall effect. In the second case, a fraction of the Landau level (usually the lowest one) is occupied and the observed effect corresponds to *the fractional quantum Hall effect* [5]. The transition between plateaus is accompanied by a peak in the ρ_{xx}, which vanishes otherwise. It can be shown that each filled Landau level gives us one chiral edge state, so the number of chiral edge states or the Hall conductivity is just the number of filled Landau levels or ν. Moreover, the bigger the magnetic field, the bigger the Landau level spacing and the fewer the number of edge modes or ν.

Close to the one-dimensional boundaries of the sample, the confinement potential bands the otherwise flat Landau bands, so the Landau levels that are below the chemical potential in the bulk are forced to cross it near the boundary as shown in Fig. 1.1. This leads to two opposite group velocities along the lower and upper edges. Therefore, the boundary of the system is a one-dimensional metal with unidirectional or so-called chiral modes. As a consequence, there are no available states to backscatter to even in the presence of impurities, so the boundary states may be deformed even in the presence of a rough edge or impurity but still move in the same direction without dissipation. Furthermore, in the bulk of the sample, the group velocity is zero because of the flatness of the Landau band, so there is no current flowing. This suggests that although the edge of the system is a one-dimensional metal, the bulk of the sample is an insulator. The existence of such robust boundary states can be tracked down as stemming from the nontrivial topology of the states in the bulk.

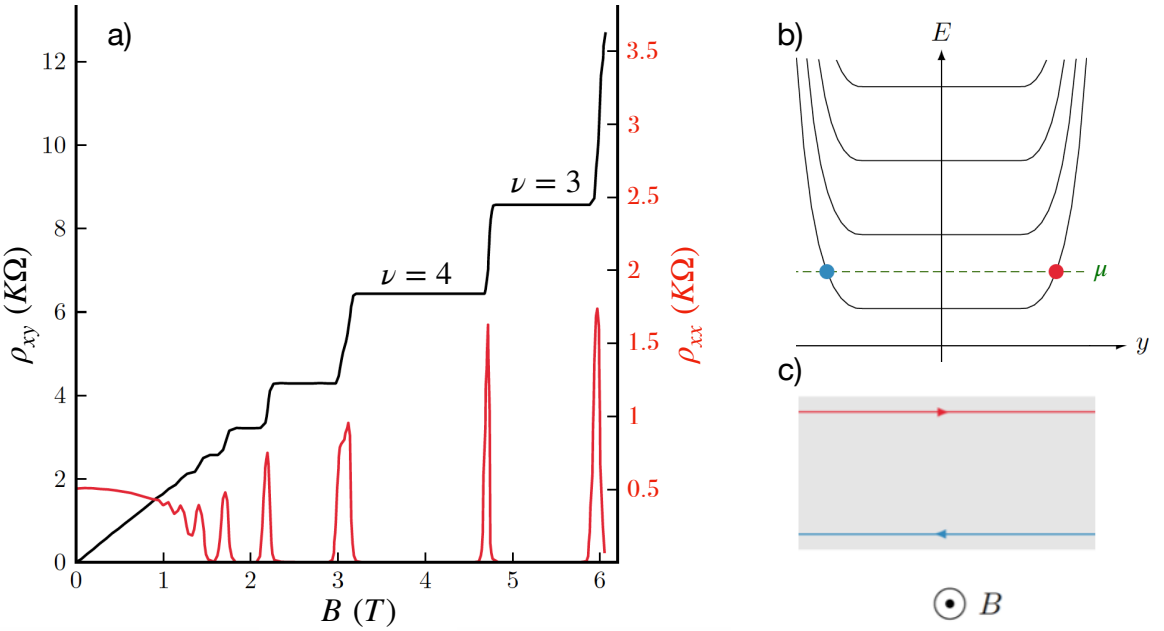

Figure 1.1: (Color online) (a) Hall resistivity (ρ_{xy}) [black curve and the left vertical axis] and longitudinal resistivity (ρ_{xx}) [red curve and the right vertical axis] in the GaAs-AlGaAs heterostructure as a function of external magnetic field at 8mK, which is adopted from Ref. [6]. (b) a schematic figure of Landau levels for a two-dimensional system where the confining potential curves the Landau levels close to the boundaries results in chiral edge states, (c) the chiral edge state.

It turned out that the number of edge states (ν) is equal to a topological invariant know-as the *Chern number* of the bands(s) below the Fermi level [7]. In transport measurements, the Hall current is carried by the edge states, each of which happens to contribute as e^2/h to the Hall conductance, which confirmed that the ν in Eq. 1.1 is the Chern number. The quantum Hall plateaus have different Chern numbers, so they are distinct topological insulators. Therefore, there has to be a metallic phase between them as already explained.

The discovery of the integer quantum Hall effect opened a new field in condensed matter and beyond. The interest in the integer quantum Hall effect comes from multiple points of views: First, with the discovery of the integer quantum Hall effect, it was found that Ginzburg-Landau paradigm is not comprehensive. The integer quantum Hall effect is the first example of a more general family of phenomena known as *topological insulators*, a key feature of which is the appearance of *symmetry-protected edge states* at their boundaries due to the existence of a nontrivial topology of the bulk bands. This general principle is called the *bulk-boundary correspondence*. Second, it is described by a beautiful theory which connects relatively modern mathematical constructs to experimentally realizable situations. Third, there is a practical interest from metrology since the integer quantum Hall effect provides an

extremely precise and reproducible measure of the fundamental constant e^2/h with a relative uncertainty lower than 10^{-9}. It is not altered by the precise geometry of the system nor by the impurities and disorder. This universality and this invariance against perturbations are a clue that the quantized Hall conductance may be related to a topological invariant which was soon recognized by TKNN (Thouless, Kohmoto, Nightingale, and den Nijs) [7].

In 1988, long before the discovery of the topological insulator, the question "can one obtain a nonzero Chern number without a magnetic field?" was answered by Haldane [8]. He considered graphene, a then hypothetical two-dimensional system of carbon atoms arranged in a hexagonal lattice. This crystal is described as two triangular sublattices, by convention called A and B. The resulting band structure has two inequivalent points or valleys in reciprocal space called $\boldsymbol{K}$ and $\boldsymbol{K'}$ around which the Hamiltonian can be described to low energies as the Dirac Hamiltonian. The Dirac points are protected by the presence of both time-reversal (time-inversion) and parity (space-inversion) symmetries. Breaking one of these symmetries opens a mass gap in the low-energy spectrum and converts the Dirac semimetal to an insulator. The inversion symmetry can be broken by changing the relative energies of the two lattices with an extra mass term in the Hamiltonian which changes the spectrum from being fully linear, gapless, and hence massless to having a gap and effective mass m at the $\boldsymbol{K}$ point. By time reversal symmetry, the mass will also be m at the $\boldsymbol{K'}$ point. This is important from a topological perspective because when integrating the Berry curvature over the Brillouin zone, contributions from the $\boldsymbol{K}$ and $\boldsymbol{K'}$ points will cancel, resulting in a trivial insulator [9]. Haldane's realization was that with a magnetic field that is zero on average but respects lattice symmetry, one could break time-reversal symmetry in such a way that the masses at $\boldsymbol{K}$ and $\boldsymbol{K'}$ have opposite signs. The result would be an insulator with nonzero Chern number known as a *Chern insulator*. It would exhibit the *quantum anomalous Hall effect* and the full quantum Hall edge states behavior would be realized without the need for an overall magnetic field. The *Haldane model* is a spinless non-interacting fermionic model defined on the honeycomb lattice in which the time-reversal symmetry is explicitly broken due to a complex second neighbour hopping amplitude with an alternating magnetic flux pattern threading the unit cell such that the total magnetic flux is zero.

In 2004, a renewed interest in the Haldane model came with the discovery of graphene [10] although it was then thought that it was necessary to break time-reversal symmetry to obtain a topological phases such as the integer quantum Hall effect or a Chern insulator. One year later, in 2005, Kane and Mele from University of Pennsylvania proposed a realization of such a phase in graphene which is known as *the Kane-Mele model* nowadays [11, 12]. This model can be understood as two copies of the Haldane model for spinful fermions, arranged in such a way that the $\mathbb{Z}$ topological invariant is reduced to a new $\mathbb{Z}_2$ topological invariant due to preserving time-reversal symmetry which can be defined for space dimensions two and three. In a time-reversal invariant system any eigenstate has a *Kramers partner*. The contribution of Kramers partners in the Chern number are opposite and cancel out. This results in the vanishing of the both total Chern number and chiral edge modes but results in the finte spin

Chern number and the emergance of new helical edge modes. This model, proposed a time-reversal invariant version of the integer quantum Hall effect known as the *quantum spin Hall effect*. Here, the crucial ingredients appear to be a band inversion near a symmetric point of the Brillouin zone and a strong spin-orbit coupling which effectively generate a momentum- and spin-dependent magnetic field. Although graphene was the system for which both the Haldane model and the Kane-Mele model were originally considered, unfortunately the spin-orbit coupling present from carbon orbitals is much too weak to produce a significant gap [13]. This led to a search for other systems composed of heavier elements for which spin-orbit coupling is typically much stronger.

Combined with contemporary theory works [14–16], a breakthrough moment came at the end of 2006 when Bernevig, Hughes and Zhang from Stanford University proposed an alternative realization in HgTe/(Hg, Cd)Te quantum wells with a uniform strain gradient [17, 18]. The effective model that was used to predict the effect is now known as *the BHZ model*, which is a 4×4 Hamiltonian derived with first order perturbation theory, named after its authors. The experimental confirmation came in the following year with an experiment conducted by Laurens W. Molenkamp's group at University of Würzburg [19]. Soon after, another realization in InAs/GaSb quantum wells [20] was proposed and confirmed experimentaly [21–23].

In 2007, it was discovered by Fu, Kane and Mele [24], and Moore and Balents [25] that the time-reversal invariant topological insulator has an equivalent version in three dimensions, which was soon experimentally observed in $Bi_{1-x}Sb_x$ in Hasan's group at Princeton University in 2008 [26] with angle-resolved photoemission spectroscopy (ARPES) measurements and later in Bi_2Te_3 or Bi_2Se_3 [27–29]. They observed a Dirac dispersion relation of surface electrons for energies in the bulk gap of the material. It should be noted here that in sharp contrast there is no integer quantum Hall effect in odd spatial dimensions.

Recently, numerous new topological insulator candidates have been found using systematic searches through a material database [30–32]. In should be noted that, nevertheless, an ideal topological insulator would be the one with a large band gap which seems to be hard to come by since the gap inversion is often a result of spin-orbit coupling, which is not easy to be enhanced.

Due to the superconducting gap, a superconductor is similar to an insulator from the energy point of view. One thing that distinguishes a superconductor from an insulator is redundant particle-hole symmetry of the BdG Hamiltonian. In addition, the ground state of a superconductor has a definite phase but does not have a definite number of Cooper pairs [33]. Therefore, adding an electron to a superconductor is the same as removing an electron or equivalently adding a hole. Studying the topology of such an "insulator" is the subject of topological superconductivity field [34, 35]. Topological superconductivity is regarded as a potential new and powerful platform in which to create, observe, and control excitations that could eventually lead to real-life applications in the field of quantum electronics. Due to built-in particle-hole redundancy, superconductors are expected under certain conditions to enter a topological phase that have been predicted to host zero-energy Majorana bound states [36,

37]. *Majorana zero modes* hold promising applications in topological quantum computation, which is based on storing and manipulating quantum bits or qubits in global form with non-Abelian particles such as Majorana fermions, which is intrinsically fault tolerant in contrast to other proposals for quantum computing [38, 39]. Therefore, a huge amount of effort has been made to find these exotic particles in various systems such as solid state and cold atom systems in the past decade.

A milestone in the topic of topological phases was achieved by Altland and Zirnbauer in the context of disordered systems in relation to Cartan symmetric spaces [40, 41]. They developed a classification for a non-interacting gapped fermionic Hamiltonian according to two basic non-spatial discrete anti-unitary symmetries that commute with the Hamiltonian: time-reversal symmetry ($\mathcal{T}$), and particle-hole symmetry ($\mathcal{P}$). The square of these symmetries can be either ± 1 or even zero when it is broken. Therefore, they lead to $3 \times 3 = 9$ different symmetry classes. However, a third unitary symmetry that anticommutes with the Hamiltonian known as chiral symmetry ($\mathcal{S} = \mathcal{T}\mathcal{P}$) should not be forgotten. It is worth noting that chiral symmetry is not a unitarily implemented symmetry as it anticommutes with the Hamiltonian. The square of chiral symmetry can always be chosen to be $+1$. Although the presence or absent of the chiral symmetry is determined by the behavior of time-reversal and particle-hole symmetries, there is a very special case where $\mathcal{S}$ is a symmetry of the system when both time-reversal and particle-hole symmetries are broken. This case raises the number of symmetry classes from nine to ten. Therefore, there are ten ways to combine all the possible symmetries of a one-particle Hamiltonian. This classification scheme is called the *periodic table of topological insulators and topological superconductors* for each spatial dimension [42]. It turned out that there are five non-interacting distinct topological insulators and superconductors in each spatial dimension. Nevertheless, not all of them have found an experimental realization. This poses an ongoing challenge in condensed matter physics. Furthermore, the road ahead is not entirely mapped, so it is still remains to have a systematic view of topological matter in the context of interacting systems.

In 2009, Kitaev recognized the Bott periodicity is hidden in Altland and Zirnbauer's classification [43]. He thus was able to generalize the classification to all spatial dimensions which is a culmination of the study of weakly interacting topological materials. Two of the possible classes, A and AIII, belong to so called *the complex classes* which have a period of two while the remaining eight classes belong to *the real classes* which have a period of eight. That is, the topological invariants in spatial dimension $d + 2$ and $d + 8$ are the same as those in dimension d for the complex and the real classes, respectively. According to this periodicity, some interesting conclusions can be drawn. To name a few, the quantum Hall effect (class A) can happen only in even spatial dimensions, or the topology of class AIII is nontrivial only in odd spatial dimensions. Although different approaches were developed to obtain this classification, the agreement of the results is not a trivial fact but it is at the core of the bulk-boundary correspondence.

The topological phases in the Altland-Zirnbauer table are protected entirely by so-called

generic, non-spatial symmetries that cannot be represented by unitary operators that commute with the Hamiltonian. Therefore, topologically protected states appear on *all* surfaces and the interfaces of the system even in the presence of weak disorder since these spatial modifications of the system do not affect a non-spatial symmetry. But what will happen if we consider ordinary spatial symmetries represented by unitary operators? This led to the discovery of *topological crystalline insulators* which has opened the door to new topological phases of matter whose topological nature arises from the richness and complexity of crystal symmetries.

In 2011 Fu, in another seminal paper, presented a three-dimensional toy model with gapless surface states protected by the combined effects of four-fold rotation (C_4) and time-reversal symmetries. This toy model manifests itself as the first example of a large class of topological crystalline insulators [44]. In 2012, one year after this theoretical prediction, the non-trivial surface states have been successfully observed [45–47]. Topological crystalline insulators are susceptible to disorder, so topological features are expected to persist only if the protecting crystal symmetry is preserved on average [48]. Moreover, *not all* surfaces of a topological crystalline insulator host topological surface states, only those that do not break the protecting crystal symmetry. For example, a topological crystalline insulator protected by a C_4 rotation symmetry will have generally topological states only on the surfaces perpendicular to the axis of rotation [44].

Topological phases of matter can be extended even to gapless phases such as gapless or Dirac superconductors (such as d-wave superconductors) and semimetals. Whereas gapped topological phases carry *dispersing* edges or surface states, gapless topological phases host *dispersionless* or *flat bands* on their edges or surfaces. The nodal-point and nodal-line semimetals are two classes of semimetals of which the touching between conduction band and valance band is a point(s) or a one-dimensional line in momentum space, respectively. A Weyl semimetal is a three dimension nodal-point topological semimetal phase without requiring any symmetry protection in contrast to the Dirac semimetals [49, 50]. They need to break at least time-reversal symmetry or inversion symmetry. Weyl bulk points feature the source and sink of Berry curvature distribution, so they always come in pairs with opposite chiralities and are connected by surface Fermi arcs. In 2015, a Weyl semimetal was experimentally discovered in Hasan's group at Princeton University [51]. The nodal-line semimetals, however, are distinct from both the Dirac semimetal and the Weyl semimetal, which are nodal-point ones [52].

In 2017, a new class of topological crystalline phases, named *higher-order topological phases* was theoretically predicted by Benalcazar, Bernevig, and Hughes in which the dipole polarization vanishes while higher electric multipole moments are quantized to fractional values [53, 54]. Nowadays, this model is known as *the BBH model*. The word "order" in this context gives the codimension of the gapless boundary modes, namely, an nth order topological insulator or topological superconductor has gapless boundary modes with codimension n. As the gapless boundary modes of all conventional topological insulators and topological

superconductors have $n = 1$, they thus belong to the first-order topological phases in this language. Therefore, conventional bulk-boundary correspondence, which states gapless topological boundary states emerge only at boundaries that are one dimension lower than the bulk, is not valid here.

Higher-order topological phases have attracted a great deal of attention because of the enrichment of boundary physics, the intriguing manifestation of crystalline symmetry and band topology in the bulk and boundaries, as well as the occurrence of new possibilities for topological phase transitions. These intriguing phases could provide new platforms for Majorana zero modes and topological quantum computing and enable unprecedented topological devices with better integration and miniaturization.

In the past two years, higher-order topological phases have been proposed in systems without quantized multiple moments [55], and in non-periodic lattices such as amorphous [56], and quasicrystalline [57] solids. Moreover, higher-order non-Hermitian topological phases [58, 59], higher-order Weyl semimetals [60, 61], and higher-order Floquet topological phases [62, 63] have attracted a great deal of attention and revealed many ubiquitous physical properties.

1.2 Contributions

This thesis is mainly based on the following three first-author publications:

I – *Majorana Corner Flat Bands in Two-Dimensional Second-Order Topological Superconductors*,
Majid Kheirkhah, Yuki Nagai, Chun Chen, and Frank Marsiglio,
Phys. Rev. B **101**, 104502 (2020).
This work has been done in collaboration with Dr. Yuki Nagai from Japan Atomic Energy Agency and Dr. Chun Chen, a former postdoctoral scholar here in the condensed matter theory division.

II – *First- and Second-Order Topological Superconductivity and Temperature-Driven Topological Phase Transitions in the Extended Hubbard Model with Spin-Orbit Coupling*,
Majid Kheirkhah, Zhongbo Yan, Yuki Nagai, and Frank Marsiglio,
Phys. Rev. Lett. **125**, 017001 (2020).
This work has been done in collaboration with Prof. Zhongbo Yan from Sun Yat-Sen University in China and Dr. Yuki Nagai.

III – *Vortex Line Topology in Iron-Based Superconductors with and without Second-Order Topology*,
Majid Kheirkhah, Zhongbo Yan, and Frank Marsiglio,
arXiv:2007.10326
This work, which is under review and has not been published yet, has been done in collaboration with Prof. Zhongbo Yan.

These publications are always referred as publication (I), (II), (III) throughout this thesis.

1.3 Organization of this thesis

This thesis is organized in six chapters as described below:

- **Chapter 2:** This chapter is a general discussion about the theoretical tools that will be used in the rest of this thesis to study the band structure topology in non-interacting crystalline solids. Apart from serving as a reference for subsequent chapters, the author also felt compelled to provide his own perspective of this quickly developing exciting field in this chapter.

- **Chapter 3:** In this chapter, which covers publication (I), we find that confining a second-order topological superconductor with a harmonic potential leads to a proliferation of Majorana corner modes. As a consequence, this results in the formation of Majorana corner flat bands which have a fundamentally different origin from that of the conventional mechanism. This is due to the fact that they arise solely from the one-dimensional gapped boundary states of the hybrid system that become gapless without the bulk gap closing under the increase of the trapping potential magnitude. The Majorana corner states are found to be robust against the strength of the harmonic trap and the transition from Majorana corner states to Majorana flat bands is merely a smooth crossover. As a harmonic trap can potentially be realized in heterostructures, this proposal paves a way to observe these Majorana corner flat bands in an experimental context.

- **Chapter 4:** In this chapter, which covers publication (II), we investigate the superconducting pairing instability of the two-dimensional extended Hubbard model with both Rashba and Dresselhaus spin-orbit coupling within the mean-field level at both zero and finite temperature. We find that both first- and second-order time-reversal symmetry breaking topological gapped phases can be achieved under appropriate parameters and temperature regimes due to the presence of a favored even-parity $s + id$ -wave pairing even in the absence of an external magnetic field or intrinsic magnetism. This results in two branches of chiral Majorana edge states on each edge or a single zero-energy Majorana corner state at each corner of the sample. Interestingly, we also find that not only does tuning the doping level lead to a direct topological phase transition between these two distinct topological gapped phases, but also using the temperature as a highly controllable and reversible tuning knob leads to different direct temperature-driven topological phase transitions between gapped and gapless topological superconducting phases. Our findings suggest new possibilities in interacting spin-orbit coupled systems by unifying both first- and higher-order topological superconductors in a simple but realistic microscopic model.

- **Chapter 5:** In this chapter, which covers publication (III), we study the potential impact of second-order topology on the vortex lines in iron-based superconductors in both weak and strong Zeeman field regimes. Recently, experimental evidence of Majorana zero modes in vortices has been observed in iron-based superconductors with band inversion near the Fermi level. It is known that iron-based superconductors with band inversion and $s_{\pm}$-wave pairing can give rise to second-order topological superconductivity, manifested by the presence of helical or chiral Majorana hinge states in three dimensions. In the weak Zeeman field regime, we find that vortex lines far away from the hinges are topologically nontrivial in the weakly doped regime, regardless of whether the second-order topology is present or not. However, when the superconductor falls into the second-order topological phase and a topological vortex line is moved close to the helical Majorana hinge states, we find that their hybridization will trivialize the vortex line and transfer the Majorana zero modes to the hinges. Furthermore, when the Zeeman field is large enough, we find that the helical Majorana hinge states are changed into chiral Majorana hinge modes and thus a chiral second-order topological superconducting phase is realized. In this regime, the vortex lines are always topologically trivial, no matter how far away they are from the chiral Majorana hinge modes. By incorporating a realistic assumption of inhomogeneous superconductivity, our findings can explain the recent experimental observation of the peculiar coexistence and evolution of topologically nontrivial and trivial vortex lines in iron-based superconductors.

- **Chapter 6:** Finally, this chapter summarizes the results obtained and presented in this thesis briefly, and provides some future directions.

Chapter 2

Topological Phases of Matter: A Brief Review

2.1 Introduction

The main goal of this chapter is to provide a general and brief introduction to the recently developed concept of topological phases of matter. This chapter contains no original results and mostly serves as a reference for the methods applied in the subsequent chapters. Most of the content of this chapter is based on several excellent sources. In particular, the author would like to mention these well-known books [64–67] and excellent review papers [34–38, 68–74].

2.2 Symmetry and topology

Symmetry is a powerful practical tool for solving problems and generalizing conclusions between systems with similar symmetries, so it is a fundamental aspect for developing physical models. It brings beauty to the world around us and also simplifies its mathematical description. In quantum mechanics, a symmetry operation is a transformation of a system that preserve the probabilities of measurements made on the system [75]. In a Hilbert space of quantum states, symmetry operations are represented by operators which act on state vectors. While some symmetries correspond to simple transformations of space and time, others describe more abstract internal degrees of freedom like particle spins and gauge fields. However, symmetries also constrain the possible dynamics of a system. Breaking of a symmetry facilitates phenomena that would not be possible otherwise.

In condensed matter systems, the amount of symmetry becomes a knob that one can turn and observe the consequences. Cooling down a drop of mercury breaks translational and rotational symmetries and makes it a solid in the process. Cooling it down even more will

break gauge symmetry turning it into a superconductor. In a step-like fashion, crystalline solids allow us to try various combinations of symmetries and observe the consequences.

It has long been recognized that whenever two phases of matter have different symmetry, they cannot be smoothly evolved into one another without hitting a phase transition. On the other hand, such a restriction is usually absent for phases with the same symmetry. The most familiar example is offered by the three common phases of water. While the liquid phase has continuous rotational and translational symmetry, the solid phase only preserves a discrete subset of them. As a consequence, the two phases are separated by a transition line in the parameter space. On the other hand, the gaseous and the liquid phase possess the same symmetry, and one can indeed connect the two without hitting a phase transition simply by circumventing the critical point.

Another important phenomenon associated with symmetry breaking is the appearance of new particles. Microscopically, phase transitions correspond to a rearrangement of the constituent building blocks, electrons and ions in the case of condensed matter systems. This rearrangement modifies the effective low-energy degrees of freedom, which manifest themselves experimentally as new species of particles. In the example of water mentioned above, breaking translational symmetry leads to the appearance of transverse phonons in the solid phase. Note that these new particles can be very different from the constituent matter: Although crystalline solids are composed entirely of fermionic electrons and nucleons, phonons always come out as bosonic particles.

The notion of symmetry is deeply integrated in the mathematical framework of condensed matter physics. According to the Wigner theorem, every symmetry of a quantum system is expressed either as a unitary operator or as an antiunitary operator on the Hilbert space [76]. The unitary operator U is a linear map with $UU^\dagger = 1$ satisfying

$$U(a|\psi\rangle + b|\phi\rangle) = aU|\psi\rangle + bU|\phi\rangle, \tag{2.1}$$

$$\langle U\psi|U\phi\rangle = \langle\psi|U^\dagger U|\phi\rangle = \langle\psi|\phi\rangle, \tag{2.2}$$

for complex coefficients a and b. However, an antiunitary operator A is an antilinear map where

$$A(a|\psi\rangle + b|\phi\rangle) = a^* A|\psi\rangle + b^* A|\phi\rangle, \tag{2.3}$$

$$\langle A\psi|A\phi\rangle = \langle\psi|AA^\dagger|\phi\rangle^* = \langle\psi|\phi\rangle^*, \tag{2.4}$$

and the Hermitian conjugate of an antiunitary operator given as

$$\langle\psi|A\phi\rangle = \langle A^\dagger\psi|\phi\rangle^*. \tag{2.5}$$

The square of an antiunitary operator such as time-reversal symmetry or particle-hole symmetry, is *only* ± 1 since applying such an operator twice should bring back the system to the state before transformation differing at most by a phase factor $A^2 = z$ where $|z| = 1$, so

$$zA = A^2 A = AA^2 = Az = z^* A,$$

$$\begin{aligned} &\Rightarrow z = z^* \quad \text{with} \quad |z| = 1, \\ &\Rightarrow z = \pm 1 \end{aligned} \tag{2.6}$$

where we used Eq. 2.3 in the first line. Because of the antiunitarity of these operators, the value of their square is unchanged upon a $U(1)$ phase multiplication, *i.e.*

$$(e^{i\phi}A)^2 = e^{i\phi}Ae^{i\phi}A = e^{i\phi}e^{-i\phi}A^2 = A^2. \tag{2.7}$$

In sharp contrast, the square of a unitary operator, such as a chiral symmetry, is a phase factor ($e^{i\theta}$) which is not well defined since it depends on the choice of gauge. The usual unitary symmetries like crystalline symmetries (*i.e.* inversion, mirror, and rotation) are represented by unitary operators that commute with the Hamiltonian, thus allowing us to block-diagonalize the Hamiltonian into sectors of different operator eigenvalues. If Hamiltonian H is invariant under an unitary transformation U, *i.e.*

$$[H, U] = 0, \tag{2.8}$$

then the physical observable corresponding to G, which is the generator of U and is a Hermitian operator such that $U = e^{iG}$, is conserved since

$$i\hbar\frac{dG}{dt} = [G, H] = 0. \tag{2.9}$$

The non-spatial symmetries act differently: they either anticommute with the Hamiltonian, or are antiunitary such that the block-diagonalization cannot be applied. Remarkably, they also do not lead to conversation laws. An antiunitary operator can be written as $A = U\mathcal{K}$ where U is a unitary matrix and $\mathcal{K}$ denotes complex conjugation, which is an antiunitary operator. In the following, we will give a brief description about time-reversal symmetry, particle-hole symmetry, and chiral symmetry.

1. **Time-reversal symmetry:** Time-reversal symmetry is an antiunitary operator that commutes with the Hamiltonian, *i.e.*

$$[H, \mathcal{T}] = 0, \tag{2.10}$$

where $\mathcal{T} = U_{\mathcal{T}}\mathcal{K}$. Therefore, if $|u\rangle$ is an eigenstate of H with energy E, then so is $\mathcal{T}|u\rangle$. There is a significant and profound difference between these two states in spinless and spinful systems which will be demonstrated in the rest of this part. This difference gives birth to the so-called *Kramers' theorem*. In spinless systems we have $\mathcal{T}^2 = +1$ which results in $U_{\mathcal{T}} = U_{\mathcal{T}}^T$. However, in spinful systems $\mathcal{T}^2 = -1$ which results in $U_{\mathcal{T}} = -U_{\mathcal{T}}^T$. Let us begin with a spinless system where $\mathcal{T}^2 = +1$ and

$$\mathcal{T}c_{j,\alpha}\mathcal{T}^{-1} = c_{j,\alpha}, \tag{2.11}$$

in the real space. Here, $c_{j,\alpha}$ refers to the fermion annihilation operator at site j and α denotes denotes all degrees of freedom other than spin. This means that the time-reversal operator leaves the spinless fermion operators unchanged in the real space which is not the case in the momentum space. When a system has translation symmetry, it is in general more convenient to deal with its Hamiltonian in the momentum space, thus it is worthy to figure out how the fermions annihilation or creation operators transform under the time reversal symmetry in that space. We have

$$\begin{aligned}\mathcal{T}c_{j,\alpha}\mathcal{T}^{-1} &= \frac{1}{\sqrt{N}}\sum_k \mathcal{T}c_{k,\alpha}e^{ik\cdot r_j}\mathcal{T}^{-1} \\ &= \frac{1}{\sqrt{N}}\sum_k e^{-ik\cdot r_j}\mathcal{T}c_{k,\alpha}\mathcal{T}^{-1} \\ &= c_{j,\alpha} = \frac{1}{\sqrt{N}}\sum_k e^{-ik\cdot r_j}\mathcal{T}c_{-k,\alpha}\mathcal{T}^{-1},\end{aligned} \tag{2.12}$$

indicating

$$\mathcal{T}c_{k,\alpha}\mathcal{T}^{-1} = c_{-k,\alpha}. \tag{2.13}$$

Therefore, for a time-reversal invariant Hamiltonian we have

$$\begin{aligned}\mathcal{T}H\mathcal{T}^{-1} &= \sum_k \mathcal{T}\psi_k^\dagger H(k)\psi_k\mathcal{T}^{-1} \\ &= \sum_k \mathcal{T}\psi_k^\dagger\mathcal{T}^{-1}\mathcal{T}H(k)\mathcal{T}^{-1}\mathcal{T}\psi_k\mathcal{T}^{-1} \\ &= \sum_k \psi_{-k}^\dagger\mathcal{T}H(k)\mathcal{T}^{-1}\psi_{-k} \\ &= \sum_k \psi_k^\dagger\mathcal{T}H(-k)\mathcal{T}^{-1}\psi_k,\end{aligned} \tag{2.14}$$

so

$$\mathcal{T}H(k)\mathcal{T}^{-1} = H(-k). \tag{2.15}$$

where ψ_k is a given Bloch state. In the Brillouin zone, there are so-called *time-reversal invariant momenta* which satisfy $\boldsymbol{k} = -\boldsymbol{k} + \boldsymbol{G}$ for reciprocal lattice vector $\boldsymbol{G}$. There are four time-reversal invariant momenta in two-dimensions for a square lattice whose lattice constant is a: $\boldsymbol{\Gamma}_1 = (0,0)$, $\boldsymbol{\Gamma}_2 = (0,\pi/a)$, $\boldsymbol{\Gamma}_3 = (\pi/a,0)$, and $\boldsymbol{\Gamma}_4 = (\pi/a,\pi/a)$. In one-dimension and three-dimensions there are two and eight time-reversal invariant momenta, respectively. At these specific points

$$H(\boldsymbol{\Gamma}_i) = H(-\boldsymbol{\Gamma}_i). \tag{2.16}$$

For spinless fermions, we can always choose a representation such that $\mathcal{T} = \mathcal{K}$ which indicates that at the time-reversal invariant momenta for spinless fermions we have,

$$\langle u(\mathbf{\Gamma}_i)|\mathcal{T}u(\mathbf{\Gamma}_i)\rangle \neq 0. \tag{2.17}$$

This means that at the time-reversal invariant momenta, $|u(\mathbf{\Gamma}_i)\rangle$ is not orthogonal to its time-reversal partner. In other words, for a spinless system the presence of time-reversal symmetry does not guarantee the existence of band degeneracy at the time-reversal invariant momenta.

Let us now turn to the spinful case which is what we have in nature. As the spin operator is a specific type of angular momentum operator, then

$$\mathcal{T}\boldsymbol{S}\mathcal{T}^{-1} = -\boldsymbol{S}, \tag{2.18}$$

which can be understood as a π rotation about an axis. The conventional choice is usually the y axis. Accordingly, the time-reversal operator is given by

$$\mathcal{T} = e^{-i\frac{\pi S_y}{\hbar}}\mathcal{K}, \tag{2.19}$$

where $\mathcal{K}$ denotes complex conjugation. Then, the square of $\mathcal{T}$ gives

$$\begin{aligned}\mathcal{T}^2 &= e^{-i\frac{\pi S_y}{\hbar}}\mathcal{K}e^{-i\frac{\pi S_y}{\hbar}}\mathcal{K} \\ &= e^{-i\frac{\pi S_y}{\hbar}}e^{i\frac{\pi S_y^*}{\hbar}} \\ &= e^{-2i\frac{\pi S_y}{\hbar}},\end{aligned} \tag{2.20}$$

where we used $\mathcal{K}^2 = 1$. For integer spin, as the eigenvalue of S_y is an integer of $\hbar$, we always have $\mathcal{T}^2 = 1$ similar to the spinless case. However, for half-integer spin systems

$$e^{-i\frac{\pi S_y}{\hbar}} = e^{-i\frac{\pi\sigma_y}{2}} = \sum_{n=0}^{\infty}\frac{1}{n!}(-\frac{i\pi\sigma_y}{2})^n = -i\sigma_y, \tag{2.21}$$

then

$$\mathcal{T}^2 = -1, \tag{2.22}$$

which is different compared with the previous cases. As we promised, this opposite sign leads to an important impact on the band structure, which will be shown shortly. Also, the form of time-reversal operator for half-integer spin systems is

$$\mathcal{T}c_{j,\alpha,\sigma}\mathcal{T}^{-1} = i(\sigma_y)_{\sigma,\sigma'}c_{j,\alpha,\sigma'}, \tag{2.23}$$

or equivalently

$$\mathcal{T}c_{j,\alpha,\uparrow}\mathcal{T}^{-1} = c_{j,\alpha,\downarrow}, \tag{2.24}$$

$$\mathcal{T} c_{j,\alpha,\downarrow} \mathcal{T}^{-1} = - c_{j,\alpha,\uparrow}. \tag{2.25}$$

It can be easily shown in the momentum space that

$$\mathcal{T} c_{k,\alpha,\sigma} \mathcal{T}^{-1} = i(\sigma_y)_{\sigma,\sigma'} c_{-k,\alpha,\sigma'}, \tag{2.26}$$

and remarkably for both $\mathcal{T}^2 = \pm 1$ cases, Eq. 2.15 is valid. As we have already promised, for half-integer spin systems, the presence of time-reversal symmetry results in Kramers' theorem since $\mathcal{T}^2 = -1$. We have

$$\begin{aligned} \langle u|\mathcal{T}u\rangle &= \sum_{n,m} u_m^* U_{mn} \mathcal{K} u_n \\ &= \sum_{n,m} u_m^* U_{mn} u_n^* \\ &= -\sum_{n,m} u_n^* U_{nm} u_m^* \\ &= -\sum_{n,m} u_n^* U_{nm} \mathcal{K} u_m = -\langle u|\mathcal{T}u\rangle, \end{aligned} \tag{2.27}$$

where we used $U_{\mathcal{T}} = -U_{\mathcal{T}}^T$ in the third line. The above equation indicates that $\langle u|\mathcal{T}u\rangle = 0$ in sharp contrast to Eq. 2.17. In other words, $|u\rangle$ and $\mathcal{T}|u\rangle$ are always orthogonal which is know as Kramers' theorem. At the time-reversal invariant momenta $\mathbf{\Gamma}_i$, as both $|u(\mathbf{\Gamma}_i)\rangle$ and $\mathcal{T}|u(\mathbf{\Gamma}_i)\rangle$ are the eigenvectors of $H(\mathbf{\Gamma}_i)$ for the same energy, the energy band at those special points is always at least doubly degenerate. As this double degeneracy is forced by the Kramers' theorem, it is known as Kramers' degeneracy. The Kramers' degeneracy has a very strong impact on the band structure: if two bands are related by time-reversal symmetry, the two bands have to cross with each other at the time-reversal invariant momenta, so there is no gap between them.

2. **Particle-hole symmetry:** Particle-hole symmetry is represented by an antiunitary operator that anticommutes with the Hamiltonian, *i.e.*

$$\{H, \mathcal{P}\} = 0, \tag{2.28}$$

where $\mathcal{P} = U_{\mathcal{P}}\mathcal{K}$ and similar to the time-reversal symmetry we have $\mathcal{P}^2 = \pm 1$ since it is an antiunitary operator. It should be noted that $\mathcal{P}^2 = -1$ holds only when the spin-rotation symmetry is preserved. In momentum space, it leads to

$$\mathcal{P} H(k) \mathcal{P}^{-1} = -H(-k). \tag{2.29}$$

Particle-hole "symmetry" is naturally a manifestation of a redundancy in *all* the Bogoliubov - de Gennes (BdG) Hamiltonians for describing quasiparticle excitations above

the superconducting ground state at the mean field level. The general BdG Hamiltonian in the momentum space can be written as

$$H_{\mathrm{BdG}} = \begin{pmatrix} H_0(\boldsymbol{k}) & \Delta(\boldsymbol{k}) \\ \Delta^\dagger(\boldsymbol{k}) & -H_0^*(\boldsymbol{k}), \end{pmatrix} \tag{2.30}$$

under the basis $(c_{\boldsymbol{k}},\ c^\dagger_{-\boldsymbol{k}})^{\mathrm{T}}$. Here, $H_0(\boldsymbol{k})$ is the normal state Hamiltonian, and $\Delta(\boldsymbol{k})$ is the superconducting pairing potential. It can be shown that $\mathcal{P}H_{\mathrm{BdG}}(\boldsymbol{k})\mathcal{P}^{-1} = -H(-\boldsymbol{k})$ for $\mathcal{P} = \tau_x\mathcal{K}$ where τ_x is the first Pauli matrix in the particle-hole space. Constructing the BdG Hamiltonian thus involves introducing a redundancy in the basis namely the hole part of the electron-hole or Nambu basis [77], which doubles the degrees of freedom. Although this redundancy leads to a symmetric energy spectrum around zero energy, this is not always the case in the momentum space. If the BdG Hamiltonian has the eigenvalue $E(\boldsymbol{k})$ whose eigenvector is $(\boldsymbol{u_k}, \boldsymbol{v_k})^T$, the particle-hole symmetry guarantees that there must be an eigenvalue $-E(-\boldsymbol{k})$ whose eigenvector is $(\boldsymbol{v}^*_{-\boldsymbol{k}}, \boldsymbol{u}^*_{-\boldsymbol{k}})^T$ where T denotes matrix transpose.

3. **Chiral symmetry:** Chiral symmetry is a unitary operator that anticommutes with the Hamiltonian, *i.e.*

$$\{H, \mathcal{S}\} = 0. \tag{2.31}$$

Although the square of chiral symmetry can be taken to be any complex phase, a gauge can be always chosen such that $\mathcal{S}^2 = 1$. However, this gauge choice will have no effect on the signs of both $\mathcal{T}^2$ and $\mathcal{P}^2$ according to Eq. 2.7. In the momentum space, chiral symmetry leads to

$$\mathcal{S}H(k)\mathcal{S}^{-1} = -H(k). \tag{2.32}$$

Furthermore, whenever the system has both $\mathcal{T}$ and $\mathcal{P}$ symmetry, then it also has $\mathcal{S} = \mathcal{T}\mathcal{P}$ symmetry although $\mathcal{S}$ can also be present when both $\mathcal{T}$ and $\mathcal{P}$ are absent. It should be noted that although chiral symmetry is a unitary operator, it does not commute with the Hamiltonian as the common symmetry operators. Moreover, contrary to particle-hole symmetry, chiral symmetry always leads to a symmetric energy spectrum around zero energy in both real and momentum space.

A whole new chapter of condensed matter physics was opened with the experimental discovery of quantum Hall effect [4]. Consequent theoretical studies [7, 78] revealed that this phenomenon has a topological origin. Topological considerations had not been foreign to condensed matter physics, for example they had been extensively used in the study of order parameter defects [79]. But the quantum Hall state was different, because here topology entered the description of the phase transition and the ordered ground state. A decade ago, the study of topological aspects of condensed matter systems underwent a second revolution with the theoretical proposal [11, 12, 18] and the consequent experimental discovery[19, 26] of

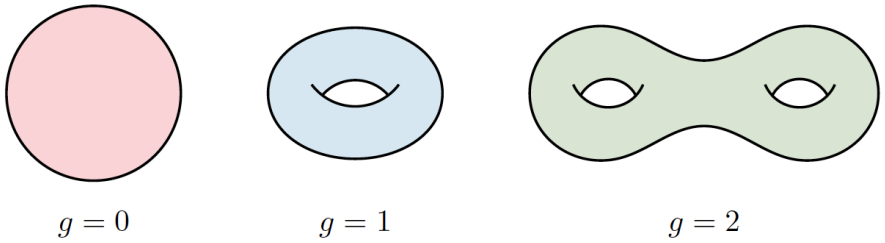

Figure 2.1: (Color online) The genus g of a closed two-dimensional surface is a topological invariant which counts the number of "holes" or "handles" in the surface.

topological insulators. These breakthrough discoveries revealed that a phase of matter with a gap in the bulk excitation spectrum is characterized not only by its symmetry, but also by certain topological quantities called *topological invariants* or *topological indices*. Whenever two phases of matter differ in their topological invariants, they cannot be evolved into one another without hitting a *topological phase transition*: a phase transition in which the underlying topology of the system changes. In such transitions, the gap in the bulk excitation spectrum has to temporarily close at the transition point if all the Hamiltonian's symmetries remain unbroken.

In mathematics, topology is the study of the properties of objects that do not change under continuous deformation. Continuous deformation means stretching, twisting, bending or any other transformation that does not involve abrupt changes such as tearing the object or breaking it apart. If it is possible to continuously deform an object into another, then the objects are topologically the same and they have the same topological invariant or topological index; otherwise, they are topologically distinct. In Fig. 2.1, three topologically distinct two-dimensional surfaces with different values of genus or "handles" g as a well-defined topological invariant are shown. Since these surfaces have different topological invariants, they are topologically distinct, and they cannot convert to each other under continuous deformation.

Topology in condensed matter physics is the study of the properties of Hamiltonians with an energy gap under continuous deformations. Here, continuous deformations are transformations that do not close the energy gap. Therefore, two gapped Hamiltonians are topologically the same if one of them can be deformed into the other one without closing the gap and breaking certain symmetries.

A nontrivial value of topological invariant in a system with gapped Hamiltonian has interesting consequences at its boundaries. As an example, consider the interface between two topologically distinct systems (each described by a Hamiltonian that is gapped in the bulk) like the interface between an ordinary or trivial insulator with topological index zero and a quantum hall insulator with topological index or Chern number one as in Fig. 2.2(a). Moving from one side to the other across the interface results in changing the topological index. As we already explained, this must close the bulk gap at the interface as in Fig. 2.2(b), so some

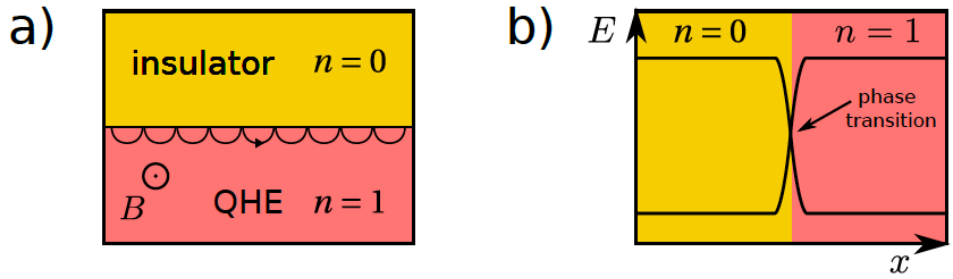

Figure 2.2: (Color online) (a) Edge states in the quantum Hall effect system. A magnetic field causes electrons to move in cyclotron orbits. Close to the interface with the ordinary insulator electrons bounce back from the edge and effectively travel along it. (b) Schematic view of the bulk-edge correspondence: at the interface between two materials with different topological invariants the energy gap vanishes. Therefore, there must be a low energy state bound to this region.

states may exist in the gap but because the bulk Hamiltonian on both sides are gapped, these metallic *boundary states* or *edge states* have to be localized at the interface [80, 81].

All these fundamental relationships between symmetry and topology in a system play a crucial role in the field of topological phases of matter and leads to the so-called *bulk-boundary correspondence* which states that there is a direct connection between the topology and the symmetries of a given Hamiltonian and its edge states.

2.3 Tenfold ways of classifying non-interacting fermionic gapped Hamiltonians

In this section, we review the complete topological classification of non-interacting fermionic gapped Hamiltonians based on the spatial dimension d of the system, and based on the presence or absence of their global symmetries, *i.e.* time-reversal symmetry ($\mathcal{T}$), particle-hole symmetry ($\mathcal{P}$), and chiral symmetry ($\mathcal{S}$) according to the Altland and Zirnbauer symmetry classification [40, 41, 73, 82] as summarized in Table 2.1.

Based on the presence or absence of time-reversal and particle-hole symmetries and the sign of their square operator, there are $3 \times 3 = 9$ different symmetry classes. Although the presence or absence of the chiral symmetry is determined by the time-reversal and particle-hole symmetries, there is a very special case where $\mathcal{S}$ is a symmetry of the system when both time-reversal and particle-hole symmetries are broken. This case raises the number of symmetry classes from nine to ten. Therefore, there are ten ways to combine all the possible symmetries of a one-particle non-interacting fermionic gapped Hamiltonian; this classification is called the *periodic table of topological insulators and topological superconductors* for each spatial dimension [42]. For example, the Hamiltonian may have no such symmetries at all like the two-dimensional integer quantum Hall effect or Chern insulators. This Hamiltonian

		$\mathcal{T}$	$\mathcal{P}$	$\mathcal{S}$	$d=1$	$d=2$	$d=3$
Standard (Wigner-Dyson)	A (unitary)	0	0	0	–	$\mathbb{Z}$	–
	AI (orthogonal)	+1	0	0	–	–	–
	AII (symplectic)	−1	0	0	–	$\mathbb{Z}_2$	$\mathbb{Z}_2$
Chiral (sublattice)	AIII (chiral unitary)	0	0	1	$\mathbb{Z}$	–	$\mathbb{Z}$
	BDI (chiral orthogonal)	+1	+1	1	$\mathbb{Z}$	–	–
	CII (chiral symplectic)	−1	−1	1	$\mathbb{Z}$	–	$\mathbb{Z}_2$
BdG	D	0	+1	0	$\mathbb{Z}_2$	$\mathbb{Z}$	–
	C	0	−1	0	–	$\mathbb{Z}$	–
	DIII	−1	+1	1	$\mathbb{Z}_2$	$\mathbb{Z}_2$	$\mathbb{Z}$
	CI	+1	−1	1	–	–	$\mathbb{Z}$

Table 2.1: The ten possible classes of single-particle non-interacting fermionic gapped Hamiltonians. They are classified according to the presence or absence of time-reversal symmetry ($\mathcal{T}$), particle-hole symmetry ($\mathcal{P}$), and chiral symmetry ($\mathcal{S}$) in spatial dimensions $d = 1, 2, 3$. In the third to the fifth columns 0 denotes the absence of a symmetry and ± 1 presents the value to which the associated operator squares if present. In the last three columns $\mathbb{Z}_2$ denotes two kinds of topologically distinct ground states, $\mathbb{Z}$ indicates that the topologically distinct ground states can be labeled by an integer, and "–" means no topological phases. The information inside this table adapted from Ref. [73].

is said to be in class A. Class AII corresponds to the quantum spin Hall insulators or two-dimensional topological insulators in $d = 2$, and three-dimensional topological insulators in $d = 3$. Class BDI in $d = 1$, corresponds to the Su-Schrieffer-Heeger model.

Moreover, such a classification is for quadratic or non-interacting fermionc systems with an energy gap. If there is additional symmetries such as mirror symmetry, then a class could be further divided to several subclasses. The classification of interacting Hamiltonians is still under progress. A non-interacting bosonic system cannot have an energy gap without the exclusion principle, so one cannot find topological invariants for free bosons by the same formalism for classification gapped Hamiltonian. Although different approaches were developed to obtain this classification such as Clifford algebra, homotopy theory, K-theory, and random matrix theory, the agreement of the classification results is not a trivial fact but it is the core of bulk-boundary correspondence.

All ten Altland and Zirnbauer symmetry classes can be grouped into three main categories: the three Wigner-Dyson or standard symmetry classes, the three chiral symmetry classes, and the four Bogoliubov-de Gennes (BdG) symmetry classes. Chiral symmetry classes can be obtained from Wigner-Dyson symmetry classes by imposing an additional chiral symmetry (Table 2.1). It turned out that there are five non-interacting distinct topological insulators and superconductors in each spatial dimension. Nevertheless, not all of them have found an experimental realization. This poses a continuous challenge to condensed matter physics.

Therefore, the road ahead is not entirely mapped and needs further investigation.

In 2009, Kitaev recognized the Bott periodicity is hidden in Altland and Zirnbauer's table [43]. He thus was able to generalize the classification to all spatial dimensions which is a culmination of the study of topological materials. Two classes A and AIII belong to so called *complex classes* if they have a period of two while the remaining eight classes belong to *the real classes* which have a period of eight. That is, the topological invariants in dimension $d+2$ and $d+8$ are the same as those in dimension d for the complex and the real classes, respectively. According to this periodicity, some interesting conclusions can be drawn. To name a few, the quantum Hall effect (class A) can happen only in even spatial dimensions, or the topology of class AIII is nontrivial only in odd spatial dimensions.

2.4 Berry Phase and charge polarization in crystalline materials

In 1984, Michael Berry in his seminal paper defined a geometric phase or a Berry phase as a quantity that is accumulated around a closed loop as a complex vector is carried around a path in its vector space [83]. These complex vectors can be taken to be unit vectors for the sake of simplicity. Let us take N complex vectors $|u_0\rangle$ to $|u_{N-1}\rangle$ around a closed loop and define the global product z as

$$z = \langle u_0|u_1\rangle\langle u_1|u_2\rangle \dots \langle u_{N-1}|u_0\rangle = |z|e^{i\phi}. \tag{2.33}$$

Then, the geometric phase or the Berry phase is defined as,

$$\phi = \mathrm{Im}(\ln z) = \mathrm{Im}(\ln \sum_{i=0}^{N-1} \langle u_i|u_{i+1}\rangle), \tag{2.34}$$

where $\mathrm{Im}(z)$ is the imaginary part of a complex number z[1]. As is obvious, for real vectors we have $\phi = 0$ since the global product is always a real number with no imaginary part. Importantly, the Berry phase is independent of the phase of each $|u_i\rangle$, so it is a gauge-invariant modulo 2π quantity. In the continuum limit, the path can be parametrized by a real parameter $0 \leqslant \lambda \leqslant 1$ such that $|u_{\lambda=0}\rangle = |u_{\lambda=1}\rangle$ and $|u_\lambda\rangle$ is a smoth and differentiable function of λ. Hence, in the continuum limit in Eq. 2.34 we will have

$$\begin{aligned}\ln\langle u_\lambda|u_{\lambda+d\lambda}\rangle =& \ln\langle u_\lambda|\{|u_\lambda\rangle + d\lambda\frac{d|u_\lambda\rangle}{d\lambda} + \dots\}\\ =& \ln(1 + d\lambda\langle u_\lambda|\partial_\lambda u_\lambda\rangle + \dots)\end{aligned}$$

[1]Note that the sign convention is not universal in Eq. 2.34, as in the literature both $\phi = \pm\mathrm{Im}(\ln z)$ have been used as the definition of Berry phase.

$$=d\lambda\langle u_\lambda|\partial_\lambda u_\lambda\rangle + \dots, \tag{2.35}$$

where $\partial_\lambda = \dfrac{d}{d\lambda}$ and we used $\ln(1+x) \simeq x$ approximation. Therefore, in the continuum limit

$$\phi = \mathrm{Im} \oint d\lambda \ \langle u_\lambda|\partial_\lambda u_\lambda\rangle. \tag{2.36}$$

Since

$$0 = \partial_\lambda\langle u_\lambda|u_\lambda\rangle = \langle u_\lambda|\partial_\lambda u_\lambda\rangle + \langle \partial_\lambda u_\lambda|u_\lambda\rangle = 2\mathrm{Re}(\langle u_\lambda|\partial_\lambda u_\lambda\rangle), \tag{2.37}$$

the value of $\langle u_\lambda|\partial_\lambda u_\lambda\rangle$ is a purely imaginary number, so Eq. 2.36 can be rewritten as the simpler form

$$\phi = -\oint d\lambda \ \langle u_\lambda|i\partial_\lambda|u_\lambda\rangle, \tag{2.38}$$

which is the well-known expression for the Berry phase in the continuous limit. The *Berry connection* or *Berry potential* is defined as

$$A(\lambda) = -\langle u_\lambda|i\partial_\lambda|u_\lambda\rangle = \mathrm{Im}\langle u_\lambda|\partial_\lambda|u_\lambda\rangle, \tag{2.39}$$

so

$$\phi = \oint A(\lambda) \ d\lambda. \tag{2.40}$$

In contrast to the Berry phase which is gauge-invariant modulo 2π, the Berry connection is not since if we do the gauge transformation

$$|\tilde{u}_\lambda\rangle = e^{-i\alpha(\lambda)}|u_\lambda\rangle, \tag{2.41}$$

we will have

$$\tilde{A}(\lambda) = -\langle \tilde{u}_\lambda|i\partial_\lambda|\tilde{u}_\lambda\rangle = A(\lambda) - \frac{d\alpha(\lambda)}{d\lambda}, \tag{2.42}$$

where

$$\alpha(\lambda = 1) - \alpha(\lambda = 0) = 2\pi n, \tag{2.43}$$

since $|\tilde{u}_{\lambda=0}\rangle = |\tilde{u}_{\lambda=1}\rangle$ for $n \in \mathbb{Z}$. All the gauge transformations given by Eq. 2.41 can be classified topologically according to the integer n in Eq. 2.43 which is known as the *winding number*. In a two-dimensional parameter space $\boldsymbol{\lambda} = (\lambda_x, \lambda_y)$, the Berry connection can be generalized to a two-dimensional vector $\boldsymbol{A} = (A_x, A_y)$ where

$$A_x = -\langle u_{\boldsymbol{\lambda}}|i\partial_{\lambda_x}|u_{\boldsymbol{\lambda}}\rangle, \tag{2.44}$$

$$A_y = -\langle u_{\boldsymbol{\lambda}}|i\partial_{\lambda_y}|u_{\boldsymbol{\lambda}}\rangle, \tag{2.45}$$

so, the Berry phase can be written as a line integral around a closed path

$$\phi = \oint \boldsymbol{A} \cdot d\boldsymbol{\lambda}. \tag{2.46}$$

According to the Stokes' theorem, Eq. 2.46 can be rewritten in term of the *Berry curvature*

$$\boldsymbol{\Omega}(\boldsymbol{\lambda}) = \boldsymbol{\nabla} \times \boldsymbol{A}(\boldsymbol{\lambda}), \tag{2.47}$$

so

$$\phi = \int_s \boldsymbol{\Omega}(\boldsymbol{\lambda}) \cdot \boldsymbol{ds}, \tag{2.48}$$

where region s is bounded by the closed path in the positive sense of circulation, so the *Berry flux* through a surface is equal to the Berry phase around its boundary. The Berry curvature similar to the Berry phase is gauge invariant.

These concepts can be even generalized to higher-dimensional parameter spaces. According to the Chern theorem, the Berry flux computed on any closed two-dimensional surface is quantized to 2π times an integer. This integer is known as *the Chern number* of that surface. In the context of the integer quantum Hall effect, this topological index ν (Eq. 1.1) is known as the TKNN number or the first Chern number, which is proportional to the surface integral of the Berry curvature over the two-dimensional Brillouin zone [7].

So far, we have explained very briefly Berry phase, Berry connection, Berry curvature, and Berry flux for some $|u_{\boldsymbol{\lambda}}\rangle$ in a generic parameter space $\boldsymbol{\lambda} = (\lambda_1, \lambda_2, \dots)$. We now turn to the main theme in condensed matter where the parameters are the wavevectors $\boldsymbol{k}$, which labels Bloch states $|\psi_{n,\boldsymbol{k}}\rangle$ of band n in the Brillouin zone. For an electron moving in the periodic potential of ions with heavy mass in a lattice, its dynamics is governed by the following Hamiltonian,

$$H(\boldsymbol{p}, \boldsymbol{r}) = \frac{p^2}{2m} + V(\boldsymbol{r}), \tag{2.49}$$

where $\boldsymbol{p} = \hbar\boldsymbol{k}$, m is the mass of electron, $V(\boldsymbol{r} + \boldsymbol{a}) = V(\boldsymbol{r})$, and $\boldsymbol{a}$ is the translation invariant vector of the lattice. Then according to the Bloch theorem,

$$|\psi_{n,\boldsymbol{k}}\rangle = e^{i\boldsymbol{k}\cdot\boldsymbol{r}}|u_{n,\boldsymbol{k}}(\boldsymbol{r})\rangle, \tag{2.50}$$

is the eigenfunction of the above Hamiltonian with energy $E_n(\boldsymbol{k})$, and $|u_{n,\boldsymbol{k}}(\boldsymbol{r})\rangle$ is the so-called cell periodic function and satisfies $|u_{n,\boldsymbol{k}}(\boldsymbol{r})\rangle = |u_{n,\boldsymbol{k}}(\boldsymbol{r} + \boldsymbol{a})\rangle$. Therefore, a Berry phase associated with band n takes the form

$$\phi_n = \oint \boldsymbol{A}_n(\boldsymbol{k}) \cdot d\boldsymbol{k}. \tag{2.51}$$

The Berry connection is

$$A_{n,\mu}(\boldsymbol{k}) = \langle u_{n,\boldsymbol{k}}|i\partial_\mu|u_{n,\boldsymbol{k}}\rangle \tag{2.52}$$

where $\partial_\mu = \dfrac{\partial}{\partial k_\mu}$. This can be also rewritten as

$$\boldsymbol{A}_n(\boldsymbol{k}) = \langle u_{n,\boldsymbol{k}} | i\boldsymbol{\nabla}_{\boldsymbol{k}} | u_{n,\boldsymbol{k}} \rangle. \tag{2.53}$$

Similarly, the Berry curvature is defined as

$$\boldsymbol{\Omega}_n(\boldsymbol{k}) = \boldsymbol{\nabla}_{\boldsymbol{k}} \times \boldsymbol{A}_n(\boldsymbol{k}). \tag{2.54}$$

We have assumed so far that band n is non-degenerate through the whole Brillouin zone. This is a significant restriction since the degeneracy between bands is common in crystalline materials. When degeneracies occur, they usually introduce a nonanalytic dependence of $|\psi_{n,\boldsymbol{k}}\rangle$ on $\boldsymbol{k}$ which is problematic for the definition of the Berry connection and Berry curvature. Nevertheless, when the bands are degenerate, all these quantities are needed to be generalized to the non-Abelian case[2].

One thing that should be emphasized here is that in the presence of certain symmetries, these quantities are forced to take certain values. The presence of inversion symmetry forces the Berry connection (the Berry curvature) to be an odd (even) function of momentum. Consider that a crystal has inversion symmetry, then

$$u_{n,\boldsymbol{k}}(\boldsymbol{r}) = u_{n,-\boldsymbol{k}}(-\boldsymbol{r}). \tag{2.55}$$

Consequently,

$$\begin{aligned} \boldsymbol{A}_n(\boldsymbol{k}) &= i\langle u_{n,\boldsymbol{k}} | \boldsymbol{\nabla}_{\boldsymbol{k}} | u_{n,\boldsymbol{k}} \rangle \\ &= i\langle u_{n,-\boldsymbol{k}} | \boldsymbol{\nabla}_{\boldsymbol{k}} | u_{n,-\boldsymbol{k}} \rangle \\ &= -i\langle u_{n,-\boldsymbol{k}} | \boldsymbol{\nabla}_{-\boldsymbol{k}} | u_{n,-\boldsymbol{k}} \rangle \\ &= -\boldsymbol{A}_n(-\boldsymbol{k}). \end{aligned} \tag{2.56}$$

For the Berry curvature, we have

$$\begin{aligned} \boldsymbol{\Omega}_n(\boldsymbol{k}) &= \boldsymbol{\nabla}_{\boldsymbol{k}} \times \boldsymbol{A}_n(\boldsymbol{k}) \\ &= \boldsymbol{\nabla}_{\boldsymbol{k}} \times [-\boldsymbol{A}_n(-\boldsymbol{k})] \\ &= \boldsymbol{\nabla}_{-\boldsymbol{k}} \times \boldsymbol{A}_n(-\boldsymbol{k}) \\ &= \boldsymbol{\Omega}_n(-\boldsymbol{k}). \end{aligned} \tag{2.57}$$

However, the presence of time-reversal symmetry forces the Berry connection (the Berry curvature) to be an even (odd) function of momentum. Thus an integration of the Berry curvature over the whole Brillouin zone gives zero value for a time-reversal invariant system. This indicates that the realization of a system with finite Chern number requires breaking

[2]For more comprehensive understanding, the author recommends the excellent review [74].

time-reversal symmetry which is the case in both quantum Hall effect and Chern insulators. Consider that a crystal has time-reversal symmetry, then

$$u_{n,\boldsymbol{k}}(\boldsymbol{r}) = u^*_{n,-\boldsymbol{k}}(\boldsymbol{r}). \tag{2.58}$$

Consequently,

$$\begin{aligned}
\boldsymbol{A}_n(\boldsymbol{k}) &= i\langle u_{n,\boldsymbol{k}}|\boldsymbol{\nabla}_{\boldsymbol{k}}|u_{n,\boldsymbol{k}}\rangle \\
&= i\langle u^*_{n,-\boldsymbol{k}}|\boldsymbol{\nabla}_{\boldsymbol{k}}|u^*_{n,-\boldsymbol{k}}\rangle \\
&= (u_{n,-\boldsymbol{k}})_a(i\boldsymbol{\nabla}_{\boldsymbol{k}})_{ab}(u^*_{n,-\boldsymbol{k}})_b \\
&= (u^*_{n,-\boldsymbol{k}})_b(i\boldsymbol{\nabla}_{\boldsymbol{k}})^*_{ba}(u_{n,-\boldsymbol{k}})_a \\
&= -i\langle u_{n,-\boldsymbol{k}}|\boldsymbol{\nabla}_{\boldsymbol{k}}|u_{n,-\boldsymbol{k}}\rangle \\
&= i\langle u_{n,-\boldsymbol{k}}|\boldsymbol{\nabla}_{-\boldsymbol{k}}|u_{n,-\boldsymbol{k}}\rangle \\
&= \boldsymbol{A}_n(-\boldsymbol{k}).
\end{aligned} \tag{2.59}$$

For the Berry curvature, we have

$$\begin{aligned}
\boldsymbol{\Omega}_n(\boldsymbol{k}) &= \boldsymbol{\nabla}_{\boldsymbol{k}} \times \boldsymbol{A}_n(\boldsymbol{k}) \\
&= \boldsymbol{\nabla}_{\boldsymbol{k}} \times \boldsymbol{A}_n(-\boldsymbol{k}) \\
&= -\boldsymbol{\nabla}_{-\boldsymbol{k}} \times \boldsymbol{A}_n(-\boldsymbol{k}) \\
&= -\boldsymbol{\Omega}_n(-\boldsymbol{k}).
\end{aligned} \tag{2.60}$$

It is clear that the presence of both time-reversal symmetry and inversion symmetry forces $\boldsymbol{\Omega}_n(\boldsymbol{k}) = 0$.

The rest of this section is devoted to making a connection between Berry phase and charge polarization in a crystalline material which is the core of *the modern theory of polarization in crystalline insulators*. In an insulator, the electrons are localized around the ions. When the charge centers of electrons are displaced away from the ions, the intrinsic polarization is finite. In crystals, the polarization density is more useful than polarization owing to the periodic structure in the real space. The polarization density $\boldsymbol{P}_\rho$ is the sum of the electric dipole moments within one unit cell. For a periodic lattice, however, the choice of unit cell is not unique as shown in Fig. 2.3 as an example.

In this figure, we choose two different unit cells. In (I), the unit cell contains an electron (blue dot) and its left ion (red dot) and

$$\boldsymbol{P}^I_\rho = -e\boldsymbol{d}, \tag{2.61}$$

where $\boldsymbol{d}$ is the vector from the ion to its nearest-neighbor electron on the right side. In (II), the unit cell contains the electron and its right ion and

$$\boldsymbol{P}^{II}_\rho = e(\boldsymbol{a} - \boldsymbol{d}), \tag{2.62}$$

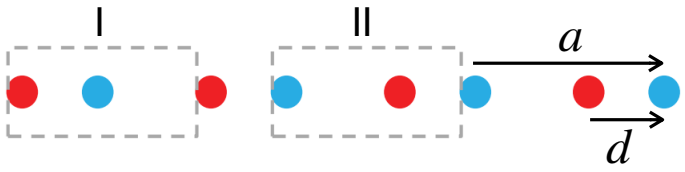

Figure 2.3: (Color online) The two dashed rectangles correspond to two different choices of unit cell. The lattice constant is a and the distance between the ion (red dot) and the electron (blue dot) inside each unit cell is d. In the case I, the electron is on the right side of the ion while the electron is on the left side of the ion in case II.

where $\boldsymbol{a}$ is the vector from the electron to its nearest-neighbour electron on the right side. It is readily seen that the two kinds of unit cells results in different polarization density indicating that the polarization density itself is not well defined.

However, it turns out that the change of polarization density does not depend on the choice of unit cell and thus is well defined and can readily be measured in experiments. For instance, we consider that the charge center of the electron moves to the right $\delta\boldsymbol{d}$. For the first case, we will have

$$\Delta \boldsymbol{P}_{\rho}^{I} = -e(\boldsymbol{d} + \delta\boldsymbol{d}) - (-e\boldsymbol{d}) = -e\ \delta\boldsymbol{d}, \tag{2.63}$$

and for the second case,

$$\Delta \boldsymbol{P}_{\rho}^{II} = e(\boldsymbol{a} - \boldsymbol{d} - \delta\boldsymbol{d}) - e(\boldsymbol{a} - \boldsymbol{d}) = -e\ \delta\boldsymbol{d}. \tag{2.64}$$

Such a key observation was made firstly by Resta in 1992 [84] based on previous works by Berry [83] and Zak [85]. About one year later, King-Smith and Vanderbilt found that the polarization density is closely related to the Berry phase, establishing the modern theory of polarization in crystalline insulators [86, 87]. This theory is formulated in terms of Berry phases, which account for the dipole moment densities in the bulk of a material. When the dipole moment densities vary over time, electronic currents appear across the bulk of the material where the polarization is changing. If this adiabatic evolution of the insulating Hamiltonian is carried over closed cycles, the electronic transport is quantized [86–88]. This quantization is given by a Chern number and in systems with charge conservation, is closely related to the Hall conductance of a Chern insulator [7].

To show this in an intuitive way, we consider a one-dimensional insulator with N lattice sites labeled as $R_l = la$. To keep the notation simple, we set $a = 1$ and use the Wannier representation to define polarization. The Wannier state is a Fourier transformation of the Bloch state,

$$|n, R_l\rangle = \frac{1}{\sqrt{N}} \sum_{k} e^{-ikR_l} |\psi_{n,k}\rangle, \tag{2.65}$$

where $|\psi_{n,k}\rangle = e^{ikx}|u_{n,k}\rangle$. The Bloch state and Wannier state satisfy the following algebra,

$$\langle \psi_{n',k'} | \psi_{n,k} \rangle = \delta_{n,n'}\delta_{k,k'}, \tag{2.66}$$

$$\langle n', R_{l'}|n, R_l\rangle = \delta_{n,n'}\delta_{l,l'}. \tag{2.67}$$

In the Wannier representation, the polarization can be defined in a natural way,

$$\begin{aligned} P &= -e\sum_{n\in\text{occ}}\sum_{l}\langle n, R_l|x - R_l|n, R_l\rangle \\ &= -\frac{e}{N}\sum_{n\in\text{occ}}\sum_{l}\sum_{k,k'}\langle u_{n,k'}|e^{ik'(R_l-x)}\frac{1}{i}\frac{\partial}{\partial k}(e^{ik(x-R_l)})|u_{n,k}\rangle \\ &= -\frac{e}{N}\sum_{n\in\text{occ}}\sum_{l}\sum_{k,k'}e^{-i(k-k')R_l}e^{i(k-k')x}\langle u_{n,k'}|i\frac{\partial}{\partial k}|u_{n,k}\rangle \\ &= -e\sum_{n\in\text{occ}}\sum_{k}\langle u_{n,k}|i\frac{\partial}{\partial k}|u_{n,k}\rangle, \end{aligned} \tag{2.68}$$

so the polarization density then is

$$\begin{aligned} P_\rho = \frac{P}{N} &= -e\sum_{n\in\text{occ}}[\frac{1}{N}\sum_{k}\langle u_{n,k}|i\frac{\partial}{\partial k}|u_{n,k}\rangle] \\ &= -e\sum_{n\in\text{occ}}\int_0^{2\pi}\frac{dk}{2\pi}A_n(k) \\ &= -e\frac{\phi}{2\pi}, \end{aligned} \tag{2.69}$$

where $A_n(k)$ is the Berry connection and ϕ is the associated Berry phase which is also know as the *Zak phase* [85]. This fundamental connection will become clearer in the rest of this chapter. In particular, in order to calculate the topological invariants for both two and three-dimensional topological insulators in class AII, one needs to define a $\mathbb{Z}_2$ time-reversal charge polarization [89, 90]. Also, higher multipole moments such as quadrupole moment or octupole moment can lead to higher-order topological phases of matter.

2.5 Topological insulators

In this section, we will study the topological insulators in one, two, and three spatial dimensions.

2.5.1 TIs in 1D: The SSH model

The Su-Schrieffer-Heeger (SSH) model was originally proposed to describe the electronic structure of polyacetylene $(C_2H_2)_n$ as one of the first organic conductive polymers discovered upon doping [81] . This model is a one-dimensional toy model which can realize the topological

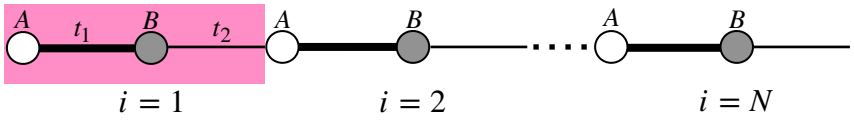

Figure 2.4: (Color online) A schematic figure of the Su-Schrieffer-Heeger (SSH) model which is a chain consisting of N unit cells where each unit cell, denoted by a pink rectangle, hosts two sites, one on sublattice A (empty circles) and the other one on sublattice B (filled circles) with staggered hopping amplitude t_1 (thick lines) for intracell hopping and t_2 (thin lines) for intercell hopping. Each sublattice hosts a single state.

band insulator phase. It describes spinless fermions hopping on a chain consisting of N unit cells where each unit cell hosts two sites; one on sublattice A and the other one on sublattice B, with staggered hopping amplitude t_1 (thick lines) for intracell hopping and t_2 (thin lines) for intercell hopping as shown in Fig. 2.4. For the sake of simplicity, we take both hopping amplitudes to be real and nonnegative *i.e.* $t_{1,2} \geqslant 0$. It is noteworthy that this model appeared before the discovery of quantum Hall effect [4].

We are interested in the ground state and the low-lying excitations of the SSH model at zero temperature and zero chemical potential (half filling) where all negative energy eigenstates of the Hamiltonian are singly occupied due to the Pauli exclusion principle. The dynamics of electrons are described by the following single-particle Hamiltonian since interactions between electrons are neglected,

$$\mathcal{H} = t_1 \sum_{i=1}^{N} c_{i,A}^{\dagger} c_{i,B} + t_2 \sum_{i=1}^{N-1} c_{i+1,A}^{\dagger} c_{i,B} + h.c., \tag{2.70}$$

where $c_{i,\alpha}^{\dagger}$ ($c_{i,\alpha}$) create (annihilate) an electron in the i-th unit cell on sublattice $\alpha \in \{A, B\}$. The long chain of the SSH model has a long bulk in the central part and two boundaries at the two ends of the chain. We first concentrate on the bulk since in the thermodynamic limit of $N \to \infty$ it is much larger than the boundaries and it will determine the most important physical properties of the model. The physics in the bulk in the thermodynamic limit should not depend on how the edges are defined, so for simplicity we set periodic boundary conditions and perform a Fourier transform due to the translational invariance by using

$$c_{i,\alpha} = \frac{1}{\sqrt{N}} \sum_{i} e^{ikr_i} c_{k,\alpha}, \tag{2.71}$$

where k is the momentum. The corresponding Bloch Hamiltonian reads

$$\begin{aligned}\mathcal{H} &= \sum_k (t_1 + t_2 e^{-ika}) c^\dagger_{k,A} c_{k,B} + \text{h.c.} \\ &= \sum_k \begin{pmatrix} c^\dagger_{k,A} & c^\dagger_{k,B} \end{pmatrix} \begin{pmatrix} 0 & t_1 + t_2 e^{-ika} \\ t_1 + t_2 e^{ika} & 0 \end{pmatrix} \begin{pmatrix} c_{k,A} \\ c_{k,B} \end{pmatrix} \\ &= \sum_k \begin{pmatrix} c^\dagger_{k,A} & c^\dagger_{k,B} \end{pmatrix} H(k) \begin{pmatrix} c_{k,A} \\ c_{k,B} \end{pmatrix},\end{aligned} \tag{2.72}$$

where

$$H(k) = \boldsymbol{d}(k) \cdot \boldsymbol{\sigma}. \tag{2.73}$$

Here, $\boldsymbol{\sigma} = (\sigma_x, \sigma_y, \sigma_z)$ where $\sigma_{x,y,z}$ are Pauli matrices acting on the sublattice indices, and $\boldsymbol{d}(k) = (d_x(k), d_y(k), d_z(k))$ for

$$d_x(k) = t_1 + t_2 \cos ka, \tag{2.74}$$

$$d_y(k) = t_2 \sin ka, \tag{2.75}$$

$$d_z(k) = 0. \tag{2.76}$$

The energy spectrum of this Hamiltonian is

$$\begin{aligned}E_\pm(k) = \pm|\boldsymbol{d}(k)| &= \pm\sqrt{(t_1 + t_2 \cos ka)^2 + (t_2 \sin ka)^2} \\ &= \pm\sqrt{(t_1 - t_2)^2 + 4 t_1 t_2 \cos^2 \frac{ka}{2}},\end{aligned} \tag{2.77}$$

which has intentionally been written in the second line form such that the eigenvalues of both the undimerized ($t_1 = t_2$) and dimerized $t_1 \neq t_2$ cases can be studied more easily. For the sake of simplicity, we set $a = 1$ in the following.

We show this dispersion relation for five choices of the parameters in Fig. 2.5. For the dimerized chain, the SSH model describes an insulator with an energy gap of $2|t_1 - t_2|$ separating the lower (filled band) from the upper (empty band). However, for the undimerized case, it is a conductor where there is no energy gap in the first Brillouin zone. As the gap due to the staggering of the hopping amplitudes opens at $k = \pm\pi$, the energy of occupied states is lowered although the energy of unoccupied states is raised. Thus, the staggering is energetically favourable which is know as *the Peierls instability*. Therefore, the dimerized case occurs naturally in many solid state systems.

Moreover, as the dimerized case corresponds to two distinct dimerizations $t_1 - t_2 < 0$ and $t_1 - t_2 > 0$, it is apparent that the case $t_1 = t_2$ corresponds to the critical point of the transition between the two different types of dimerization. According to the energy spectra,

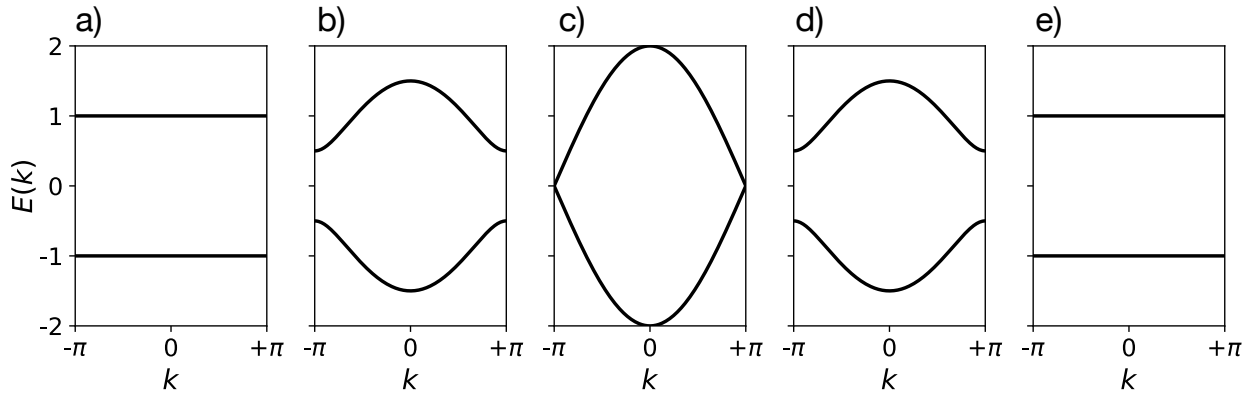

Figure 2.5: The band structure of the SSH model at half filling ($\mu = 0$) for different values of intracell and intercell hopping amplitudes: a) $t_1 = 1$, $t_2 = 0$, b) $t_1 = 1$, $t_2 = 0.5$, c) $t_1 = t_2 = 1$, d) $t_1 = 0.5$, $t_2 = 1$, e) $t_1 = 0$, $t_2 = 1$.

it is apparent that they have the same ground state energy. However, they correspond to two distinct topological phases. To see this intuitively, we consider the two fully dimerized cases as showed in Fig. 2.6. In both cases the SSH chain falls apart to a sequence of disconnected dimers whose energy spectra are *flat bands*. It means the energy eigenvalues are independent of the wavenumber or momentum and the group velocity is zero, which again shows that if the chain falls apart into dimers, an electron inserted into the chain will not spread along the chain.

- Case $t_2 = 0$: The energy spectra become two dispersionless flat bands where $E(k) = \pm t_1$. In real space, one can see that all unit cells are decoupled while within each unit cell, the hoping strength is finite as shown in the top row of Fig. 2.6.
- Case $t_1 = 0$: The energy spectra again become two flat bands where $E(k) = \pm t_2$. It is clear that this case is quite distinct from the above-mentioned case. In real space, one can see that all unit cells are coupled while within each unit cell the hoping strength is zero as the bottom row of Fig. 2.6 illustrates. In this case, however, the operators associated with the two ends of the chain do not enter the Hamiltonian. Therefore, there are four distinct edge states for a chain with the same energy.

A question may arise: Can we lift this four-fold degeneracy in second limit case? We can lift this degeneracy by adding a term like $c^\dagger_{1,A} c_{N,B}$ to the Hamiltonian. However, this is not a physical term if the chain is long enough since it is non-local. We are only going to consider *local* terms. This term becomes local in the closed chain with periodic boundary conditions. A second way to lift the end state degeneracy is by adding an explicit local impurity for each end. This keeps the Hamiltonian local. It turns out that the end states are not protected

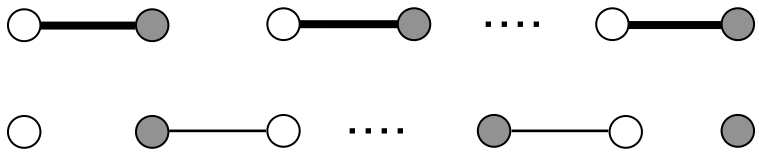

Figure 2.6: Schematic figure of two limiting cases in the SSH model. In the top row $t_2 = 0$ corresponding to the topologically trivial case with no edge states. In the bottom row $t_1 = 0$ corresponding to the topologically non-trivial case with edge states.

by a small perturbation, so the end states are not topological in that sense. Nevertheless, a topological interpretation to the end states can be given when we consider them as protected by a symmetry. In the following we will show that a chiral symmetry is sufficient to protect end states *i.e.* the second way is not compatible with this symmetry.

Although the dispersion relation (the magnitude of vector $\boldsymbol{d}(\boldsymbol{k})$ given by Eq. 2.77) or the band structure is useful to calculate a number of physical properties of the bulk of the system such as group velocities, effective mass, to name but few, there is important information about the bulk that cannot be revealed by only studying the band structure. In this section, we will show that in addition to the magnitude of $\boldsymbol{d}(\boldsymbol{k})$ vector, its direction contains important information. For the SSH model, as the wavenumber sweeps the entire Brillouin zone ($k = -\pi \to \pi$), the endpoint of the two-dimensional $\boldsymbol{d}(\boldsymbol{k})$ vector traces out a closed circle of radius t_2 on the $d_x d_y$-plane whose center is at the $(t_1, 0)$ point as given by Eq. 2.78 and shown in Fig. 2.7 for five different values of the hopping amplitudes; in particular, the equation governing $d_x(k)$ and $d_y(k)$, with k a parameter, is

$$\left\{d_x(k) - t_1\right\}^2 + d_y^2(k) = t_2^2. \tag{2.78}$$

The topology of this closed circle can be characterized by an integer known as the bulk winding number ($\mathcal{W}$). This integer number counts the number of times the loop winds around the origin of the $d_x d_y$-plane. In Fig. 2.7, we show five different closed circles corresponding to different parameters in the Hamiltonian. In Figs. 2.7(a)(b), $\mathcal{W} = 0$, in Fig. 2.7(c) the winding number is undefined since that path crosses the origin and hence the bulk gap is closed, and in Figs. 2.7(d)(e) $\mathcal{W} = 1$. For more general two-band insulators, this path is a closed loop due to the periodicity of the bulk momentum-space Hamiltonian.

In the following, we will show the generality of these properties and the link between the bulk winding number and the presence or absence of edge states which is known as bulk-boundary correspondence. In the case of the SSH model, all these properties are related to a property of the model known as chiral symmetry. The SSH model has chiral symmetry for $\mathcal{S} = \sigma_z$ which guarantees that the energy spectrum is symmetric about $E = 0$. If we choose the chiral symmetry operator to be a diagonal matrix in some basis, the Hamiltonian $H(k)$

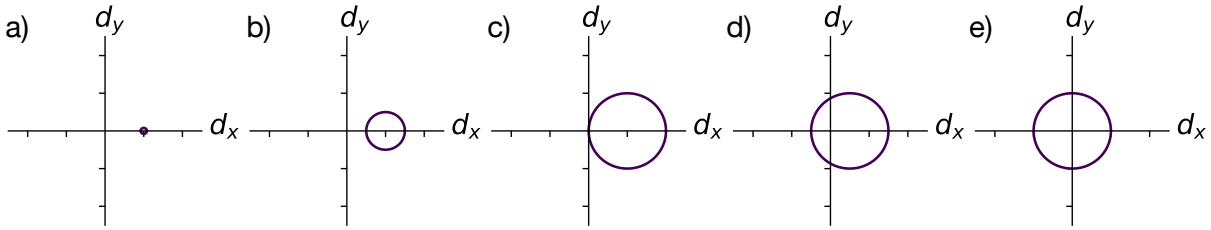

Figure 2.7: The path of the endpoint of the vector $\boldsymbol{d}(k)$ representing the bulk Hamiltonian on the $d_x d_y$- plane, as the wavenumber is swept across the Brillouin zone for different values of intracell and intercell hopping amplitudes: a) $t_1 = 1$, $t_2 = 0$, b) $t_1 = 1$, $t_2 = 0.5$, c) $t_1 = t_2 = 1$, d) $t_1 = 0.5$, $t_2 = 1$, e) $t_1 = 0$, $t_2 = 1$.

will be block off-diagonal in that basis of the form,

$$H(k) = \begin{pmatrix} 0 & q_k \\ q_k^\dagger & 0 \end{pmatrix}, \tag{2.79}$$

where q_k is a matrix for more than two bands. The presence of chiral symmetry allows the definition of winding number for SSH model in one-dimension as

$$\mathcal{W} = \frac{i}{2\pi} \int_0^{2\pi} \mathrm{tr}(q_k^{-1} \partial_k q_k) dk, \tag{2.80}$$

so

$$\begin{aligned}
\mathcal{W} &= \frac{i}{2\pi} \int_0^{2\pi} \frac{d_x + i d_y}{d_x^2 + d_y^2} (\partial_k d_x - i \partial_k d_y) dk \\
&= \frac{i}{4\pi} \int_0^{2\pi} \frac{\partial_k (d_x^2 + d_y^2)}{d_x^2 + d_y^2} dk + \frac{1}{2\pi} \int_0^{2\pi} \frac{d_x \partial_k d_y - d_y \partial_k d_x}{d_x^2 + d_y^2} dk \\
&= \frac{i}{4\pi} \ln[E_\pm^2(k)] \Big|_{k=0}^{k=2\pi} + \frac{1}{2\pi} \int_0^{2\pi} \frac{d_x \partial_k d_y - d_y \partial_k d_x}{d_x^2 + d_y^2} dk \\
&= 0 + \frac{1}{2\pi} \int_{\theta_k=0}^{\theta_k=2\pi} d\theta_k \\
&= \frac{1}{2\pi} (\theta_{k=2\pi} - \theta_{k=0}),
\end{aligned} \tag{2.81}$$

where $E_\pm(k)$ are the eigenvalues given by Eq. 2.77 and we defined $d_x(k) = |\boldsymbol{d}(k)| \cos\theta_k$ and $d_y(k) = |\boldsymbol{d}(k)| \sin\theta_k$. As both d_x and d_y are periodic functions of k, the value of $(\theta_{k=2\pi} - \theta_{k=0})$ must be equal to 2π times an integer number. This number counts the number of times that the two-dimensional unit vector $\boldsymbol{d}(k)$ encircles the origin. That is why this integer is dubbed winding number.

Now, let us go come back to the two special cases. If $t_2 = 0$, we have $H(k) = t_1\sigma_x$ which indicates that θ_k is fixed at zero *i.e.* $\theta_{k=0} = \theta_{k=2\pi} = 0$, so $\mathcal{W} = 0$. For the case $t_1 = 0$, however, we have

$$H(k) = t_2(\cos k\sigma_x + \sin k)\sigma_y, \tag{2.82}$$

so

$$\mathcal{W} = \frac{1}{2\pi}(\theta_{k=2\pi} - \theta_{k=0}) = \frac{1}{2\pi}(2\pi - 0) = 1. \tag{2.83}$$

This big difference in the winding number explains why the two cases have different boundary physics. When $t_1 > t_2$, the topological invariant (the winding number) is zero, so the system is topologically trivial and does not harbor zero-energy boundary modes. However, when $t_1 < t_2$, the topological invariant is finite, so the system is topologically non-trivial.

2.5.2 TIs in 2D: Quantum spin Hall insulator

The history of the quantum spin Hall effect starts with the pursuit of a topological phase based on a spin-orbit interaction which respects time-reversal symmetry. Electrons moving with a component of velocity perpendicular to an electric field experience a magnetic field in their rest frames that couples to their spins in the typical Zeeman fashion. In the laboratory frame, this results in an energy splitting between the two spin directions proportional to momentum. Without a magnetic field, this phase would effectively be protected by time reversal symmetry, with topological properties distinct from quantum Hall effect.

In 2004, a renewed interest in the Haldane model came with the discovery of graphene [10], and one year later, in 2005, Kane and Mele from University of Pennsylvania proposed a realization of such a phase in graphene which is known as *the Kane-Mele model* [11, 12]. Although graphene was the system for which both the Haldane model and the Kane-Mele model were originally considered, unfortunately the spin-orbit coupling derived from carbon orbitals is much too weak to produce a significant gap [13]. This led to a search for other systems composed of heavier elements for which spin-orbit coupling is typically much stronger.

Combined with contemporary theory works [14–16], a breakthrough moment came at the end of 2006 when Bernevig, Hughes and Zhang from Stanford University proposed an alternative realization in HgTe/(Hg,Cd)Te quantum wells with uniform strain gradient [18]. This development ultimately led to the discovery of *the quantum spin Hall effect* which can be thought of as the sum of two opposite copies of the Haldane model. The effective model that was used to predict the effect is now known as *the BHZ model*, named after its authors. The experimental confirmation came in the following year with an experiment conducted by Molenkamp's group at University of Würzburg [19]. Soon after, another realization in InAs/GaSb quantum wells [20] was proposed and confirmed experimentaly [21–23].

The Quantum spin Hall insulator belongs to class AII in $d = 2$ in the Altland-Zirnbauer classification [see Table 2.1], so it is characterized by a $\mathbb{Z}_2$ topological invariant. In the following, we will give a brief description about it. There are two distinct possibilities for

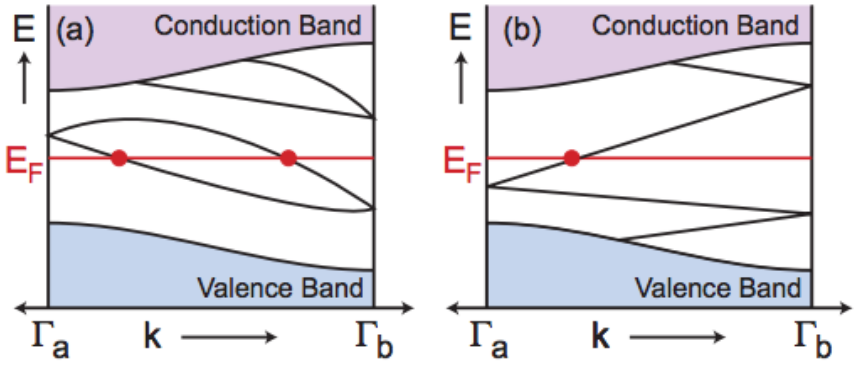

Figure 2.8: (Color online) Two distinct possibilities for the edge states of a two-dimensional time-reversal invariant system. The figure is adapted from [68].

the structure of edge states in a two-dimensional time-reversal invariant system, which are represented in a band diagram as lines crossing the bulk gap as shown in Fig. 2.8. The symmetry always requires a two-fold degeneracy as a results of Kramers' theorem, so that the band structure is mirror symmetric about zero momentum with the accompanying spin flip. However, at the time-reversal invariant momenta $\Gamma_a = 0$ and $\Gamma_b = \pi/a$ the time reversed states are at the same momentum. Between these particular so-called *Kramers partners*, spin-orbit coupling can split them apart by spin. They can recombine again in one of two ways: either pairwise, so that the Fermi energy always intersects an even number of Kramers pairs [Fig. 2.8 (a)], or in a sort of non-pairwise manner with an odd number of crossings [Fig. 2.8 (b)]. These two possibilities are topologically different. In the former case, we could smoothly modify the Hamiltonian so as to push the edge states out the gap. However, in the latter case, there will always be at least one Kramer pair at all energies in the gap, so that the presence of edge states is a topological property.

Once again, we have two distinct classes of Hamiltonians. Just as the Chern number classifies Hamiltonians with an integer ($\mathbb{Z}$), in this case the two classes can be thought of as either zero or one ($\mathbb{Z}_2$). The corresponding topological invariant ν can be defined as the number of Kramers pairs at any given energy in the gap modulo 2. Therefore, in Fig. 2.8 (a), we have a topologically trivial two-dimensional insulator ($\nu = 0$) with no edge states, while in Fig. 2.8 (b), we have a topologically non-trivial two-dimensional insulator ($\nu = 1$) known as the quantum spin Hall insulator or *two-dimensional topological insulator*.

Although in the quantum Hall effect the time-reversal symmetry is broken and there are either clockwise or counter-clockwise metallic *chiral* edge states, in the quantum spin Hall effect the time-reversal symmetry is preserved and there are both left and right moving metallic *helical* edge states on each edge of the sample with opposite spins. This results in the presence of only charge (spin) current around the sample in the former (latter) case.

Furthermore, while backscattering is disallowed in the quantum Hall effect because the two directions of propagation are physically separated by an insulating bulk, in the quantum spin Hall effect each edge has two directions of propagation on top of each other. Instead, backscattering is forbidden by spin polarization and the presence of time-reversal symmetry.

There are several ways to formulate ν using the bulk properties, as we have done for the Chern number. However, as all those ways are somewhat more abstract, we only state the final conclusion here to simplify the discussion. In the presence of time-reversal symmetry a $\mathbb{Z}_2$ charge polarization can be defined for half-integer spin systems [89] where the corresponding $\mathbb{Z}_2$ index is given by

$$(-1)^\nu = \delta_1\delta_2\delta_3\delta_4, \tag{2.84}$$

where

$$\delta_i = \frac{\sqrt{\det[\omega(\Gamma_i)]}}{\mathrm{Pf}[\omega(\Gamma_i)]} = \pm 1, \tag{2.85}$$

and $\mathbf{\Gamma}_i$ are the four time-reversal invariant momenta in the two-dimensional Brillouin zone. Here, ω is a unitary matrix defined by

$$\omega_{mn}(\boldsymbol{k}) = \langle u_{m,-\boldsymbol{k}}|\mathcal{T}|u_{n,\boldsymbol{k}}\rangle. \tag{2.86}$$

The matrix $\omega_{mn}(\boldsymbol{k})$ is antisymmetric at time-reversal invariant momenta allowing for the definition of the Pfaffian. In general, Pfaffian(A) is abbreviated as $\mathrm{Pf}(A)$ for an antisymmetric matrix A [91]. The determinant of such a matrix can always be expressed as

$$\det(A) = \mathrm{Pf}^2(A). \tag{2.87}$$

For a $(2N+1)\times(2N+1)$ antisymmetric matrix, both determinant and Pfaffian are zero. However, for a $2N\times 2N$ antisymmetric matrix the Pfaffian is given by,

$$\mathrm{Pf}(A) = \frac{1}{2^N N!}\sum_{\sigma_1\neq\cdots\neq\sigma_{2N}} \epsilon^{\sigma_1\sigma_2\ldots\sigma_{2N}}\prod_{i=1}^{N} A_{\sigma_{2i-1},\sigma_{2i}}, \tag{2.88}$$

where $\epsilon^{\sigma_1\sigma_2\ldots\sigma_{2N}}$ is an antisymmetric tensor. If the order $\sigma_1\sigma_2\ldots\sigma_{2N}$ is an even permutation of $(1,2,\ldots,2N)$, we will have $\epsilon^{\sigma_1\sigma_2\ldots\sigma_{2N}} = 1$. Otherwise, it will be equal to -1. For example, for

$$A = \begin{pmatrix} 0 & a \\ -a & 0 \end{pmatrix}, \tag{2.89}$$

we have

$$\mathrm{Pf}(A) = \frac{1}{2^1 1!}(\epsilon^{12}A_{12} + \epsilon^{21}A_{21}) = \frac{1}{2}(A_{12} - A_{21}) = a. \tag{2.90}$$

The analysis of two-dimensional topological insulators can naturally be generalized to three dimensions, which is the subject of the next section.

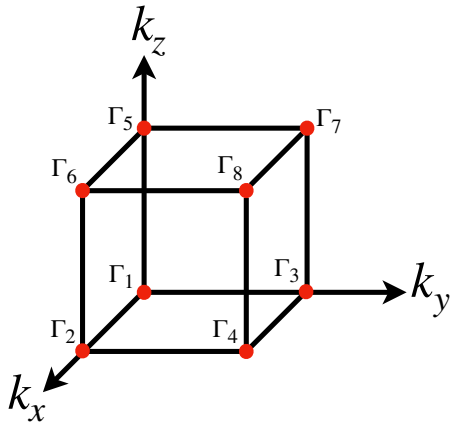

Figure 2.9: Eight time-reversal invariant momenta $\mathbf{\Gamma}_i$ $(i = 1, 2, \ldots, 8)$ are shown with red points for a cubic lattice in reciprocal wave vector space. There are six time-reversal invariant two-dimensional planes that map to themselves under time-reversal transformation. Each plane can be assigned a $\mathbb{Z}_2$ topological invariant.

2.5.3 TIs in 3D: Strong and weak TIs

Three-dimensional topological insulators belong to class AII in $d = 3$ in the Altland-Zirnbauer classification [see Table 2.1], so it is characterized again by a $\mathbb{Z}_2$ topological invariant. If we now consider the surface states inside a bulk band gap of a material with time reversal symmetry, there now will be four points in reciprocal space with Kramers' degeneracy. The question, just as in the two-dimensional case, is how they connect between the various degeneracy points: does a line at constant energy connecting two time-reversal invariant momenta cross through an even or odd number of surface states? To simplify the discussion again, consider a cubic Brillouin zone as shown in Fig. 2.9. In particular, the points on the $k_x k_y$ plane map to themselves under time-reversal symmetry, so this plane has a corresponding $\mathbb{Z}_2$ index which is given by

$$(-1)^{\nu} = \delta_1 \delta_2 \delta_3 \delta_4 = z_0, \tag{2.91}$$

where δ_i is given by Eq. 2.85. Due to the symmetry of the lattice, the $k_x k_z$ and $k_y k_z$ planes also have their own $\mathbb{Z}_2$ indices y_0 and x_0, respectively. In addition, the planes at front, right and top sides of the cube also map to themselves under time-reversal symmetry, so there are three more $\mathbb{Z}_2$ indices x_+, y_+, and z_+. Hence, there are six $\mathbb{Z}_2$ indices. However, these numbers are not independent of each other since

$$x_0 x_+ = y_0 y_+ = z_0 z_+ = \prod_{i=1}^{8} \delta_i. \tag{2.92}$$

Hence, due to these two relations, there are only four independent $\mathbb{Z}_2$ indices that characterize a three-dimensional topological insulator. One can choose $(z_0 z_+, x_+, y_+, z_+)$ or

$(\nu_0;\nu_1,\nu_2,\nu_3)$ where,

$$(-1)^{\nu_0} = \prod_{n=1}^{8} \delta_i, \tag{2.93}$$

$$(-1)^{\nu_1} = \delta_2\delta_4\delta_6\delta_8, \tag{2.94}$$

$$(-1)^{\nu_2} = \delta_3\delta_4\delta_7\delta_8, \tag{2.95}$$

$$(-1)^{\nu_3} = \delta_5\delta_6\delta_7\delta_8. \tag{2.96}$$

The ν_0 is known as the strong topological insulator index, and (ν_1,ν_2,ν_3) are known as the weak topological insulator indices. These indices were discovered in 2007 by Moore and Balents, Fu and Kane independently [24, 25]. A few months later, Fu and Kane showed that in the presence of inversion symmetry

$$\delta_i = \prod_{n\in \text{occ}} \zeta_n(\mathbf{\Gamma}_i), \tag{2.97}$$

where $\zeta_n(\mathbf{\Gamma}_i)$ is know as the parity eigenvalue of occupied energy band n at point $\mathbf{\Gamma}_i$ [90]. This formula gives a much easier way for calculating δ_i in an inversion symmetric system than the one given by Eq. 2.85.

In total, there are 16 topologically distinct insulators in three dimensions. The phases with $\nu_0 = 1$ are called *strong topological insulators*, whereas phases with $\nu_0 = 0$ but $\nu_i = 1$ for at least one $i = 1,2,3$ are called *weak topological insulators*. The latter are dubbed "weak" because the weak invariants (ν_1,ν_2,ν_3) are not robust against translational-symmetry breaking perturbations. One can naively stack the two-dimensional materials to form a three-dimensional structure. In the early days, this attempt to build a three-dimensional quantum Hall system failed. An essential reason is that there is no non-zero Chern number in odd dimensions. The situation is different for the case of a topological insulator, where one can actually build a weak topological insulator in this way.

The values of the $\mathbb{Z}_2$ invariants have important implications on the structure of the surface states [24, 90]. The surface Brillouin zone of a three-dimensional time-reversal invariant system is a two-dimensional surface with four inequivalent time-reversal invariant points. Due to Kramers' theorem, any generic band crossing of surface states at these points is a two-dimensional Dirac point with Dirac-cone dispersion. The result is the simple surface Hamiltonian

$$H_{\text{surface}} = \hbar v_F \boldsymbol{\sigma}\cdot\boldsymbol{k}, \tag{2.98}$$

where $\boldsymbol{\sigma}$ refers to Pauli matrices for spin in contrast to graphene where it refers to the sublattice space. Interestingly, there is also no spin or valley degeneracy but instead just a single Dirac cone. A strong topological insulator has an odd number of surface Dirac cones and its surface states form a two dimensional *topological metal* [24]. These exotic

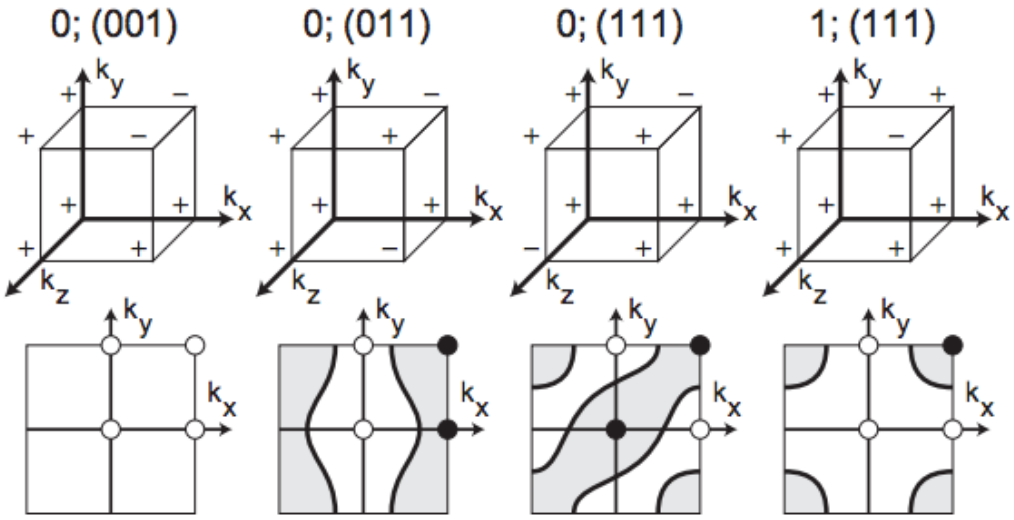

Figure 2.10: Schematic figiure of four examples of parity distributions at time-reversal invariant momenta are shown in the first octant of the Brillouin zone. The strong (ν_0) and weak (ν_1, ν_2, ν_3) topological indices can be calculated accordingly. The top row shows the sign of δ_i at the Γ_i. In the bottom, the band structure in $k_x k_y$ plane for each case is plotted where white and black dots at the four corners represent the projected parities *i.e.* the product of two parities along k_z direction. The energy dispersion of a surface state between a black dot and white dot cross the Fermi surface. The gray regions are filled and the white regions are empty and they are separated by thick lines indicating the Fermi surface. The figure is adopted from Ref. [90].

two-dimensional metallic surface states form a unique phase which cannot be realized in a conventional system for which the Dirac points must come in pairs [92]. In contrast, a weak topological insulator has an even number of surface Dirac cones. These surface states have several interesting properties arising from this spin-momentum locking. A loop around the Dirac cone results in a π Berry phase due to the full 2π precession of the spin, similar to graphene and the pseudospin.

In Fig. 2.10, which is adopted from Ref. [90], four examples of parity distributions at time-reversal invariant momenta are shown in the first octant of the Brillouin zone. The strong (ν_0) and weak (ν_1, ν_2, ν_3) topological indices can be calculated accordingly. The top row shows the sign of δ_i at eight time-reversal invariant momenta $\mathbf{\Gamma}_i$. In the bottom row, the band structure in $k_x k_y$ plane for each case is plotted where white and black dots at the four corners represent the projected parities *i.e.* the product of two parities along k_z direction. The energy dispersion of a surface state between a black dot and white dot cross the Fermi surface. The gray regions are filled bands and the white regions are empty bands and they are separated by thick lines indicating the Fermi surface.

In 2008, the first strong three-dimensional topological insulator was discovered by the Hasan group at Princeton University in $Bi_{1-x}Sb_x$ by performing angle-resolved photoemis-

sion spectroscopy to directly image the band structure [26], and later Bi_2Te_3 or Bi_2Se_3 [27–29]. In contrast, although the stacking of two-dimensional quantum spin Hall insulators to build a three-dimensional weak topological insulator is a promising recipe, the preparation of weak topological insulators has so far been challenging. Nonetheless, some materials such as $Bi_{14}Rh_3I_9$ have recently been verified to realize a weak topological insulator [93, 94].

Recently, numerous new topological insulator candidates have been found using systematic searches through a material database [30–32]. In should be noted that, nevertheless, an ideal topological insulator would be the one with a large band gap which seems to be hard to come by since the gap inversion is often a result of spin-orbit coupling, which is not easy to be enhanced.

2.6 Topological superconductors

Due to the superconducting gap, a superconductor is similar to an insulator from the energy point of view. One thing that distinguishes a superconductor from an insulator is redundant paticle-hole symmetry of the BdG Hamiltonian. In addition, the ground state of a superconductor has a definite phase but does not have a definite number of Cooper pairs [33]. Therefore, adding an electron to a superconductor is the same as removing an electron or equivalently adding a hole. In this section, we will study the topology of such an "insulator" in one and two spatial dimensions.

2.6.1 Superconductivity and the BdG formalism

In 1911, three years after liquefying of helium, Onnes in Leiden observed that the electrical resistance of various metals such as mercury disappeared completely below a critical temperature [95]. This discovery initialized the fertile field of superconductivity.

In 1933, about two decades later, another hallmark of superconductivity, the perfect diamagnetism, was found by Meissner and Ochsenfeld [96]. This distinct property of superconductors, which is know as the *Meissner effect*, makes a superconductor different from a perfect conductor. Therefore, superconductivity is a distinct phase of matter with two key properties: zero electrical resistance (perfect conductance), and expulsion of magnetic field (perfect diamagnetism).

In 1935, the first piece of understanding superconductivity was provided by Fritz and London [97]. They proposed a relation between the current density and the vector potential inside a superconductor. This equation allows for determination of the magnetic field inside a superconductor and leads to the introduction of *the penetration length* (λ). This length describes the characteristic size over which an external magnetic field penetrates a superconductor and therefore the London theory serves as a theoretical framework to explain the Meissner effect.

In 1950, Ginzburg and Landau introduced the notion of coherence length (ξ) which can be interpreted as the smallest scale on which superconductivity can appear [98]. Superconductivity was now equipped with two characteristic length-scales: the penetration length λ, and the coherence length ξ. It turned out that $\kappa = \lambda/\xi$ gives a good criterion between type I ($\kappa > 1\sqrt{2}$) and type II ($\kappa < 1/\sqrt{2}$) superconductors.

Although an explanation of the superconductivity phenomena eluded many scientists, a clear understanding of its microscopic mechanism arose through a big breakthrough made by Cooper who found that two electrons on the Fermi surface inevitably form a bound state for arbitrarily small attractive interaction [99]. He showed that the Fermi surface is unstable to such a perturbation which will lower the energy of the system. While the electron itself is a fermion, the two-electron bound state will behave like a boson. Bosons will undergo Bose-Einstein condensation for sufficiently low temperature resulting in the superfluid phenomena. A combination of this two-electron physical picture suggested that superconductors can be explained as the superfluid of two-electron bound states which were later dubbed *Cooper pairs*.

In 1957, Bardeen, Cooper, and Schrieffer proposed their microscopic scenario for superconductivity [100, 101] today known as *the BSC theory*. Their theory stems from the electron-phonon interaction described by Fröhlich [102] and suggested by the isotope effect [103, 104]. Far above (below) the Fermi energy, the excitations are primarily electron-like (hole-like) quasiparticles. Close to the Fermi energy they are coherent particle-hole mixtures (*i.e.* a superposition between particle-like and hole-like states). These elementary quasiparticle excitations are commonly known as *Bogoliubons*, with well-defined spins and momenta.

Superconductivity can be treated by two different approaches. First of these is the GinzburgLandau theory [98] which concentrates on superconducting electrons and accounts for the macroscopic quantum mechanics of the superconducting state. While this approach is very successful in the prediction of vortex lattices [105] and describing the electrodynamics of superconductors, it does not treat superconductivity at a microscopic level due to its phenomenological nature [106]. Since we are interested in a microscopic treatment, this approach is not covered in this thesis. Instead we will make use of BCS theory of superconductivity in the rest of this thesis. This theory could, together with its extensions, account for most experimental observations, forming a very concise and beautiful picture of superconductivity, today known as *the conventional theory of superconductivity*.

Conventional superconductors are either elements or alloys, typically with critical temperature below 30 K, whose properties are well understood by BCS theory. In these materials, superconductivity is induced by the electron-phonon interaction which gives rise to an attractive interaction between electrons and overcomes their repulsive Coulomb interaction. The picture of a perfectly understood superconductivity started to fracture in 1979 with the discovery of several materials which could not be explained with the BCS theory. The picture completely shattered in 1986 when Bednorz and Müller observed superconductivity in the compound $La_{2-x}Ba_xCuO_4$ with critical tempreature $T_c = 35K$ [107]. Since then, a great

number of materials have been found which exhibit superconductivity, either directly or in proximity to a superconductor, that does not fit in the BCS model. These materials are commonly called *high-temperature or unconventional superconductors*, and generally refer to materials with transition temperatures higher than 30 K which cannot be described by BSC theory.

Although many aspects of the high-temperature superconductors are similar to those in the conventional superconductors (*e.g.* quasiparticle pairs and persistent currents brought about by a net attractive electron-electron interaction), there are also many important differences. For example, conventional superconductivity arises in metals whose normal state follows Landau-Fermi liquid theory with well-defined propagating degrees of freedom (phonons). Hence, the pairing interaction responsible for superconductivity (the electron-phonon interaction) is well-known and and its role in superconductivity is fully described by BCS/Eliashberg theory [108]. High-temperature superconductors, on the other hand, arise in charge-transfer insulators whose low energy dynamics can be described by effective Mott insulators, where the propagating degrees of freedom is unknown [70]. Furthermore, while conventional superconductors are formally defined to break only $U(1)$ gauge symmetry, unconventional superconductors break additional symmetries. The additional broken symmetries give rise to a much richer landscape of physics. For example, electrons of opposite spins and momenta are paired with a singlet s-wave pairing symmetry in conventional superconductivity, while the electrons can be paired with equal spins in unconventional superconductors, know as triplet pairing symmetry. Both spin-triplet and spin-singlet superconductivity pairing symmetries or even a mixture of them are possible in the unconventional superconductors.

As an example of unconventional superconductors, and of particular interest for this thesis, is the family of superconductors discovered by Bednorz and Müller. These are commonly called *cuprates* due to the existence of copper-oxide (CuO_2) planes in this family. Superconductivity is mainly constricted to these planes, with a suppression of propagation between planes. The order parameter of the cuprates breaks the fourfold rotation symmetry of the crystal lattice, and was shown around later to have an anisotropic spin-singlet d-wave pairing symmetry [71].

A mean field approach to superconductivity is provided by the Bogoliubov-de Gennes approach which was first introduced in order to describe the effect of inhomogeneities in superconductors [109]. Depending on the detailed mechanism, the two electrons in a Cooper pair can form spin-singlet (s-wave, d-wave) or spin-triplet (p-wave, f-wave) pairs. Let us begin with the mean-field formalism for a conventional s-wave superconductor. We will see more interesting cases later. We start with a simple metal described by the non-interacting second-quantized Hamiltonian,

$$H_0 = \sum_{\boldsymbol{k},\sigma} \epsilon(\boldsymbol{k}) c^\dagger_{\boldsymbol{k},\sigma} c_{\boldsymbol{k},\sigma}, \tag{2.99}$$

where $\boldsymbol{k} = (k_x, k_y)$ is a point in the first Brillouin zone, σ is spin, and $c^\dagger_{\boldsymbol{k},\sigma}(c_{\boldsymbol{k},\sigma})$ creates

(annihilates) a quasiparticle with momentum $\boldsymbol{k}$ and spin σ. In addition,

$$\epsilon(\boldsymbol{k}) = -2t(\cos k_x + \cos k_y) - \mu, \tag{2.100}$$

where t is the hopping amplitude from one site to its nearest-neighbour sites of a square lattice whose lattice constant is a, and μ is the chemical potential which defines the Fermi surface. For the sake of simplicity, we take both $a = 1$ and $t = 1$ from now on. The many-body ground state can be obtained by filling all the levels below the Fermi energy,

$$|G\rangle = \prod_{\substack{\boldsymbol{k},\sigma \\ \epsilon(\boldsymbol{k})<0}} c^\dagger_{\boldsymbol{k},\sigma}|0\rangle \tag{2.101}$$

where the vacuum $|0\rangle$ is defined by $c_{\boldsymbol{k},\sigma}|0\rangle = 0$ for all $\boldsymbol{k}$ and σ. By using fermion anticommutation relations, we can rewrite this Hamiltonian as

$$\begin{aligned} H_0 &= \frac{1}{2}\sum_{\boldsymbol{k},\sigma} \epsilon(\boldsymbol{k})\{c^\dagger_{\boldsymbol{k},\sigma}c_{\boldsymbol{k},\sigma} - c_{\boldsymbol{k},\sigma}c^\dagger_{\boldsymbol{k},\sigma}\} + \frac{1}{2}\sum_{\boldsymbol{k}} \epsilon(\boldsymbol{k}) \\ &= \frac{1}{2}\sum_{\boldsymbol{k},\sigma} \{\epsilon(\boldsymbol{k})c^\dagger_{\boldsymbol{k},\sigma}c_{\boldsymbol{k},\sigma} - \epsilon(-\boldsymbol{k})c_{-\boldsymbol{k},\sigma}c^\dagger_{-\boldsymbol{k},\sigma}\} + \frac{1}{2}\sum_{\boldsymbol{k}} \epsilon(\boldsymbol{k}) \\ &= \frac{1}{2}\sum_{\boldsymbol{k}} \Psi^\dagger_{\boldsymbol{k}} H_{BdG}(\boldsymbol{k})\Psi_{\boldsymbol{k}} + \frac{1}{2}\sum_{\boldsymbol{k}} \epsilon(\boldsymbol{k}), \end{aligned} \tag{2.102}$$

where we define the spinor $\Psi^T_{\boldsymbol{k}} = (c_{\boldsymbol{k}\uparrow}\ c_{\boldsymbol{k}\downarrow}\ c^\dagger_{-\boldsymbol{k}\uparrow}\ c^\dagger_{-\boldsymbol{k}\downarrow})$ and

$$H_{BdG}(\boldsymbol{k}) = \begin{pmatrix} \epsilon(\boldsymbol{k}) & 0 & 0 & 0 \\ 0 & \epsilon(\boldsymbol{k}) & 0 & 0 \\ 0 & 0 & -\epsilon(-\boldsymbol{k}) & 0 \\ 0 & 0 & 0 & -\epsilon(-\boldsymbol{k}) \end{pmatrix}, \tag{2.103}$$

and we have dropped the constant and introduced the subscript BdG, which stands for Bogoliubov-de Gennes, to label the Bloch Hamiltonian written in this *redundant* formalism because we have actually created an artificial redundancy by effectively doubling the degrees of freedom. Although this is complicating our description of what was a simple free-fermion problem, it will become more important when we consider superconducting pairing. Thus, instead of having two degrees of freedom, one band and two spins, the BdG Hamiltonian has four. We now have four energy eigenvalues of the BdG Hamiltonian, namely, two copies of $\epsilon(\boldsymbol{k})$ and two copies of $-\epsilon(-\boldsymbol{k})$. It should be noted that only two out of the four bands give independent quasiparticles states.

Moreover, this Hamiltonian has particle-hole "symmetry" because of this redundancy, so we are reserved about calling this a symmetry because what we have really done is to introduce a redundancy into our description of this non interacting metal.

The point of this formalism is to show that the easiest way to solve for the quasiparticle bands of a mean-field superconductor is to write the Hamiltonian in this BdG form. The pairing potential, which we will introduce, simply couples the upper and lower blocks of the BdG Hamiltonian we provided for the metal. We begin by studying the conventional s-wave, singlet pairing potential of the form

$$\begin{aligned} H_{SC} &= \sum_{\boldsymbol{k}} (\Delta c^{\dagger}_{\boldsymbol{k}\uparrow} c^{\dagger}_{-\boldsymbol{k}\downarrow} + \Delta^* c_{-\boldsymbol{k}\downarrow} c_{\boldsymbol{k}\uparrow}) \\ &= \frac{1}{2} \sum_{\boldsymbol{k}} (\Delta c^{\dagger}_{\boldsymbol{k}\uparrow} c^{\dagger}_{-\boldsymbol{k}\downarrow} - \Delta c^{\dagger}_{-\boldsymbol{k}\downarrow} c^{\dagger}_{\boldsymbol{k}\uparrow} + \Delta^* c_{-\boldsymbol{k}\downarrow} c_{\boldsymbol{k}\uparrow} - \Delta^* c_{\boldsymbol{k}\uparrow} c_{-\boldsymbol{k}\downarrow}), \end{aligned} \tag{2.104}$$

where Δ is a complex number representing the superconducting order parameter. H_{SC} at mean-field level, is not invariant under arbitrary gauge transformations ($c_{\boldsymbol{k}} \to e^{i\phi(\boldsymbol{k})} c_{\boldsymbol{k}}$), if we consider Δ as a conventional gauge-invariant order parameter. This leads to a non-conservation of charge, *i.e.* only the parity of the number of electrons is conserved. This term captures the physics of two electrons or holes combining to form a Cooper pair or a Cooper pair breaking apart into its constituents. Now, let us consider the total Hamiltonian of the metal with a homogeneous pairing potential,

$$H = H_0 + H_{SC} = \frac{1}{2} \sum_{\boldsymbol{k}} \Psi^{\dagger}_{\boldsymbol{k}} \mathcal{H}_{BdG}(\boldsymbol{k}) \Psi_{\boldsymbol{k}}, \tag{2.105}$$

and

$$\mathcal{H}_{BdG}(\boldsymbol{k}) = \begin{pmatrix} \epsilon(\boldsymbol{k}) & 0 & 0 & \Delta \\ 0 & \epsilon(\boldsymbol{k}) & -\Delta & 0 \\ 0 & -\Delta^* & -\epsilon(-\boldsymbol{k}) & 0 \\ \Delta^* & 0 & 0 & -\epsilon(-\boldsymbol{k}) \end{pmatrix}. \tag{2.106}$$

It is worth mentioning that the choice of spinor is not unique, so we can choose different and appropriate bases or spinors to make the problem easier in some cases. For example, because some components of the BdG Hamiltonian are zero here, by choosing $\Psi^T_{\boldsymbol{k}} = (c_{\boldsymbol{k}\uparrow}\ c^{\dagger}_{-\boldsymbol{k}\downarrow}\ c_{\boldsymbol{k}\downarrow}\ c^{\dagger}_{-\boldsymbol{k}\uparrow})$, we can get the following block-diagonal form of the BdG Hamiltonian,

$$H_{BdG}(\boldsymbol{k}) = \begin{pmatrix} \epsilon(\boldsymbol{k}) & \Delta & 0 & 0 \\ \Delta^* & -\epsilon(-\boldsymbol{k}) & 0 & 0 \\ 0 & 0 & \epsilon(\boldsymbol{k}) & -\Delta \\ 0 & 0 & -\Delta^* & -\epsilon(-\boldsymbol{k}) \end{pmatrix}. \tag{2.107}$$

Thus, each block can be considered separately which will be obviously easier than considering a four by four matrix. Let us consider one block and find an equation for calculating the superconducting order parameter Δ. The final result will be independent of choosing a block.

Accordingly, we will have

$$H = \sum_{\boldsymbol{k}} \begin{pmatrix} c^\dagger_{\boldsymbol{k}\uparrow} & c_{-\boldsymbol{k}\downarrow} \end{pmatrix} \begin{pmatrix} \epsilon_{\boldsymbol{k}} & \Delta \\ \Delta^* & -\epsilon_{\boldsymbol{k}} \end{pmatrix} \begin{pmatrix} c_{\boldsymbol{k}\uparrow} \\ c^\dagger_{-\boldsymbol{k}\downarrow} \end{pmatrix}. \tag{2.108}$$

where we used $\epsilon_{\boldsymbol{k}} = \epsilon(\boldsymbol{k}) = \epsilon(-\boldsymbol{k})$, assuming inversion symmetry in the real space lattice. This BdG Hamiltonian can be diagonalized by a Bogoliubov transformation by incorporating some unitary operator $\mathcal{U}$ such that

$$\begin{aligned} H &= \sum_{\boldsymbol{k}} \begin{pmatrix} c^\dagger_{\boldsymbol{k}\uparrow} & c_{-\boldsymbol{k}\downarrow} \end{pmatrix} \mathcal{U}\mathcal{U}^\dagger \begin{pmatrix} \epsilon_{\boldsymbol{k}} & \Delta \\ \Delta^* & -\epsilon_{\boldsymbol{k}} \end{pmatrix} \mathcal{U}\mathcal{U}^\dagger \begin{pmatrix} c_{\boldsymbol{k}\uparrow} \\ c^\dagger_{-\boldsymbol{k}\downarrow} \end{pmatrix} \\ &= \sum_{\boldsymbol{k}} \begin{pmatrix} c^\dagger_{\boldsymbol{k}\uparrow} & c_{-\boldsymbol{k}\downarrow} \end{pmatrix} \mathcal{U} \begin{pmatrix} E_{\boldsymbol{k}} & 0 \\ 0 & -E_{-\boldsymbol{k}} \end{pmatrix} \mathcal{U}^\dagger \begin{pmatrix} c_{\boldsymbol{k}\uparrow} \\ c^\dagger_{-\boldsymbol{k}\downarrow} \end{pmatrix} \\ &= \sum_{\boldsymbol{k}} \begin{pmatrix} \gamma^\dagger_{\boldsymbol{k}\uparrow} & \gamma_{-\boldsymbol{k}\downarrow} \end{pmatrix} \begin{pmatrix} E_{\boldsymbol{k}} & 0 \\ 0 & -E_{-\boldsymbol{k}} \end{pmatrix} \begin{pmatrix} \gamma_{\boldsymbol{k}\uparrow} \\ \gamma^\dagger_{-\boldsymbol{k}\downarrow} \end{pmatrix} \\ &= \sum_{\boldsymbol{k},\sigma} E_{\boldsymbol{k}} \gamma^\dagger_{\boldsymbol{k}\sigma} \gamma_{\boldsymbol{k}\sigma} - \sum_{\boldsymbol{k}} E_{-\boldsymbol{k}}, \end{aligned} \tag{2.109}$$

where,

$$\begin{pmatrix} c_{\boldsymbol{k}\uparrow} \\ c^\dagger_{-\boldsymbol{k}\downarrow} \end{pmatrix} = \mathcal{U} \begin{pmatrix} \gamma_{\boldsymbol{k}\uparrow} \\ \gamma^\dagger_{-\boldsymbol{k}\downarrow} \end{pmatrix} = \begin{pmatrix} u_{\boldsymbol{k}} & -v^*_{-\boldsymbol{k}} \\ v_{\boldsymbol{k}} & u^*_{-\boldsymbol{k}} \end{pmatrix} \begin{pmatrix} \gamma_{\boldsymbol{k}\uparrow} \\ \gamma^\dagger_{-\boldsymbol{k}\downarrow} \end{pmatrix}. \tag{2.110}$$

The order parameter given by

$$\Delta = -\frac{U}{N} \sum_{\boldsymbol{q}} \langle c_{\boldsymbol{q}\uparrow} c_{-\boldsymbol{q}\downarrow} \rangle = -\frac{U}{N} \sum_{\boldsymbol{q}} u_{\boldsymbol{q}} v^*_{\boldsymbol{q}} \tanh(\frac{\beta E_{\boldsymbol{q}}}{2}). \tag{2.111}$$

Here, $U < 0$ is an attractive on-site interaction in the Hubbard model, and $\beta = 1/k_B T$ where T is temperature and k_B is the Boltzmann constant. Diagonalizing the BdG Hamiltonian leads to the following eigenvalue

$$E_{\boldsymbol{k}} = \sqrt{\epsilon^2_{\boldsymbol{k}} + |\Delta|^2}, \tag{2.112}$$

with its associated eigenvector

$$|E_{\boldsymbol{k}}\rangle = \begin{pmatrix} \dfrac{\epsilon_{\boldsymbol{k}} + E_{\boldsymbol{k}}}{\Delta^*} \\ 1 \end{pmatrix}, \tag{2.113}$$

which is not normalized. Let $A|E_{\boldsymbol{k}}\rangle$ be the normalized eigenvector, then we have

$$\begin{aligned}
\Delta &= -\frac{U}{N}\sum_{\boldsymbol{q}} u_{\boldsymbol{q}} v_{\boldsymbol{q}}^{*} \tanh(\frac{\beta E_{\boldsymbol{q}}}{2}) \\
&= -\frac{U}{N}\sum_{\boldsymbol{q}} |A|^2 (\frac{\epsilon_{\boldsymbol{q}} + E_{\boldsymbol{q}}}{\Delta^{*}})(1) \tanh(\frac{\beta E_{\boldsymbol{q}}}{2}) \\
&= -\frac{U}{N}\sum_{\boldsymbol{q}} \frac{|\Delta|^2}{(\epsilon_{\boldsymbol{q}} + E_{\boldsymbol{q}})^2 + |\Delta|^2} (\frac{\epsilon_{\boldsymbol{q}} + E_{\boldsymbol{q}}}{\Delta^{*}}) \tanh(\frac{\beta E_{\boldsymbol{q}}}{2}) \\
&= -\frac{U}{N}\sum_{\boldsymbol{q}} \frac{\Delta(\epsilon_{\boldsymbol{q}} + E_{\boldsymbol{q}})}{(\epsilon_{\boldsymbol{q}} + E_{\boldsymbol{q}})^2 + |\Delta|^2} \tanh(\frac{\beta E_{\boldsymbol{q}}}{2}) \\
&= -\frac{U}{N}\sum_{\boldsymbol{q}} \frac{\Delta(\epsilon_{\boldsymbol{q}} + E_{\boldsymbol{q}})}{\epsilon_{\boldsymbol{q}}^2 + E_{\boldsymbol{q}}^2 + 2\epsilon_{\boldsymbol{q}} E_{\boldsymbol{q}} + |\Delta|^2} \tanh(\frac{\beta E_{\boldsymbol{q}}}{2}) \\
&= -\frac{U}{N}\sum_{\boldsymbol{q}} \frac{\Delta(\epsilon_{\boldsymbol{q}} + E_{\boldsymbol{q}})}{2\epsilon_{\boldsymbol{q}}^2 + 2\epsilon_{\boldsymbol{q}} E_{\boldsymbol{q}} + 2|\Delta|^2} \tanh(\frac{\beta E_{\boldsymbol{q}}}{2}) \\
&= -\frac{U}{N}\sum_{\boldsymbol{q}} \frac{\Delta(\epsilon_{\boldsymbol{q}} + E_{\boldsymbol{q}})}{2E_{\boldsymbol{q}}^2 + 2\epsilon_{\boldsymbol{q}} E_{\boldsymbol{q}}} \tanh(\frac{\beta E_{\boldsymbol{q}}}{2}) \\
&= -\frac{U}{N}\sum_{\boldsymbol{q}} \frac{\Delta}{2E_{\boldsymbol{q}}} \tanh(\frac{\beta E_{\boldsymbol{q}}}{2}),
\end{aligned} \tag{2.114}$$

so,

$$\Delta = -\frac{U}{N}\sum_{\boldsymbol{q}} \frac{\Delta}{2E_{\boldsymbol{q}}} \tanh(\frac{\beta E_{\boldsymbol{q}}}{2}), \tag{2.115}$$

which is the famous superconductivity gap equation which can be solved self-consistently. In Chapter 4, we will use these techniques to obtain different gap equations for a more complicated situation where the superconductivity order parameter is a complex momentum-dependent function in the presence of spin-orbit coupling. In that situation, the full BdG Hamiltonian has to be considered since it cannot be rewritten as the block-diagonal form.

2.6.2 TSCs in 1D: Majorana fermions and Kitaev's model

In 1928, Paul Dirac proposed his relativistic wave function for spin one-half fermionic particles in his seminal paper [110]; his equation reads as

$$(i\gamma^{\mu}\partial_{\mu} - m)\psi = 0. \tag{2.116}$$

Here, γ^{μ} denotes 4×4 Dirac matrices obeying the rules of Clifford algebra $\{\gamma^{\mu}, \gamma^{\nu}\} = 2g^{\mu\nu}$ where $g^{\mu\nu}$ is the Minkowski space-time metric whose signature is (-1, +1, +1, +1), m is the

electron rest mass in the vacuum, and $c = 1$. Dirac found a suitable set of these matrices given by

$$\gamma^0 = \sigma^0 \otimes \tau^3, \qquad \gamma^{\mu=1,2,3} = i\sigma^\mu \otimes \tau^2, \tag{2.117}$$

where the Pauli matrices σ and τ refer to the spin and charge degrees of freedom, respectively. In the language of quantum field theory, if a given field creates a particle and annihilates its anti-particle, the complex conjugate of that field, however, will create the anti-particle and annihilate the particle. Therefore, for a complex field since $\psi \neq \psi^*$, the particle and the anti-particle are two distinct objects. In other words, Dirac predicted the notion of anti-particles: for any particle satisfying the Dirac equation of motion, there exists a conjugated solution associated with its anti-particle with the same mass but opposite charge. Dirac's prediction was confirmed later by the discovery of positron [111]. The relativistic fermionic particles governed by the Dirac equation are known as *Dirac fermions*.

In 1937, Ettore Majorana, in his famous paper [112], found a basis where the four Dirac matrices are purely imaginary

$$\tilde{\gamma}^0 = \sigma^2 \otimes \tau^1, \qquad \tilde{\gamma}^1 = i\sigma^3 \otimes \tau^0, \tag{2.118}$$

$$\tilde{\gamma}^2 = -i\sigma^2 \otimes \tau^2, \qquad \tilde{\gamma}^3 = -i\sigma^1 \otimes \tau^0. \tag{2.119}$$

This led him to the fascinating conclusion that the Dirac equation in Majorana's representation is real (since all $i\gamma^\mu$ matrices in the Dirac equation are real for pure imaginary $\tilde{\gamma}^\mu$ matrices), so that it can describe the evolution of real fermionic fields. The fact that ψ can be a real fermionic field results in the interesting fact that there are fermionic particles which are their own anti-particles known an *Majorana fermions*! A Dirac fermion can always be written as a superposition of two Majorana fermions like a complex number that can be written by using two real numbers.

Moreover, the state of two spatially separated Majorana fermions is robust against local perturbations, and adiabatic exchange of them changes the state up to a phase other that 0 and π due to their non-Abelian anyonic nature. Due to these two fascinating properties of Majorana fermions, Majorana in his short life unintentionally uncovered the most profound problem in quantum computing by his discovery. Owing to its non-Abelian exchange statistics, Majorana fermions may finally act as a basic building block or qubit, the quantum analogue of a classical bit, for *topological quantum computing* which is fault-tolerant [38, 39]. Nowadays, engineering systems hosting Majoranas is a very active area of research although finding them in nature is immensely difficult. In fact, the existence of Majorana particles has remained as elusive as Majorana himself, who disappeared without a trace during a boat trip less than a year after he came up with his equation.

In fact, superconductivity appears to be the natural playground since it allows Bogoliubov excitations made of electrons and holes with an inherent particle-hole symmetry in the BdG Hamiltonian [113]. Using the Bogoliubov transformation, the Bogoliubov quasiparticle with energy $+E$ can be written as $d^\dagger = uc^\dagger + vc$, which is a superposition of an electron and a

hole. According to the particle-hole symmetry, there has to be a Bogoliubov anti-quasiparticle $d = v^* c^\dagger + u^* c$ with energy $-E$. It is clear now that we can get Majoran fermions ($d = d^\dagger$) if and only if $u = v^*$ which happens only at $E = 0$. Therefore, the zero-energy Bogoliubov quasiparticles of a superconductor behave like Majorana fermions thanks to the particle-hole symmetry. Moreover, if the pairing symmetry of the superconductor is spin-singlet (Cooper pair with opposite spins), the Bogoliubov transformation does not allow $d = d^\dagger$ even at zero-energy, so the two electrons in the Cooper pair should possess no spin (spinless), which is not the case in nature, or have the same spins. These kinds of superconductors are known as spin-triplet superconductors. They are very rare in nature but they can be created effectively by a spin-singlet superconductor subjected to spin-orbit coupling and Zeeman field.

In 2001, Alexei Kitaev introduced his famous toy model for a one-dimensional spinless superconductor which can support Majorana zero modes [114]. The beauty of this model lies in its simplicity. In the rest of this section we will review the basic properties of Kitaev's model. In particular, the intimate connection between topology and Majorana edge states will become apparent. Kitaev's one-dimensional tight-binding Hamiltonian in the real space for N sites with open-boundary conditions is given by

$$\mathcal{H} = \sum_{i=1}^{N-1} (-t c_i^\dagger c_{i+1} + \Delta c_i c_{i+1}) + h.c. - \mu \sum_{i=1}^{N} c_i^\dagger c_i, \tag{2.120}$$

where t is the nearest-neighbor hopping amplitude, Δ is the superconducting pairing potential, which is taken to be a real number for the sake of simplicity, μ is the chemical potential, and $h.c.$ stands for Hermitian conjugate. Note that the electrons in this model are spinless, so we have an unconventional p-wave superconducting pairing that differs from the usual s-wave pairing where the Cooper pairs are formed by electrons with opposite spins. Taking period boundary conditions ($c_{N+1} = c_1$) and performing Fourier transformation leads to

$$\mathcal{H} = \sum_k (-2t \cos k - \mu) c_k^\dagger c_k - \sum_k (i\Delta \sin k \; c_k^\dagger c_{-k}^\dagger + h.c.), \tag{2.121}$$

which can be rewritten as

$$\mathcal{H} = \frac{1}{2} \sum_k \begin{pmatrix} c_k^\dagger & c_{-k} \end{pmatrix} H(k) \begin{pmatrix} c_k \\ c_{-k}^\dagger \end{pmatrix}, \tag{2.122}$$

up to some constant term. Here,

$$H(k) = d_y(k)\tau_y + d_z(k)\tau_z, \tag{2.123}$$

for

$$d_y(k) = 2\Delta \sin k, \tag{2.124}$$

$$d_z(k) = -2t\cos k - \mu, \tag{2.125}$$

where $\tau_{y,z}$ are Pauli matrices acting on particle-hole space. One can check particle-hole symmetry $\mathcal{P}H(k)\mathcal{P}^{-1} = -H(-k)$ for $\mathcal{P} = \tau_x\mathcal{K}$ where $\mathcal{P}^2 = 1$. Moreover, one can also see that the superconducting order-parameter $\Delta(k) = \Delta\sin k$ is momentum dependent and it is odd under inversion operation *i.e* $\Delta(k) = -\Delta(-k)$. The energy spectra of the BdG Hamiltonian (2.123) is given by,

$$E(k) = \pm\sqrt{(2t\cos k + \mu)^2 + 4\Delta^2\sin^2 k}, \tag{2.126}$$

so the energy gap is closed at $\mu = \pm 2t$. As the BdG Hamiltonian only contains two Pauli matrices, the experience from the Su-Schrieffer-Heeger (see subsection 2.5.1) tell us that the topological nontrivial region is the $|\mu| < 2t$ region. This corresponds to the picture that the trajectory of the end of vector $\boldsymbol{d}(k) = (d_y(k), d_z(k))$ in the k_yk_z plane will enclose the origin when k goes across the whole Brillouin zone. However, the reason that we can use this picture is because this Hamiltonian has an additional chiral symmetry whose operator is $\mathcal{S} = \tau_z$.

The most remarkable step made by Kitaev is decomposing the Dirac fermion operator into two Majorana fermion operators which are self-conjugate [114],

$$c_j = \frac{1}{2}(\gamma_{2j-1} + i\gamma_{2j}), \tag{2.127}$$

$$c_j^\dagger = \frac{1}{2}(\gamma_{2j-1} - i\gamma_{2j}). \tag{2.128}$$

This is analogous to the decomposition of a complex number to two real numbers. The usual fermions satisfy the anticommutation relation $\{c_i, c_j^\dagger\} = \delta_{i,j}$. Given this, we should have

$$\{\gamma_i, \gamma_j^\dagger\} = 2\delta_{i,j}, \tag{2.129}$$

which leads to $\{\gamma_i, \gamma_j\} = 2\delta_{i,j}$ by using of $\gamma_i^\dagger = \gamma_i$. Remarkably, $\gamma_i^2 = 1$ not zero! Using the Majorana operators, the Hamiltonian (2.120) can be written as,

$$\mathcal{H} = \frac{i}{2}\sum_{j=1}^{N-1}\Big\{(\Delta + t)\gamma_{2j}\gamma_{2j+1} + (\Delta - t)\gamma_{2j-1}\gamma_{2j+2}\Big\} - \frac{i\mu}{2}\sum_{j=1}^{N}\gamma_{2j-1}\gamma_{2j}. \tag{2.130}$$

Let us focus on two limiting cases:

- $\Delta = t = 0$ and $\mu < 0$: For this case, the Hamiltonian reduces to

$$H_1 = -\frac{i\mu}{2}\sum_{j=1}^{N}\gamma_{2j-1}\gamma_{2j}. \tag{2.131}$$

  The ground state of H_1 satisfies,

$$c_j|\Psi\rangle = 0, \tag{2.132}$$

  for $j = 1, 2, \ldots, N$.

- $\Delta = t > 0$ and $\mu = 0$: For this case the Hamiltonian reduces to

$$H_2 = it \sum_{j=1}^{N-1} \gamma_{2j}\gamma_{2j+1}. \tag{2.133}$$

One can easily see that γ_1 and γ_{2N} do not enter in H_2. In other words, the two Majorana fermions at the boundary do not couple with other Majorana fermions in this case, so this case is topologically non-trivial such that one zero energy state is localized at each end of a one-dimensional model. As these zero-energy states are self-conjugate, they are dubbed Majorana zero modes. By defining a non-local fermion

$$\tilde{c} = \frac{1}{2}(\gamma_1 + i\gamma_{2N}), \tag{2.134}$$

$$\tilde{c}^\dagger = \frac{1}{2}(\gamma_1 - i\gamma_{2N}), \tag{2.135}$$

one can check that $[H_2, \tilde{c}] = [H_2, \tilde{c}^\dagger] = 0$. If $|\Psi_0\rangle$ is the ground state of H_2 satisfying $\tilde{c}|\Psi_0\rangle = 0$, then $|\Psi_1\rangle = \tilde{c}^\dagger|\Psi_0\rangle = 0$ is also the ground state of the Hamiltonian. In other words, the ground state is doubly degenerate and the number of occupied fermions in the two ground states differs by one. As *the fermion parity* (the parity of the number of fermions) is a good quantum number, this is equivalent to saying that the two ground states $|\Psi_0\rangle$, $|\Psi_1\rangle$ have different fermion parity; one is odd and the other one is even. It is worth noting here that the interacting part of the Hamiltonian before mean-field decoupling is invariant under gauge transformation $c_{k,\sigma} \to e^{i\theta}c_{k,\sigma}$, so for all the values of θ, it has $U(1)$ symmetry. However, after performing mean-field decoupling, the $U(1)$ symmetry is broken to $\mathbb{Z}_2$ symmetry since θ can only take two values 0, π such that the Hamiltonian remains unchanged. The fermion parity is defined as

$$P_f = (-1)^{\sum_{\boldsymbol{k},\sigma} \hat{n}_{\boldsymbol{k},\sigma}}, \tag{2.136}$$

where $\hat{n}_{\boldsymbol{k},\sigma} = c^\dagger_{\boldsymbol{k},\sigma}c_{\boldsymbol{k},\sigma}$ is the particle number operator.

By performing Fourier transformation on the Majorana operators,

$$\gamma_{2j-1} = \frac{1}{N}\sum_k \gamma_{1,k}e^{ikj}, \tag{2.137}$$

$$\gamma_{2j} = \frac{1}{N}\sum_k \gamma_{2,k}e^{ikj}, \tag{2.138}$$

and using $\gamma_j = \gamma_j^\dagger$ or equivalently $\gamma_k^\dagger = \gamma_{-k}$, the Majorana-representation of the Hamiltonian becomes,

$$\mathcal{H} = \frac{i}{4}\sum_k \psi_k^\dagger \mathcal{A}(k)\psi_k, \tag{2.139}$$

where $\psi_k^T = (\gamma_{1,-k},\ \gamma_{2,-k})$ and

$$\mathcal{A}(k) = \begin{pmatrix} 0 & \varsigma_k \\ -\varsigma_k^* & 0 \end{pmatrix}, \tag{2.140}$$

where $\varsigma_k = -2t\cos k - \mu - 2i\Delta \sin k$. A topological phase transition takes place only when the determinant of $\mathcal{A}(k)$ vanishes. It is noteworthy that for more general cases, the $\mathcal{A}(k)$ matrix is also off-diagonal. At two time-reversal invariant momenta $k = 0, \pi$, the matrix $\mathcal{A}(k)$ is antisymmetric, so the Pfaffian can be defined. Kitaev showed that the topological invariant is simply given by [43]

$$\begin{aligned} (-1)^\nu &= \mathrm{sgn}[\mathrm{Pf}(\mathcal{A}(k=0))]\ \mathrm{sgn}[\mathrm{Pf}(\mathcal{A}(k=\pi))] \\ &= \mathrm{sgn}(-2t-\mu)\ \mathrm{sgn}(2t-\mu), \end{aligned} \tag{2.141}$$

where in the second line we used Eq. 2.90. Therefore, for $|\mu| < 2t$ one has $\nu = 1$ (topologically non-trivial), and for $|\mu| > 2t$ one has $\nu = 0$ (topologically trivial) resulting in a $\mathbb{Z}_2$ classification.

To get an even better intuition, let us consider the low energy continuum Hamiltonian briefly. Expanding the BdG Hamiltonian (2.123) around $k = 0$ and taking only the first-order terms gives

$$H_{\text{eff}} = -(2t+\mu)\tau_z + 2\Delta k \tau_y. \tag{2.142}$$

This is precisely a Dirac Hamiltonian which is linear in momentum k with mass term $m = -2t - \mu$, so the boundary between topologically trivial and nontrivial phases is now encoded in the sign of mass, and $m = 0$ corresponds to the critical point *i.e.* the topological phase transition at which the bulk energy gap closes and the mass term switches sign. Now we allow the mass term to vary with position x in such a way that

$$\lim_{x\to\pm\infty} m(x) = \pm m, \tag{2.143}$$

$$m(x=0) = 0. \tag{2.144}$$

Then, $x = 0$ corresponds to a domain wall separating two regions of space where m is negative for $(x < 0)$ and is positive for $(x > 0)$. To be able to use this mass term in the Hamiltonian, the Bloch Hamiltonian has to be rewritten in real space as

$$H(x) = m(x)\tau_z - 2i\Delta\tau_y\partial_x, \tag{2.145}$$

where we substituted $k \to -i\partial_x$. Solving the Schrödinger equation for zero-energy states gives

$$H(x)\phi(x) = [m(x)\tau_z - 2i\Delta\tau_y\partial_x]\phi(x) = 0. \tag{2.146}$$

This first-order differential equation can be solved by multiplying the equation from the left side by τ_y and using $\tau_y\tau_z = i\tau_x$ and $\tau_y^2 = 1$, so

$$\partial_x\phi(x) = \frac{m(x)}{2\Delta}\tau_x\phi(x), \tag{2.147}$$

The solution can be derived as

$$\phi(x) = \exp(\pm \int_0^x \frac{m(x')}{2\Delta} dx') \frac{1}{\sqrt{2}} \begin{pmatrix} 1 \\ \pm 1 \end{pmatrix}. \tag{2.148}$$

However, due to the fact that $m(x)$ changes sign at $x = 0$, only one of the solutions will be normalizable. If the sign of the mass term did not change, there would be no normalizable solutions. This Majorana zero mode is localized at the interface or $x = 0$. This special behavior due to the sign change of Dirac mass was first obtained by Jackiw and Rebbi in 1976 [80].

Candidate host materials for Majorana fermions are Sr_2RuO_4 which is a spinful p-wave material [115], the A-phase of superfluid ^{3}He, the fractional quantum Hall phase with filling fraction $\nu = 5/2$ known as the Moore-Read state [116], and zero-energy bound states in the core of vortices in a chiral $p_x + ip_y$ superconductor [116–119]. While odd-parity superconductors generally provide a natural realization of topological superconductors [114, 120–123], their scarcity in nature turns out to be a serious obstacle from an experimental point of view. It is also possible to find them in the hybrid structure of a three-dimentional topological insulator and conventional s-wave superconductor [124]. Fortunately, the combination of spin-orbit coupling and Zeeman field enable the realization of effective odd-parity superconductivity on the basis of abundant even-parity superconductivity, providing a more readily accessible route for the realization of topological superconductors [125–131]. Over the past decade, remarkable progress along this route has been witnessed [132–140].

In the next section, we will study Majorana zero modes in the context of vortices in a two-dimensional chiral $p_x + ip_y$ superconductors. This mechanism will be used for interpreting the results of Chapter 5.

2.6.3 TSCs in 2D: Chiral $p_x + ip_y$ superconductors and vortex bound state

In two dimensions, the simplest realization of topological superconductor phases is the chiral p-wave pairing with $p_x + ip_y$ pairing symmetry. The Hamiltonian for such a system in momentum space is given as

$$\mathcal{H} = \frac{1}{2} \sum_{\boldsymbol{k}} \psi_{\boldsymbol{k}}^\dagger H(\boldsymbol{k}) \psi_{\boldsymbol{k}}, \tag{2.149}$$

for $\boldsymbol{k} = (k_x, k_y)$, and $\psi_{\boldsymbol{k}}^T = (c_{\boldsymbol{k}},\ c_{-\boldsymbol{k}}^\dagger)$, where

$$H(\boldsymbol{k}) = \sum_{i=x,y,z} d_i(k) \tau_i, \tag{2.150}$$

with

$$d_x(k) = 2\Delta \sin k_x, \tag{2.151}$$

$$d_y(k) = 2\Delta \sin k_y, \tag{2.152}$$
$$d_z(k) = -2t(\cos k_x + \cos k_y) - \mu. \tag{2.153}$$

This Hamiltonian has particle-hole symmetry for $\mathcal{P} = \tau_x\mathcal{K}$ and does not have time-reversal symmetry, so the Hamiltonian is characterized by a non-zero Chern number.

Although chiral $p_x + ip_y$ topological superconductors (class D), and both integer quantum Hall effect and Chern insulators (class A) all break time-reversal symmetry and all are characterized by a non-zero Chern number, class D describes superconductors and class A describes insulators which leads to distinct chiral boundary modes. The chiral Majorana boundary excitation for a topological superconductor is neutral since Majorana zero modes are an equal superposition of electron (negative charge) and hole (positive charge), so the boundary Majorana zero-modes of a topological superconductor cannot transport charge current in sharp contrast to quantum Hall effect. However, they can transport thermal current since there is no difference for the energy current carried by electrons and holes. Therefore, the thermal conductivity of the edges is an experimental observable which is directly related to the Chern number in a chiral topological superconductor.

Assume a chiral $p_x + ip_y$ superconductor with two different geometries: a disk with one edge and a cylinder with two edges. For an edge of length L, the smallest difference between two momenta along the edge is $2\pi/L$, so the energy difference between two levels is $v2\pi/L$ where v is the velocity of dispersing chiral Majorana modes. For a disk, which has one edge, there cannot be a single state at momentum $p = 0$ at energy $E = 0$. If such a state was there, the spectrum would contain an odd number of states which is not possible since the number of eigenvalues of a given BdG Hamiltonian is *always* an even number. One way to introduce such a state is to have *antiperiodic boundary conditions* so the spectrum of the edge will be at momentum $\pi(2n + 1)/L$ for $n \in \mathbb{Z}$. For a cylinder, however, as two edges are present, *periodic boundary conditions* are allowed where the momentum is given by $2\pi n/L$ for $n \in \mathbb{Z}$. Therefore, it is possible to get a zero mode at $p = 0$ for a cylinder.

Now, let us add a single vortex inside the disk far away from the edge. What can be the impact of this vortex on the edge? The vortex induces a phase 2π in unit of $h/2e$ where h is Planck's constant and e is the charge of an electron. This implies that the antiperiodic boundary conditions on the edge without vortex changes to periodic boundary conditions in the presence of a vortex, so the spectrum on the edge is translated by π/L compared to the case without the vortex, making it have an energy level at $p = 0$ with energy $E = 0$. This would mean that the spectrum has an odd number of levels. However, this cannot be true, so we are missing one unpaired level! Where is it? Since the only difference with the case with no vortex is the vortex itself, we draw the conclusion that the missing level is associated with the vortex and is a bound state in the vortex. Since it is unpaired and really bound to the vortex, it has to rest exactly at $E = 0$, so spinless chiral superconductors have a single Majorana zero mode in their vortex core. At the same time, a single Majorana zero mode appears on the edge.

It turns out that an even Chern number topological superconductor has no Majorana zero modes in the vortex while an odd Chern number topological superconductor has one Majorana zero mode in its core. This shows that vortices in a topological superconductors are classified by a $\mathbb{Z}_2$ number which is Chern number mod 2.

2.7 Crystalline and higher-order topological phases

We have discussed different realizations of topological phases of matter so far. The topological phases in the Altland-Zirnbauer table are protected entirely by so-called generic, non-spatial symmetries that cannot be represented by unitary operators that commute with the Hamiltonian. Therefore, topologically protected states appear on all surfaces and the interfaces of the system even in the presence of weak disorder since these spatial modifications of the system do not affect a non-spatial symmetry. But what will happen if we consider ordinary spatial symmetries represented by unitary operators? This led to the discovery of *topological crystalline insulators* which has opened the door to new topological phases of matter whose topological nature arises from the richness and complexity of crystal symmetries.

In 2011 Fu, in another seminal paper, presented a three-dimensional toy model with gapless surface states protected by the combined effects of four-fold rotation (C_4) and time-reversal symmetries. This toy model represents the first example of a large class of topological crystalline insulators [44]. In 2012, one year after this theoretical prediction, the non-trivial surface states were successfully observed [45–47].

Those spatial symmetries are point-group symmetries such as inversion [141, 142], mirror [143–145], and rotation [44], in addition to space-group symmetries such as glide planes and screw axes or a combination of them [32, 146, 147]. These symmetries have been recently extended to include magnetic space groups [148–150]. Moreover, all these crystal symmetries can even enrich the topological phases in the Altland-Zirnbauer table [151]. This has been done for several cases, such as systems with inversion symmetry or mirror symmetry. These crystalline symmetries lead to new topological invariants such as *mirror Chern number* [151].

Topological crystalline insulators are susceptible to disorder, so topological features are expected to persist only if the protecting crystal symmetry is preserved on average [48]. Moreover, *not all* surfaces of a topological crystalline insulator host topological surface states, only those that do not break the protecting crystal symmetry. For example, a topological crystalline insulator protected by a C_4 rotation symmetry will have generally topological states only on the surfaces perpendicular to the axis of rotation [44].

In 2017, a new class of topological crystalline phases, named *higher-order topological phases* was theoretically predicted by Benalcazar, Bernevig, and Hughes in which the dipole polarization vanishes while higher electric multipole moments are quantized to fractional values [53, 54]. Nowadays, this model is known as *the BBH model*. The word "order" in this context gives the codimension of the gapless boundary modes, namely, an nth order topolog-

ical insulator or topological superconductor has gapless boundary modes with codimension n. As the gapless boundary modes of all conventional topological insulators and topological superconductors have $n = 1$, they thus belong to the first-order topological phases in this language. Therefore, conventional bulk-boundary correspondence, which states gapless topological boundary states emerge only at boundaries that are one dimension lower than the bulk, is not valid here.

First-order or conventional topological phases ($n = 1$) host gapless edge states. *Second-order topological phases* ($n = 2$) have gapped edge states with a fractional dipole moment, and electric charge accumulated at the four corners of two-dimensional finite systems. *Third-order topological phases* ($n = 3$) host gapped surface states with a fractional quadrupole moment, gapped hinge states with a fractional dipole moment, and electric charge accumulated at the eight corners of three-dimensional finite systems [53]. In the context of higher-order topological superconductors, these corner and hinge modes are know as *Majorana corner states* and *Majorana hinge states*, respectively [152–155].

Higher-order topological phases have attracted a great deal of attention because of the enrichment of boundary physics, the intriguing manifestation of crystalline symmetry and band topology at the bulk and boundaries, as well as the occurrence of new possibilities for topological phase transitions. These intriguing phases could provide new platforms for Majorana zero modes and topological quantum computing and enable unprecedented topological devices with better integration and miniaturization.

In the last two years, higher-order topological phases have been proposed in systems without quantized multiple moments [55], and in non-periodic lattices such as amorphous [56], and quasicrystalline [57] solids. Moreover, higher-order non-Hermitian topological phases [58, 59], higher-order Weyl semimetals [60, 61], and higher-order Floquet topological phases [62, 63] have attracted a great deal of attention and revealed many ubiquitous physical properties.

Chapter 3

Majorana Corner Flat Bands in Second-Order Topological Superconductors

3.1 Introduction

In this chapter, which is based on publication (I), we will show that a two-dimensional topological insulator in proximity to a high-temperature $d_{x^2-y^2}$-wave superconductor can lead to a second-order topological superconductor, which hosts Majorana corner states. In terms of the conventional bulk-boundary correspondence, these materials are topologically trivial since both bulk and boundary states are gapped. However, there are robust gapless states on the "edge" of the boundary of these materials. In d-spatial dimensions, n-th order topological insulators and superconductors have $(d-n)$-dimensional gapless localized modes.

It will be shown that confining this second-order topological superconductor with a harmonic potential leads to a proliferation of Majorana corner modes. As a consequence, this results in the formation of *Majorana corner flat bands* which have a fundamentally different origin from that of the conventional mechanism. This is due to the fact that they arise solely from the one-dimensional gapped boundary states of the hybrid system that becomes gapless without the bulk gap closing under the increase of the trapping potential magnitude. The Majorana corner states are found to be robust against the strength of the harmonic trap and the transition from Majorana corner states to Majorana flat bands is merely a smooth crossover. As a harmonic trap can potentially be realized in heterostructures, this proposal paves a way to observe these Majorana corner flat bands in an experimental context.

3.2 The origin of Majorana corner states

Let us introduce the Bogoliubov-de Gennes (BdG) Hamiltonian of a two-dimensional topological insulator, also known as quantum spin Hall insulator, in proximity with a d-wave superconductor which is given by,

$$\mathcal{H} = \frac{1}{2}\sum_{ij} \boldsymbol{\psi}_i^\dagger \begin{pmatrix} \hat{H}_{ij}^{\mathrm{N}} & \hat{\Delta}_{ij} \\ \hat{\Delta}_{ij}^\dagger & -\hat{H}_{ij}^{\mathrm{N}*} \end{pmatrix} \boldsymbol{\psi}_j. \tag{3.1}$$

Here, $\boldsymbol{\psi}_i^\dagger = (c_{i,a,\uparrow}^\dagger, c_{i,b,\uparrow}^\dagger, c_{i,a,\downarrow}^\dagger, c_{i,b,\downarrow}^\dagger, c_{i,a,\uparrow}, c_{i,b,\uparrow}, c_{i,a,\downarrow}, c_{i,b,\downarrow})$, and $c_{i,\alpha,\beta}^\dagger(c_{i,\alpha,\beta})$ denotes the creation (annihilation) operator of an electron at site $i = (i_x, i_y)$, in orbital $\alpha \in (a, b)$, with spin $\beta \in (\uparrow, \downarrow)$. The normal state and superconducting parts of the Hamiltonian are $4N \times 4N$ complex matrices for a square lattice with N sites and they are given by

$$\hat{H}_{ij}^{\mathrm{N}} = m_{ij}\sigma_z s_0 + A_{ij}^x \sigma_x s_z + A_{ij}^y \sigma_y s_0 - \mu\delta_{ij}\sigma_0 s_0, \tag{3.2}$$

$$\hat{\Delta}_{ij} = -\,\mathrm{i}\Delta_{ij}\sigma_0 s_y, \tag{3.3}$$

respectively. The mass term is

$$m_{ij} = m_0\delta_{ij} - \frac{t}{2}(\delta_{i,i+\hat{x}} + \delta_{i,i-\hat{x}} + \delta_{i,i+\hat{y}} + \delta_{i,i-\hat{y}}), \tag{3.4}$$

where m_0 is on-site orbital-dependent energy, and t is the intra-orbital nearest neighbor hopping magnitude along the x and y directions with unit vectors $\hat{x}$ and $\hat{y}$. The $\sigma_{x,y,z}$ and $s_{x,y,z}$ are Pauli matrices acting on orbital and spin degree of freedoms, respectively, and σ_0 and s_0 are 2×2 unit matrices. Moreover,

$$A_{ij}^x = -\frac{\mathrm{i}\lambda}{2}(\delta_{i,i+\hat{x}} - \delta_{i,i-\hat{x}}), \tag{3.5}$$

$$A_{ij}^y = -\frac{\mathrm{i}\lambda}{2}(\delta_{i,i+\hat{y}} - \delta_{i,i-\hat{y}}), \tag{3.6}$$

are the spin-orbit coupling terms with magnitude λ. The symbol i denoting pure imaginary number should not be confused with the site-index that generally occurs subscripted. The chemical potential is given by μ, and the d-wave superconductivity order parameter with $d_{x^2-y^2}$-wave symmetry is expressed as,

$$\Delta_{ij} = \frac{\Delta_d}{2}(\delta_{i,i+\hat{x}} + \delta_{i,i-\hat{x}} - \delta_{i,i+\hat{y}} - \delta_{i,i-\hat{y}}). \tag{3.7}$$

The corresponding BdG Hamiltonian in momentum space for a square lattice with a unit lattice constant can be written as

$$\mathcal{H} = \frac{1}{2}\sum_{\boldsymbol{k}} \Psi^\dagger_{\boldsymbol{k}} \mathcal{H}_{\mathrm{BdG}}(\boldsymbol{k}) \Psi_{\boldsymbol{k}}, \tag{3.8}$$

where $\Psi^\dagger_{\boldsymbol{k}} = (c^\dagger_{\boldsymbol{k},a,\uparrow}, c^\dagger_{\boldsymbol{k},b,\uparrow}, c^\dagger_{\boldsymbol{k},a,\downarrow}, c^\dagger_{\boldsymbol{k},b,\downarrow}, c_{-\boldsymbol{k},a,\uparrow}, c_{-\boldsymbol{k},b,\uparrow}, c_{-\boldsymbol{k},a,\downarrow}, c_{-\boldsymbol{k},b,\downarrow})$ and,

$$\begin{aligned}\mathcal{H}_{\mathrm{BdG}}(\boldsymbol{k}) = {} & m(\boldsymbol{k})\sigma_z s_0 \tau_z + \lambda \sin k_x \sigma_x s_z \tau_0 + \lambda \sin k_y \sigma_y s_0 \tau_z \\ & + \Delta(\boldsymbol{k})\sigma_0 s_y \tau_y - \mu \sigma_0 s_0 \tau_z. \end{aligned} \tag{3.9}$$

Here, $\tau_{x,y,z}$ are Pauli matrices in particle-hole space, τ_0 is the 2×2 unit matrix, and

$$\Delta(\boldsymbol{k}) = \Delta_d(\cos k_x - \cos k_y), \tag{3.10}$$

$$m(\boldsymbol{k}) = m_0 - t(\cos k_x + \cos k_y). \tag{3.11}$$

It should be noted that the above Hamiltonian without d-wave pairing (the normal state part) becomes the paradigmatic Bernevig-Hughes-Zhang (BHZ) model of two-dimensional topological insulators [18]. The eigenvalues of this part of the Hamiltonian are given by

$$E(\boldsymbol{k}) = \pm\sqrt{m^2(\boldsymbol{k}) + \lambda^2(\sin^2 k_x + \sin^2 k_y)} - \mu. \tag{3.12}$$

Hence, the insulating gap as an important quantity in our analysis in section 3.3, is given by $m(\boldsymbol{k} = 0) = |m_0 - 2t|$. Moreover, the BdG Hamiltonian possesses both particle-hole symmetry ($\mathcal{P}$) and time-reversal symmetry ($\mathcal{T}$)

$$\mathcal{P}\mathcal{H}^*_{\mathrm{BdG}}(\boldsymbol{k})\mathcal{P}^{-1} = -\mathcal{H}_{\mathrm{BdG}}(-\boldsymbol{k}), \tag{3.13}$$

$$\mathcal{T}\mathcal{H}^*_{\mathrm{BdG}}(\boldsymbol{k})\mathcal{T}^{-1} = \mathcal{H}_{\mathrm{BdG}}(-\boldsymbol{k}), \tag{3.14}$$

where $\mathcal{P} = \sigma_0 s_0 \tau_x$ and $\mathcal{T} = i\sigma_0 s_y \tau_0$. The intrinsic particle-hole symmetry of the BdG Hamiltonian guarantees that the eigenstates whose eigenvalues are zero satisfy the Majorana conditions as discussed in Appendix A. The combination of these two anti-unitary symmetries gives rise to a unitary chiral symmetry ($\mathcal{S}$),

$$\mathcal{S}\mathcal{H}_{\mathrm{BdG}}(\boldsymbol{k})\mathcal{S}^{-1} = -\mathcal{H}_{\mathrm{BdG}}(\boldsymbol{k}), \tag{3.15}$$

where $\mathcal{S} = -i\mathcal{P}\mathcal{T}$.

The helical edge states of a topological insulator can be described as one-dimensional massless Dirac fermions. These gapless edge states can be gapped out by the induced d-wave superconductivity which introduces a Dirac mass as is shown in Fig. 3.1(a). In this figure, the energy spectra in the cylinder geometry where the x direction is taken to be

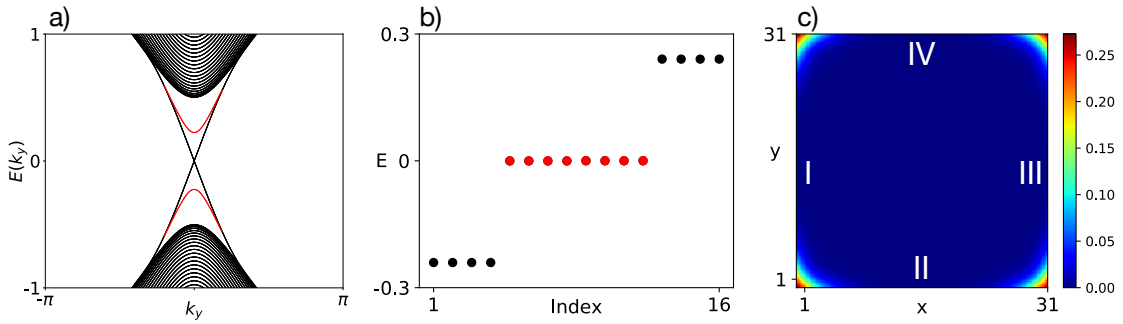

Figure 3.1: (Color online) (a) The edge states in a cylinder geometry where the x direction is taken to be open while the y direction is periodic without (solid black line) and with (solid red line) the d-wave superconductivity. The helical edge states of the two-dimensional topological insulator are gapped out by the induced superconductivity. (b) The fourteen smallest eigenvalues of the BdG Hamiltonian in real space and the eight zero energy Majorana corner states in red color, (c) the probability profile of the eight Majorana zero modes which are localized at the four corners of the sample. The four boundaries of the square sample are labelled by (I), (II), (III), and (IV) for the use in the edge theory. Common parameters are $m_0 = 1.5$, $\mu = 0$, $t = \lambda = 1$, and $\Delta_d = 0.5$. In (b)(c), we used a 31×31 square lattice with open boundary conditions.

open while the y direction is periodic without (solid black line) and with (solid red line) the d-wave superconductivity is plotted for a given set of parameters. It illustrates that the helical edge states of the two-dimensional topological insulator are gapped out by d-wave pairing. In Fig. 3.1(b), the energies near zero and the probability profile of the four Majorana Kramers pairs (eight Majorana zero modes) are shown from the diagonalization of the BdG Hamiltonian in real space for a 31×31 square lattice with open boundary conditions. Due to pairing symmetry, the sign of Dirac mass changes at adjacent one-dimensional boundaries of the two-dimensional topological insulator. This results in the appearance of one pair of zero energy Majorana Kramers pairs as a domain-wall excitation at each corner of the sample known as Majorana corner states as shown in Fig. 3.1(c).

In order to enhance our intuitive understanding, we take $\mu = 0$ and focus on the continuum model by expanding the lattice BdG Hamiltonian (3.9) to the second-order around $\boldsymbol{k} = (0, 0)$ point in the first Brillouin zone,

$$H = (m + \frac{t}{2}k_x^2 + \frac{t}{2}k_y^2)\sigma_z s_0 \tau_z + \lambda(k_x \sigma_x s_z \tau_0 + k_y \sigma_y s_0 \tau_z) - \frac{\Delta_d}{2}(k_x^2 - k_y^2)\sigma_0 s_y \tau_y, \tag{3.16}$$

where $m = m_0 - 2t < 0$ is assumed to ensure that the two-dimensional insulator without pairing is topologically nontrivial. In Fig. 3.1(c), the four boundaries of the square sample are labelled by (I), (II), (III), and (IV) for the use in the edge theory. First, we focus on boundary (I) of the square sample and replace $k_x \to -i\partial_x$, so the Hamiltonian can be written as $H = H_0 + H_p$ where

$$H_0(-i\partial_x, k_y) = (m - \frac{t}{2}\partial_x^2)\sigma_z s_0 \tau_z - i\lambda \sigma_x s_z \tau_0 \partial_x, \tag{3.17}$$

$$H_p(-i\partial_x, k_y) = \lambda k_y \sigma_y s_0 \tau_z + \frac{\Delta_d}{2}\sigma_0 s_y \tau_y \partial_x^2, \tag{3.18}$$

where k_y^2 is omitted. Here, H_p is treated as a perturbation when the pairing is relatively small which is the case in real samples. By solving the eigenvalue equation $H_0\phi_n(x) = E_n\phi_n(x)$, we will find the following four zero-energy solutions under the boundary condition $\phi_n(x = 0) = \phi_n(x = \infty) = 0$ where

$$\phi_n(x) = c\ \sin(\kappa_1 x)e^{-\kappa_2 x}e^{ik_y y}\ \chi_n, \tag{3.19}$$

and

$$|c|^2 = 4|\frac{\kappa_2(\kappa_1^2 + \kappa_2^2)}{\kappa_1^2}|, \tag{3.20}$$

for $\kappa_1 = \sqrt{|\frac{2m}{t}| - (\frac{\lambda}{t})^2}$, $\kappa_2 = \lambda/t$ and

$$\chi_1 = |\sigma_y = -1\rangle \otimes |\uparrow\rangle \otimes |\tau_z = +1\rangle, \tag{3.21}$$
$$\chi_2 = |\sigma_y = +1\rangle \otimes |\downarrow\rangle \otimes |\tau_z = +1\rangle, \tag{3.22}$$
$$\chi_3 = |\sigma_y = +1\rangle \otimes |\uparrow\rangle \otimes |\tau_z = -1\rangle, \tag{3.23}$$
$$\chi_4 = |\sigma_y = -1\rangle \otimes |\downarrow\rangle \otimes |\tau_z = -1\rangle. \tag{3.24}$$

In this basis, the matrix elements of H_p are given by,

$$H^{\mathrm{I}}_{n,m}(k_y) = \int_0^\infty dx\ \phi_n^*(x)H_p(-i\partial_x, k_y)\phi_m^*(x). \tag{3.25}$$

Therefore, the low-energy effective Hamiltonian for boundary (I) reads as,

$$H^{\mathrm{I}}(k_y) = -\lambda k_y s_z + M_{\mathrm{I}} s_y \tau_y, \tag{3.26}$$

where the Dirac mass is

$$M_{\mathrm{I}} = \frac{\Delta_d}{2}\int_0^\infty dx\ \phi_n^*(x)\partial_x^2\phi_n^*(x) = \frac{m}{t}\Delta_d = (\frac{m_0}{t} - 2)\Delta_d. \tag{3.27}$$

Similarly, for the other three boundaries we have,

$$H^{\mathrm{II}}(k_x) = \lambda k_x s_z + M_{\mathrm{II}} s_y \tau_y, \tag{3.28}$$
$$H^{\mathrm{III}}(k_y) = \lambda k_y s_z + M_{\mathrm{III}} s_y \tau_y, \tag{3.29}$$
$$H^{\mathrm{IV}}(k_x) = -\lambda k_x s_z + M_{\mathrm{IV}} s_y \tau_y, \tag{3.30}$$

where

$$M_{\mathrm{II}} = -(\frac{m_0}{t} - 2)\Delta_d, \tag{3.31}$$

$$M_{\mathrm{III}} = +(\frac{m_0}{t} - 2)\Delta_d, \tag{3.32}$$

$$M_{\mathrm{IV}} = -(\frac{m_0}{t} - 2)\Delta_d. \tag{3.33}$$

Therefore, by adding proximity-induced d-wave superconductivity, the helical gapless boundary modes of the two-dimensional topological insulator become gapped such that the one-dimensional effective systems along the vertical and horizontal boundaries have different topological invariants or Dirac masses as we have shown. Hence, there should be gapless zero modes at four intersections or corners of the two-dimensional topological insulator known as Majorana corner states analogous to the Jackiw-Rebbi zero modes [80]. In a time-reversal invariant system, Majorana corner states manifest themselves as *Majorana Kramers pairs*, which are protected zero-energy modes localized at the four corners of the two-dimensional topological insulator in proximity with a d-wave superconductor. Through this work, we set $m_0 = 1.5$, $\mu = 0$, $t = \lambda = 1$, and $\Delta_d = 0.5$.

3.3 Majorana corner flat bands

Majorana corner states are robust in a two-dimensional topological insulator in proximity with either cuprate-based or iron-based high-temperature superconductors [152]. In such a system, modest edge imperfections do not affect the Majorana corner states while big edge imperfections just create new corners that host their own Majorana corner states. This study suggests that the shape of the system is important and it has some effects on the Majorana corner states. In this section we are going to study the effects of a harmonic potential as an example of a gradual confining potential on the Majorana corner states by adding the following two-dimensional single particle potential

$$V_i = v_{\mathrm{trap}}\big\{(i_x - i_x^c)^2 + (i_y - i_y^c)^2\big\}\sigma_0 s_0, \tag{3.34}$$

to the normal state part of the Hamiltonian (Eq. 3.2) where v_{trap} is the harmonic potential magnitude, and $i^c = (i_x^c, i_y^c)$ is the coordinate of the central site of the square lattice which we take as the origin.

Here, there is no well-defined edge associated with a gradual confining potential and near a Majorana corner state, there is no additional corner where additional Majorana corner states can appear. In the limit of a harmonic potential whose magnitude is much larger than the insulating gap, the region near the four corners of two-dimensional topological insulator in proximity with a d-wave superconductor becomes the location for unconventional superconductivity. It should be pointed out that in the homogeneous system by increasing the chemical potential there is a topological phase transition with bulk gap closing. Moreover, a time-reversal invariant d-wave superconductor with [110] surface, has zero-energy flat dispersion due to a nontrivial one-dimensional winding number at a large enough chemical potential

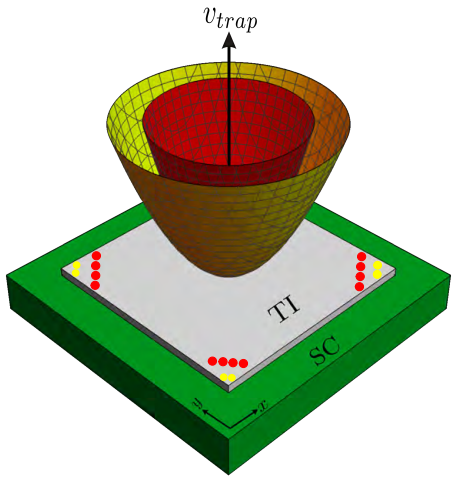

Figure 3.2: (Color online) Schematic figure of a two-dimensional topological insulator in proximity with a high-temperature d-wave superconductor in the presence of two different two-dimensional harmonic potentials, where the red paraboloid has larger potential magnitude than the yellow one. The Majorana zero modes are shown by red and yellow points. The number of Majorana corner states (yellow points) gradually increases as the harmonic potential magnitude increases which results in the formation of Majorana corner flat bands (red points).

[130, 156–158]. Therefore, there might be a transition from Majorana corner states to Majorana flat bands in a nonhomogeneous system with increasing harmonic potential magnitude. The question arises: to what degree can the number of Majorana corner states be varied as we change the magnitude of a confining potential? Will a topological phase transition occur as the bulk gap closes, or will there be a crossover as the bulk gap continues to decrease without closing?

We will show that in a second-order topological superconductors with a confining harmonic potential the Majorana corner states-Majorana flat bands transition is merely a crossover: the number of the Majorana zero modes gradually increases, as shown schematically in Fig. 3.2, while there is no two-dimensional bulk gap closing as the harmonic potential magnitude increases. We find that the increase of the number of Majorana zero modes indicates the appearance of new Majorana states originating from the fact that *only* one-dimensional gapped boundary modes become gapless *without* closing the bulk gap as illustrated in Fig. 3.3. This eventually leads to a new kind of Majorana flat bands which we call *Majorana corner flat bands*. It is found that two-dimensional bulk states do not become gapless with increasing the harmonic potential magnitude in a system with open-boundary conditions, *i.e.*, the host system for the Majorana corner states. We show that the crossover behavior is important for explaining the increase in the number of Majorana zero modes. In contrast, in a system with periodic boundary conditions, the two-dimensional bulk gap is closed if the potential

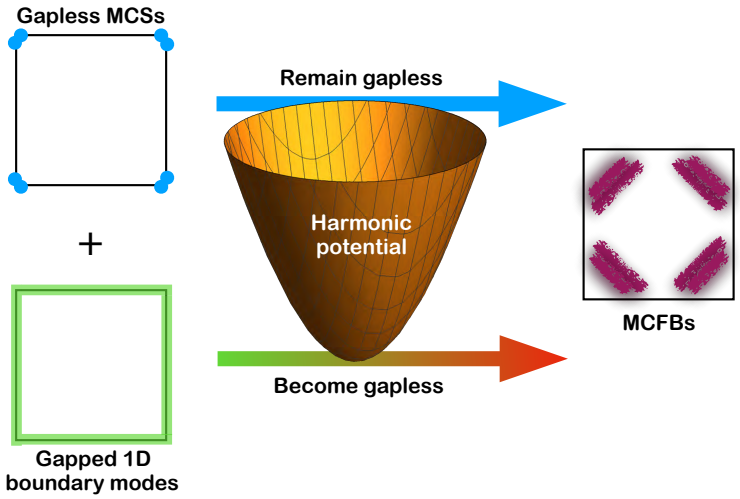

Figure 3.3: (Color online) Schematic figure of the procedure by which Majorana corner states become Majorana corner flat bands. (Left panel) There is no harmonic potential. The system has topologically distinct one-dimensional gapped modes on the adjacent boundaries which leads to gapless Majorana corner states at the intersection of two different boundaries, *i.e.*, corners. (Right panel) After including the harmonic potential, the gapless Majorana corner states remain gapless. However, the one-dimensional gapped boundary modes become gapless modes.

magnitude at the corners, $v_{\text{trap}}(r_c)$, becomes larger than the insulating gap. We confirm that, under sharp potentials such as a circular potential, the two-dimensional bulk gap is closed in both open-boundary conditions and periodic boundary conditions systems.

We argue that in a second-order topological superconductor, the Majorana corner states-Majorana corner flat bands transition is actually a crossover in the open-boundary conditions system with increasing the harmonic potential magnitude: the number of Majorana zero modes gradually increases while there is no bulk gap closing as is illustrated in Fig. 3.4. It can be seen that there are branches of eigenvalues whose values decrease from 0.5 with increasing the harmonic potential magnitude although the bulk gap remains open. We find that the proliferation of the Majorana zero modes originates from the fact that only one-dimensional gapped boundary modes becomes gapless without the two-dimensional bulk gap closing.

In contrast, in the system with periodic boundary conditions with an increasing harmonic potential magnitude, the two-dimensional bulk gap is closed if the potential magnitude at the four corners $[v_{\text{trap}}(r_c)]$ of the two-dimensional topological insulator becomes larger than the insulating gap as shown in Fig. 3.5. In this case, by increasing the harmonic potential magnitude there are no Majorana zero modes because there are no one-dimensional gapped boundary modes to become gapless. We have verified that the same behavior persists for

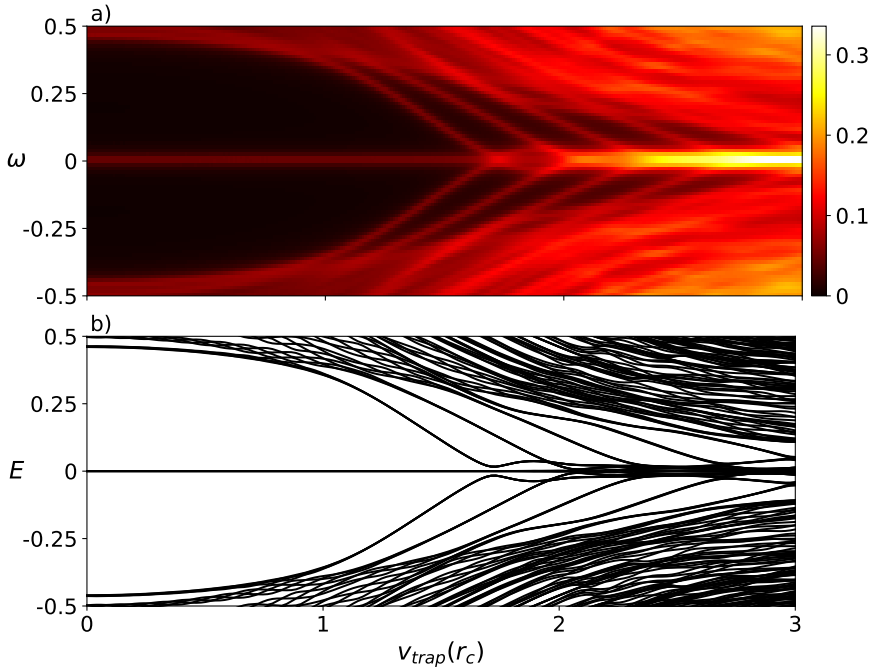

Figure 3.4: (Color online) (a) Density of states, and (b) the eigenvalues of the BdG Hamiltonian as a function of $v_{\rm trap}(r_c)$ for a 51×51 square lattice with open-boundary conditions. The unit of all values is $|m(\boldsymbol{k}=0)|$.

larger systems.

To see the Majorana corner states-Majorana corner flat bands transition in more detail, we show the real space dependence of the zero-energy local density of states in Fig. 3.6. In the region outside the black circles of the two lower middle panels of this figure, the harmonic potential magnitude is larger than the insulating gap locally, so Figs. 3.6(b), 3.6(e), and 3.6(h) indicate that Majorana corner states are robust even outside this circle. Moreover, the region outside the circles can host Majorana corner flat bands, and the additional Majorana zero modes originate from only one-dimensional gapped boundary modes that become gapless.

3.4 Flatness and the origin of Majorana corner flat bands

It should be noted that an exact zero-energy eigenvalue cannot be obtained in the theoretical calculations for a finite system because of finite size effects. Thus,"zero" energy has to be defined. An eigenvalue can be considered as a zero-energy mode in such a finite system if its magnitude is very small. Therefore, the eigenvalue E_i can be considered as a zero-energy eigenvalue if it satisfies $|E_i| \leq \varepsilon$ condition for a very small ε. By using of this definition for zero-energy modes, we show that as the harmonic trap magnitude is increased, the number

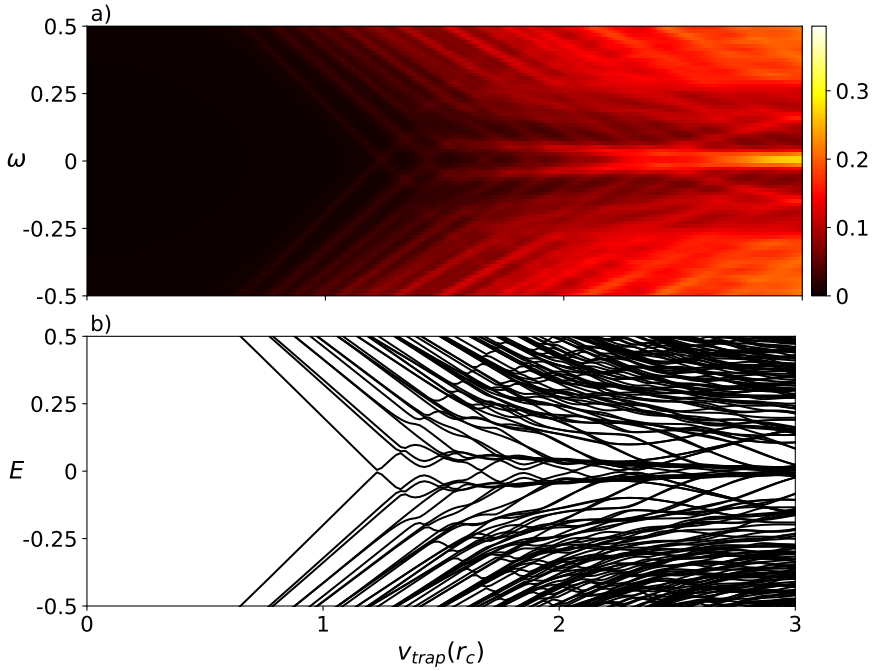

Figure 3.5: (Color online) (a) Density of states, and (b) eigenvalues of the BdG Hamiltonian as a function of $v_{\rm trap}(r_c)$ for a 51×51 square lattice with periodic boundary conditions. The unit of all values is $|m(\boldsymbol{k}=0)|$.

of zero-energy eigenvalue increases *independent* of the value of ε for large enough lattice. In Fig. 3.7, the ratio between the number of eigenvalues inside the $|E_i| \leq \varepsilon$ interval, say N_f, and the number of boundary states, which is proportional to the size of the lattice along the x or y-direction, is plotted as a function of system size. This figure clearly illustrates that this ratio is increasing in the thermodynamic limit, and a truly flat band appears by increasing the harmonic trap magnitude if finite-size effects are suppressed.

In Fig. 3.8, we plot the density of states (DOS) for the same parameters as in Fig. 3.6. It can be clearly seen that the number of Majorana zero modes increases without the bulk gap closing as the harmonic potential magnitude increases in the weak potential limit. The states that appear close to zero energy in this figure are boundary states not bulk states according to Fig. 3.9, where the origin of Majorana corner flat bands is shown. In Fig. 3.9, we show that Majorana corner flat bands originate from only gapped states localized at one-dimensional boundaries. In this figure we plot the square of the wave function's amplitude associated with only blue points. As the harmonic potential magnitude is increased, the energy corresponding to these one-dimensional boundary states become smaller, and they become more localized around the corners. By increasing the harmonic potential magnitude, more and more one-dimensional gapped modes become gapless.

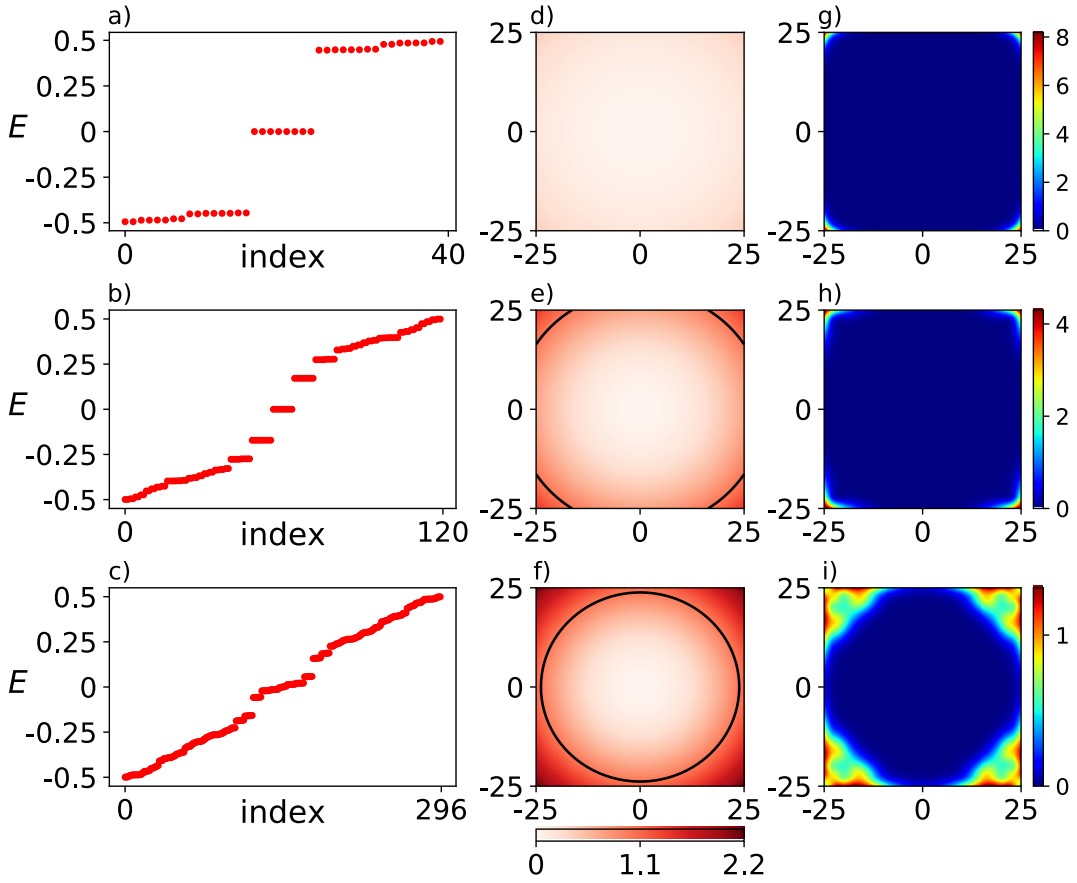

Figure 3.6: (Color online) (a,b,c) Eigenvalues of the BdG Hamiltonian, (d,e,f) contour plot of the two-dimensional harmonic potential, and (g,h,i) zero-energy local density of states for a 51×51 square lattice with open-boundary conditions in the presence of three different harmonic potential magnitudes $v_{\rm trap}(r_c) =$ 0.4 (a,d,g), 1.4 (b,e,h), and 2.2 (c,f,i). Outside the two black circles $v_{\rm trap}(r_c) > |m(\boldsymbol{k}=0)|$, *i.e.*, the harmonic potential magnitude is larger than the insulating gap locally. Both the eigenvalues and harmonic potential magnitude are given in units of $|m(\boldsymbol{k}=0)|$. The smearing factor in the Lorentzian function for plotting the local density of states is 0.005 in units of $|m(\mathbf{k}=0)|$.

3.5 Circular potential

Let us define the circular potential as $V_i = v_{\rm circ}$ for $(i_x - i_x^c)^2 + (i_y - i_y^c)^2 > R^2$ where $v_{\rm circ}$ is the strength of the circular potential, and $i^c = (i_x^c, i_y^c)$ is the coordinate of the central site of a two-dimensional sample. Here, we take $R = N_x/2$ where N_x is the number of sites along x-axis direction. In the circle with perimeter R the potential is zero. As shown in Figs. 3.10 and 3.11, the bulk gap closes for both open-boundary conditions and periodic boundary conditions

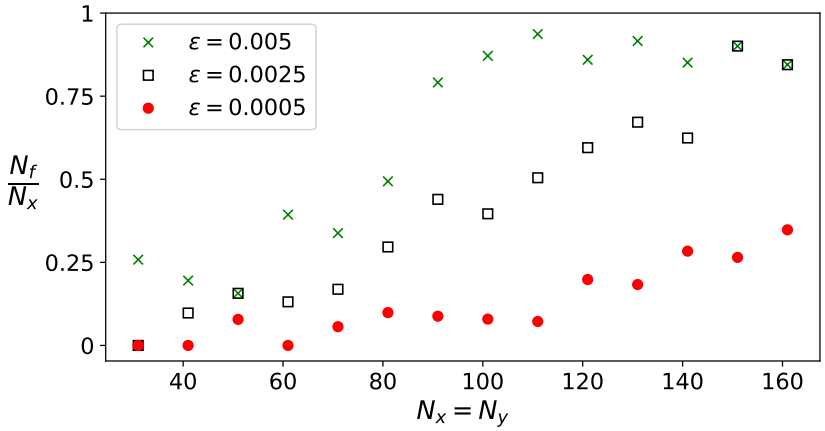

Figure 3.7: (Color online) The ratio between the number of eigenvalues inside the $|E_i| \leq \varepsilon$ interval and N_x as a function of the length of the boundaries of the square lattice with open-boundary conditions for three different values of ε with $v_{\text{trap}}(r_c) = 1.1|m(\boldsymbol{k} = 0)|$.

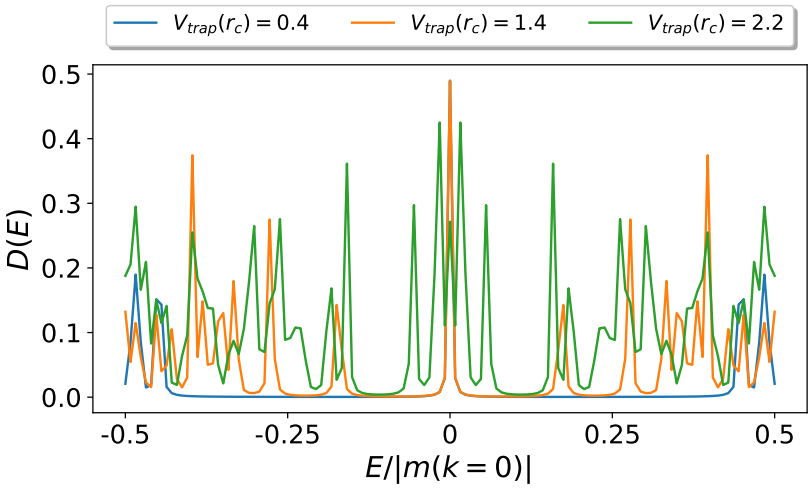

Figure 3.8: (Color online) Density of states as a function of energy in the unit of the insulating gap value for the same parameters as the Fig. 3.6. The bulk gap remains open as the harmonic potential magnitude increases in the weak potential limit.

for a circular potential, so there is no crossover and no Majorana corner flat bands in the presence of a circular potential which is not similar to the case of the harmonic potential.

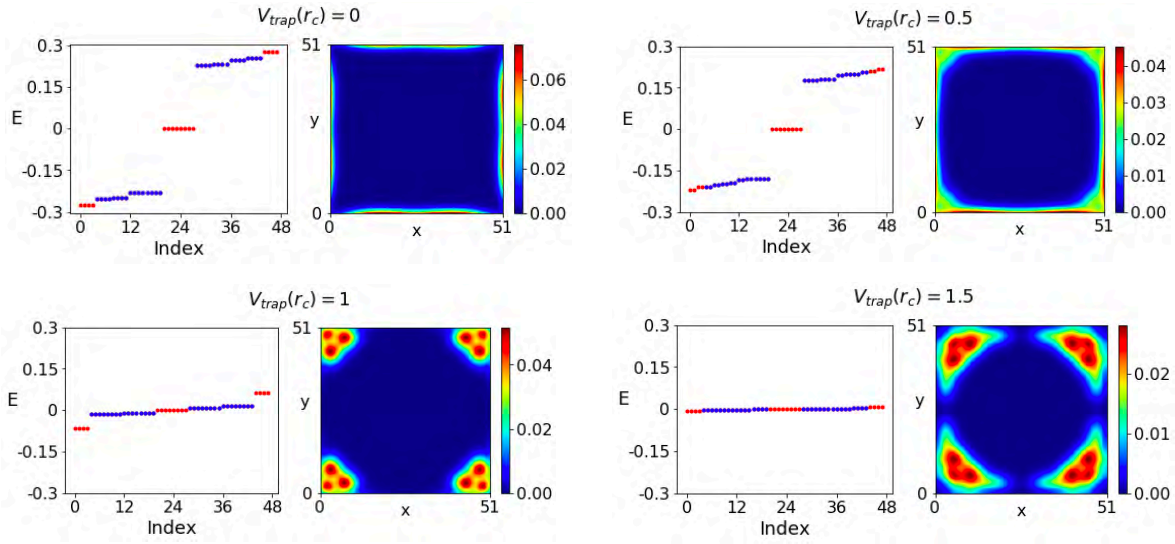

Figure 3.9: (Color online) Eigenvalues of the BdG Hamiltonian and the square of the wave function's amplitude for different values of $v_{\text{trap}}(r_c)$ and for a 51×51 square lattice with open-boundary conditions. The square of the wave function's amplitude is plotted only for the eigenvalues that are denoted with blue color. They are gapped boundary states that become gapless by increasing the harmonic potential magnitude.

3.6 Discussion

Let us discuss the difference between conventional Majorana flat bands in a d-wave superconductor and Majorana corner flat bands in our system. In a superconductor with order parameter symmetry $d_{x^2-y^2}$, it is well known that there are Andreev flat bound states, which appear at the [110] surface. On the other hand, there is no zero-energy bound state at the [100] and [010] surfaces [159, 160]. For this nodal superconductor, it is possible to define a one-dimensional partial Brillouin zone by fixing the $(d-1)$-dimensional momentum $\boldsymbol{k}_{||}$ at a certain point [156, 159, 161, 162]. As long as the pair potential in such a partial Brillouin zone is fully gapped, we can define the one-dimensional winding number as the topological invariant of a nodal topological superconductor:

$$\mathcal{W}(\boldsymbol{k}_{||}) = \frac{1}{2\pi} \operatorname{Im} \int dk_{\perp} \partial_{k_{\perp}} \ln \det(q), \tag{3.35}$$

where $k_{\perp}$ is the momentum in a one-dimensional Brillouin zone, and $\boldsymbol{k}_{||}$ is the momentum parallel to the surface that we consider. Moreover, in Eq. (3.35), $q(\boldsymbol{k})$ is the off-diagonal block of the BdG Hamiltonian in the basis that diagonalizes the chiral symmetry operator such that

$$\det q(\boldsymbol{k}) = \left\{ m^2(\boldsymbol{k}) + (\Delta(\boldsymbol{k}) + i\mu)^2 + \lambda^2 \sin^2 k_x + \lambda^2 \sin^2 k_y \right\}^2. \tag{3.36}$$

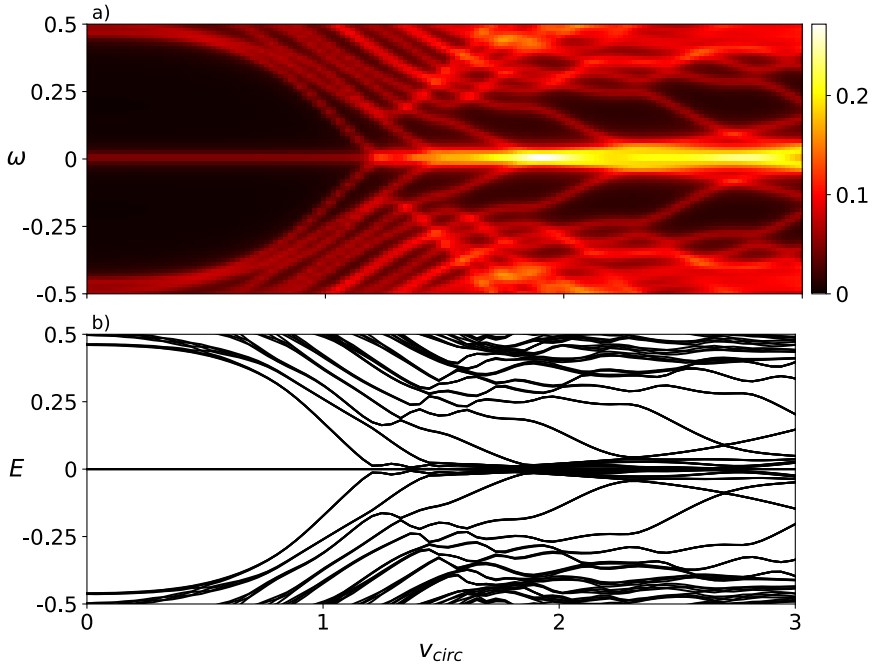

Figure 3.10: (Color online) (a) Density of states, and (b) eigenvalues of the BdG Hamiltonian as a function of v_{circ} for a 51×51 square lattice with open-boundary conditions. The unit of all values is $|m(\boldsymbol{k}=0)|$.

For a finite winding number, there are $|\mathcal{W}(\boldsymbol{k}_{||})|$-fold degenerate zero-energy modes at a surface parallel to $\boldsymbol{k}_{||}$. Such highly degenerate surface bound states are known as Majorana flat bands because the energy dispersion is independent of $\boldsymbol{k}_{||}$ [163].

A two-dimensional homogeneous topological insulator in proximity with a d-wave superconductor becomes a superconductor with increasing chemical potential. This transition is a topological phase transition with bulk gap closing since a d-wave superconductor order parameter has line nodes. In this homogeneous system with large enough chemical potential, there are Majorana flat bands at the [110] surface because of the nontrivial value of the winding number. The origin of these Majorana flat bands are Andreev bound states [156]. However, here we find that in the case of Majorana corner flat bands not only is there no two-dimensional bulk gap closing in the open-boundary conditions system with increasing harmonic potential magnitude, but also the number of Majorana zero modes increases only because of the reduction of the energy of the one-dimensional boundary gapped modes. Also note that although Majorana corner states are exponentially localized at the corners of the system, Majorana corner flat bands are localized close to the four corners in the weak potential limit.

Although Majorana corner flat bands consist of many very spatially close Majorana zero

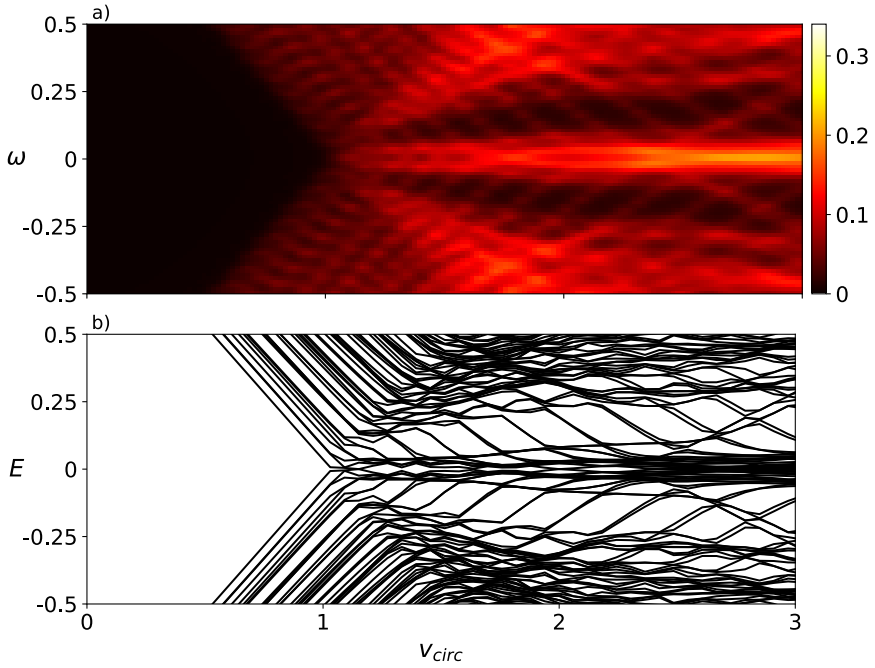

Figure 3.11: (Color online) (a) Density of states, and (b) eigenvalues of the BdG Hamiltonian as a function of v_{circ} for a 51×51 square lattice with periodic boundary conditions. The unit of all values is $|m(\boldsymbol{k} = 0)|$.

modes, they cannot hybridize and become gapped out. This is in contrast to the fact that Majorana corner states hybridize and annihilate if they are brought close together. The reasons for the weak hybridization can naturally be explained by the use of the one-dimensional boundary modes, time-reversal symmetry, and the crossover behavior as follows. Without a confining potential, the wave function of Majorana corner states and one-dimensional gapped boundary modes are orthogonal because they are eigenvectors of the BdG Hamiltonian with different energies. The wave functions gradually change with changing the harmonic potential magnitude and remain orthogonal since there is no bulk gap closing. Therefore, the crossover makes the Majorana corner flat bands stable by preserving the orthogonality of these wave functions. In addition, it is known that both Majorana flat bands in a d-wave superconductor, and Majorana corner states in a second-order topological superconductor are protected by time-reversal symmetry [152, 156]. In our system, in zero and strong potential limits, the system is a second-order topological superconductor and d-wave superconductor, respectively. Therefore, the time-reversal symmetry protects the Majorana corner flat bands in the weak potential limit since this phenomenon is a crossover.

3.7 Summary

It has been recently proposed that a second-order topological superconductor hosts Majorana corner states localized at the four corners of a two-dimensional topological insulator in proximity with some unconventional high-temperature superconductors. This work provides a theoretical framework to make only one-dimensional gapped boundary modes gapless without closing the bulk gap in two-dimensional second-order topological superconductors. Second-order topological superconductors always have $(d-1)$-dimensional *gapped* boundary modes and $(d-2)$-dimensional gapless modes in d-spatial dimensions. Our results suggest that increasing the gradual potential magnitude proliferates the number of Majorana corner states by making *only* one-dimensional gapped boundary modes gapless *without* closing the bulk gap. This finally leads to a new kind of Majorana flat band, namely Majorana corner flat bands. In contrast to the conventional mechanism, Majorana corner flat bands cannot be characterized by a one-dimensional winding number and only originate from one-dimensional gapped boundary modes that become gapless without closing the bulk gap.

It also has been shown that the presence of time-reversal symmetry during the Majorana corner states-Majorana corner flat bands crossover prevent Majorana corner states from hybridizing and protect Majorana corner flat bands. There might be a topological invariant for this particular inhomogeneous system to characterize the crossover, but finding that in real-space is a mathematically challenging task and beyond the scope of this thesis.

In experiment, if one can observe the Majorana corner states in second-order topological superconductors, such as a hybrid structure of topological insulator and an unconventional superconductor or even cold atom systems, one can also observe the Majorana corner states-Majorana corner flat bands crossover and Majorana corner flat bands by adding a gradual confining potential such as a harmonic potential. More precisely speaking, for having a hybrid structure of topological insulator and an unconventional superconductor, a monolayer of WTe_2 as a high-temperature topological insulator [164, 165] can be exploited in proximity to a d-wave high-temperature cuprate superconductor. In this hybrid solid-state systems, some potentials can be applied by using electron double-layer transistors [166–168], which can be used to apply an electric field to the sample. Normally the potentials generated by the electron double-layer transistor techniques have sharp edges. Nevertheless, there might be some possibilities in the future or other advanced techniques to control the sharpness of this trapping potential in order to approach a harmonic potential. This work might open up new prospects for realizing Majorana zero modes and its applications in quantum computation and information, which will be left for future investigations.

Chapter 4

Higher-Order Spin-Singlet Topological Superconductivity in Extended Hubbard Model with Spin-Orbit Coupling

4.1 Introduction

In this chapter, which is based on publication (II), we investigate the superconducting pairing instability of the two-dimensional extended Hubbard model with both Rashba and Dresselhaus spin-orbit coupling within the mean-field approximation at both zero and finite temperature. We find that both first- and second-order time-reversal symmetry breaking topological gapped phases can be achieved under appropriate parameter and temperature regimes due to the presence of a favored even-parity $s + id$-wave pairing even in the absence of an external magnetic field or intrinsic magnetism. This results in two branches of chiral Majorana edge states on each edge or a single zero-energy Majorana corner state at each corner of the sample. Interestingly, we also find that not only does tuning the doping level lead to a direct topological phase transition between these two distinct topological gapped phases, but also using the temperature as a highly controllable and reversible tuning knob leads to different direct temperature-driven topological phase transitions between gapped and gapless topological superconducting phases. Our findings suggest new possibilities in interacting spin-orbit coupled systems by unifying both first- and higher-order topological superconductors in a simple but realistic microscopic model.

4.2 Spin-orbit coupling

Spin-orbit coupling is ubiquitous in condensed matter systems and responsible for many remarkable phenomena [169–184]. In recent years, a surge of research interest in spin-orbit coupling was stimulated by the discovery that spin-orbit coupling plays a critical role in realizing various topological phases, ranging from noninteracting or weakly correlated topological insulators and topological superconductors to strongly correlated topological phases [34, 68, 185, 186]. Among them, topological superconductors are noticeable as they harbor Majorana modes which are believed to be a possibility for the building blocks of topological quantum computation [36, 38, 39, 187, 188]. While odd-parity superconductors generally provide a natural realization of topological superconductors [114, 119–123], their scarcity in nature turns out to be a serious obstacle from an experimental point of view. Fortunately, spin-orbit coupling enables the realization of effective odd-parity superconductivity on the basis of abundant even-parity superconductivity, providing a more readily accessible route for the realization of topological superconductors [124–131]. Over the past decade, remarkable progress along this route has been witnessed [132–140].

The general three dimensional spin-orbit coupling Hamiltonian in the SI units can be written as,

$$H = -\frac{e\hbar}{4m^2c^2}\boldsymbol{\sigma}\cdot\{\boldsymbol{E}\times(\boldsymbol{p}-\frac{e}{c}\boldsymbol{A})\}, \tag{4.1}$$

by an expansion in powers of v/c in the Dirac equation. Here, $\boldsymbol{\sigma} = (\sigma_x, \sigma_y, \sigma_z)$ are Pauli matrices, $\boldsymbol{E} = (E_x, E_y, E_z)$ is the electric field, v is the speed of electron, and c is the speed of light. In two dimensional solid state systems, the structure inversion asymmetry and the bulk inversion asymmetry can give rise to the well-known Rashba and Dresselhaus spin-orbit couplings, respectively. In real space, Rashba and Dresselhaus spin-orbit couplings for a square lattice read as,

$$H^R_{\rm SOC} = i\lambda_R \sum_{i,\alpha,\beta}(c^\dagger_{i,\alpha}s_y^{\alpha\beta}c_{i+\hat{x},\beta} - c^\dagger_{i,\alpha}s_x^{\alpha\beta}c_{i+\hat{y},\beta}) + \text{H.c.}, \tag{4.2}$$

$$H^D_{\rm SOC} = i\lambda_D \sum_{i,\alpha,\beta}(c^\dagger_{i,\alpha}s_y^{\alpha\beta}c_{i+\hat{y},\beta} - c^\dagger_{i,\alpha}s_x^{\alpha\beta}c_{i+\hat{x},\beta}) + \text{H.c.}, \tag{4.3}$$

where $c^\dagger_{i,\alpha}(c_{i,\alpha})$ is the creation (annihilation) operator at site i with spin $\alpha = (\uparrow,\downarrow)$. The unit vector along the x (y) direction is represented by $\hat{x}$ ($\hat{y}$), and $s_{x,y}$ are Pauli matrices in spin space. The abbreviation H.c. stands for Hermitian conjugation, and the symbol i in the beginning of both second and third lines (and elsewhere) is taken to denote the pure imaginary number and should not be confused with the site index which generally occurs as a subscript.

4.3 Theoretical formalism

The two-dimensional extended Hubbard model, which provides a simple description for short-ranged interacting systems [189], reads as

$$\begin{aligned} H = & -t \sum_{\langle i,j\rangle,\alpha} c^{\dagger}_{i,\alpha} c_{j,\alpha} + \text{H.c.} - \mu \sum_{i,\alpha} c^{\dagger}_{i,\alpha} c_{i,\alpha} \\ & + i\lambda_R \sum_{i,\alpha,\beta} (c^{\dagger}_{i,\alpha} s_y^{\alpha\beta} c_{i+\hat{x},\beta} - c^{\dagger}_{i,\alpha} s_x^{\alpha\beta} c_{i+\hat{y},\beta}) + \text{H.c.} \\ & + i\lambda_D \sum_{i,\alpha,\beta} (c^{\dagger}_{i,\alpha} s_y^{\alpha\beta} c_{i+\hat{y},\beta} - c^{\dagger}_{i,\alpha} s_x^{\alpha\beta} c_{i+\hat{x},\beta}) + \text{H.c.} \\ & + U \sum_i \hat{n}_{i,\uparrow} \hat{n}_{i,\downarrow} + \frac{V}{2} \sum_{\langle i,j\rangle,\alpha} \hat{n}_{i,\alpha} \hat{n}_{j,\bar{\alpha}}, \end{aligned} \tag{4.4}$$

where $\langle i,j\rangle$ denotes summation over nearest-neighbor sites, $c^{\dagger}_{i,\alpha}(c_{i,\alpha})$ is the creation (annihilation) operator at site i with spin $\alpha = (\uparrow,\downarrow)$, $\hat{n}_{i,\alpha} = c^{\dagger}_{i,\alpha} c_{i,\alpha}$, t is the nearest-neighbor hopping amplitude, μ is the chemical potential, λ_R (λ_D) is the Rashba (Dresselhaus) spin-orbit coupling amplitude, U is the on-site repulsive ($U > 0$) interaction strength, and V is the nearest-neighbor attractive ($V < 0$) interaction strength. The unit vector along the x (y) direction is represented by $\hat{x}$ ($\hat{y}$), and $s_{x,y}$ are Pauli matrices in spin space. The abbreviation H.c. stands for Hermitian conjugation, and the symbol i in the beginning of both second and third lines (and elsewhere) is taken to denote the pure imaginary number and should not be confused with the site index which generally occurs as subscripts.

Although in the presence of spin-orbit coupling, odd- and even-parity pairings can generally coexist, we restrict ourselves to even-parity pairing for the sake of clarity and simplicity. The last line of the Hamiltonian (4.4) at the mean-field level in momentum space can be rewritten as,

$$H_{int} = \frac{1}{N} \sum_{\boldsymbol{k},\boldsymbol{q}} (U + V\zeta_{\boldsymbol{k}-\boldsymbol{q}}) c^{\dagger}_{\boldsymbol{k},\uparrow} c^{\dagger}_{-\boldsymbol{k},\downarrow} c_{-\boldsymbol{q},\downarrow} c_{\boldsymbol{q},\uparrow}, \tag{4.5}$$

where

$$\zeta_{\boldsymbol{k}-\boldsymbol{q}} = \sum_{\boldsymbol{\delta}} e^{-i(\boldsymbol{k}-\boldsymbol{q})\cdot\boldsymbol{\delta}} = 2\big\{\cos(k_x - q_x) + \cos(k_y - q_y)\big\}, \tag{4.6}$$

and $\boldsymbol{\delta}$ represents the coordinates of the four nearest-neighbours of a given site in a square lattice with unit lattice constant. Note that we have dropped terms corresponding to pairing with non-zero center-of-mass momentum. Performing mean-field decoupling by considering only the even-parity superconducting order-parameter and ignoring constant terms leads to

the following quadratic Hamiltonian,

$$H_{int}^{MF} = \frac{1}{2}\sum_{\boldsymbol{k}} \Delta_{\alpha\beta}(\boldsymbol{k}) c^{\dagger}_{\boldsymbol{k},\alpha} c^{\dagger}_{-\boldsymbol{k},\beta} + \text{H.c.}, \tag{4.7}$$

where the even-parity superconducting order-parameter can be written as

$$\Delta_{\alpha\beta}(\boldsymbol{k}) = i\Delta(\boldsymbol{k}) s_y^{\alpha\beta}, \tag{4.8}$$

and

$$\Delta(\boldsymbol{k}) = -\frac{1}{N}\sum_{\boldsymbol{q}} \left\{U + \frac{V}{2}(\zeta_{\boldsymbol{k}+\boldsymbol{q}} + \zeta_{\boldsymbol{k}-\boldsymbol{q}})\right\} \langle c_{\boldsymbol{q}\uparrow} c_{-\boldsymbol{q}\downarrow}\rangle. \tag{4.9}$$

It is obvious that $\Delta(-\boldsymbol{k}) = \Delta(\boldsymbol{k})$ by using of the fact that $\zeta_{\boldsymbol{k}}$ is an even function of $\boldsymbol{k}$, *i.e.* $\zeta_{\boldsymbol{k}} = \zeta_{-\boldsymbol{k}}$. It can be shown that,

$$\zeta_{\boldsymbol{k}+\boldsymbol{q}} + \zeta_{\boldsymbol{k}-\boldsymbol{q}} = 8\big\{\eta_s(\boldsymbol{k})\eta_s(\boldsymbol{q}) + \eta_d(\boldsymbol{k})\eta_d(\boldsymbol{q})\big\}, \tag{4.10}$$

where

$$\eta_s(\boldsymbol{k}) = \frac{1}{2}(\cos k_x + \cos k_y), \tag{4.11}$$

$$\eta_d(\boldsymbol{k}) = \frac{1}{2}(\cos k_x - \cos k_y). \tag{4.12}$$

This leads to the following superconducting gap function,

$$\Delta(\boldsymbol{k}) = \Delta_0^c + \Delta_s^c \eta_s(\boldsymbol{k}) + \Delta_d^c \eta_d(\boldsymbol{k}), \tag{4.13}$$

where Δ_0^c, Δ_s^c, and Δ_d^c are momentum-independent complex numbers that represent on-site s-, extended s-, and d-wave superconductivity, respectively. Finally, the total Hamiltonian in the Nambu space can be written as,

$$H = \frac{1}{2}\sum_{\boldsymbol{k}} \Psi^{\dagger}_{\boldsymbol{k}} \mathcal{H}(\boldsymbol{k}) \Psi_{\boldsymbol{k}}, \tag{4.14}$$

with $\Psi^{\mathrm{T}}_{\boldsymbol{k}} = (c_{\boldsymbol{k}\uparrow},\ c_{\boldsymbol{k}\downarrow},\ c^{\dagger}_{-\boldsymbol{k}\downarrow}, -c^{\dagger}_{-\boldsymbol{k}\uparrow})$ and

$$\mathcal{H}(\boldsymbol{k}) = \tau_z\big\{\xi(\boldsymbol{k})s_0 + l_x(\boldsymbol{k})s_x + l_y(\boldsymbol{k})s_y\big\} + \Delta(\boldsymbol{k})\tau_x s_0, \tag{4.15}$$

where $\tau_{x,y,z}$ are Pauli matrices in particle-hole space, and

$$\xi_{\boldsymbol{k}} = -2t(\cos k_x + \cos k_y) - \mu, \tag{4.16}$$

is the kinetic energy measured from the Fermi energy. The spin-orbit coupling vector given by

$$\boldsymbol{l}(\boldsymbol{k}) = \boldsymbol{l}_R(\boldsymbol{k}) + \boldsymbol{l}_D(\boldsymbol{k}) = (l_x(\boldsymbol{k}), l_y(\boldsymbol{k})), \tag{4.17}$$

where

$$\boldsymbol{l}_R(\boldsymbol{k}) = 2\lambda_R(\sin k_y, -\sin k_x), \tag{4.18}$$
$$\boldsymbol{l}_D(\boldsymbol{k}) = 2\lambda_D(\sin k_x, -\sin k_y), \tag{4.19}$$

represents the Rashba and Dresselhaus spin-orbit coupling, respectively. The three pairing amplitudes inside Eq. (4.13) satisfy the following self-consistent superconducting gap equations,

$$\Delta_0^c = -\frac{U}{4N}\sum_{\boldsymbol{k},\sigma}\Delta(\boldsymbol{k})\mathcal{F}_\sigma(\boldsymbol{k}), \tag{4.20}$$

$$\Delta_s^c = -\frac{V}{N}\sum_{\boldsymbol{k},\sigma}\Delta(\boldsymbol{k})\eta_s(\boldsymbol{k})\mathcal{F}_\sigma(\boldsymbol{k}), \tag{4.21}$$

$$\Delta_d^c = -\frac{V}{N}\sum_{\boldsymbol{k},\sigma}\Delta(\boldsymbol{k})\eta_d(\boldsymbol{k})\mathcal{F}_\sigma(\boldsymbol{k}), \tag{4.22}$$

where N denotes the number of sites, $\sigma = \pm 1$, and

$$\mathcal{F}_\sigma(\boldsymbol{k}) = \frac{1}{E_{\boldsymbol{k}}^\sigma}\tanh(\frac{\beta E_{\boldsymbol{k}}^\sigma}{2}). \tag{4.23}$$

Here, β is the inverse of temperature and

$$E_{\boldsymbol{k}}^\sigma = \sqrt{\varepsilon_\sigma^2(\boldsymbol{k}) + |\Delta(\boldsymbol{k})|^2}, \tag{4.24}$$

are the two excitation spectra of the BdG Hamiltonian, where

$$\varepsilon_\sigma(\boldsymbol{k}) = \xi(\boldsymbol{k}) + \sigma l(\boldsymbol{k}), \tag{4.25}$$

refers to the normal-state spectra with $l(\boldsymbol{k})$ the magnitude of the $\boldsymbol{l}(\boldsymbol{k})$ vector.

To capture the phases of the three pairings, we define $\Delta_\alpha^c = \Delta_\alpha e^{i\phi_\alpha}$ for $\alpha \in \{0, s, d\}$, with Δ_α and ϕ_α being real numbers. Accordingly, the three complex self-consistent equations given by Eqs. (4.20)-(4.22) can be separated into six real equations. By solving the self-consistent equations numerically, we find that, when both s- and d-wave superconducting order parameter are nonvanishing, their phases favor $\phi_s = \phi_0$ and $\phi_d = \phi_0 \pm \pi/2$ ("±"

are degenerate in energy). Therefore, the superconducting order parameter can be written explicitly as

$$\Delta(\boldsymbol{k}) = \Delta_0 + \Delta_s\eta_s(\boldsymbol{k}) + i\Delta_d\eta_d(\boldsymbol{k}), \tag{4.26}$$

and, accordingly, the six real self-consistent superconducting gap equations are reduced to

$$\Delta_0 = -\frac{U}{4N}\sum_{\boldsymbol{k},\sigma}\big\{\Delta_0 + \Delta_s\eta_s(\boldsymbol{k})\big\}\mathcal{F}_\sigma(\boldsymbol{k}), \tag{4.27}$$

$$\Delta_s = -\frac{V}{N}\sum_{\boldsymbol{k},\sigma}\eta_s(\boldsymbol{k})\big\{\Delta_0 + \Delta_s\eta_s(\boldsymbol{k})\big\}\mathcal{F}_\sigma(\boldsymbol{k}), \tag{4.28}$$

$$1 = -\frac{V}{N}\sum_{\boldsymbol{k},\sigma}\eta_d^2(\boldsymbol{k})\mathcal{F}_\sigma(\boldsymbol{k}). \tag{4.29}$$

It should be noted that, when s- and d-wave pairing coexist, the last term of the BdG Hamiltonian (4.15) should be rewritten as $\big\{[\Delta_0 + \Delta_s\eta_s(\boldsymbol{k})]\tau_x - \Delta_d\eta_d(\boldsymbol{k})\tau_y\big\}s_0$. Furthermore, the mean-field real-space Hamiltonian can be rewritten as,

$$H = \frac{1}{2}\sum_{ij}\begin{pmatrix}\boldsymbol{c}_i^\dagger & \boldsymbol{c}_i\end{pmatrix}\begin{pmatrix}A_{ij} & B_{ij}\\ -B_{ij}^* & -A_{ij}^*\end{pmatrix}\begin{pmatrix}\boldsymbol{c}_j\\ \boldsymbol{c}_j^\dagger\end{pmatrix}, \tag{4.30}$$

where $\boldsymbol{c}_i^\dagger = (c_{i,\uparrow}^\dagger,\ c_{i,\downarrow}^\dagger)$ and $\boldsymbol{c}_i = (c_{i,\uparrow},\ c_{i,\downarrow})$ for $i = (i_x, i_y)$. The hermitian property of H, and the canonical anti-commutation relation $\{c_i, c_j^\dagger\} = \delta_{ij}$ imply that the $2N \times 2N$ complex matrix A and B satisfy $A^\dagger = A$ and $B^{\mathrm{T}} = -B$ relations, respectively, where N is the number of sites and T stands for transpose. The components of A and B matrices are given by,

$$A_{ij} = s_0A_{ij}^0 + s_xA_{ij}^x + s_yA_{ij}^y, \tag{4.31}$$

$$B_{ij} = s_y(i\Delta_{ij}^s - \Delta_{ij}^d), \tag{4.32}$$

where

$$A_{ij}^0 = -t(\delta_{j,i+\hat{x}} + \delta_{j,i-\hat{x}} + \delta_{j,i+\hat{y}} + \delta_{j,i-\hat{y}}) - \mu\delta_{ij}, \tag{4.33}$$

$$A_{ij}^x = -i\lambda_R(\delta_{j,i+\hat{y}} - \delta_{j,i-\hat{y}}) - i\lambda_D(\delta_{j,i+\hat{x}} - \delta_{j,i-\hat{x}}), \tag{4.34}$$

$$A_{ij}^y = +i\lambda_R(\delta_{j,i+\hat{x}} - \delta_{j,i-\hat{x}}) + i\lambda_D(\delta_{j,i+\hat{y}} - \delta_{j,i-\hat{y}}), \tag{4.35}$$

$$\Delta_{ij}^s = \Delta_0\delta_{ij} + \frac{\Delta_s}{4}(\delta_{j,i+\hat{x}} + \delta_{j,i-\hat{x}} + \delta_{j,i+\hat{y}} + \delta_{j,i-\hat{y}}), \tag{4.36}$$

$$\Delta_{ij}^d = \frac{\Delta_d}{4}(\delta_{j,i+\hat{x}} + \delta_{j,i-\hat{x}} - \delta_{j,i+\hat{y}} - \delta_{j,i-\hat{y}}). \tag{4.37}$$

Throughout this chapter, we set the hopping amplitude $t = 1$ as the energy unit and $\{\lambda_R, U, V\} = \{0.3, 2, -5\}$, unless we clearly mention otherwise. However, they are not unique, and different sets of parameters will yield a qualitatively similar phase diagram.

4.4 Results

We first perform the self-consistent calculations at zero temperature. For definiteness, we consider that only λ_D and μ are tunable parameters. We restrict ourselves to the positive parameter regime and present the corresponding phase diagram in Fig. 4.1. The result reveals the existence of three distinct types of pairing including time-reversal symmetry preserving s- and d-wave, as well as the time-reversal symmetry breaking $s+id$-wave. The s- and $s+id$-wave pairing regimes are gapped except at some critical lines and points, respectively[1], while the d-wave pairing regime corresponds to a nodal superconducting phase since it cannot open a bulk gap. Moreover, the time-reversal symmetry preserving gapped s-wave pairing belongs to the symmetry class DIII characterized by a $\mathbb{Z}_2$ invariant ν [190] and the time-reversal symmetry preserving gapless d-wave pairing is considered as a topologically nontrivial phase, though gapless, because it harbors topologically protected gapless Majorana modes on the boundary[2].

Let us now focus on the interesting regime with $s+id$-wave pairing which consists of three time-reversal symmetry breaking topologically distinct phases, including first- and second-order topological superconductivity and a topologically trivial superconductivity, as shown in the blue color region of Fig. 4.1. Since the time-reversal symmetry is broken in this regime, the system belongs to the symmetry class D characterized by the Chern number [73]. To reveal the underlying topological property in a simple and transparent way, here we perform a basis transformation which maps the combination of spin-orbit coupling and even-parity $s+id$-wave pairing to an effective odd-parity pairing [125].

After the transformation (see Appendix B for more details), the four-band BdG Hamiltonian can be decoupled into two independent parts, *i.e.*,

$$\mathcal{H}(\boldsymbol{k}) = \mathcal{H}_+(\boldsymbol{k}) \oplus \mathcal{H}_-(\boldsymbol{k}), \tag{4.38}$$

with

$$\mathcal{H}_\pm(\boldsymbol{k}) = \begin{pmatrix} |\xi_k| \pm l(\boldsymbol{k}) & \Delta_\pm(\boldsymbol{k}) \\ \Delta_\pm^*(\boldsymbol{k}) & -|\xi_k| \mp l(\boldsymbol{k}) \end{pmatrix}, \tag{4.39}$$

where

$$\Delta_\pm(\boldsymbol{k}) = \frac{l_x(\boldsymbol{k}) \mp i l_y(\boldsymbol{k})}{l(\boldsymbol{k})} [\Delta_0 + \Delta_s \eta_s(\boldsymbol{k}) \mp i \Delta_d \eta_d(\boldsymbol{k})]. \tag{4.40}$$

It is apparent that $\Delta_\pm(-\boldsymbol{k}) = -\Delta_\pm(\boldsymbol{k})$, confirming the odd-parity nature. As is known, the band topology of an odd-parity superconductor is determined by the relative configuration

[1] By pure s-wave pairing we mean $\Delta_0 + \Delta_s \eta_s(\boldsymbol{k})$ when at least one of the Δ_0 or Δ_s values is finite. It should be noted that pure s-wave pairing has pairing line nodes only when $|\Delta_0/\Delta_s| \leqslant 1$.

[2] Here, $\mathbb{Z}_2$ invariant is defined as $\nu = \prod_i [sgn(\Delta_i)]^{m_i}$ where $sgn(\Delta_i)$ represents the sign of the pairing on the i-th spin-split Fermi surface, and m_i denotes the number of time-reversal invariant points within the i-th Fermi surface.

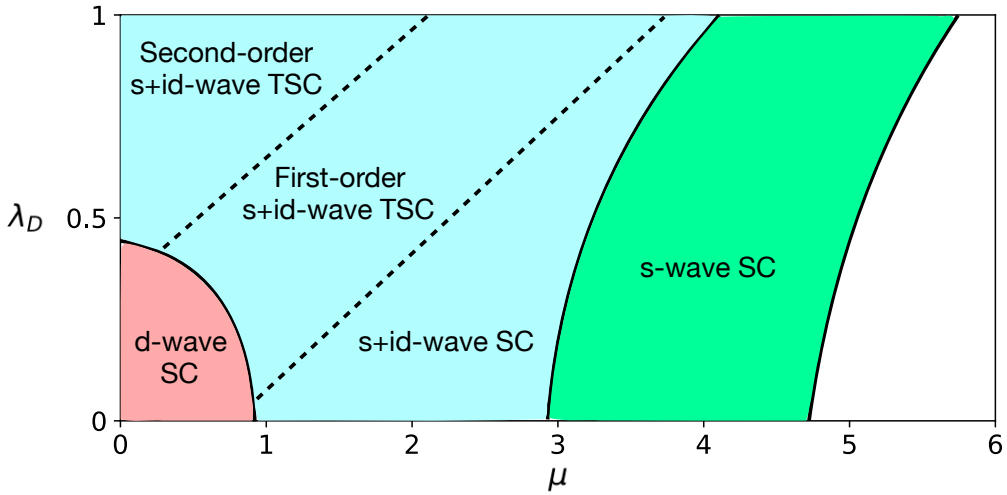

Figure 4.1: (Color online) Zero-temperature phase diagram for $\{t, \lambda_R, U, V\} = \{1, 0.3, 2, -5\}$. The phase diagram contains d-wave superconductivity (red color region), $s + id$-wave superconductivity (blue color region), and s-wave superconductivity (green color region). The time-reversal symmetry breaking $s + id$-wave superconductivity phase consists of three topologically distinct phases, including first- and second-order topological superconductor and topologically trivial superconductivity.

of the Fermi surfaces and the pairing nodes, and there exists a simple relation between the Chern number (C) and the number of Fermi surfaces (N_F) enclosing one time-reversal invariant point[3], which is $(-1)^C = (-1)^{N_F}$ [120]. The number of Fermi surfaces of $\mathcal{H}(\boldsymbol{k})$ must be even since the normal state has time-reversal symmetry, which implies that C must be an even integer. In addition, the gapped energy spectra of $\mathcal{H}_+(\boldsymbol{k})$ implies the absence of a Fermi surface, which is defined as the constant-energy contour satisfying $|\xi_k| + l(\boldsymbol{k}) = 0$, while $\mathcal{H}_-(\boldsymbol{k})$ has either zero or two Fermi surfaces, depending on the chemical potential μ. As the absence of Fermi surfaces always implies a trivial superconductor, only the situation that $\mathcal{H}_-(\boldsymbol{k})$ has two Fermi surfaces is of interest. When C is a nonzero even integer, the system corresponds to a first-order topological superconductor with C branches of Majorana chiral edge states. However, when $C = 0$, the system is either a topologically trivial superconductor or a second-order topological superconductor, depending on whether the two Fermi surfaces of $\mathcal{H}_-(\boldsymbol{k})$ can be continuously deformed to annihilate with each other without crossing any removable Dirac pairing nodes (not at time-reversal invariant points) or not.

Interestingly, we notice that $\mathcal{H}_-(\boldsymbol{k})$ takes a form similar to the toy model realizing second-order topological superconductivity proposed in Ref. [191]. Here, there are four removable

[3]Another important point is that if the normal state of a superconductor does not have a Fermi surface, the underlying topology must be trivial since such a phase can continuously transform to the limit $|\mu| \to \infty$ without the closing of either the bulk or the boundary gap.

Dirac pairing nodes whose net sum of winding number, defined as

$$\omega = \frac{1}{2\pi i} \oint \Delta_-^{-1} \partial_k \Delta_- dk, \tag{4.41}$$

with the closed integration contour enclosing only the interested pairing node, is zero lying between the two Fermi surfaces, and therefore the system realizes a second-order topological superconductor.

Another way to understand this picture is via the edge theory. To be specific, when the four removable Dirac pairing nodes of $\mathcal{H}_-(\boldsymbol{k})$ lie between the two Fermi surfaces, it means that, if we neglect the d-wave pairing, the line nodes of s-wave pairing (satisfying $\Delta_0 + \Delta_s \eta_s = 0$) can be chosen to lie between the two Fermi surfaces. Since without the d-wave pairing, the full Hamiltonian restores the time-reversal symmetry, then according to the formula $\nu = \prod_i [sgn(\Delta_i)]^{m_i}$ [190] we have $\nu = -1$, indicating the realization of a first-order time-reversal invariant topological superconductor that hosts a pair of helical Majorana edge states. Bringing back the d-wave pairing, the helical edge states are gapped out due to the breaking of time-reversal symmetry. However, as the d-wave pairing itself has line nodes along the directions $k_x = \pm k_y$, four Majorana zero modes will be left at the four corners when we use open-boundary conditions in both x and y directions [154, 192].

Based on the above analysis, we find that, within the $s + id$-wave pairing regime, the change of topology only takes place when the Fermi surfaces cross the removable Dirac pairing nodes at which both $\Delta_0 + \Delta_s \eta_s = 0$ and $\Delta_d \eta_d = 0$ are simultaneously fulfilled. As for the parameters considered, we find $\Delta_0 \ll \Delta_s, \Delta_d$; these nodes are almost fixed at the four points $\boldsymbol{Q}_{\pm,\pm} = (\pm\pi/2, \pm\pi/2)$. Therefore, the condition for topological phase transitions can be very accurately described by the normal-state condition $|\xi_{\boldsymbol{Q}_{\pm,\pm}}| - l(\boldsymbol{Q}_{\pm,\pm}) = 0$. It is straightforward to find that the solutions give two straight lines satisfying (see Appendix C for details)

$$|\mu| = 2\sqrt{2}|\lambda_R \pm \lambda_D|, \tag{4.42}$$

which correspond to the two dashed lines in the blue color region of Fig. 4.1.

To support the above analysis, we further diagonalize the mean-field BdG Hamiltonian in real space given in Eq. 4.30. To be specific, we fix $\lambda_D = 0.6$ and study the evolution of boundary modes with μ. The results are presented in Fig. 4.2. In accordance with the phase diagram in Fig. 4.1, we know that $\mu_{c,1} \simeq 3\sqrt{2}/5 \simeq 0.85$ and $\mu_{c,2} \simeq 9\sqrt{2}/5 \simeq 2.55$ are two critical points in the regime with $s+id$-wave pairing. Within each phase, we show one representative configuration of Fermi surfaces and pairing nodes [Figs. 4.2(b)–4.2(e)]. Fig. 4.2(b) shows that, within the regime $0 < \mu < \mu_{c,1}$, the four pairing nodes at $(\pm\pi/2, \pm\pi/2)$ are located between the two concentric Fermi surfaces enclosing (π, π), indicating the realization of a second-order topological superconductor [191]. To demonstrate this phase, we consider a square sample with open-boundary conditions in both x and y directions. A diagonalization of the real-space Hamiltonian does confirm the existence of four Majorana corner modes [see Fig. 4.2(f)] and, therefore, the realization of a second-order topological superconductor.

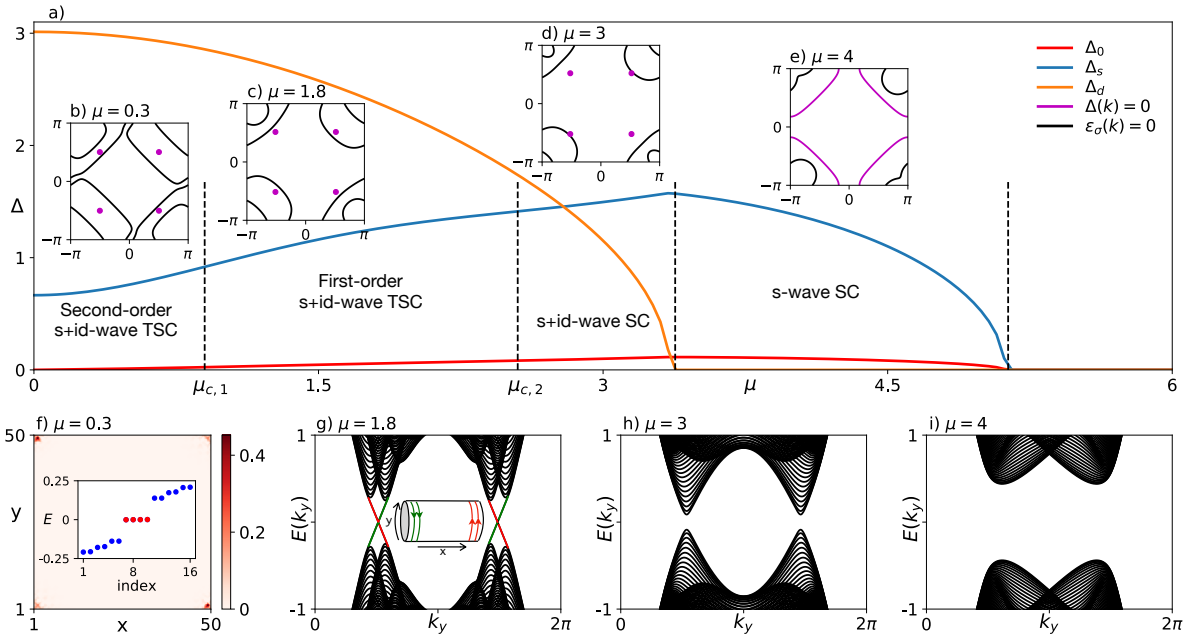

Figure 4.2: (Color online) Common parameters: $\{t, \lambda_R, \lambda_D, U, V\} = \{1, 0.3, 0.6, 2, -5\}$ (a) The dependence of $\Delta_{0,s,d}$ on μ at zero temperature. The dashed lines perpendicular to the μ axis correspond to phase boundaries. The four insets (b)–(e) show four representative configurations of Fermi surfaces (black) and pairing nodes (purple points or lines) in the four distinct phases. (b) $\mu = 0.3$, (c) $\mu = 1.8$, (d) $\mu = 3$, and (e) $\mu = 4$ [for this value, one of the Fermi surfaces becomes a point at (π, π)]. (f) The probability density profiles of four Majorana corner states (red points of the inset) and the eigenvalues of the BdG Hamiltonian around zero energy in real space for a 50×50 square lattice with open-boundary conditions in both x and y directions. (g)–(i) Energy spectrum for cylindrical geometry with open-boundary condition only along the x direction. The inset of (g) shows the distribution of chiral Majorana edge states in real space.

Within the regime $\mu_{c,1} < \mu < \mu_{c,2}$, only two of the four pairing nodes at $(\pm\pi/2, \pm\pi/2)$ remain to be located between the two Fermi surfaces, as shown in Fig. 4.2(c). As one pairing node takes the same winding number as its inversion partner, the transition from the configuration in Fig. 4.2(b) to that in Fig. 4.2(c) suggests a change of Chern number by two. In other words, a first-order topological superconductor with $C = 2$ is realized in the regime $\mu_{c,1} < \mu < \mu_{c,2}$. To demonstrate this phase, we consider a cylinder geometry with open-boundary conditions only along the x direction. The numerical result confirms the existence of two chiral Majorana modes on each edge [see Fig. 4.2(g)] and, therefore, the realization of a first-order topological superconductor with $C = 2$. Remarkably, the above results suggest that a topological phase transition between second- and first-order topological superconductors takes place at $\mu_{c,1}$[4]. Numerical calculations reveal the absence

[4]When the Fermi surface is anisotropic, it is a general feature that topologically trivial and second-order

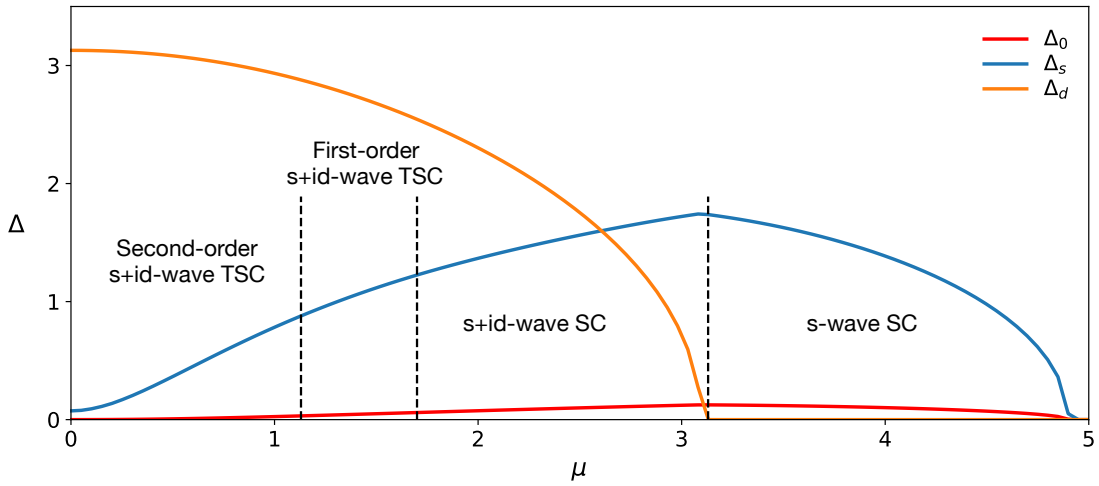

Figure 4.3: (Color online) Chemical potential dependency of $\Delta_{0,s,d}$ at zero-temperature for $\{t, \lambda_R, \lambda_D, U, V\} = \{1, 0.1, 0.5, 2, -5\}$.

of gapless boundary modes [Figs. 4.2(h) and 4.2(i)] in the regime $\mu > \mu_{c,2}$ indicating that the Hamiltonian is trivial in topology in this regime.

Although we used some specific parameters here to show some numerical results, it does not mean that these parameters are unique. In fact, different parameters can be chosen and these will yield a qualitatively similar phase diagram. To demonstrate this, we use, for example, smaller values for the spin-orbit coupling magnitudes compared to the ones above and show the results in Fig. 4.3. The result is quite similar to the one shown in Fig. 4.2 above.

So far, we have restricted the results to the zero-temperature limit. By performing self-consistent calculations at finite temperature, we find that, for a given configuration of Fermi surfaces, different pairing types exhibit different temperature dependence. As a result, the favored pairing can undergo a dramatic change at some critical temperature. To be specific, Fig. 4.4 shows two examples whose ground states at zero temperature are second- and first-order $s + id$-wave topological superconductors. From this figure, it is readily seen that the increase of temperature leads to a change of the favored pairing from a gapped $s + id$-wave topological superconductor to a d-wave gapless superconductor at a parameter-dependent critical temperature. Since the d-wave pairing leads to the realization of a nodal or Dirac superconductor, it indicates that the temperature itself provides a way to tune the underlying

topological $s + id$-wave phases are separated by an intervening first-order topological phase. This fact can be understood by inspecting the configurations of both Fermi surfaces and pairing nodes. It is not hard to see that when the Fermi surface is anisotropic, the four pairing nodes cannot simultaneously move outside all Fermi surfaces.

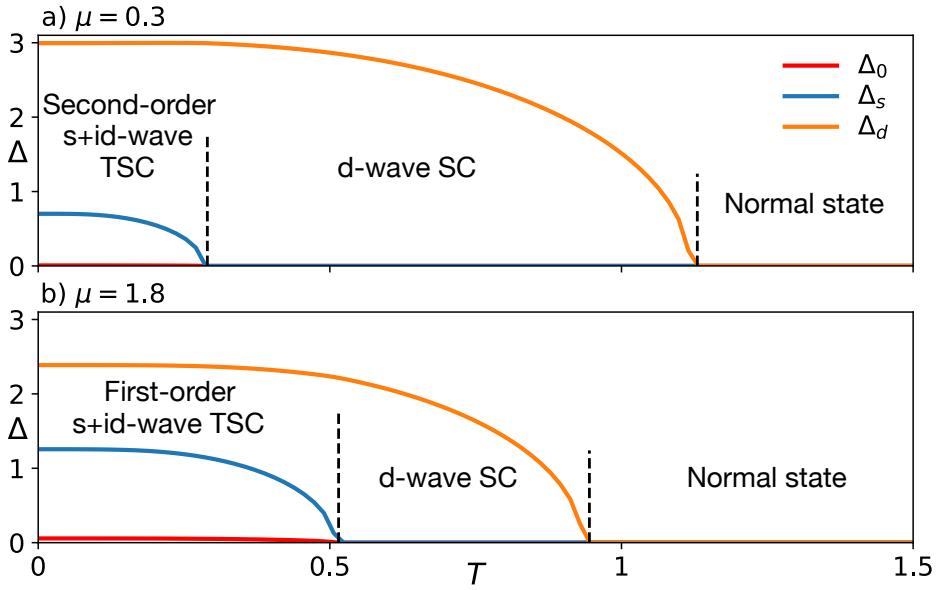

Figure 4.4: (Color online) Temperature-driven topological phase transitions. Here $\{t, \lambda_R, \lambda_D, U, V\} = \{1, 0.3, 0.6, 2, -5\}$, and (a) $\mu = 0.3$, (b) $\mu = 1.8$. Tuning the temperature can change both the favored pairing and the underlying topology.

topological properties.

4.5 Summary

In this chapter, we showed that both first- and second-order time-reversal symmetry breaking topological superconductivity as well as the topological phase transition between them can emerge in the extended Hubbard model with both Rashba and Dresselhaus spin-orbit coupling, even in the absence of an external magnetic field or magnetic order. Moreover, we demonstrated that, with appropriate Fermi surface structure, tuning only the temperature can result in interesting topological phase transitions in this system.

Our findings are relevant to many systems where both spin-orbit couplings and interactions are tunable, including InSb [125] or InGaAs [193] quantum wells in proximity to a high-temperature iron-based superconductor, which has an order parameter with $s + id$-wave superconducting pairing symmetry [194–196], oxide interfaces like $LaAlO_3/SrTiO_3$ [197, 198], and cold atom systems [199].

Chapter 5

Vortex Line Topology in Iron-Based Superconductors with and without Second-Order Topology

5.1 Introduction

In this chapter, which is based on publication (III), we investigated the potential impact of second-order topology on the vortex lines in iron-based superconductors in both weak and strong Zeeman field regimes. Recently, experimental evidence of Majorana zero modes in vortices has been observed in iron-based superconductors with band inversion near the Fermi level. It is known that iron-based superconductors with band inversion and $s_{\pm}$-wave pairing can give rise to second-order topological superconductivity, manifested by the presence of helical or chiral Majorana hinge states in three dimensions. In the weak Zeeman field regime, we find that vortex lines far away from the hinges are topologically nontrivial in the weakly doped regime, regardless of whether the second-order topology is present or not. However, when the superconductor falls into the second-order topological phase and a topological vortex line is moved close to the helical Majorana hinge states, we find that their hybridization will trivialize the vortex line and transfer the Majorana zero modes to the hinges. Furthermore, when the Zeeman field is large enough, we find that the helical Majorana hinge states are changed into chiral Majorana hinge modes and thus a chiral second-order topological superconducting phase is realized. In this regime, the vortex lines are always topologically trivial, no matter how far away they are from the chiral Majorana hinge modes. By incorporating a realistic assumption of inhomogeneous superconductivity, our findings can explain the recent experimental observation of the peculiar coexistence and evolution of topologically nontrivial and trivial vortex lines in iron-based superconductors.

Topological superconductors and iron-based superconductors have been two mainstreams

of the superconducting field for more than one decade. The great interest in topological superconductors lies in the various kinds of Majorana modes, like zero-dimensional localized Majorana zero modes and one-dimensional propagating helical and chiral Majorana modes, which hold promising applications in topological quantum computation [114, 124, 127, 200–203]. For iron-based superconductors, the great interest lies in their high superconducting transition temperature (T_c), strongly correlated nature and pairing mechanisms leading to the emergence of unconventional pairings [204–209], such as the widely-known $s_{\pm}$-wave pairing [210, 211]. As iron-based superconductors commonly have multiple bands near the Fermi energy, the possibility of the occurrence of band inversion with a realization of topological superconductivity through the Fu-Kane mechanism [124] has attracted considerable theoretical interest in the past few years [212–216].

Recently, several groups have experimentally observed that above T_c, band inversion occurs between the bands near the Fermi energy in a series of iron-based superconductors, and below T_c, the surface Dirac cones associated with the inverted band structure are gapped by the bulk superconductivity [139, 217–223]. The Fu-Kane mechanism is thus fulfilled in a single-material platform, unlike the various actively-studied heterostructures composed of different pieces of materials [136–138, 224, 225]. Therefore, the observation of compelling experimental evidence for vortex Majorana zero modes in iron-based superconductors, like zero-bias peak with nearly quantized height and other ordered discrete peaks in the scanning tunneling spectroscopy [139, 219–223], has generated tremendous interest [226–237]. Notably, in these iron-based superconductors, trivial vortex lines without Majorana zero modes are observed to coexist with topological vortex lines with Majorana zero modes [139, 219, 220, 238]. While mechanisms like pairing change induced by a Zeeman field or spatially dependent surface states have been proposed to explain this peculiar experimental finding [219, 233, 239], a conclusive understanding is still far from established.

Another remarkable advance in topological superconductors is the recent birth of the concept named higher-order topological superconductors [54, 152–155, 240–270]. It is interesting that several theoretical works have revealed that a combination of inverted band structure and $s_{\pm}$-wave pairing can also give rise to second-order topological superconductivity [152, 153, 155], which is manifested by the presence of Majorana corner modes in two dimensions (2D) and Majorana hinge modes in three dimensions. Remarkably, experimental evidence for the existence of Majorana hinge modes in a three dimensional iron-based superconductor has also been reported [271]. These previous works motivate us to study the open question about the potential impact of second-order topology on the vortex lines in three dimensional iron-based superconductors.

By focusing on the weakly doped regime of most interest and relevance to the experiments, our main findings can be summarized as follows: (i) In the weak Zeeman field regime, we find that if the second-order topology is absent, then the vortex line will bind one Majorana zero mode at each end [see Fig. 5.1(a)], regardless of its position, resembling the situation with conventional s-wave pairing [272]. (ii) When the second-order topology is present, a vortex

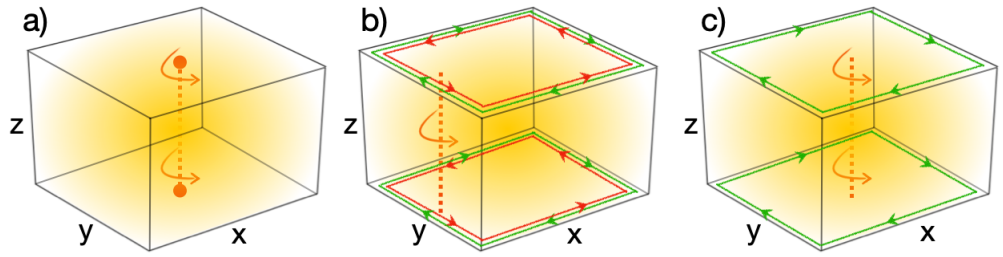

Figure 5.1: (Color online) Schematic diagrams. (a) For a superconductor with a single band inversion, when the chemical potential crosses the surface bands in the normal state and there are no gapless modes on the boundary in the superconducting state, the vortex line will bind one robust Majorana zero mode at each end, regardless of its position. (b) When the superconductor is a second-order topological superconductor with helical Majorana hinge modes, a close-to-hinge vortex line will not bind robust Majorana zero modes at its ends because of hybridization with the helical Majorana hinge modes. (c) When the superconductor is a second-order topological superconductor with chiral Majorana hinge modes, the vortex line terminated at the surfaces with Zeeman-field-dominated Dirac mass will not bind Majorana zero modes even when it is far away from the hinges.

line far away from the hinges will also bind one Majorana zero mode at each end. However, if topological vortex line is moved close to the hinges, it will be trivialized by hybridizing with the helical Majorana modes [see Fig. 5.1(b)]. Because Majorana zero modes are always created or annihilated in pairs, this $\mathbb{Z}_2$ nature leads to the transfer of robust Majorana zero modes to the hinges. (iii) While the helical Majorana hinge modes are counter-intuitively quite stable against the Zeeman field, they will become chiral Majorana hinge modes when the Zeeman field is larger than a critical value. In this regime, Majorana zero modes are absent in the vortex cores, no matter how far away they are from the chiral Majorana hinge modes [see Fig. 5.1(c)]. Nevertheless, Majorana zero modes can appear on the hinges if the number of vortex lines is odd.

5.2 Theoretical formalism

The inverted band structure of iron-based superconductors near the Fermi level can be described by a four-band minimal model of three dimensional topological insulators [34, 68]. In combination with the $s_{\pm}$-wave pairing, the underlying physics can be described by the Bogoliubov-de Gennes Hamiltonian as

$$H = \frac{1}{2}\sum_{\boldsymbol{k}} \begin{pmatrix} \boldsymbol{c}_{\boldsymbol{k}}^{\dagger}, & \boldsymbol{c}_{-\boldsymbol{k}} \end{pmatrix} \begin{pmatrix} H_0(\boldsymbol{k}) & \Delta(\boldsymbol{k}) \\ \Delta^{\dagger}(\boldsymbol{k}) & -H_0^{*}(-\boldsymbol{k}) \end{pmatrix} \begin{pmatrix} \boldsymbol{c}_{\boldsymbol{k}} \\ \boldsymbol{c}_{-\boldsymbol{k}}^{\dagger} \end{pmatrix}, \tag{5.1}$$

where $\boldsymbol{c_k} = (c_{\boldsymbol{k},a,\uparrow}, c_{\boldsymbol{k},b,\uparrow}, c_{\boldsymbol{k},a,\downarrow}, c_{\boldsymbol{k},b,\downarrow})^{\mathrm{T}}$ and

$$H_0(\boldsymbol{k}) = m(\boldsymbol{k})\sigma_z s_0 + 2\lambda \sum_{i=x,y,z} \sin k_i \sigma_x s_i - \mu\sigma_0 s_0 + \sigma_0 \boldsymbol{h}\cdot\boldsymbol{s}, \tag{5.2}$$

$$\Delta(\boldsymbol{k}) = i\Delta(\boldsymbol{k})\sigma_0 s_y, \tag{5.3}$$

where $\boldsymbol{s} = (s_x, s_y, s_z)$, and $\boldsymbol{h} = (h_x, h_y, h_z)$ denotes the Zeeman field which is assumed to be present accompanying the generation of vortex lines. The Pauli matrices σ and s act in orbital (a, b) and spin $(\uparrow, \downarrow)$ degrees of freedom, respectively, and σ_0 and s_0 are the unit matrices. Here, T stands for matrix transpose, λ denotes the strength of spin-orbit coupling, μ is the chemical potential, $H_0(\boldsymbol{k})$ describes the normal state, and $\Delta(\boldsymbol{k})$ represents the $s_{\pm}$-wave pairing given by

$$\Delta(\boldsymbol{k}) = \Delta_0 + \Delta_s(\cos k_x + \cos k_y), \tag{5.4}$$

where for notational simplicity, the lattice constants have been set to unity throughout this work, and Δ_0 and Δ_s represent on-site and extended s-wave superconducting pairing magnitudes, respectively. The $m(\boldsymbol{k})$ term characterize the band inversion as

$$m(\boldsymbol{k}) = m_0 - 2t \sum_{i=x,y,z} \cos k_i, \tag{5.5}$$

where m_0 is an on-site orbital dependent energy, and t denotes the hopping amplitude. The BdG Hamiltonian (5.1) can also be written in a more compact form,

$$\begin{aligned}\mathcal{H}(\boldsymbol{k}) = {} & m(\boldsymbol{k})\sigma_z s_0 \tau_z + 2\lambda \sum_{i=x,y,z} \sin k_i \sigma_x s_i \tau_z - \mu\sigma_0 s_0 \tau_z \\ & + \sigma_0 \boldsymbol{h}\cdot\boldsymbol{s}\tau_0 - \Delta(\boldsymbol{k})\sigma_0 s_0 \tau_x,\end{aligned} \tag{5.6}$$

with the basis $\psi_{\boldsymbol{k}}^{\mathrm{T}} = (\boldsymbol{c}_k, -i\sigma_0 s_y \boldsymbol{c}_{-k}^{\dagger})$ where $\boldsymbol{c}_k = (c_{\boldsymbol{k},a,\uparrow}, c_{\boldsymbol{k},b,\uparrow}, c_{\boldsymbol{k},a,\downarrow}, c_{\boldsymbol{k},b,\downarrow})^{\mathrm{T}}$. Here, the Pauli matrices τ acts on the particle-hole degree of freedom. The eigenvalues of the BdG Hamiltonian for $\boldsymbol{h} = 0$ are given by,

$$E_{(\pm,\pm)}(\boldsymbol{k}) = \pm\sqrt{\varepsilon_{\pm}^2(\boldsymbol{k}) + \Delta^2(\boldsymbol{k})}, \tag{5.7}$$

where

$$\varepsilon_{\pm}(\boldsymbol{k}) = \mu \pm \sqrt{m^2(\boldsymbol{k}) + 4\lambda^2 \sum_{i=x,y,z} \sin^2 k_i}. \tag{5.8}$$

When the equal-energy contour $m(\boldsymbol{k}) = 0$, known as the band inversion surface, encloses a single time-reversal invariant momentum, the normal state hosts a topological gap and a single Dirac cone on each surface [90]. After becoming superconducting below T_c, the surface Dirac cones are gapped by the superconductivity. For a conventional s-wave pairing, *i.e.*,

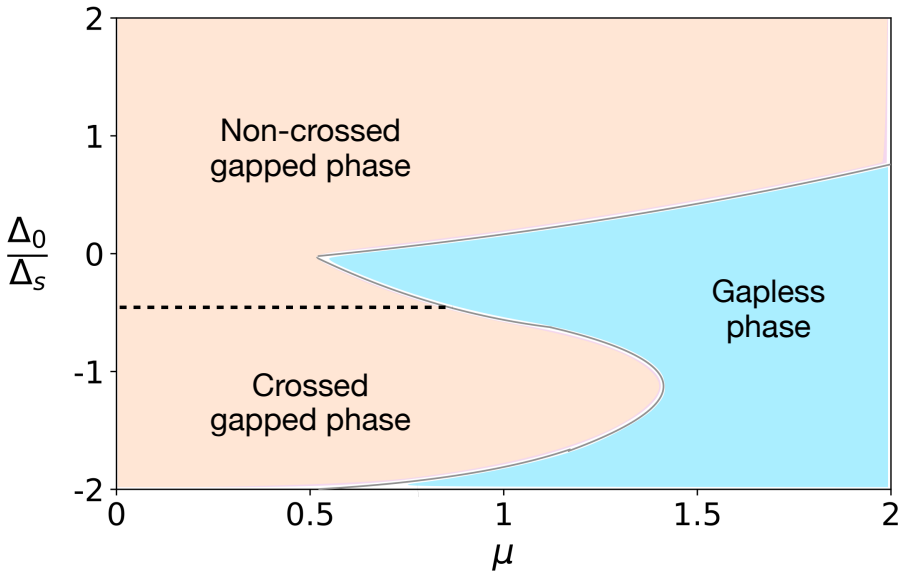

Figure 5.2: (Color online) The phase diagram consists of gapped (orange region) and gapless (blue region) phases. We take $t = 1$, $m_0 = 2.5$, $\lambda = 0.5$, and $\boldsymbol{h} = 0$ in the absence of vortex lines. The horizontal dashed line divides the gapped phase into two distinct topological phases. The crossed gapped phase corresponds to a gapped second-order topological superconducting phase with the underlying band inversion surface and pairing node surface crossing with each other. The noncrossed gapped phase corresponds to a gapped trivial superconducting phase with the underlying band inversion surface and pairing node surface separated in the Brillouin zone.

$\Delta(\boldsymbol{k}) = \Delta_0$ in Eq. (5.4), it is known that its induced Dirac mass on the surfaces is uniform if the effect of disorder is negligible. In other words, there does not exist any kind of gapless boundary modes. However, for the $s_{\pm}$-wave pairing given in Eq. (5.4), it has been shown in Ref. [155] that even though the first-order topology is trivial, a nontrivial time-reversal invariant second-order topology, which is manifested by the presence of helical Majorana hinge modes, can be achieved in this system.

Because $s_{\pm}$-wave pairing has nodes when $|\Delta_0| < 2|\Delta_s|$, the superconductor can be gapless when the Fermi surface intersects with the pairing nodes. As the location of pairing nodes is determined by $\Delta(\boldsymbol{k}) = 0$, and the location of Fermi surface is determined by $\varepsilon_-(\boldsymbol{k}) = 0$, we can numerically determine the phase boundary which separates the gapped phase from the gapless phase by checking when the contour for $\Delta(\boldsymbol{k}) = 0$ intersects with the contour for $\varepsilon_-(\boldsymbol{k}) = 0$. The phase boundary is shown in Fig. 5.2.

As the energy bands of the concerned iron-based superconductors are gapped, therefore, in this work we are interested in the gapped regime. Within the gapped regime, the phase can be further divided as second-order topological superconductor and trivial superconductor. At $\mu = 0$, when the band inversion surface and pairing node surface cross, the system is

a second-order topological superconductor with helical Majorana hinge modes. If we start with the crossing case, it is expected that a transition from the second-order topological superconducting phase to the trivial superconducting phase should happen. It is known that a topological phase transition from a first-order topological phase to a trivial phase is always associated with the closure of the bulk energy gap as long as the symmetry class does not change. However, a topological phase transition from a second-order topological phase to a trivial phase in general does not require the closure of the bulk energy gap; what it requires is the closure of the energy gap of the surface states. Interestingly, for the set of isotropic parameters considered in this work, we found that the closure of surface energy gap coincides with the closure of the bulk energy gap, indicating that the phase boundary of the second-order topological superconducting phase with a finite bulk gap coincides with the gapped-gapless phase boundary. These findings establish the phase diagram in Fig. 5.2.

In this chapter, we follow the experiments and focus on the configurations presented in Fig. 5.1, where the vortex lines are generated along the z direction. To illustrate the key physics in a clear way, we simplify the real situation with multiple vortex lines to an ideal situation with just a single π-flux vortex line. Such a simplification is justified in the weak-field regime, where the vortex lines are dilute and well-separated from each other. To simulate such a configuration, we assume that both on-site and nearest-neighbor pairings follow such a spatial dependence,

$$\Delta_{0,s}(\boldsymbol{r}) = \Delta_{0,s} \tanh(\frac{\sqrt{\bar{x}^2+\bar{y}^2}}{\xi})\frac{\bar{x}+i\bar{y}}{\sqrt{\bar{x}^2+\bar{y}^2}}, \tag{5.9}$$

where ξ denotes the superconducting coherence length, $\bar{x} = x - x_c$ and $\bar{y} = y - y_c$, with (x_c, y_c) denoting the core of the vortex in the xy plane, and (x, y) representing the coordinates of the lattice sites for on-site pairing $\Delta_0(\boldsymbol{r})$ and the coordinates of the lattice-bond centers for nearest-neighbor pairing $\Delta_s(\boldsymbol{r})$. The superconducting coherence length ξ will not be determined through self-consistent calculations, instead we will set its value by hand since the topological property of the vortex line in the weakly doped regime is insensitive to its value. It is noteworthy that similar forms can be adopted if one wants to study vortex lines along other directions.

The corresponding real space BdG Hamiltonian can be given by

$$H = \frac{1}{2}\sum_{i,j}\begin{pmatrix}\boldsymbol{c}_i^\dagger, & \boldsymbol{c}_i\end{pmatrix}\begin{pmatrix}H_{0;ij} & \Delta_{ij} \\ -\Delta_{ij}^* & -H_{0;ij}^*\end{pmatrix}\begin{pmatrix}\boldsymbol{c}_j \\ \boldsymbol{c}_j^\dagger\end{pmatrix}, \tag{5.10}$$

with the basis $\boldsymbol{c}_i = (c_{i,a,\uparrow}, c_{i,b,\uparrow}, c_{i,a,\downarrow}, c_{i,b,\downarrow})^{\mathrm{T}}$ and

$$H_{0;ij} = \sum_{\nu=0,x,y,z} A_{ij}^\nu s_\nu, \tag{5.11}$$

$$\Delta_{ij} = i\big\{\Delta_0\delta_{ij} + \frac{\Delta_s}{2}(\delta_{j,i+\hat{x}} + \delta_{j,i-\hat{x}} + \delta_{j,i+\hat{y}} + \delta_{j,i-\hat{y}})\big\}\sigma_0 s_y, \tag{5.12}$$

where

$$A^0_{ij} = \big\{m_0\delta_{ij} - t\sum_{\nu=x,y,z}(\delta_{j,i+\hat{\nu}} + \delta_{j,i-\hat{\nu}})\big\}\sigma_z - \mu\delta_{ij}\sigma_0, \tag{5.13}$$

$$A^\alpha_{ij} = -i\lambda(\delta_{j,i+\hat{\alpha}} - \delta_{j,i-\hat{\alpha}})\sigma_x + h_\alpha\delta_{ij}\sigma_0, \tag{5.14}$$

are four $2N \times 2N$ matrices for $N = L_xL_yL_z$ and $\alpha \in \{x, y, z\}$. In the presence of a π-flux vortex line, let us say along the z direction, we need only modify the Δ_{ij} matrix. In this case, we should replace the site-independent real numbers Δ_0 and Δ_s with the site-dependent complex numbers given by Eq. (5.9).

At $\mu = 0$ and $\boldsymbol{h} = 0$, we can establish a simple geometric criterion for the realization of nontrivial time-reversal invariant second-order topology. The geometric picture of the criterion is the crossing of the band inversion surface and the pairing node surface, which is the equal-energy contour $\Delta(\boldsymbol{k}) = 0$. The logic behind this statement is as follows. The Hamiltonian (5.1) at $\mu = \boldsymbol{h} = 0$ can be divided into two parts, *i.e.*, $H = H_e + H_o$, where H_e and H_o represent respectively the even-parity and odd-parity parts. Because $\{H_e, H_o\} = 0$, the even-parity part H_e plays the role of Dirac mass. When the energy spectra of H_e are gapless, H will be topologically nontrivial since the existence of nodes in H_e implies the existence of domain walls of Dirac mass on the boundary. Such kinds of geometric criteria are universally applicable to higher-order topological models as long as the condition that all terms of the Hamiltonian anticommute with each other is fulfilled [54, 240, 260].

To show the validity of the geometric criterion explicitly, let us consider a cubic geometry with open boundary condition in two directions and periodic boundary condition in the remaining direction. As shown in the first row of Fig. 5.3, when the band inversion surface and the pairing node surface do not cross [see the orange and the blue surfaces in Fig. 5.3(a)], there is no gapless hinge mode [Figs. 5.3(b)-5.3(d)], confirming the trivial topology. On the contrary, when the band inversion surface and the pairing node surface cross, helical Majorana modes are found to appear on the interfacing hinges between z-normal surfaces and x- and y-normal surfaces [Figs. 5.3(f) and 5.3(g)], with their distributions the same as in Fig. 5.1(b) (here without vortex lines).

When μ or $\boldsymbol{h}$ becomes nonzero, surely the above simple geometric criterion generally no longer holds because these two terms do not anticommute with all odd-parity terms in the Hamiltonian. Nevertheless, the second-order topology can survive even when the normal state becomes metallic. Generally, it is known that gapless helical modes will become gapped when the time-reversal symmetry is lifted by the Zeeman field. However, here we find that the helical Majorana hinge modes shown in Figs. 5.3(f) and 5.3(g) are counter-intuitively quite robust against the Zeeman field. Only when the Zeeman field is strong enough to dominate

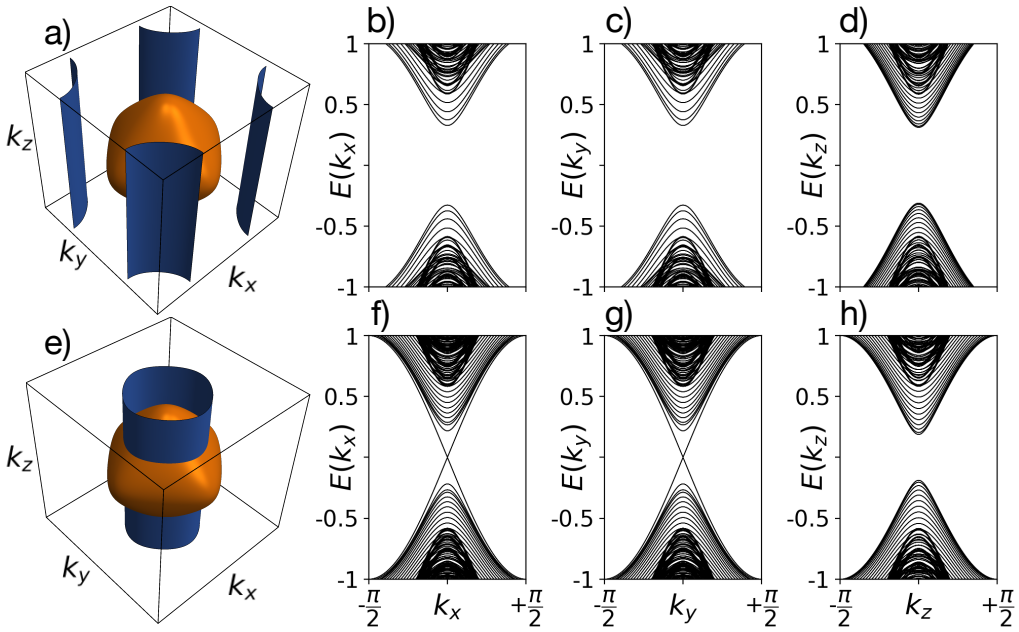

Figure 5.3: (Color online) (a)-(d) No gapless modes appear on the hinges when the band inversion surface in orange and the pairing node surface in blue do not cross. (e)-(h) Helical Majorana modes appear on the hinges between z-normal surfaces and x- and y-normal surfaces when the band inversion surface and the pairing node surface cross. Common parameters are: $t = 1$, $m_0 = 2.5$, $\lambda = 0.5$, $\mu = 0$, $\boldsymbol{h} = 0$ and $\Delta_0 = 0.25$. (a)-(d) $\Delta_s = 0.25$, (e)-(h) $\Delta_s = -0.25$, without vortex lines. The two directions with open boundary conditions are y and z in (b)(f), x and z in (c)(g), and x and y in (d)(h), and their lengths contain 24 lattice sites.

over the superconductivity-induced Dirac mass on some of the surfaces, *e.g.*,

$$|h_z| > \sqrt{\mu^2 + (\Delta_0 + 2\Delta_s)^2}, \tag{5.15}$$

will the nature of the domain walls change and the helical Majorana hinge modes will become chiral Majorana hinge modes as illustrated in Fig. 5.1(c) (see Appendix E for more details). We find that the robustness of the helical Majorana hinge modes is simply because the Zeeman field cannot directly act on the subspace of the domain walls. These results suggest that the simple Hamiltonian (5.1) can realize both time-reversal invariant and chiral second-order topological superconductors.

Throughout the main text, we have chosen $t = 1$ as the unit of energy, $m_0 = 2.5$, $\lambda = 0.5$, so that a band inversion takes place at the $\Gamma = (0, 0, 0)$. It is worth noting that for this set of parameters, the band edges are located at $(0, \pi, 0)$ and $(\pi, 0, 0)$, with the energy gap $E_g = 1.0$. The normal state becomes metallic when $\mu > 0.5$. We only consider positive μ because the results are symmetric about $\mu = 0$.

5.3 Second-order topology without vortex lines

In this section, we focus on the uniform case without vortex lines, so we will study a homogeneous iron-based superconductor.

5.3.1 The effects of Zeeman field on the helical Majorana hinge modes

In the previous section, we showed that in the absence of a Zeeman field, the Majorana hinge modes are helical due to the preservation of time-reversal symmetry. In this section, we show the impact of the Zeeman field on the Majorana hinge modes in the absence of vortex lines in detail. Naively, one may expect that the introduction of a Zeeman field would immediately gap the helical Majorana hinge modes due to the breaking of time-reversal symmetry. However, the actual results are in contradiction with this expectation!

While the magnetic field will generate vortices due to the orbital effect, in this section we neglect the generation of vortex lines and focus on the effect from the Zeeman field to the helical Majorana hinge modes. In Fig. 5.4 and Fig. 5.5, we show the evolution of the energy spectra with respect to Zeeman field. The underlying cubic geometry takes on open boundary conditions in the y and z directions and periodic boundary condition in the x direction. In Fig. 5.4, the magnetic field is applied in the z direction *i.e.* $\boldsymbol{h} = (0, 0, h_z)$, and in Fig. 5.5, the magnetic field is applied in the [111] direction *i.e.* $\boldsymbol{h} = (h, h, h)$. For comparison, the result for the time-reversal invariant case ($\boldsymbol{h} = 0$) is presented in Fig. 5.4(a). In Fig. 5.4(b) and Fig. 5.5(a), one can see that the Majorana hinge modes remain gapless in a small applied field. Moreover, the degeneracy of the Majorana hinge modes does not change even though the degeneracy of other higher-energy spectra is lifted due to the breaking of time-reversal symmetry. The helical Majorana hinge modes are found to remain intact until the Zeeman field becomes larger than an orientation-dependent critical value. In Fig. 5.4(c) and Fig. 5.5(b), the results show that when the Zeeman field becomes a little larger than the critical value, half of the gapless Majorana hinge modes become gapped. We find that this corresponds to a transition from a second-order topological superconductor with helical Majorana hinge modes to a second-order topological superconductor with chiral Majorana hinge modes. With a further increase of Zeeman field, these chiral Majorana hinge modes become more separated from other modes in energy, as shown in Figs. 5.4(d) and 5.4(e) and Figs. 5.5(c) and 5.5(d).

In the following, we develop an analytic theory to explain the robustness of helical Majorana hinge modes against the Zeeman field. Following the standard procedure, we first perform a lower-energy expansion of the lattice Hamiltonian in Eq. (5.6) around the band-inversion momentum. Without loss of generality, we still consider that the band inversion

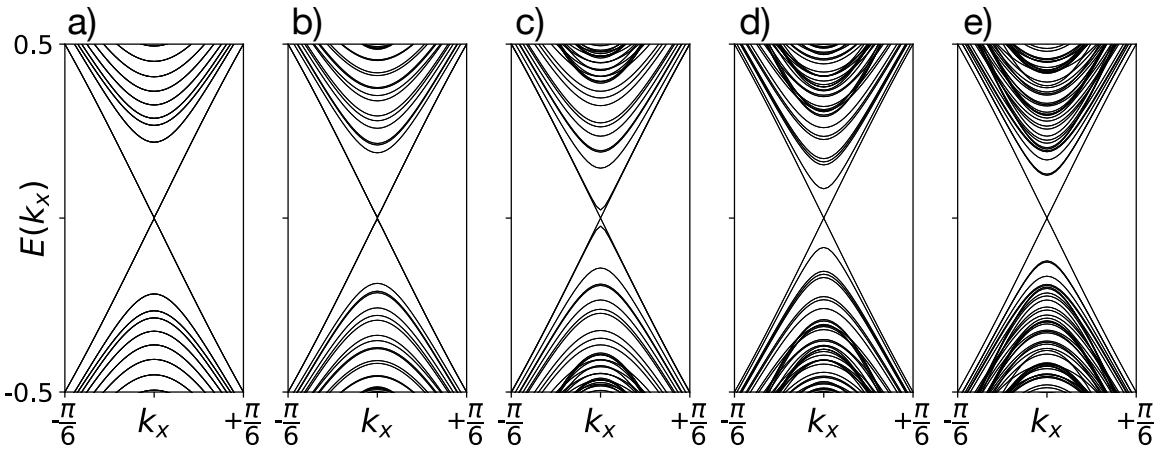

Figure 5.4: The effects of Zeeman field (no vortex lines) to the helical Majorana hinge modes. Common parameters are $t = 1$, $m_0 = 2.5$, $\lambda = 0.5$, $\mu = 0$, $\Delta_0 = -\Delta_s = 0.25$, $h_x = h_y = 0$. The lengths along the y and z directions contain $L_y = L_z = 24$ lattice sites. (a) $h_z = 0$, (b) $h_z = 0.1$, (c) $h_z = 0.2$, (d) $h_z = 0.3$, (e) $h_z = 0.4$. In (a) (b), the gapless modes traversing the gap are four-fold degenerate (read from data), corresponding to four pairs of helical Majorana hinge modes. (c) shows the spectra just crossing the transition from a second-order topological superconductor with helical Majorana hinge modes to a second-order topological superconductor with chiral Majorana hinge modes. In (d) (e), the gapless modes traversing the gap are two-fold degenerate (read from data), corresponding to four branches of chiral Majorana hinge modes.

occurs at the Γ point. Accordingly, the low-energy continuum Hamiltonian reads

$$\begin{aligned}\mathcal{H}(\boldsymbol{k}) = (m + tk^2)\sigma_z s_0 \tau_z + 2\lambda \sigma_x \boldsymbol{k} \cdot \boldsymbol{s} \tau_z - \mu \sigma_0 s_0 \tau_z + \sigma_0 \boldsymbol{h} \cdot \boldsymbol{s} \tau_0 \\ - [\Delta_0 + 2\Delta_s - \frac{\Delta_s}{2}(k_x^2 + k_y^2)]\sigma_0 s_0 \tau_x,\end{aligned} \tag{5.16}$$

where $m = m_0 - 6t$. For simplicity, we focus on $\mu = 0$ in the following and take t and λ to be positive. Let us first derive the low-energy Hamiltonian for the surface states on the z-normal surfaces. To proceed, let us consider a semi-infinite sample with $0 \leq z < +\infty$. The presence of a boundary breaks the translational symmetry in the z direction, so the k_z in the Hamiltonian (5.16) needs to be replaced by $-i\partial_z$. Following Ref. [152], we divide the Hamiltonian into two parts, $\mathcal{H} = \mathcal{H}_1 + \mathcal{H}_2$, where

$$\mathcal{H}_1(k_x, k_y, -i\partial_z) = [m + t(k_x^2 + k_y^2) - t\partial_z^2]\sigma_z s_0 \tau_z - 2i\lambda \partial_z \sigma_x s_z \tau_z, \tag{5.17}$$

$$\mathcal{H}_2(k_x, k_y, -i\partial_z) = 2\lambda \sigma_x (k_x s_x + k_y s_y)\tau_z + \sigma_0 \boldsymbol{h} \cdot \boldsymbol{s} \tau_0 - [\Delta_0 + 2\Delta_s - \frac{\Delta_s}{2}(k_x^2 + k_y^2)]\sigma_0 s_0 \tau_x. \tag{5.18}$$

In the division, we have taken $\mathcal{H}_2$ as a perturbation, which is quite accurate when the pairing amplitude and the strength of Zeeman field are small. By solving the eigenvalue equation

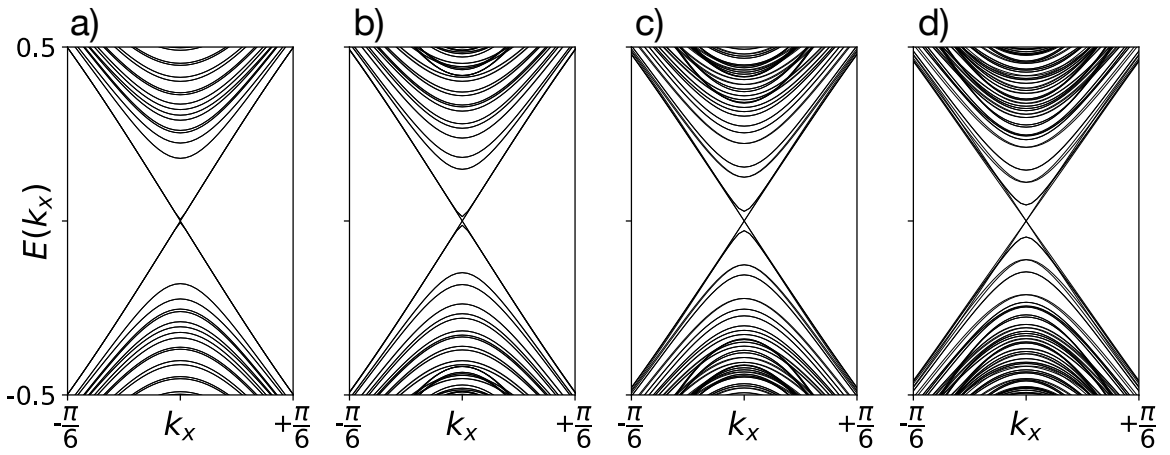

Figure 5.5: The effects of Zeeman field (no vortex lines) to the helical Majorana hinge modes. Common parameters are $t = 1$, $m_0 = 2.5$, $\lambda = 0.5$, $\mu = 0$, $\Delta_0 = -\Delta_s = 0.25$. The lengths along the y and z directions contain $L_y = L_z = 24$ lattice sites. $\boldsymbol{h} = (h, h, h)$, with (a) $h = 0.05$, (b) $h = 0.1$, (c) $h = 0.15$, (d) $h = 0.2$. In (a) (b), the gapless modes traversing the gap are four-fold degenerate (read from data), corresponding to four pairs of helical Majorana hinge modes. (c) shows the spectra just crossing the transition from a second-order topological superconductor with helical Majorana hinge modes to a second-order topological superconductor with chiral Majorana hinge modes. In (d), the gapless modes traversing the gap are two-fold degenerate (read from data), corresponding to four branches of chiral Majorana hinge modes.

$\mathcal{H}_1(k_x, k_y, -i\partial_z)\psi_\alpha(z) = E_\alpha\psi_\alpha(z)$ with the boundary condition $\psi_\alpha(0) = \psi_\alpha(+\infty) = 0$, one can find that there exist four zero-energy solutions. The wave functions $\psi_\alpha(z)$ can be compactly written as

$$\psi_\alpha(z) = \mathcal{N}\sin(\kappa_1 z)e^{-\kappa_2 z}e^{ik_x x}e^{ik_y y}\chi_\alpha, \tag{5.19}$$

with normalization given by $|\mathcal{N}|^2 = |4\kappa_2(\kappa_1^2 + \kappa_2^2)/\kappa_1^2|$. The two parameters κ_1 and κ_2 are respectively given by $\kappa_1 = \sqrt{\frac{[t(k_x^2+k_y^2)-m]}{t} - \left(\frac{\lambda}{t}\right)^2}$ and $\kappa_2 = \frac{\lambda}{t}$. The most important information is contained in χ_α. Here χ_α satisfy $\sigma_x s_z \tau_0 \chi_\alpha = -\chi_\alpha$. We can explicitly choose solutions as

$$\chi_1 = |\sigma_y = -1\rangle \otimes |s_z = 1\rangle \otimes |\tau_z = 1\rangle, \tag{5.20}$$
$$\chi_2 = |\sigma_y = 1\rangle \otimes |s_z = -1\rangle \otimes |\tau_z = 1\rangle, \tag{5.21}$$
$$\chi_3 = |\sigma_y = -1\rangle \otimes |s_z = 1\rangle \otimes |\tau_z = -1\rangle, \tag{5.22}$$
$$\chi_4 = |\sigma_y = 1\rangle \otimes |s_z = -1\rangle \otimes |\tau_z = -1\rangle. \tag{5.23}$$

By projecting $\mathcal{H}_2$ into the four-dimensional space spanned by χ_α, we obtain the low-energy Hamiltonian for the surface states on the $z = 0$ surface, which reads

$$\mathcal{H}_{\text{eff}}(k_x, k_y) = 2\lambda(k_y s_x - k_x s_y)\tau_z + M_{\text{Z}} s_z + M_{\text{S}}\tau_x, \tag{5.24}$$

where $M_{\rm Z} = h_z$ denotes the Dirac mass induced by the Zeeman field, and $M_{\rm S} = \Delta_0 + 2\Delta_s$ in the leading order denotes the Dirac mass induced by the superconductivity. It is easy to see that for the Zeeman field, only the component perpendicular to the concerned surface contributes to the Dirac mass. It is worth noting that the two Dirac mass terms commute with each other, and a closure of the surface gap happens at $M_{\rm Z} = M_{\rm S}$. That is, when $M_{\rm Z}$ becomes larger than $M_{\rm S}$, the nature of the Dirac mass on the surface will change from a superconductivity-dominated one to a Zeeman-field-dominated one.

With Eq. (5.24), now we can explain why the helical Majorana hinge modes are stable against the Zeeman field when its strength is below the critical value. To proceed, let us consider that the y direction also becomes open and a domain wall hosting Majorana helical modes is formed at the boundary. Following the same steps, we divide the Hamiltonian (5.24) into two parts, $\mathcal{H}_{\rm eff} = \mathcal{H}_{\rm eff;1} + \mathcal{H}_{\rm eff;2}$, where

$$\mathcal{H}_{\rm eff;1}(k_x, -i\partial_y) = -2i\lambda\partial_y s_x\tau_z + M_{\rm S}(y)\tau_x, \tag{5.25}$$

$$\mathcal{H}_{\rm eff;2}(k_x, k_y) = -2\lambda k_x s_y\tau_z + M_{\rm Z}s_z. \tag{5.26}$$

As explained previously, such a division is justified when the Zeeman field, so $M_{\rm Z}$, is small. From our analysis above, one can immediately read from $\mathcal{H}_{\rm eff;1}$ that the space for the low-energy modes is spanned by $\tilde{\chi}_\alpha$ which satisfy either $s_x\tau_y\tilde{\chi}_\alpha = \tilde{\chi}_\alpha$ or $s_x\tau_y\tilde{\chi}_\alpha = -\tilde{\chi}_\alpha$ [the sign depends on the detail of the profile of $M_{\rm S}(y)$]. That is, the two-dimensional space for the helical Majorana modes is spanned either by $(|s_x = 1\rangle \otimes |\tau_y = 1\rangle, |s_x = -1\rangle \otimes |\tau_y = -1\rangle)$ or by $(|s_x = 1\rangle \otimes |\tau_y = -1\rangle, |s_x = -1\rangle \otimes |\tau_y = 1\rangle)$. Projecting $\mathcal{H}_{\rm eff;2}$ into these two possible two-dimensional spaces, one can find that the low-energy Hamiltonian on the hinge is given by

$$\mathcal{H}_{\rm hinge}(k_x) = -2\lambda k_y s_y. \tag{5.27}$$

One can immediately see that in the weak field regime (the regime for which the perturbative treatment is justified), the presence of Zeeman field does not alter the helical nature, though the time-reversal symmetry is broken. According to Eq. (5.24), we know that a closure of the surface gap happens at $M_{\rm Z} = M_{\rm S}$. This indicates that when the Dirac mass term induced by the Zeeman field is equal to the one induced by superconductivity, a surface topological phase transition occurs, accompanying a change of the nature of domain walls.

5.3.2 Helical and chiral Majorana hinge modes for a finite-size sample

In this section, we show the dispersion of Majorana hinge modes for a cubic geometry in the absence of vortex lines. As shown in Figs. 5.6(a)-5.6(c), one can find that for the second-order topological superconducting phase with helical Majorana hinge modes, the eigenenergies of the helical Majorana hinge modes show a four-fold degeneracy (a factor two is from the helical nature, and the other factor two is from the equivalence between the top and bottom surfaces)

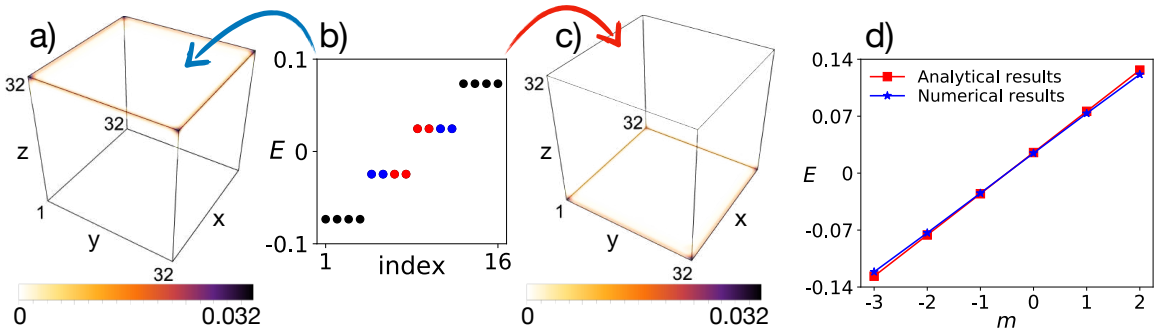

Figure 5.6: (Color online) The dispersions of helical Majorana hinge modes for a finite-size system in the absence of vortex lines. Common parameters are $t = 1$, $m_0 = 2.5$, $\lambda = 0.5$, $\mu = 0$, $\Delta_0 = -\Delta_s = 0.25$, and $\boldsymbol{h} = 0$. All directions take open boundary conditions and their lengths contain $L_x = L_y = L_z = 32$ lattice sites. (a)(c) The probability density profile of the hinge states. (b) The 16 energy eigenvalues closest to zero energy. No robust Majorana zero mode exists. (d) Comparison between the analytical (red line) and the numerical (blue line) small eigenvalues. The results show an excellent agreement.

and a regular jump. Most importantly, there is no zero-energy mode which is not due to finite size effects. Similar results are also found for the second-order topological superconducting phase with chiral Majorana hinge modes, as shown in Fig. 5.7.

To understand the absence of zero-energy modes (Majorana zero modes), one needs to note that the periodic motion of the helical or chiral Majorana modes along the hinges of the top and bottom z-normal surfaces will lead the momentum to be quantized discretely. Accordingly, the dispersion of the helical or chiral Majorana modes will follow $E = \pm v q_m$, with

$$q_m = (2m + \alpha)\frac{\pi}{L}, \tag{5.28}$$

where L denotes the total length of the closed path [here $L = 2(L_x + L_y) - 4$], m is an integer, and $\alpha = 0$ and 1 refer to periodic and antiperiodic boundary condition, respectively. According to Eq. (5.27), we further have $v = 2\lambda$ for the helical case (we do not have an accurate analytical expression of v for the chiral case since the previous analytical treatment loses its accuracy when the Zeeman field is strong). Apparently, there exists a big difference between the two kinds of boundary conditions. For the periodical boundary condition, it is readily seen that q_m can take zero value ($q_0 = 0$), so the helical or chiral hinges modes will contain Majorana zero modes. In contrast, for the antiperiodic boundary condition, it is readily seen that q_m cannot take zero value, so there is no Majorana zero mode for the helical or chiral hinge modes. The absence of Majorana zero modes in Fig. 5.6(b) and Fig. 5.7(b) thus indicates that these propagating Majorana modes take an antiperiodic boundary condition. As shown in Fig. 5.6(d), the analytical results for the helical case, *i.e.*, $E = \pm 2\lambda(2m + 1)\pi/L$, agree very well with the numerical results shown in Fig. 5.6(b), demonstrating the correctness of our analytical analysis. The antiperiodic boundary condition of the helical

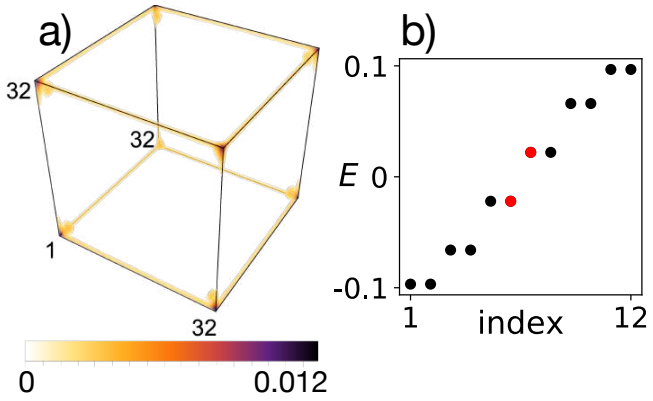

Figure 5.7: (Color online) The dispersions of chiral Majorana hinge modes for a finite-size system in the absence of vortex lines. Common parameters are $t = 1$, $m_0 = 2.5$, $\lambda = 0.5$, $\mu = 0$, $\Delta_0 = -\Delta_s = 0.25$, and $\boldsymbol{h} = (h_x, h_y, h_z) = (0, 0, 0.3)$. All directions take open boundary conditions and their lengths contain $L_x = L_y = L_z = 32$ lattice sites. (a) The probability density profile of the hinge states. (b) The 12 energy eigenvalues closest to zero energy. No robust Majorana zero mode exists.

or chiral Majorana modes can be understood from the fact that these low-energy Majorana modes originate from the gapless Dirac surface states which has an intrinsic π Berry phase.

Interestingly, when a π-flux vortex line is inserted along the z direction, the closed path that the helical or chiral Majorana modes propagate along will enclose the vortex line, so the helical or chiral Majorana modes will pick up an additional π phase from the π-flux vortex line. Accordingly, the boundary condition of these propagating Majorana modes will change from an antiperiodic one to a periodic one. Then the helical or chiral Majorana modes will contain Majorana zero modes according to our analysis.

5.4 Interplay of second-order topology and vortex lines

In this section, we focus on the non-uniform case with vortex lines, so we will study an inhomogeneous iron-based superconductor. As the vortex line breaks the time-reversal symmetry but preserves the translational symmetry in the z direction, the system can be viewed as a quasi-1D superconductor belonging to the class D of the Atland-Zirnbauer classification [273, 274]. Accordingly, whether Majorana zero modes exist or not is characterized by the $\mathbb{Z}_2$ invariant [91, 114],

$$\nu = \mathrm{sgn}\{\mathrm{Pf}[H_{\mathrm{M}}(0)]\} \cdot \mathrm{sgn}\{\mathrm{Pf}[H_{\mathrm{M}}(\pi)]\}, \tag{5.29}$$

where $H_{\mathrm{M}}(k_z)$ represents the Hamiltonian in the Majorana representation and "Pf" is a shorthand notation of Pfaffian (see Appendix D for more details). Here, $\nu = -1$ and $+1$ indicate the presence and absence of one robust Majorana zero mode at each end of the

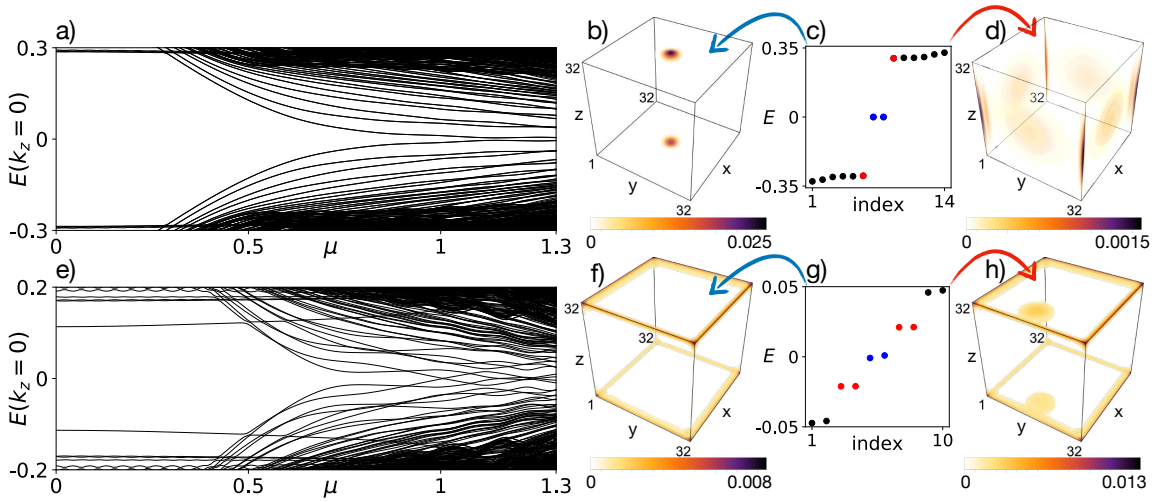

Figure 5.8: (Color online) The evolution of energy dispersions at $k_z = 0$ with respect to the doping level and the locations of Majorana zero modes. (a)-(d) and (e)-(h) show the results without and with second-order topology, respectively. For the parameters considered, the normal state becomes metallic when $\mu > 0.5$, and we restrict $\mu < 1.3$ to guarantee the vortex-free bulk spectrum to be gapped. Because the conduction bands of the normal state have two degenerate minima at the two time-reversal invariant momenta $(0, \pi, 0)$ and $(\pi, 0, 0)$, (a) shows that the lowest excitation spectrum has a double degeneracy (read from data) when the vortex line is located at the center of the system. As the energy gap of the vortex line remains non-zero in (a), we have $\nu = -1$ for $0 < \mu < 1.3$. In (c), the two blue dots correspond to two robust Majorana zero modes, and the two red dots correspond to two high energy modes. (b) shows that the probability density of the Majorana zero modes is strongly localized at the ends of the vortex line, and (d) shows that the two high energy modes correspond to gapped surface states. In (e), the vortex line is centered at $(x_c, y_c) = (6.01, 16.01)$ so that it is very close to the hinges of the x-normal surface. The accidental double degeneracy of the lowest excitation spectrum shown in (a) is lifted since the position of the vortex line does not preserve the C_4 rotation symmetry of the uniform Hamiltonian. One can find from (e) that the gap closes at $\mu \approx 1$, which signals a vortex phase transition with ν changing from -1 to 1. In (g), the two blue dots also correspond to two robust Majorana zero modes (not at exact zero energy due to finite-size effects). (f) shows that the probability density of the robust Majorana zero modes is localized on the hinges. (h) the probability density of the four modes in red suggests that they originate from the hybridization of the helical Majorana hinge modes and vortex-end Majorana zero modes. Common parameters are $t = 1$, $m_0 = 2.5$, $\lambda = 0.5$, $\boldsymbol{h} = 0$, $\xi = 4$, and $\Delta_0 = 0.25$. In (a)-(d), $\Delta_s = 0.25$ and in (e)-(h), $\Delta_s = -0.25$. In (a)(e), $L_x = L_y = 32$ lattice sites, and in (b)-(d) and (f)-(h), $\mu = 0$, $L_x = L_y = L_z = 32$ lattice sites.

quasi-1D superconductor, respectively. The expression of the $\mathbb{Z}_2$ invariant suggests that only the band information at the two time-reversal invariant momenta is important.

We first study the configuration in Fig. 5.3(a) for which the band topology of the homogeneous case is trivial. Since the band inversion takes place at the Γ point, we only need to focus on the dispersion at $k_z = 0$ in the weakly doped regime. From Fig. 5.8(a), we find that the vortex line has a finite energy gap and the $\mathbb{Z}_2$ invariant is $\nu = -1$ in the weakly doped

regime[1]. When all sides of the sample are open, we find, as expected, that each end of the vortex line binds one robust Majorana zero mode, as shown in Figs. 5.8(b)-5.8(d).

Next we study the configuration in Fig. 5.3(e) for which the second-order topology is nontrivial. We first consider that the Zeeman field is negligible, which can be a good approximation for materials with small g factor. From a local surface perspective, the effects of on-site and extended s-wave pairings are equivalent, namely, both of them induce a Dirac mass to gap the surface Dirac cones. Since the Dirac mass is nearly uniform far away from the hinges, regardless of whether the second-order topology is trivial or nontrivial, then a π-flux vortex far away from the hinges will also bind one robust Majorana zero mode at its core in the weakly-doped regime even when the second-order topology is nontrivial. However, this picture will dramatically change when the vortex line is moved close to the hinges. To see this, we consider that the vortex line is very close to the x-normal boundary [see Fig. 5.1(b)]. The results in Fig. 5.8(e) indicate that the dispersion of the vortex line remains gapped in the weakly doped regime. However, the results in Figs. 5.8(f)-5.8(h) indicate that the Majorana zero modes are no longer localized at the vortex ends, instead they are localized along the hinges with helical Majorana modes.

To show that the formula in Eq. (5.29) indeed faithfully characterizes the topological property, here we provide a concrete example with a vortex phase transition and show that the $\mathbb{Z}_2$ invariant ν predicts this topological phase transition precisely. As is known, a change of the topological invariant is associated with the closure of the energy gap. Because here the topological invariant ν is of $\mathbb{Z}_2$ nature, if the gap closure occurs between two bands with double degeneracy [which is the situation shown in Fig. 5.8(a)], then such gap closures do not change ν. As the degeneracy of bands requires some symmetry protection [it is a C_{4z} rotation symmetry in Fig. 5.8(a)], in order to avoid such issues, here we consider lifting the C_{4z} rotation symmetry of the Hamiltonian in Eq. (5.1) by setting the strengths of the spin-orbit coupling terms to be anisotropic, *i.e.*, $2\lambda \sum_{i=x,y,z} \sin k_i \sigma_x s_i \to 2 \sum_{i=x,y,z} \lambda_i \sin k_i \sigma_x s_i$, with $\lambda_x \neq \lambda_y$. To be specific, we also consider that the band inversion occurs at the $k_z = 0$ plane, so that the vortex phase transition is associated with the gap closure at $k_z = 0$. As shown in Fig. 5.9(a), the energy dispersions at $k_z = 0$ show a gap closure at $\mu_c = 0.85$ for the set of parameters we consider.

By contrast, the energy dispersions at $k_z = \pi$ are found to remain gapped for the range of doping level we consider, as shown in Fig. 5.9(b). A combination of Figs. 5.9(a) and 5.9(b) indicates that a vortex phase transition should occur at μ_c. Figs. 5.9(c) and 5.9(d) show respectively the corresponding evolution of $\mathrm{sgn}\{\mathrm{Pf}[H_M(0)]\}$ and $\mathrm{sgn}\{\mathrm{Pf}[H_M(\pi)]\}$. One can see that $\mathrm{sgn}\{\mathrm{Pf}[H_M(0)]\}$ jumps from -1 to 1 exactly at μ_c where the energy dispersions at $k_z = 0$ get closed. Meanwhile, one can see that $\mathrm{sgn}\{\mathrm{Pf}[H_M(\pi)]\}$ keeps its value 1 for the range of μ considered, agreeing with the fact that the band inversion does not occur at the $k_z = \pi$ plane and the energy dispersions remain gapped as shown in Fig. 5.9(b). A combination of

[1] We have only shown $\mu > 0$ as the result is symmetric about $\mu = 0$.

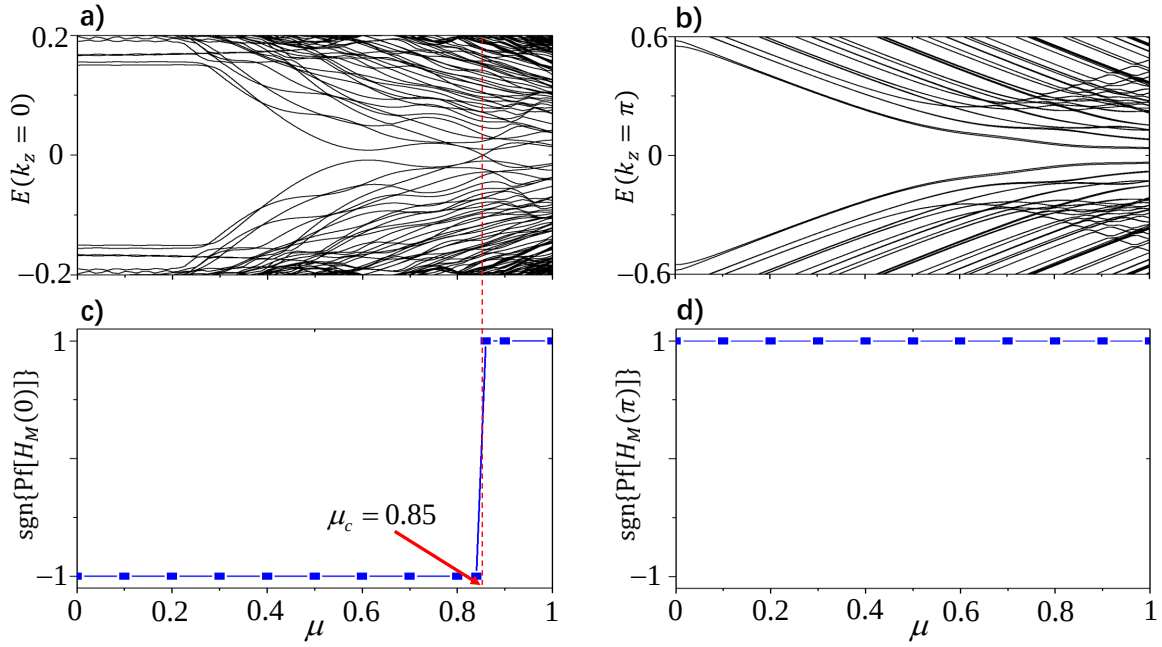

Figure 5.9: (Color online) Vortex phase transitions characterized by the $\mathbb{Z}_2$ invariant. (a) The evolution of the energy dispersions at $k_z = 0$ with respect to the doping level μ. A gap closure occurs at $\mu_c = 0.85$ for the parameters considered. (b) The evolution of the energy dispersions at $k_z = \pi$ with respect to the doping level μ. The energy dispersion remains gapped for the range of μ that we consider here. (c) sgn{Pf[$H_M(0)$]} jumps from -1 to 1 when μ goes across μ_c. (d) sgn{Pf[$H_M(\pi)$]} retains the value 1. A combination of (c) and (d) indicates that the $\mathbb{Z}_2$ invariant ν changes from -1 for $\mu < \mu_c$ to 1 for $\mu > \mu_c$. Common parameters are: $t = 1$, $m_0 = 2.5$, $\lambda_x = 0.25$, $\lambda_y = \lambda_z = 0.5$, $\Delta_0 = -\Delta_s = 0.25$, $\boldsymbol{h} = 0$, $\xi = 4$, and the vortex line is located at the center of the xy plane. The lengths along the x and y directions contain $L_x = L_y = 20$ lattice sites. (a) and (c) share the same horizontal coordinates, and (b) and (d) share the same horizontal coordinates.

Figs. 5.9(c) and 5.9(d) indicates that the $\mathbb{Z}_2$ invariant ν jumps from -1 for $\mu < \mu_c$ to 1 for $\mu > \mu_c$, demonstrating that the $\mathbb{Z}_2$ invariant given in Eq. (5.29) can precisely predict the vortex phase transition.

The underlying reason for this transfer of robust Majorana zero modes from the vortex ends to the hinges is as follows. When the helical Majorana modes go along the hinges of the z-normal surfaces, they will pick up a π phase from the π-flux vortex line after one circle, which will accordingly change their boundary conditions. It is known that the linear dispersion of the helical Majorana modes for a finite-size system should follow $E = \pm v q_m$, with v a constant and the discrete momentum q_m determined by the boundary condition $e^{iq_m L} = 1$ (periodic, $q_m = 2m\pi/L$) or -1 [antiperiodic, $q_m = (2m+1)\pi/L$], where m is an integer, and L is the total length of the closed path along the hinges. Notably, here we find that the π-flux vortex line will change the boundary condition from an antiperiodic one to

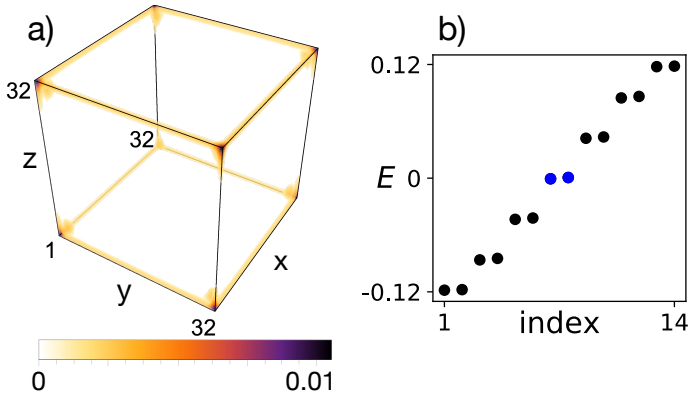

Figure 5.10: (Color online) (a) The probability density of Majorana zero modes [the two blue dots in (b)] for a second-order topological superconductor with chiral Majorana hinge modes are also localized on the hinges rather than at the vortex ends. We take $t = 1$, $m_0 = 2.5$, $\lambda = 0.5$, $\xi = 4$, $\boldsymbol{h} = (h_x, h_y, h_z) = (0, 0, 0.3)$, $\mu = 0$, $\Delta_0 = -\Delta_s = 0.25$, and $L_x = L_y = L_z = 32$ lattice sites.

a periodic one. As a result, each pair of helical Majorana modes will contain two Majorana zero modes. Let us focus on the top z-normal surface. When the vortex line is moved close to the hinges, the Majorana zero mode at the top vortex end will hybridize with the two Majorana zero modes on the hinges and then get split. Nevertheless, the $\mathbb{Z}_2$ nature of the Majorana zero modes guarantees that one of the three will remain robust[2], which turns out to be mostly localized along the hinges.

Finally, we take the Zeeman field into account and study the situation with chiral Majorana hinge modes. For the z-directional Zeeman field, we find that the condition for the realization of a chiral second-order topological superconductor with chiral Majorana hinge modes is given by Eq. (5.15) while maintaining a finite bulk gap (see Appendix E for more details). In this regime, we find that the vortex line also does not bind robust Majorana zero modes, and the Majorana zero modes also appear on the hinges, as shown in Figs. 5.10(a) and 5.10(b). Notably, the trivialization of the vortex line in this regime does not depend on the distance away from the chiral Majorana modes Notably, the trivialization of the vortex line in this regime does not depend on the distance away from the chiral Majorana modes as well as the existence of other vortex lines. This can be intuitively understood by noting that the vortex-end Majorana zero modes must originate from certain gapless modes in the normal state, so the prerequisite is that the chemical potential crosses the surface bands. As the z-directional Zeeman field opens a gap of size $2|h_z|$ to the Dirac surface states in the normal state, the condition for the chemical potential to cross the surface bands is $|\mu| > |h_z|$, which is apparently not compatible with the condition for the chiral second-order topologi-

[2]The energy of one of the three modes will be pinned at zero if the coupling between the top and bottom surfaces is negligible.

cal superconductor. When h_z is finite and the chemical potential crosses the surface bands ($|\mu| > |h_z|$), the scenario is found to be similar to the one at the limit $h_z = 0$. That is, whether the vortex line binds robust Majorana zero modes or not depends on its position to the hinges which harbor counter-propagating gapless Majorana modes. It is worth noting that, in the regime with chiral Majorana hinge modes, the presence of Majorana zero modes on the hinges is similar to the helical case. That is, an odd number of π fluxes can change the boundary condition of the chiral Majorana hinge modes, consequently allowing the presence of Majorana zero modes [200].

5.4.1 Vortex lines far away from the helical Majorana hinge modes

Based on a local perspective of surface Dirac mass, we have argued that when the vortex line is far away from the hinges, the existence of helical Majorana modes on the hinges should have negligible impact on the vortex line, so the vortex line will host robust Majorana zero modes at its ends in the weakly doped regime. In this section, we provide numerical results to support this argument. In Fig. 5.11, we show the result for a cubic lattice with size $L_x = L_y = L_z = 32$ lattice sites. A z-directional π-flux vortex line is inserted at the center of the xy plane. According to our previous analysis, the six modes close to zero energy in Fig. 5.11(b) correspond to two vortex-end Majorana zero modes and four hinge Majorana zero modes. However, because of the finite-size effect, the modes within the top or bottom surface will hybridize with each other, and the modes of the two surfaces also have finite coupling, so all modes are split away from the zero energy (if the length along the z direction increases to infinity, then because the particle-hole symmetry of the superconductor forces the Majorana zero modes to be created or annihilated in pairs, two of the modes will take

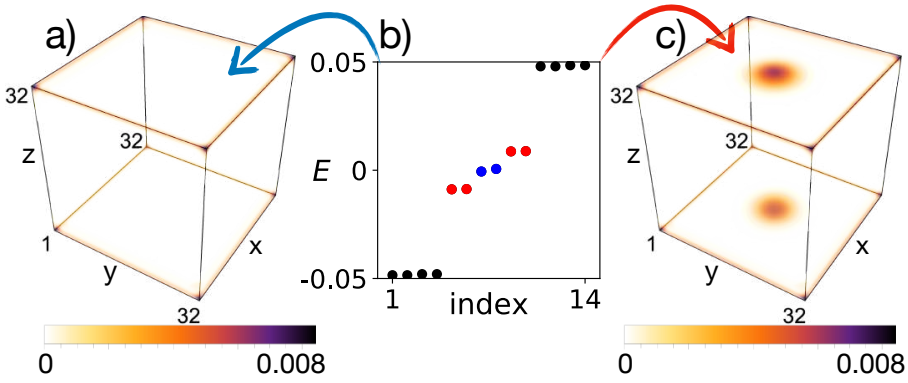

Figure 5.11: (Color online) Common parameters are $t = 1$, $m_0 = 2.5$, $\lambda = 0.5$, $\mu = 0$, $\xi = 4$, $\boldsymbol{h} = 0$, and $\Delta_0 = -\Delta_s = 0.25$. All directions take open boundary conditions and their lengths contain $L_x = L_y = L_z = 32$ lattice sites. The vortex line is at the center of xy-plane.

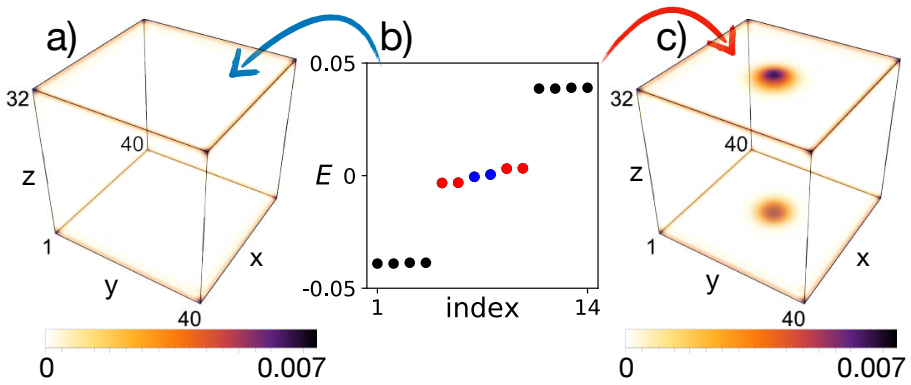

Figure 5.12: (Color online) Common parameters are $t = 1$, $m_0 = 2.5$, $\lambda = 0.5$, $\mu = 0$, $\xi = 4$, $\boldsymbol{h} = 0$, and $\Delta_0 = -\Delta_s = 0.25$. All directions take open boundary conditions and their lengths contain $L_x = L_y = 40$, and $L_z = 32$ lattice sites. The vortex line is at the center of xy plane and in the z direction.

exactly zero energy, even though the system size of the xy plane is finite). To show that the increase of the distance between the vortex line and the helical Majorana modes will decrease their hybridization, we further consider a cubic lattice with size $L_x = L_y = 40$ and $L_z = 32$ lattice sites, with the result shown in Fig. 5.12. Compared to Fig. 5.11, it is readily seen that the energy of the four red modes approaches zero energy. As these four modes correspond to two hinge modes and two vortex-end modes [see Fig. 5.11(c) and Fig. 5.12(c)], the decrease of their energy splitting indicates that the hybridization of the vortex-end and hinge Majorana zero modes decreases with the increase of the distance between the vortex line and the hinges. Therefore, it is justified to expect that for vortex lines far away from the hinges, the vortex-end bound states will take exactly zero energy, restoring their exact self-conjugate ($\gamma = \gamma^\dagger$) nature.

5.4.2 Vortex lines close to the hinges without gapless hinge modes

We have shown when a topological vortex line is moved close to the hinges with helical Majorana modes, their hybridization will trivialize the vortex line. For comparison, in this section we consider that the vortex line is also moved close to the hinges, but the hinges do not host helical Majorana modes. Similar to Fig. 5.8(e), we find that the accidental double degeneracy of the lowest-energy spectrum exhibited in the spectrum of Fig. 5.8(a) is lifted when the vortex line is no longer located at the center of the system since the C_{4z} rotation symmetry is broken, as shown in Fig. 5.13(a). Nevertheless, this lifting of degeneracy does not affect the vortex line topology in the weakly doped regime since the dispersion of the vortex line remains gapped. As expected, in the weakly doped regime, the two lowest-energy modes are strongly localized at the vortex ends, as shown in Figs. 5.13(b)-5.13(d). These

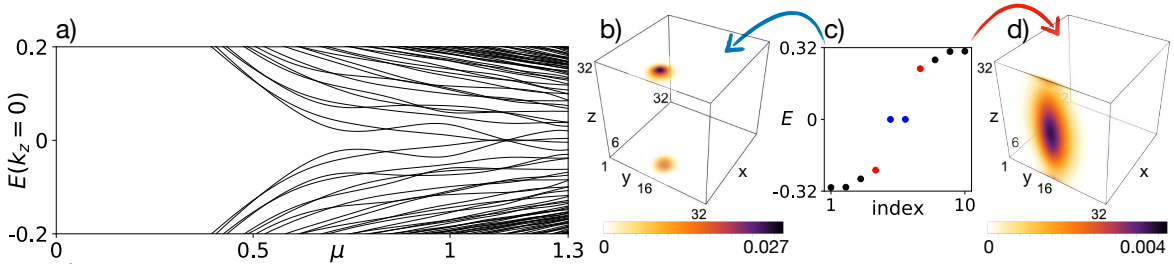

Figure 5.13: (Color online) Common parameters are $t = 1$, $m_0 = 2.5$, $\lambda = 0.5$, $\mu = 0$, $\xi = 4$, $\boldsymbol{h} = 0$, and $\Delta_0 = \Delta_s = 0.25$. All directions take open boundary conditions and their lengths contain $L_x = L_y = L_z = 32$ lattice sites. The vortex line is at $(x_c, y_c) = (6.01, 16.01)$ point and in the z direction.

results demonstrate that the trivialization of the vortex line for the case with helical Majorana modes does indeed originate from their hybridization.

5.4.3 Vortex lines in the x direction

So far, we have restricted ourselves to vortex lines generated in the z direction in order to be directly comparable with the experiments. Here we provide the results for vortex lines generated in the x direction for completeness. It is worth noting that because the results for vortex lines generated in the y direction are the same due to the C_{4z} rotation symmetry, we will not show them to avoid repetition.

As the vortex line is forced to be trivial when the Zeeman field dominates over the superconductivity, here we focus on the case with vanishing Zeeman field. Similar to the z-directional vortex line, a local surface perspective suggests that an x-directional vortex line will harbor Majorana zero modes at its ends when its position is far away from the hinges and the doping level is low. Nevertheless, there exists a qualitative difference between the x-directional and z-directional vortex lines. The difference is that for an x-directional vortex line, the closed path that the helical Majorana modes propagate along does not enclose the vortex line. As a result, the helical Majorana modes will not pick up an additional π phase from the vortex line after going around the hinges for one circle. In other words, the helical Majorana modes will keep their antiperiodic boundary condition when the vortex line is generated along the x direction, and so the helical Majorana modes will not contain zero-energy modes. The absence of Majorana zero modes on the hinges indicates that the vortex-end Majorana zero modes cannot directly couple with the helical Majorana hinge modes due to the constraint from the intrinsic particle-hole symmetry of superconductors (a Majorana zero mode can get split only when it couples with another Majorana zero mode). Anyway, because the helical Majorana modes provide some gapless channels which connect the two x-normal surfaces, they will enhance the coupling of the two Majorana zero modes at the vortex ends when the vortex line is moved close to the hinges with helical Majorana

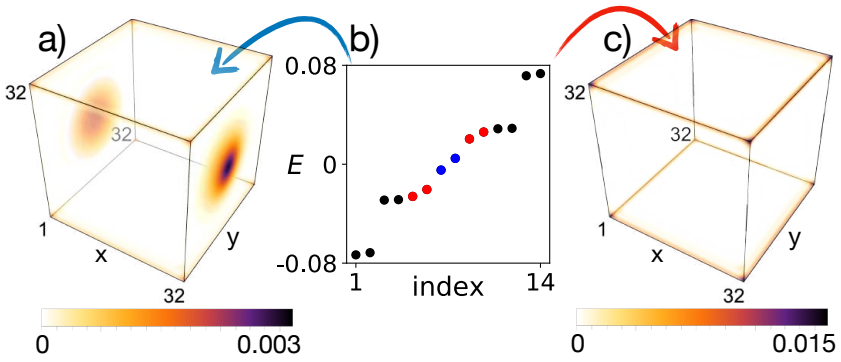

Figure 5.14: (Color online) Common parameters are $t = 1$, $m_0 = 2.5$, $\lambda = 0.5$, $\mu = 0$, $\xi = 4$, $\Delta_0 = -\Delta_s = 0.25$, and $\boldsymbol{h} = 0$. All directions take open boundary conditions and their lengths contain $L_x = L_y = L_z = 32$ lattice sites. (a) The wave functions of the two lowest-energy modes [the two blue dots shown in (b)] are mostly localized at the vortex ends. (b) The 14 energy eigenvalues closest to zero energy. (c) The wave functions of the four finite-energy modes in red color are localized along the hinges, indicating that they correspond to the helical Majorana modes.

modes. This enhancement of coupling can also split the vortex-end Majorana zero modes, but now there will be no robust Majorana zero mode on the hinges. In Fig. 5.14, we show the results for a geometry with size $L_x = L_y = L_z = 32$ lattice sites. Fig. 5.14(a) shows that the two lowest-energy modes have most weight at the vortex ends, suggesting the vortex line to be topological. Compared to Fig. 5.11(b) or Fig. 5.12(b), the pattern of the near-zero-energy modes in Fig. 5.14(b) indicates that the helical Majorana modes keep the antiperiodic boundary condition when the vortex line is generated in the x direction.

5.5 Discussions and Conclusions

Let us now apply our findings to explain the coexistence of topological and trivial vortex lines observed in experiments. On the experimental side, strong signatures of helical Majorana modes have been observed in $FeTe_{0.55}Se_{0.45}$ not only at the hinges [271], but also at certain crystalline domain walls [229]. According to our theory, when the positions of the generated vortex lines are close to these helical Majorana modes, their hybridizations can trivialize the vortex-line topology, which accordingly provides an explanation for the existence of trivial vortex lines even in the weak Zeeman field regime. Moreover, some of the topological vortex lines are observed in experiments to be trivialized with the increase of magnetic field [275]. Since the positions of these vortex lines do not change, according to our theory, their trivialization is potentially caused by a change of the surface Dirac-mass nature.

It is noteworthy that the superconducting pairing gap has been observed to display considerable inhomogeneity on the surface of $FeTe_{0.55}Se_{0.45}$, using scanning tunneling microscopy

[229, 276]. Meanwhile, the chemical potential also inevitably displays certain fluctuations in real space. Therefore, the increase of magnetic field will increase the regions dominated by the Zeeman field, which will consequently increase the ratio of trivial vortex lines, agreeing with the experiment observation.

In conclusion, we have developed a mechanism to explain the peculiar coexistence and evolution of topological and trivial vortex lines in iron-based superconductors, hopefully advance our understanding of the topological physics in these materials.

Chapter 6

Summary and Future Directions

In summary, the aim of this thesis was to study the Majorna zero modes in the context of higher-order topological superconductivity. In particular, we considered high-temperature superconductivity in cuprates in both chapters 3 and 4, and iron-based superconductors in chapter 5.

After a general overview and discussion about the theoretical tools in both chapters 1 and 2, we showed that confining a second-order topological superconductor with a harmonic potential leads to a proliferation of Majorana corner modes in chapter 3. As a consequence, this results in the formation of Majorana corner flat bands which have a fundamentally different origin from that of the conventional mechanism. This is due to the fact that they arise solely from the one-dimensional gapped boundary states of the hybrid system that become gapless without the bulk gap closing under the increase of the trapping potential magnitude. The Majorana corner states are found to be robust against the strength of the harmonic trap and the transition from Majorana corner states to Majorana flat bands is merely a smooth crossover. As a harmonic trap can potentially be realized in heterostructures, this proposal paves a way to observe these Majorana corner flat bands in an experimental context.

In chapter 4, we investigated the superconducting pairing instability of the two-dimensional extended Hubbard model with both Rashba and Dresselhaus spin-orbit coupling within the mean-field level at both zero and finite temperature. We find that both first- and second-order time-reversal symmetry breaking topological gapped phases can be achieved under appropriate parameters and temperature regimes due to the presence of a favored even-parity $s + id$ -wave pairing even in the absence of an external magnetic field or intrinsic magnetism. This results in two branches of chiral Majorana edge states on each edge or a single zero-energy Majorana corner state at each corner of the sample. Interestingly, we also find that not only does tuning the doping level lead to a direct topological phase transition between these two distinct topological gapped phases, but also using the temperature as a highly controllable

and reversible tuning knob leads to different direct temperature-driven topological phase transitions between gapped and gapless topological superconducting phases. Our findings suggest new possibilities in interacting spin-orbit coupled systems by unifying both first- and higher-order topological superconductors in a simple but realistic microscopic model.

In chapter 5, we study the potential impact of second-order topology on the vortex lines in iron-based superconductors in both weak and strong Zeeman field regimes. Recently, experimental evidence of Majorana zero modes in vortices has been observed in iron-based superconductors with band inversion near the Fermi level. It is known that iron-based superconductors with band inversion and $s_{\pm}$-wave pairing can give rise to second-order topological superconductivity, manifested by the presence of helical or chiral Majorana hinge states in three dimensions. In the weak Zeeman field regime, we find that vortex lines far away from the hinges are topologically nontrivial in the weakly doped regime, regardless of whether the second-order topology is present or not. However, when the superconductor falls into the second-order topological phase and a topological vortex line is moved close to the helical Majorana hinge states, we find that their hybridization will trivialize the vortex line and transfer the Majorana zero modes to the hinges. Furthermore, when the Zeeman field is large enough, we find that the helical Majorana hinge states are changed into chiral Majorana hinge modes and thus a chiral second-order topological superconducting phase is realized. In this regime, the vortex lines are always topologically trivial, no matter how far away they are from the chiral Majorana hinge modes. By incorporating a realistic assumption of inhomogeneous superconductivity, our findings can explain the recent experimental observation of the peculiar coexistence and evolution of topologically nontrivial and trivial vortex lines in iron-based superconductors.

As an extension of the studies in chapter 3, it would be interesting to find a topological invariant in real space, which characterizes Majorana corner flat bands, by incorporating Chern marker [277]. Another possible extension is considering other superconducting pairing symmetries such as extended s-wave pairing in the presence of a harmonic potential. In chapter 4, it would be promising to investigate the effects of external magnetic field on the different phases inside the phase diagram. An in-plane magnetic field, could result in the Fulde-Ferrell-Larkin-Ovchinnikov (FFLO) phase [278, 279] or Cooper pairs with finite momentum. Also, considering odd-parity pairing terms inside the Hamiltonian and extending the results seems interesting. For future study on chapter 5, it would be interesting to consider three-dimensional weak topological insulators.

There is a lot more to learn. We hope to continue the investigations described in this thesis to uncover more and more mysteries hidden in topological superconductors.

Bibliography

[1] VL Berezinskii. Destruction of long-range order in one-dimensional and two-dimensional systems having a continuous symmetry group i. classical systems. *Sov. Phys. JETP*, 32(3):493–500, 1971.

[2] VL Berezinskii. Destruction of long-range order in one-dimensional and two-dimensional systems possessing a continuous symmetry group. ii. quantum systems. *Sov. Phys. JETP*, 34(3):610–616, 1972.

[3] John Michael Kosterlitz and David James Thouless. Ordering, metastability and phase transitions in two-dimensional systems. *Journal of Physics C: Solid State Physics*, 6(7):1181, 1973.

[4] K. v. Klitzing, G. Dorda, and M. Pepper. New method for high-accuracy determination of the fine-structure constant based on quantized Hall resistance. *Phys. Rev. Lett.*, 45:494–497, Aug 1980.

[5] JP Eisenstein and HL Stormer. The fractional quantum Hall effect. *Science*, 248(4962):1510–1516, 1990.

[6] Klaus von Klitzing. The quantized Hall effect. *Rev. Mod. Phys.*, 58:519–531, Jul 1986.

[7] D. J. Thouless, M. Kohmoto, M. P. Nightingale, and M. den Nijs. Quantized Hall conductance in a two-dimensional periodic potential. *Phys. Rev. Lett.*, 49:405–408, Aug 1982.

[8] F. D. M. Haldane. Model for a quantum Hall effect without Landau levels: Condensed-matter realization of the "parity anomaly". *Phys. Rev. Lett.*, 61:2015–2018, Oct 1988.

[9] David Hsieh, Yuqi Xia, Dong Qian, L Wray, JH Dil, Fedorov Meier, J Osterwalder, L Patthey, JG Checkelsky, Nai Phuan Ong, et al. A tunable topological insulator in the spin helical Dirac transport regime. *Nature*, 460(7259):1101–1105, 2009.

[10] Andre K Geim and Konstantin S Novoselov. The rise of graphene. In *Nanoscience and technology: a collection of reviews from nature journals*, pages 11–19. World Scientific, 2010.

[11] C. L. Kane and E. J. Mele. $\mathbb{Z}_2$ topological order and the quantum spin hall effect. *Phys. Rev. Lett.*, 95:146802, Sep 2005.

[12] C. L. Kane and E. J. Mele. Quantum spin Hall effect in graphene. *Phys. Rev. Lett.*, 95:226801, Nov 2005.

[13] Yugui Yao, Fei Ye, Xiao-Liang Qi, Shou-Cheng Zhang, and Zhong Fang. Spin-orbit gap of graphene: First-principles calculations. *Phys. Rev. B*, 75:041401, Jan 2007.

[14] Shuichi Murakami, Naoto Nagaosa, and Shou-Cheng Zhang. Dissipationless quantum spin current at room temperature. *Science*, 301(5638):1348–1351, 2003.

[15] Jairo Sinova, Dimitrie Culcer, Q. Niu, N. A. Sinitsyn, T. Jungwirth, and A. H. MacDonald. Universal intrinsic spin Hall effect. *Phys. Rev. Lett.*, 92:126603, Mar 2004.

[16] Shuichi Murakami, Naoto Nagaosa, and Shou-Cheng Zhang. Spin-Hall insulator. *Phys. Rev. Lett.*, 93:156804, Oct 2004.

[17] B. Andrei Bernevig and Shou-Cheng Zhang. Quantum spin Hall effect. *Phys. Rev. Lett.*, 96:106802, Mar 2006.

[18] B Andrei Bernevig, Taylor L Hughes, and Shou-Cheng Zhang. Quantum spin Hall effect and topological phase transition in HgTe quantum wells. *Science*, 314(5806):1757–1761, 2006.

[19] Markus König, Steffen Wiedmann, Christoph Brüne, Andreas Roth, Hartmut Buhmann, Laurens W Molenkamp, Xiao-Liang Qi, and Shou-Cheng Zhang. Quantum spin Hall insulator state in HgTe quantum wells. *Science*, 318(5851):766–770, 2007.

[20] Chaoxing Liu, Taylor L. Hughes, Xiao-Liang Qi, Kang Wang, and Shou-Cheng Zhang. Quantum spin Hall effect in inverted type-II semiconductors. *Phys. Rev. Lett.*, 100:236601, Jun 2008.

[21] Ivan Knez, Rui-Rui Du, and Gerard Sullivan. Evidence for helical edge modes in inverted InAs/GaSb quantum wells. *Phys. Rev. Lett.*, 107:136603, Sep 2011.

[22] Ivan Knez, Charles T. Rettner, See-Hun Yang, Stuart S. P. Parkin, Lingjie Du, Rui-Rui Du, and Gerard Sullivan. Observation of edge transport in the disordered regime of topologically insulating InAs/GaSb quantum wells. *Phys. Rev. Lett.*, 112:026602, Jan 2014.

[23] Lingjie Du, Ivan Knez, Gerard Sullivan, and Rui-Rui Du. Robust helical edge transport in gated InAs/GaSb bilayers. *Phys. Rev. Lett.*, 114:096802, Mar 2015.

[24] Liang Fu, C. L. Kane, and E. J. Mele. Topological insulators in three dimensions. *Phys. Rev. Lett.*, 98:106803, Mar 2007.

[25] J. E. Moore and L. Balents. Topological invariants of time-reversal-invariant band structures. *Phys. Rev. B*, 75:121306, Mar 2007.

[26] David Hsieh, Dong Qian, Lewis Wray, Yiman Xia, Yew San Hor, Robert Joseph Cava, and M Zahid Hasan. A topological Dirac insulator in a quantum spin Hall phase. *Nature*, 452(7190):970–974, 2008.

[27] YL Chen, James G Analytis, J-H Chu, ZK Liu, S-K Mo, Xiao-Liang Qi, HJ Zhang, DH Lu, Xi Dai, Zhong Fang, et al. Experimental realization of a three-dimensional topological insulator, Bi_2Te_3. *science*, 325(5937):178–181, 2009.

[28] David Hsieh, Yuqi Xia, L Wray, Dong Qian, Arijeet Pal, JH Dil, J Osterwalder, F Meier, G Bihlmayer, CL Kane, et al. Observation of unconventional quantum spin textures in topological insulators. *Science*, 323(5916):919–922, 2009.

[29] Yuqi Xia, Dong Qian, David Hsieh, L Wray, Arijeet Pal, Hsin Lin, Arun Bansil, DHYS Grauer, Yew San Hor, Robert Joseph Cava, et al. Observation of a large-gap topological-insulator class with a single Dirac cone on the surface. *Nature physics*, 5(6):398–402, 2009.

[30] Barry Bradlyn, L Elcoro, Jennifer Cano, MG Vergniory, Zhijun Wang, C Felser, MI Aroyo, and B Andrei Bernevig. Topological quantum chemistry. *Nature*, 547(7663):298–305, 2017.

[31] Elizabeth Gibney. Thousands of exotic 'topological' materials discovered through sweeping search. *Nature*, 560(7717):151–153, 2018.

[32] Hoi Chun Po, Ashvin Vishwanath, and Haruki Watanabe. Symmetry-based indicators of band topology in the 230 space groups. *Nature communications*, 8(1):1–9, 2017.

[33] Philippe Andre Martin and François Rothen. *Many-body problems and quantum field theory: an introduction*. Springer Science & Business Media, 2013.

[34] Xiao-Liang Qi and Shou-Cheng Zhang. Topological insulators and superconductors. *Reviews of Modern Physics*, 83(4):1057, 2011.

[35] Masatoshi Sato and Yoichi Ando. Topological superconductors: a review. *Reports on Progress in Physics*, 80(7):076501, 2017.

[36] Jason Alicea. New directions in the pursuit of Majorana fermions in solid state systems. *Reports on progress in physics*, 75(7):076501, 2012.

[37] Steven R. Elliott and Marcel Franz. Colloquium: Majorana fermions in nuclear, particle, and solid-state physics. *Rev. Mod. Phys.*, 87:137–163, Feb 2015.

[38] Chetan Nayak, Steven H. Simon, Ady Stern, Michael Freedman, and Sankar Das Sarma. Non-Abelian anyons and topological quantum computation. *Rev. Mod. Phys.*, 80:1083–1159, Sep 2008.

[39] Biao Lian, Xiao-Qi Sun, Abolhassan Vaezi, Xiao-Liang Qi, and Shou-Cheng Zhang. Topological quantum computation based on chiral Majorana fermions. *Proceedings of the National Academy of Sciences*, 115(43):10938–10942, 2018.

[40] Martin R Zirnbauer. Riemannian symmetric superspaces and their origin in random-matrix theory. *Journal of Mathematical Physics*, 37(10):4986–5018, 1996.

[41] Alexander Altland and Martin R. Zirnbauer. Nonstandard symmetry classes in mesoscopic normal-superconducting hybrid structures. *Phys. Rev. B*, 55:1142–1161, Jan 1997.

[42] Shinsei Ryu, Andreas P Schnyder, Akira Furusaki, and Andreas WW Ludwig. Topological insulators and superconductors: tenfold way and dimensional hierarchy. *New Journal of Physics*, 12(6):065010, 2010.

[43] Alexei Kitaev. Periodic table for topological insulators and superconductors. 1134(1):22–30, 2009.

[44] Liang Fu. Topological crystalline insulators. *Phys. Rev. Lett.*, 106:106802, Mar 2011.

[45] P Dziawa, BJ Kowalski, K Dybko, R Buczko, A Szczerbakow, M Szot, E Łusakowska, T Balasubramanian, Bastian M Wojek, MH Berntsen, et al. Topological crystalline insulator states in $Pb_{1-x}Sn_xSe$. *Nature materials*, 11(12):1023–1027, 2012.

[46] Y Tanaka, Zhi Ren, T Sato, K Nakayama, S Souma, T Takahashi, Kouji Segawa, and Yoichi Ando. Experimental realization of a topological crystalline insulator in SnTe. *Nature Physics*, 8(11):800–803, 2012.

[47] Su-Yang Xu, Chang Liu, N Alidoust, M Neupane, D Qian, I Belopolski, JD Denlinger, YJ Wang, H Lin, LA a Wray, et al. Observation of a topological crystalline insulator phase and topological phase transition in $Pb_{1-x}Sn_xTe$. *Nature communications*, 3(1):1–11, 2012.

[48] Ken Shiozaki and Masatoshi Sato. Topology of crystalline insulators and superconductors. *Phys. Rev. B*, 90:165114, Oct 2014.

[49] N. P. Armitage, E. J. Mele, and Ashvin Vishwanath. Weyl and Dirac semimetals in three-dimensional solids. *Rev. Mod. Phys.*, 90:015001, Jan 2018.

[50] Shin-Ming Huang, Su-Yang Xu, Ilya Belopolski, Chi-Cheng Lee, Guoqing Chang, BaoKai Wang, Nasser Alidoust, Guang Bian, Madhab Neupane, Chenglong Zhang, et al. A Weyl fermion semimetal with surface Fermi arcs in the transition metal monopnictide TaAs class. *Nature communications*, 6:7373, 2015.

[51] Su-Yang Xu, Ilya Belopolski, Nasser Alidoust, Madhab Neupane, Guang Bian, Chenglong Zhang, Raman Sankar, Guoqing Chang, Zhujun Yuan, Chi-Cheng Lee, et al. Discovery of a Weyl fermion semimetal and topological Fermi arcs. *Science*, 349(6248):613–617, 2015.

[52] Zhongbo Yan, Ren Bi, Huitao Shen, Ling Lu, Shou-Cheng Zhang, and Zhong Wang. Nodal-link semimetals. *Phys. Rev. B*, 96:041103, Jul 2017.

[53] Wladimir A Benalcazar, B Andrei Bernevig, and Taylor L Hughes. Electric multipole moments, topological multipole moment pumping, and chiral hinge states in crystalline insulators. *Physical Review B*, 96(24):245115, 2017.

[54] Wladimir A Benalcazar, B Andrei Bernevig, and Taylor L Hughes. Quantized electric multipole insulators. *Science*, 357(6346):61–66, 2017.

[55] Wladimir A. Benalcazar, Tianhe Li, and Taylor L. Hughes. Quantization of fractional corner charge in C_n-symmetric higher-order topological crystalline insulators. *Phys. Rev. B*, 99:245151, Jun 2019.

[56] Adhip Agarwala, Vladimir Juričić, and Bitan Roy. Higher-order topological insulators in amorphous solids. *Phys. Rev. Research*, 2:012067, Mar 2020.

[57] Rui Chen, Chui-Zhen Chen, Jin-Hua Gao, Bin Zhou, and Dong-Hui Xu. Higher-order topological insulators in quasicrystals. *Phys. Rev. Lett.*, 124:036803, Jan 2020.

[58] Elisabet Edvardsson, Flore K. Kunst, and Emil J. Bergholtz. Non-Hermitian extensions of higher-order topological phases and their biorthogonal bulk-boundary correspondence. *Phys. Rev. B*, 99:081302, Feb 2019.

[59] Tao Liu, Yu-Ran Zhang, Qing Ai, Zongping Gong, Kohei Kawabata, Masahito Ueda, and Franco Nori. Second-order topological phases in non-Hermitian systems. *Phys. Rev. Lett.*, 122:076801, Feb 2019.

[60] Motohiko Ezawa. Higher-order topological insulators and semimetals on the breathing kagome and pyrochlore lattices. *Phys. Rev. Lett.*, 120:026801, Jan 2018.

[61] Hai-Xiao Wang, Zhi-Kang Lin, Bin Jiang, Guang-Yu Guo, and Jian-Hua Jiang. Higher-order Weyl semimetals. *Phys. Rev. Lett.*, 125:146401, Sep 2020.

[62] Haiping Hu, Biao Huang, Erhai Zhao, and W. Vincent Liu. Dynamical singularities of Floquet higher-order topological insulators. *Phys. Rev. Lett.*, 124:057001, Feb 2020.

[63] Yang Peng and Gil Refael. Floquet second-order topological insulators from nonsymmorphic space-time symmetries. *Phys. Rev. Lett.*, 123:016806, Jul 2019.

[64] B Andrei Bernevig and Taylor L Hughes. *Topological insulators and topological superconductors*. Princeton University Press, 2013.

[65] David Vanderbilt. *Berry Phases in Electronic Structure Theory: Electric Polarization, Orbital Magnetization and Topological Insulators*. Cambridge University Press, 2018.

[66] Claudio Chamon, Mark O Goerbig, Roderich Moessner, and Leticia F Cugliandolo. *Topological Aspects of Condensed Matter Physics: Lecture Notes of the Les Houches Summer School: Volume 103, August 2014*, volume 103. Oxford University Press, 2017.

[67] Mikio Nakahara. *Geometry, topology and physics*. CRC Press, 2003.

[68] M Zahid Hasan and Charles L Kane. Colloquium: topological insulators. *Reviews of Modern Physics*, 82(4):3045, 2010.

[69] Manfred Sigrist and Kazuo Ueda. Phenomenological theory of unconventional superconductivity. *Reviews of Modern physics*, 63(2):239, 1991.

[70] Patrick A Lee, Naoto Nagaosa, and Xiao-Gang Wen. Doping a Mott insulator: Physics of high-temperature superconductivity. *Reviews of modern physics*, 78(1):17, 2006.

[71] CC Tsuei and JR Kirtley. Pairing symmetry in cuprate superconductors. *Reviews of Modern Physics*, 72(4):969, 2000.

[72] Yoichi Ando and Liang Fu. Topological crystalline insulators and topological superconductors: From concepts to materials. *Annu. Rev. Condens. Matter Phys.*, 6(1):361–381, 2015.

[73] Ching-Kai Chiu, Jeffrey C. Y. Teo, Andreas P. Schnyder, and Shinsei Ryu. Classification of topological quantum matter with symmetries. *Rev. Mod. Phys.*, 88:035005, Aug 2016.

[74] Di Xiao, Ming-Che Chang, and Qian Niu. Berry phase effects on electronic properties. *Rev. Mod. Phys.*, 82:1959–2007, Jul 2010.

[75] Jun John Sakurai and Eugene D Commins. Modern quantum mechanics, revised edition, 1995.

[76] Eugene Wigner. *Group theory: and its application to the quantum mechanics of atomic spectra*, volume 5. Elsevier, 2012.

[77] Yoichiro Nambu. Quasi-particles and gauge invariance in the theory of superconductivity. *Phys. Rev.*, 117:648–663, Feb 1960.

[78] R. B. Laughlin. Quantized Hall conductivity in two dimensions. *Phys. Rev. B*, 23:5632–5633, May 1981.

[79] N. D. Mermin. The topological theory of defects in ordered media. *Rev. Mod. Phys.*, 51:591–648, Jul 1979.

[80] R. Jackiw and C. Rebbi. Solitons with fermion number 1/2. *Phys. Rev. D*, 13:3398–3409, Jun 1976.

[81] W. P. Su, J. R. Schrieffer, and A. J. Heeger. Solitons in polyacetylene. *Phys. Rev. Lett.*, 42:1698–1701, Jun 1979.

[82] Peter Heinzner, A Huckleberry, and Martin R Zirnbauer. Symmetry classes of disordered fermions. *Communications in mathematical physics*, 257(3):725–771, 2005.

[83] Michael Victor Berry. Quantal phase factors accompanying adiabatic changes. *Proceedings of the Royal Society of London. A. Mathematical and Physical Sciences*, 392(1802):45–57, 1984.

[84] Raffaele Resta. Theory of the electric polarization in crystals. *Ferroelectrics*, 136(1):51–55, 1992.

[85] J. Zak. Berry's phase for energy bands in solids. *Phys. Rev. Lett.*, 62:2747–2750, Jun 1989.

[86] R. D. King-Smith and David Vanderbilt. Theory of polarization of crystalline solids. *Phys. Rev. B*, 47:1651–1654, Jan 1993.

[87] David Vanderbilt and R. D. King-Smith. Electric polarization as a bulk quantity and its relation to surface charge. *Phys. Rev. B*, 48:4442–4455, Aug 1993.

[88] D. J. Thouless. Quantization of particle transport. *Phys. Rev. B*, 27:6083–6087, May 1983.

[89] Liang Fu and C. L. Kane. Time-reversal polarization and a $\mathbb{Z}_2$ adiabatic spin pump. *Phys. Rev. B*, 74:195312, Nov 2006.

[90] Liang Fu and C. L. Kane. Topological insulators with inversion symmetry. *Phys. Rev. B*, 76:045302, Jul 2007.

[91] M. Wimmer. Algorithm 923: Efficient numerical computation of the Pfaffian for dense and banded skew-symmetric matrices. *ACM Trans. Math. Softw.*, 38(4):30:1–30:17, August 2012.

[92] Holger Bech Nielsen and Masao Ninomiya. The Adler-Bell-Jackiw anomaly and Weyl fermions in a crystal. *Physics Letters B*, 130(6):389–396, 1983.

[93] Bertold Rasche, Anna Isaeva, Michael Ruck, Sergey Borisenko, Volodymyr Zabolotnyy, Bernd Büchner, Klaus Koepernik, Carmine Ortix, Manuel Richter, and Jeroen Van Den Brink. Stacked topological insulator built from bismuth-based graphene sheet analogues. *Nature materials*, 12(5):422–425, 2013.

[94] Christian Pauly, Bertold Rasche, Klaus Koepernik, Marcus Liebmann, Marco Pratzer, Manuel Richter, Jens Kellner, Markus Eschbach, Bernhard Kaufmann, Lukasz Plucinski, et al. Subnanometre-wide electron channels protected by topology. *Nature Physics*, 11(4):338–343, 2015.

[95] H Kamerlingh Onnes. The resistance of pure mercury at helium temperatures. *Commun. Phys. Lab. Univ. Leiden, b*, 120, 1911.

[96] Walther Meissner and Robert Ochsenfeld. Ein neuer effekt bei eintritt der supraleitfähigkeit. *Naturwissenschaften*, 21(44):787–788, 1933.

[97] Fritz London and Heinz London. The electromagnetic equations of the supraconductor. *Proceedings of the Royal Society of London. Series A-Mathematical and Physical Sciences*, 149(866):71–88, 1935.

[98] V Ginzburg and L Landau. On the theory of superconductivity, zh. lksper. *Teoret. Fiz*, 20:1064–1082, 1950.

[99] Leon N. Cooper. Bound electron pairs in a degenerate Fermi gas. *Phys. Rev.*, 104:1189–1190, Nov 1956.

[100] J. Bardeen, L. N. Cooper, and J. R. Schrieffer. Theory of superconductivity. *Phys. Rev.*, 108:1175–1204, Dec 1957.

[101] J. Bardeen, L. N. Cooper, and J. R. Schrieffer. Microscopic theory of superconductivity. *Phys. Rev.*, 106:162–164, Apr 1957.

[102] Herbert Fröhlich. Theory of the superconducting state. i. the ground state at the absolute zero of temperature. *Physical Review*, 79(5):845, 1950.

[103] Emanuel Maxwell. Isotope effect in the superconductivity of mercury. *Phys. Rev.*, 78:477–477, May 1950.

[104] C. A. Reynolds, B. Serin, W. H. Wright, and L. B. Nesbitt. Superconductivity of isotopes of mercury. *Phys. Rev.*, 78:487–487, May 1950.

[105] Alexei Alexeyevich Abrikosov. The magnetic properties of superconducting alloys. *Journal of Physics and Chemistry of Solids*, 2(3):199–208, 1957.

[106] Michael Tinkham. *Introduction to superconductivity*. Courier Corporation, 2004.

[107] J George Bednorz and K Alex Müller. Possible high T_c superconductivity in the Ba-La-Cu-O system. *Zeitschrift für Physik B Condensed Matter*, 64(2):189–193, 1986.

[108] F Marsiglio. Eliashberg theory: A short review. *Annals of Physics*, page 168102, 2020.

[109] Pierre-Gilles De Gennes. *Superconductivity of metals and alloys*. CRC Press, 2018.

[110] Paul Adrien Maurice Dirac. The quantum theory of the electron. *Proceedings of the Royal Society of London. Series A, Containing Papers of a Mathematical and Physical Character*, 117(778):610–624, 1928.

[111] Carl D. Anderson. The positive electron. *Phys. Rev.*, 43:491–494, Mar 1933.

[112] Ettore Majorana. Teoria simmetrica dellelettrone e del positrone. *Il Nuovo Cimento (1924-1942)*, 14(4):171, 1937.

[113] Frank Wilczek. Majorana returns. *Nature Physics*, 5(9):614, 2009.

[114] A Yu Kitaev. Unpaired Majorana fermions in quantum wires. *Physics-Uspekhi*, 44(10S):131, 2001.

[115] G Ml Luke, Y Fudamoto, KM Kojima, MI Larkin, J Merrin, B Nachumi, YJ Uemura, Y Maeno, ZQ Mao, Y Mori, et al. Time-reversal symmetry-breaking superconductivity in Sr_2RuO_4. *Nature*, 394(6693):558–561, 1998.

[116] Gregory Moore and Nicholas Read. Non-Abelions in the fractional quantum Hall effect. *Nuclear Physics B*, 360(2-3):362–396, 1991.

[117] C Caroli, PG De Gennes, and J Matricon. Bound fermion states on a vortex line in a type II superconductor. *Physics Letters*, 9(4):307–309, 1964.

[118] N. Read and Dmitry Green. Paired states of fermions in two dimensions with breaking of parity and time-reversal symmetries and the fractional quantum Hall effect. *Phys. Rev. B*, 61:10267–10297, Apr 2000.

[119] GE Volovik. Fermion zero modes on vortices in chiral superconductors. *Journal of Experimental and Theoretical Physics Letters*, 70(9):609–614, 1999.

[120] Masatoshi Sato. Topological odd-parity superconductors. *Physical Review B*, 81(22):220504, 2010.

[121] Liang Fu and Erez Berg. Odd-parity topological superconductors: Theory and application to $Cu_xBi_2Se_3$. *Phys. Rev. Lett.*, 105:097001, Aug 2010.

[122] Nicholas Read and Dmitry Green. Paired states of fermions in two dimensions with breaking of parity and time-reversal symmetries and the fractional quantum Hall effect. *Physical Review B*, 61(15):10267, 2000.

[123] Shingo Yonezawa, Kengo Tajiri, Suguru Nakata, Yuki Nagai, Zhiwei Wang, Kouji Segawa, Yoichi Ando, and Yoshiteru Maeno. Thermodynamic evidence for nematic superconductivity in $Cu_xBi_2Se_3$. *Nature Physics*, 13(2):123–126, 2017.

[124] Liang Fu and C. L. Kane. Superconducting proximity effect and Majorana fermions at the surface of a topological insulator. *Phys. Rev. Lett.*, 100:096407, Mar 2008.

[125] Jason Alicea. Majorana fermions in a tunable semiconductor device. *Phys. Rev. B*, 81:125318, Mar 2010.

[126] Jay D. Sau, Roman M. Lutchyn, Sumanta Tewari, and S. Das Sarma. Generic new platform for topological quantum computation using semiconductor heterostructures. *Phys. Rev. Lett.*, 104:040502, Jan 2010.

[127] Yuval Oreg, Gil Refael, and Felix von Oppen. Helical liquids and Majorana bound states in quantum wires. *Phys. Rev. Lett.*, 105:177002, Oct 2010.

[128] Roman M. Lutchyn, Jay D. Sau, and S. Das Sarma. Majorana fermions and a topological phase transition in semiconductor-superconductor heterostructures. *Phys. Rev. Lett.*, 105:077001, Aug 2010.

[129] Masatoshi Sato, Yoshiro Takahashi, and Satoshi Fujimoto. Non-Abelian topological order in s-wave superfluids of ultracold fermionic atoms. *Phys. Rev. Lett.*, 103:020401, Jul 2009.

[130] Chris L. M. Wong and K. T. Law. Majorana Kramers doublets in $d_{x^2-y^2}$-wave superconductors with Rashba spin-orbit coupling. *Phys. Rev. B*, 86:184516, Nov 2012.

[131] Fan Zhang, CL Kane, and EJ Mele. Time-reversal-invariant topological superconductivity and Majorana Kramers pairs. *Physical review letters*, 111(5):056402, 2013.

[132] V. Mourik, K. Zuo, S. M. Frolov, S. R. Plissard, E. P. A. M. Bakkers, and L. P. Kouwenhoven. Signatures of Majorana fermions in hybrid superconductor-semiconductor nanowire devices. *Science*, 336(6084):1003–1007, 2012.

[133] Anindya Das, Yuval Ronen, Yonatan Most, Yuval Oreg, Moty Heiblum, and Hadas Shtrikman. Zero-bias peaks and splitting in an Al-InAs nanowire topological superconductor as a signature of Majorana fermions. *Nature Physics*, 8(12):887–895, 2012.

[134] Leonid P Rokhinson, Xinyu Liu, and Jacek K Furdyna. The fractional ac Josephson effect in a semiconductor-superconductor nanowire as a signature of Majorana particles. *Nature Physics*, 8(11):795–799, 2012.

[135] MT Deng, CL Yu, GY Huang, Marcus Larsson, Philippe Caroff, and HQ Xu. Anomalous zero-bias conductance peak in a Nb-InSb nanowire-Nb hybrid device. *Nano letters*, 12(12):6414–6419, 2012.

[136] Stevan Nadj-Perge, Ilya K. Drozdov, Jian Li, Hua Chen, Sangjun Jeon, Jungpil Seo, Allan H. MacDonald, B. Andrei Bernevig, and Ali Yazdani. Observation of Majorana fermions in ferromagnetic atomic chains on a superconductor. *Science*, 346(6209):602–607, 2014.

[137] Hao Zhang, Chun-Xiao Liu, Sasa Gazibegovic, Di Xu, John A Logan, Guanzhong Wang, Nick van Loo, Jouri DS Bommer, Michiel WA de Moor, Diana Car, Roy L. M. Op het Veld, Petrus J. van Veldhoven, Sebastian Koelling, Marcel A. Verheijen, Mihir Pendharkar, Daniel J. Pennachio, Borzoyeh Shojaei, Joon Sue Lee, Chris J. Palmstrm, Erik P. A. M. Bakkers, S. Das Sarma, and Leo P. Kouwenhoven. Quantized Majorana conductance. *Nature*, 556:74, March 2018.

[138] Hao-Hua Sun, Kai-Wen Zhang, Lun-Hui Hu, Chuang Li, Guan-Yong Wang, Hai-Yang Ma, Zhu-An Xu, Chun-Lei Gao, Dan-Dan Guan, Yao-Yi Li, Canhua Liu, Dong Qian, Yi Zhou, Liang Fu, Shao-Chun Li, Fu-Chun Zhang, and Jin-Feng Jia. Majorana zero mode detected with spin selective Andreev reflection in the vortex of a topological superconductor. *Phys. Rev. Lett.*, 116:257003, Jun 2016.

[139] Dongfei Wang, Lingyuan Kong, Peng Fan, Hui Chen, Shiyu Zhu, Wenyao Liu, Lu Cao, Yujie Sun, Shixuan Du, John Schneeloch, et al. Evidence for Majorana bound states in an iron-based superconductor. *Science*, 362(6412):333–335, 2018.

[140] R. M. Lutchyn, E. P. A. M. Bakkers, L. P. Kouwenhoven, P. Krogstrup, C. M. Marcus, and Y. Oreg. Majorana zero modes in superconductor-semiconductor heterostructures. *Nature Reviews Materials*, 3(5):52–68, 2018.

[141] Taylor L. Hughes, Emil Prodan, and B. Andrei Bernevig. Inversion-symmetric topological insulators. *Phys. Rev. B*, 83:245132, Jun 2011.

[142] Yuan-Ming Lu and Dung-Hai Lee. Inversion symmetry protected topological insulators and superconductors. *arXiv preprint arXiv:1403.5558*, 2014.

[143] Timothy H Hsieh, Hsin Lin, Junwei Liu, Wenhui Duan, Arun Bansil, and Liang Fu. Topological crystalline insulators in the SnTe material class. *Nature communications*, 3(1):1–7, 2012.

[144] Ching-Kai Chiu, Hong Yao, and Shinsei Ryu. Classification of topological insulators and superconductors in the presence of reflection symmetry. *Phys. Rev. B*, 88:075142, Aug 2013.

[145] Alexander Lau, Jeroen van den Brink, and Carmine Ortix. Topological mirror insulators in one dimension. *Phys. Rev. B*, 94:165164, Oct 2016.

[146] Robert-Jan Slager, Andrej Mesaros, Vladimir Juričić, and Jan Zaanen. The space group classification of topological band-insulators. *Nature Physics*, 9(2):98–102, 2013.

[147] Jorrit Kruthoff, Jan de Boer, Jasper van Wezel, Charles L. Kane, and Robert-Jan Slager. Topological classification of crystalline insulators through band structure combinatorics. *Phys. Rev. X*, 7:041069, Dec 2017.

[148] Chen Fang, Matthew J. Gilbert, and B. Andrei Bernevig. New class of topological superconductors protected by magnetic group symmetries. *Phys. Rev. Lett.*, 112:106401, Mar 2014.

[149] Rui-Xing Zhang and Chao-Xing Liu. Topological magnetic crystalline insulators and corepresentation theory. *Phys. Rev. B*, 91:115317, Mar 2015.

[150] Haruki Watanabe, Hoi Chun Po, and Ashvin Vishwanath. Structure and topology of band structures in the 1651 magnetic space groups. *Science advances*, 4(8):eaat8685, 2018.

[151] Jeffrey C. Y. Teo, Liang Fu, and C. L. Kane. Surface states and topological invariants in three-dimensional topological insulators: Application to $Bi_{1-x}Sb_x$. *Phys. Rev. B*, 78:045426, Jul 2008.

[152] Zhongbo Yan, Fei Song, and Zhong Wang. Majorana corner modes in a high-temperature platform. *Phys. Rev. Lett.*, 121:096803, Aug 2018.

[153] Qiyue Wang, Cheng-Cheng Liu, Yuan-Ming Lu, and Fan Zhang. High-temperature Majorana corner states. *Physical review letters*, 121(18):186801, 2018.

[154] Yuxuan Wang, Mao Lin, and Taylor L Hughes. Weak-pairing higher order topological superconductors. *Physical Review B*, 98(16):165144, 2018.

[155] Rui-Xing Zhang, William S. Cole, and S. Das Sarma. Helical hinge Majorana modes in iron-based superconductors. *Phys. Rev. Lett.*, 122:187001, May 2019.

[156] Masatoshi Sato, Yukio Tanaka, Keiji Yada, and Takehito Yokoyama. Topology of Andreev bound states with flat dispersion. *Physical Review B*, 83(22):224511, 2011.

[157] Chris LM Wong, Jie Liu, KT Law, and Patrick A Lee. Majorana flat bands and unidirectional Majorana edge states in gapless topological superconductors. *Physical Review B*, 88(6):060504, 2013.

[158] Yuki Nagai, Yukihiro Ota, and K Tanaka. Time-reversal symmetry breaking and gapped surface states due to spontaneous emergence of new order in d-wave nanoislands. *Physical Review B*, 96(6):060503, 2017.

[159] Akito Daido and Youichi Yanase. Majorana flat bands, chiral Majorana edge states, and unidirectional Majorana edge states in noncentrosymmetric superconductors. *Physical Review B*, 95(13):134507, 2017.

[160] Satoshi Kashiwaya, Yukio Tanaka, Masao Koyanagi, Hiroshi Takashima, and Koji Kajimura. Origin of zero-bias conductance peaks in high-T_c superconductors. *Physical Review B*, 51(2):1350, 1995.

[161] Keiji Yada, Masatoshi Sato, Yukio Tanaka, and Takehito Yokoyama. Surface density of states and topological edge states in noncentrosymmetric superconductors. *Physical Review B*, 83(6):064505, 2011.

[162] Andreas P Schnyder and Shinsei Ryu. Topological phases and surface flat bands in superconductors without inversion symmetry. *Physical Review B*, 84(6):060504, 2011.

[163] Satoshi Ikegaya, Shingo Kobayashi, and Yasuhiro Asano. Symmetry conditions of a nodal superconductor for generating robust flat-band Andreev bound states at its dirty surface. *Physical Review B*, 97(17):174501, 2018.

[164] Xiaofeng Qian, Junwei Liu, Liang Fu, and Ju Li. Quantum spin Hall effect in two-dimensional transition metal dichalcogenides. *Science*, 346(6215):1344–1347, 2014.

[165] Sanfeng Wu, Valla Fatemi, Quinn D Gibson, Kenji Watanabe, Takashi Taniguchi, Robert J Cava, and Pablo Jarillo-Herrero. Observation of the quantum spin Hall effect up to 100 Kelvin in a monolayer crystal. *Science*, 359(6371):76–79, 2018.

[166] LJ Li, ECT O?Farrell, KP Loh, Goki Eda, B Özyilmaz, and AH Castro Neto. Controlling many-body states by the electric-field effect in a two-dimensional material. *Nature*, 529(7585):185, 2016.

[167] CH Ahn, A Bhattacharya, M Di Ventra, James N Eckstein, C Daniel Frisbie, ME Gershenson, AM Goldman, IH Inoue, Jochen Mannhart, Andrew J Millis, et al. Electrostatic modification of novel materials. *Reviews of Modern Physics*, 78(4):1185, 2006.

[168] Martin Weisheit, Sebastian Fähler, Alain Marty, Yves Souche, Christiane Poinsignon, and Dominique Givord. Electric field-induced modification of magnetism in thin-film ferromagnets. *Science*, 315(5810):349–351, 2007.

[169] E. I. Rashba. Symmetry of energy bands in crystals of wurtzite-type: I. symmetry of bands disregarding spin-orbit interaction. *Soviet Physics-Solid State*, 1(3):368–380, 1959.

[170] E. I. Rashba and V. I. Sheka. Symmetry of energy bands in crystals of wurtzite type: II. symmetry of bands with spin-orbit interaction included. *Fiz. Tverd. Tela: Collected Papers 2: 62-76*, 1959.

[171] R. J. Elliott. Spin-orbit coupling in band theory – character tables for some "double" space groups. *Phys. Rev.*, 96:280–287, Oct 1954.

[172] G. Dresselhaus, A. F. Kip, and C. Kittel. Spin-orbit interaction and the effective masses of holes in Germanium. *Phys. Rev.*, 95:568–569, Jul 1954.

[173] G. Dresselhaus. Spin-orbit coupling effects in Zinc blende structures. *Phys. Rev.*, 100:580–586, Oct 1955.

[174] G. Dresselhaus, A. F. Kip, and C. Kittel. Cyclotron resonance of electrons and holes in Silicon and Germanium crystals. *Phys. Rev.*, 98:368–384, Apr 1955.

[175] Sergey D Ganichev and Leonid E Golub. Interplay of Rashba/Dresselhaus spin splittings probed by photogalvanic spectroscopy—a review. *physica status solidi b*, 251(9):1801–1823, 2014.

[176] Aurelien Manchon, Hyun Cheol Koo, Junsaku Nitta, SM Frolov, and RA Duine. New perspectives for Rashba spin–orbit coupling. *Nature materials*, 14(9):871–882, 2015.

[177] Gustav Bihlmayer, O Rader, and R Winkler. Focus on the Rashba effect. *New journal of physics*, 17(5):050202, 2015.

[178] Lev P. Gor'kov and E. I. Rashba. Superconducting 2D system with lifted spin degeneracy: Mixed singlet-triplet state. *Phys. Rev. Lett.*, 87:037004, Jul 2001.

[179] P. A. Frigeri, D. F. Agterberg, A. Koga, and M. Sigrist. Superconductivity without inversion symmetry: MnSi versus $CePt_3Si$. *Phys. Rev. Lett.*, 92:097001, Mar 2004.

[180] Victor M. Edelstein. Magnetoelectric effect in polar superconductors. *Phys. Rev. Lett.*, 75:2004–2007, Sep 1995.

[181] Mark H. Fischer, Manfred Sigrist, and Daniel F. Agterberg. Superconductivity without inversion and time-reversal symmetries. *Phys. Rev. Lett.*, 121:157003, Oct 2018.

[182] Yuki Nagai, Shintaro Hoshino, and Yukihiro Ota. Critical temperature enhancement of topological superconductors: A dynamical mean-field study. *Phys. Rev. B*, 93:220505, Jun 2016.

[183] S. L. Goertzen, K. Tanaka, and Yuki Nagai. Self-consistent study of Abelian and non-Abelian order in a two-dimensional topological superconductor. *Phys. Rev. B*, 95:064509, Feb 2017.

[184] Victor Galitski and Ian B. Spielman. Spin-orbit coupling in quantum gases. *Nature*, 494(7435):49–54, 2013.

[185] Joel E Moore. The birth of topological insulators. *Nature*, 464(7286):194, 2010.

[186] D. A. Pesin and Leon Balents. Mott physics and band topology in materials with strong spin-orbit interaction. *Nat. Phys.*, 6:376, 2010.

[187] D. A. Ivanov. Non-abelian statistics of half-quantum vortices in p-wave superconductors. *Phys. Rev. Lett.*, 86:268–271, Jan 2001.

[188] A Yu Kitaev. Fault-tolerant quantum computation by anyons. *Annals of Physics*, 303(1):2–30, 2003.

[189] R. Micnas, J. Ranninger, and S. Robaszkiewicz. Superconductivity in narrow-band systems with local nonretarded attractive interactions. *Rev. Mod. Phys.*, 62:113–171, Jan 1990.

[190] Xiao-Liang Qi, Taylor L. Hughes, and Shou-Cheng Zhang. Topological invariants for the Fermi surface of a time-reversal-invariant superconductor. *Phys. Rev. B*, 81:134508, Apr 2010.

[191] Zhongbo Yan. Higher-order topological odd-parity superconductors. *Phys. Rev. Lett.*, 123:177001, Oct 2019.

[192] Zhigang Wu, Zhongbo Yan, and Wen Huang. Higher-order topological superconductivity: Possible realization in Fermi gases and Sr_2RuO_4. *Physical Review B*, 99(2):020508, 2019.

[193] Junsaku Nitta, Tatsushi Akazaki, Hideaki Takayanagi, and Takatomo Enoki. Gate control of spin-orbit interaction in an inverted $In_{0.53}Ga_{0.47}As/In_{0.52}Al_{0.48}As$ heterostructure. *Phys. Rev. Lett.*, 78:1335–1338, Feb 1997.

[194] Wei-Cheng Lee, Shou-Cheng Zhang, and Congjun Wu. Pairing state with a time-reversal symmetry breaking in FeAs-based superconductors. *Phys. Rev. Lett.*, 102:217002, May 2009.

[195] G. R. Stewart. Superconductivity in iron compounds. *Rev. Mod. Phys.*, 83:1589–1652, Dec 2011.

[196] R. P. Day, G. Levy, M. Michiardi, B. Zwartsenberg, M. Zonno, F. Ji, E. Razzoli, F. Boschini, S. Chi, R. Liang, P. K. Das, I. Vobornik, J. Fujii, W. N. Hardy, D. A. Bonn, I. S. Elfimov, and A. Damascelli. Influence of spin-orbit coupling in iron-based superconductors. *Phys. Rev. Lett.*, 121:076401, Aug 2018.

[197] Nicolas Reyren, S Thiel, AD Caviglia, L Fitting Kourkoutis, German Hammerl, Christoph Richter, CW Schneider, Thilo Kopp, A-S Rüetschi, Didier Jaccard, et al. Superconducting interfaces between insulating oxides. *Science*, 317(5842):1196–1199, 2007.

[198] M. Ben Shalom, M. Sachs, D. Rakhmilevitch, A. Palevski, and Y. Dagan. Tuning spin-orbit coupling and superconductivity at the $SrTiO_3/LaAlO_3$ interface: A magnetotransport study. *Phys. Rev. Lett.*, 104:126802, Mar 2010.

[199] Jay D. Sau, Rajdeep Sensarma, Stephen Powell, I. B. Spielman, and S. Das Sarma. Chiral Rashba spin textures in ultracold Fermi gases. *Phys. Rev. B*, 83:140510, Apr 2011.

[200] N. Read and Dmitry Green. Paired states of fermions in two dimensions with breaking of parity and time-reversal symmetries and the fractional quantum Hall effect. *Phys. Rev. B*, 61:10267–10297, Apr 2000.

[201] D. A. Ivanov. Non-abelian statistics of half-quantum vortices in p-wave superconductors. *Phys. Rev. Lett.*, 86:268–271, Jan 2001.

[202] Chetan Nayak, Steven H. Simon, Ady Stern, Michael Freedman, and Sankar Das Sarma. Non-abelian anyons and topological quantum computation. *Rev. Mod. Phys.*, 80:1083–1159, Sep 2008.

[203] Jason Alicea, Yuval Oreg, Gil Refael, Felix Von Oppen, and Matthew PA Fisher. Non-Abelian statistics and topological quantum information processing in 1D wire networks. *Nature Physics*, 7(5):412, 2011.

[204] Johnpierre Paglione and Richard L. Greene. High-temperature superconductivity in iron-based materials. *Nature Physics*, 6(9):645–658, Sep 2010.

[205] P J Hirschfeld, M M Korshunov, and I I Mazin. Gap symmetry and structure of Fe-based superconductors. *Reports on Progress in Physics*, 74(12):124508, oct 2011.

[206] G. R. Stewart. Superconductivity in iron compounds. *Rev. Mod. Phys.*, 83:1589–1652, Dec 2011.

[207] Andrey Chubukov. Pairing mechanism in Fe-based superconductors. *Annual Review of Condensed Matter Physics*, 3(1):57–92, 2012.

[208] Elbio Dagotto. Colloquium: The unexpected properties of alkali metal iron selenide superconductors. *Rev. Mod. Phys.*, 85:849–867, May 2013.

[209] Pengcheng Dai. Antiferromagnetic order and spin dynamics in iron-based superconductors. *Rev. Mod. Phys.*, 87:855–896, Aug 2015.

[210] I. I. Mazin, D. J. Singh, M. D. Johannes, and M. H. Du. Unconventional superconductivity with a sign reversal in the order parameter of $LaFeAsO_{1-x}F_x$. *Phys. Rev. Lett.*, 101:057003, Jul 2008.

[211] Fa Wang and Dung-Hai Lee. The electron-pairing mechanism of iron-based superconductors. *Science*, 332(6026):200–204, 2011.

[212] Zhijun Wang, P. Zhang, Gang Xu, L. K. Zeng, H. Miao, Xiaoyan Xu, T. Qian, Hongming Weng, P. Richard, A. V. Fedorov, H. Ding, Xi Dai, and Zhong Fang. Topological nature of the $FeSe_{0.5}Te_{0.5}$ superconductor. *Phys. Rev. B*, 92:115119, Sep 2015.

[213] Xianxin Wu, Shengshan Qin, Yi Liang, Heng Fan, and Jiangping Hu. Topological characters in $Fe(Te_{1-x}Se_x)$ thin films. *Phys. Rev. B*, 93:115129, Mar 2016.

[214] Gang Xu, Biao Lian, Peizhe Tang, Xiao-Liang Qi, and Shou-Cheng Zhang. Topological superconductivity on the surface of Fe-based superconductors. *Phys. Rev. Lett.*, 117:047001, Jul 2016.

[215] Ning Hao and Jiangping Hu. Topological quantum states of matter in iron-based superconductors: from concept to material realization. *National Science Review*, 6(2):213–226, 2019.

[216] Andreas Kreisel, Peter J Hirschfeld, and Brian M Andersen. On the Remarkable Superconductivity of FeSe and its Close Cousins. *Symmetry*, 12(9):1402, 2020.

[217] Peng Zhang, Koichiro Yaji, Takahiro Hashimoto, Yuichi Ota, Takeshi Kondo, Kozo Okazaki, Zhijun Wang, Jinsheng Wen, GD Gu, Hong Ding, et al. Observation of topological superconductivity on the surface of an iron-based superconductor. *Science*, 360(6385):182–186, 2018.

[218] Peng Zhang, Zhijun Wang, Xianxin Wu, Koichiro Yaji, Yukiaki Ishida, Yoshimitsu Kohama, Guangyang Dai, Yue Sun, Cedric Bareille, Kenta Kuroda, et al. Multiple topological states in iron-based superconductors. *Nature Physics*, 15(1):41, 2019.

[219] Lingyuan Kong, Shiyu Zhu, Michał Papaj, Hui Chen, Lu Cao, Hiroki Isobe, Yuqing Xing, Wenyao Liu, Dongfei Wang, Peng Fan, et al. Half-integer level shift of vortex bound states in an iron-based superconductor. *Nature Physics*, pages 1–7, 2019.

[220] T Machida, Y Sun, S Pyon, S Takeda, Y Kohsaka, T Hanaguri, T Sasagawa, and T Tamegai. Zero-energy vortex bound state in the superconducting topological surface state of Fe (Se, Te). *Nature materials*, page 1, 2019.

[221] Qin Liu, Chen Chen, Tong Zhang, Rui Peng, Ya-Jun Yan, Chen-Hao-Ping Wen, Xia Lou, Yu-Long Huang, Jin-Peng Tian, Xiao-Li Dong, Guang-Wei Wang, Wei-Cheng Bao, Qiang-Hua Wang, Zhi-Ping Yin, Zhong-Xian Zhao, and Dong-Lai Feng. Robust and clean Majorana zero mode in the vortex core of high-temperature superconductor $(Li_{0.84}Fe_{0.16})$OHFeSe. *Phys. Rev. X*, 8:041056, Dec 2018.

[222] C Chen, Q Liu, TZ Zhang, D Li, PP Shen, XL Dong, Z-X Zhao, T Zhang, and DL Feng. Quantized conductance of Majorana zero mode in the vortex of the topological superconductor $(Li_{0.84}Fe_{0.16})$OHFeSe. *Chinese Physics Letters*, 36(5):057403, 2019.

[223] Shiyu Zhu, Lingyuan Kong, Lu Cao, Hui Chen, Michał Papaj, Shixuan Du, Yuqing Xing, Wenyao Liu, Dongfei Wang, Chengmin Shen, Fazhi Yang, John Schneeloch, Ruidan Zhong, Genda Gu, Liang Fu, Yu-Yang Zhang, Hong Ding, and Hong-Jun Gao. Nearly quantized conductance plateau of vortex zero mode in an iron-based superconductor. *Science*, 367(6474):189–192, 2020.

[224] V. Mourik, K. Zuo, S. M. Frolov, S. R. Plissard, E. P. A. M. Bakkers, and L. P. Kouwenhoven. Signatures of Majorana fermions in hybrid superconductor-semiconductor nanowire devices. *Science*, 336(6084):1003–1007, 2012.

[225] Antonio Fornieri, Alexander M. Whiticar, F. Setiawan, Elías Portolés, Asbjørn C. C. Drachmann, Anna Keselman, Sergei Gronin, Candice Thomas, Tian Wang, Ray Kallaher, Geoffrey C. Gardner, Erez Berg, Michael J. Manfra, Ady Stern, Charles M. Marcus, and Fabrizio Nichele. Evidence of topological superconductivity in planar Josephson junctions. *Nature*, 569(7754):89–92, May 2019.

[226] Kun Jiang, Xi Dai, and Ziqiang Wang. Quantum anomalous vortex and Majorana zero mode in iron-based superconductor Fe(Te,Se). *Phys. Rev. X*, 9:011033, Feb 2019.

[227] X.-L. Peng, Y. Li, X.-X. Wu, H.-B. Deng, X. Shi, W.-H. Fan, M. Li, Y.-B. Huang, T. Qian, P. Richard, J.-P. Hu, S.-H. Pan, H.-Q. Mao, Y.-J. Sun, and H. Ding. Observation of topological transition in high-T_c superconducting monolayer $FeTe_{1-x}Se_x$ films on $SrTiO_3$(001). *Phys. Rev. B*, 100:155134, Oct 2019.

[228] Ching-Kai Chiu, T Machida, Yingyi Huang, T Hanaguri, and Fu-Chun Zhang. Scalable Majorana vortex modes in iron-based superconductors. *Science Advances*, 6(9):eaay0443, 2020.

[229] Zhenyu Wang, Jorge Olivares Rodriguez, Lin Jiao, Sean Howard, Martin Graham, G. D. Gu, Taylor L. Hughes, Dirk K. Morr, and Vidya Madhavan. Evidence for dispersing 1D Majorana channels in an iron-based superconductor. *Science*, 367(6473):104–108, 2020.

[230] Cheng Chen, Kun Jiang, Yi Zhang, Chaofei Liu, Yi Liu, Ziqiang Wang, and Jian Wang. Atomic line defects and zero-energy end states in monolayer Fe(Te,Se) high-temperature superconductors. *Nature Physics*, 16(5):536–540, May 2020.

[231] Yi Zhang, Kun Jiang, Fuchun Zhang, Jian Wang, and Ziqiang Wang. Atomic line defects in unconventional superconductors as a new route toward one dimensional topological superconductors. *arXiv preprint arXiv:2004.05860*, 2020.

[232] Xianxin Wu, Jia-Xin Yin, Chao-Xing Liu, and Jiangping Hu. Topological magnetic line defects in Fe(Te, Se) high-temperature superconductors. *arXiv preprint arXiv:2004.05848*, 2020.

[233] Areg Ghazaryan, P. L. S. Lopes, Pavan Hosur, Matthew J. Gilbert, and Pouyan Ghaemi. Effect of zeeman coupling on the Majorana vortex modes in iron-based topological superconductors. *Phys. Rev. B*, 101:020504, Jan 2020.

[234] Shengshan Qin, Lunhui Hu, Congcong Le, Jinfeng Zeng, Fu-chun Zhang, Chen Fang, and Jiangping Hu. Quasi-1D topological nodal vortex line phase in doped superconducting 3D Dirac semimetals. *Phys. Rev. Lett.*, 123:027003, Jul 2019.

[235] Shengshan Qin, Lunhui Hu, Xianxin Wu, Xia Dai, Chen Fang, Fu-Chun Zhang, and Jiangping Hu. Topological vortex phase transitions in iron-based superconductors. *Science Bulletin*, 64(17):1207 – 1214, 2019.

[236] Elio J. König and Piers Coleman. Crystalline-symmetry-protected helical Majorana modes in the Iron Pnictides. *Phys. Rev. Lett.*, 122:207001, May 2019.

[237] Zhongbo Yan, Zhigang Wu, and Wen Huang. Vortex end Majorana zero modes in superconducting Dirac and Weyl semimetals. *Phys. Rev. Lett.*, 124:257001, Jun 2020.

[238] Mingyang Chen, Xiaoyu Chen, Huan Yang, Zengyi Du, Xiyu Zhu, Enyu Wang, and Hai-Hu Wen. Discrete energy levels of Caroli-de Gennes-Matricon states in quantum limit in $FeTe_{0.55}Se_{0.45}$. *Nature Communications*, 9(1):970, Mar 2018.

[239] Xianxin Wu, Suk Bum Chung, Chao-xing Liu, and Eun-Ah Kim. Topological orders competing for the Dirac surface state in FeSeTe surfaces. *arXiv preprint arXiv:2004.13068*, 2020.

[240] Frank Schindler, Ashley M. Cook, Maia G. Vergniory, Zhijun Wang, Stuart S. P. Parkin, B. Andrei Bernevig, and Titus Neupert. Higher-order topological insulators. *Science Advances*, 4(6), 2018.

[241] Josias Langbehn, Yang Peng, Luka Trifunovic, Felix von Oppen, and Piet W. Brouwer. Reflection-symmetric second-order topological insulators and superconductors. *Phys. Rev. Lett.*, 119:246401, Dec 2017.

[242] Hassan Shapourian, Yuxuan Wang, and Shinsei Ryu. Topological crystalline superconductivity and second-order topological superconductivity in nodal-loop materials. *Phys. Rev. B*, 97:094508, Mar 2018.

[243] Eslam Khalaf. Higher-order topological insulators and superconductors protected by inversion symmetry. *Phys. Rev. B*, 97:205136, May 2018.

[244] Max Geier, Luka Trifunovic, Max Hoskam, and Piet W. Brouwer. Second-order topological insulators and superconductors with an order-two crystalline symmetry. *Phys. Rev. B*, 97:205135, May 2018.

[245] Xiaoyu Zhu. Tunable Majorana corner states in a two-dimensional second-order topological superconductor induced by magnetic fields. *Phys. Rev. B*, 97:205134, May 2018.

[246] Chen-Hsuan Hsu, Peter Stano, Jelena Klinovaja, and Daniel Loss. Majorana Kramers pairs in higher-order topological insulators. *Phys. Rev. Lett.*, 121:196801, Nov 2018.

[247] Tao Liu, James Jun He, and Franco Nori. Majorana corner states in a two-dimensional magnetic topological insulator on a high-temperature superconductor. *Phys. Rev. B*, 98:245413, Dec 2018.

[248] Zhigang Wu, Zhongbo Yan, and Wen Huang. Higher-order topological superconductivity: Possible realization in Fermi gases and Sr_2RuO_4. *Phys. Rev. B*, 99:020508, Jan 2019.

[249] Yanick Volpez, Daniel Loss, and Jelena Klinovaja. Second-order topological superconductivity in π-junction Rashba layers. *Phys. Rev. Lett.*, 122:126402, Mar 2019.

[250] Rui-Xing Zhang, William S. Cole, Xianxin Wu, and S. Das Sarma. Higher-order topology and nodal topological superconductivity in Fe(Se,Te) heterostructures. *Phys. Rev. Lett.*, 123:167001, Oct 2019.

[251] Xianxin Wu, Xin Liu, Ronny Thomale, and Chao-Xing Liu. High-T_c Superconductor Fe(Se,Te) Monolayer: an Intrinsic, Scalable and Electrically-tunable Majorana Platform. *arXiv preprint arXiv:1905.10648*, 2019.

[252] Yi-Ting Hsu, William S. Cole, Rui-Xing Zhang, and Jay D. Sau. Inversion-protected higher-order topological superconductivity in monolayer WTe_2. *Phys. Rev. Lett.*, 125:097001, Aug 2020.

[253] Chuanchang Zeng, T. D. Stanescu, Chuanwei Zhang, V. W. Scarola, and Sumanta Tewari. Majorana corner modes with solitons in an attractive Hubbard-Hofstadter model of cold atom optical lattices. *Phys. Rev. Lett.*, 123:060402, Aug 2019.

[254] Nick Bultinck, B. Andrei Bernevig, and Michael P. Zaletel. Three-dimensional superconductors with hybrid higher-order topology. *Phys. Rev. B*, 99:125149, Mar 2019.

[255] Sayed Ali Akbar Ghorashi, Xiang Hu, Taylor L. Hughes, and Enrico Rossi. Second-order Dirac superconductors and magnetic field induced Majorana hinge modes. *Phys. Rev. B*, 100:020509, Jul 2019.

[256] Yang Peng and Yong Xu. Proximity-induced Majorana hinge modes in antiferromagnetic topological insulators. *Phys. Rev. B*, 99:195431, May 2019.

[257] Xiaoyu Zhu. Second-order topological superconductors with mixed pairing. *Phys. Rev. Lett.*, 122:236401, Jun 2019.

[258] Katharina Laubscher, Daniel Loss, and Jelena Klinovaja. Fractional topological superconductivity and parafermion corner states. *Phys. Rev. Research*, 1:032017, Nov 2019.

[259] Xiao-Hong Pan, Kai-Jie Yang, Li Chen, Gang Xu, Chao-Xing Liu, and Xin Liu. Lattice-symmetry-assisted second-order topological superconductors and Majorana patterns. *Phys. Rev. Lett.*, 123:156801, Oct 2019.

[260] Zhongbo Yan. Higher-order topological odd-parity superconductors. *Phys. Rev. Lett.*, 123:177001, Oct 2019.

[261] Zhongbo Yan. Majorana corner and hinge modes in second-order topological insulator/superconductor heterostructures. *Phys. Rev. B*, 100:205406, Nov 2019.

[262] S. Franca, D. V. Efremov, and I. C. Fulga. Phase-tunable second-order topological superconductor. *Phys. Rev. B*, 100:075415, Aug 2019.

[263] Song-Bo Zhang and Björn Trauzettel. Detection of second-order topological superconductors by Josephson junctions. *Phys. Rev. Research*, 2:012018, Jan 2020.

[264] Junyeong Ahn and Bohm-Jung Yang. Higher-order topological superconductivity of spin-polarized fermions. *Phys. Rev. Research*, 2:012060, Mar 2020.

[265] Suman Jyoti De, Udit Khanna, and Sumathi Rao. Magnetic flux periodicity in second order topological superconductors. *Phys. Rev. B*, 101:125429, Mar 2020.

[266] Bitan Roy. Higher-order topological superconductors in $\mathcal{P}$-, $\mathcal{T}$-odd quadrupolar Dirac materials. *Phys. Rev. B*, 101:220506, Jun 2020.

[267] Ya-Jie Wu, Junpeng Hou, Yun-Mei Li, Xi-Wang Luo, Xiaoyan Shi, and Chuanwei Zhang. In-plane Zeeman-field-induced Majorana corner and hinge modes in an s-wave superconductor heterostructure. *Phys. Rev. Lett.*, 124:227001, Jun 2020.

[268] Sayed Ali Akbar Ghorashi, Taylor L. Hughes, and Enrico Rossi. Vortex and surface phase transitions in superconducting higher-order topological insulators. *Phys. Rev. Lett.*, 125:037001, Jul 2020.

[269] Li Chen, Bin Liu, Gang Xu, and Xin Liu. Lattice distortion induced first and second order topological phase transition in rectangular high-T_c superconducting monolayer. *arXiv preprint arXiv:1909.10402*, 2019.

[270] Jingjing Niu, Tongxing Yan, Yuxuan Zhou, Ziyu Tao, Xiaole Li, Weiyang Liu, Libo Zhang, Song Liu, Zhongbo Yan, Yuanzhen Chen, et al. Simulation of Higher-Order Topological Phases and Related Topological Phase Transitions in a Superconducting Qubit. *arXiv preprint arXiv:2001.03933*, 2020.

[271] Mason J. Gray, Josef Freudenstein, Shu Yang F. Zhao, Ryan O?Connor, Samuel Jenkins, Narendra Kumar, Marcel Hoek, Abigail Kopec, Soonsang Huh, Takashi Taniguchi, Kenji Watanabe, Ruidan Zhong, Changyoung Kim, G. D. Gu, and K. S. Burch. Evidence for helical hinge zero modes in an Fe-based superconductor. *Nano Letters*, 19(8):4890–4896, 2019.

[272] Pavan Hosur, Pouyan Ghaemi, Roger S. K. Mong, and Ashvin Vishwanath. Majorana modes at the ends of superconductor vortices in doped topological insulators. *Phys. Rev. Lett.*, 107:097001, Aug 2011.

[273] Andreas P. Schnyder, Shinsei Ryu, Akira Furusaki, and Andreas W. W. Ludwig. Classification of topological insulators and superconductors in three spatial dimensions. *Phys. Rev. B*, 78:195125, Nov 2008.

[274] Alexei Kitaev. Periodic table for topological insulators and superconductors. In *AIP Conference Proceedings*, volume 1134, pages 22–30. AIP, 2009.

[275] Xiaoyu Chen, Mingyang Chen, Wen Duan, Xiyu Zhu, Huan Yang, and Hai-Hu Wen. Observation and characterization of the zero energy conductance peak in the vortex core state of $FeTe_{0.55}Se_{0.45}$. *arXiv preprint arXiv:1909.01686*, 2019.

[276] U. R. Singh, S. C. White, S. Schmaus, V. Tsurkan, A. Loidl, J. Deisenhofer, and P. Wahl. Spatial inhomogeneity of the superconducting gap and order parameter in $FeSe_{0.4}Te_{0.6}$. *Phys. Rev. B*, 88:155124, Oct 2013.

[277] Duc-Thanh Tran, Alexandre Dauphin, Nathan Goldman, and Pierre Gaspard. Topological Hofstadter insulators in a two-dimensional quasicrystal. *Phys. Rev. B*, 91:085125, Feb 2015.

[278] Peter Fulde and Richard A. Ferrell. Superconductivity in a strong spin-exchange field. *Phys. Rev.*, 135:A550–A563, Aug 1964.

[279] AI Larkin and Yu N Ovchinnikov. Nonuniform state of superconductors. *Soviet Physics-JETP*, 20(3):762–762, 1965.

Appendix A

Majorana Condition

Although the BdG Hamiltonian in Chapter 3 is an $8N \times 8N$ matrix, by changing the basis it can be written as a block diagonal matrix where each block is an $4N \times 4N$ matrix and N is the number of lattice sites. In this section, it is shown that the zero modes of each of these $4N \times 4N$ blocks meets the Majorana conditions. The Hamiltonian can be rewritten as,

$$\mathcal{H} = \frac{1}{2}\Psi^\dagger \hat{H} \Psi, \tag{A.1}$$

here $\boldsymbol{\psi}_i^\dagger = (c_{i,a,\uparrow}^\dagger, c_{i,b,\uparrow}^\dagger, c_{i,a,\downarrow}^\dagger, c_{i,b,\downarrow}^\dagger, c_{i,a,\uparrow}, c_{i,b,\uparrow}, c_{i,a,\downarrow}, c_{i,b,\downarrow})$ and,

$$\hat{H} = \begin{pmatrix} H_n & \Delta \\ \Delta^\dagger & -H_n^* \end{pmatrix}, \tag{A.2}$$

where

$$H_n = \begin{pmatrix} H_1 & 0 \\ 0 & H_2 \end{pmatrix}, \quad \Delta = \begin{pmatrix} 0 & -\Delta \\ \Delta & 0 \end{pmatrix}. \tag{A.3}$$

The BdG equations are

$$\hat{H} \begin{pmatrix} \vec{u}_1 \\ \vec{u}_2 \\ \vec{v}_1 \\ \vec{v}_2 \end{pmatrix} = E \begin{pmatrix} \vec{u}_1 \\ \vec{u}_2 \\ \vec{v}_1 \\ \vec{v}_2 \end{pmatrix}, \tag{A.4}$$

or

$$H_1 \vec{u}_1 - \Delta \vec{v}_2 = E \vec{u}_1, \tag{A.5}$$
$$H_2 \vec{u}_2 + \Delta \vec{v}_1 = E \vec{u}_2, \tag{A.6}$$

$$\Delta^* \vec{u}_2 - H_1^* \vec{v}_1 = E\vec{v}_1, \tag{A.7}$$
$$-\Delta^* \vec{u}_1 - H_2^* \vec{v}_2 = E\vec{v}_2. \tag{A.8}$$

So, we have an $4N \times 4N$ matrix:

$$\begin{pmatrix} H_1 & -\Delta \\ -\Delta^* & -H_2^* \end{pmatrix} \begin{pmatrix} \vec{u}_1 \\ \vec{v}_2 \end{pmatrix} = E \begin{pmatrix} \vec{u}_1 \\ \vec{v}_2 \end{pmatrix}. \tag{A.9}$$

Then, it can be shown that,

$$-H_1^* \vec{u}_1^* + \Delta^* \vec{v}_2^* = -E\vec{u}_1^*, \tag{A.10}$$
$$-H_2^* \vec{u}_2^* - \Delta^* \vec{v}_1^* = -E\vec{u}_2^*, \tag{A.11}$$
$$-\Delta \vec{u}_2^* + H_1 \vec{v}_1^* = -E\vec{v}_1^*, \tag{A.12}$$
$$\Delta \vec{u}_1^* + H_2 \vec{v}_2^* = -E\vec{v}_2^*, \tag{A.13}$$

or

$$\hat{H} \begin{pmatrix} \vec{v}_1^* \\ \vec{v}_2^* \\ \vec{u}_1^* \\ \vec{u}_2^* \end{pmatrix} = -E \begin{pmatrix} \vec{v}_1^* \\ \vec{v}_2^* \\ \vec{u}_1^* \\ \vec{u}_2^* \end{pmatrix}. \tag{A.14}$$

Therefore, if $(\vec{u}_1^i, \vec{u}_2^i, \vec{v}_1^i, \vec{v}_2^i)$ is an eigenstate with energy E_i, then $(\vec{v}_1^{i*}, \vec{v}_2^{i*}, \vec{u}_1^{i*}, \vec{u}_2^{i*})$ is an eigenstate with energy $-E_i$ which should be expected because of particle-hole symmetry. This means that if $E = 0$, we have the following relations,

$$\vec{u}_1^i = \vec{v}_1^{i*} \qquad\qquad \vec{u}_2^i = \vec{v}_2^{i*}. \tag{A.15}$$

In other words, if we have $(\vec{u}_1^i, \vec{v}_2^i)$ with the energy E_i, we can obtain eigenstates $(\vec{u}_2^i, \vec{v}_1^i) = (\vec{v}_2^{i*}, \vec{u}_1^{i*})$ with the energy $-E_i$. It means by finding only the eigenvalues and eigenstates of the $4N \times 4N$ Hamiltonian in Eq. (A.9), one can find all eigenvalues and eigenstates of the $8N \times 8N$ Hamiltonian in Eq. (A.2) much more easily due to the particle-hole symmetry. In the rest of this section, we will show that all the zero modes of the $4N \times 4N$ Hamiltonian satisfy Majorana conditions.

The unitary matrix that diagonalizes the matrix $\hat{H}$ is expressed as

$$\hat{U} = \begin{pmatrix} \hat{u} & \hat{v}^* \\ \hat{v} & \hat{u}^* \end{pmatrix}, \quad \hat{H} = \hat{U} \begin{pmatrix} \hat{E} & 0 \\ 0 & -\hat{E} \end{pmatrix} \hat{U}^\dagger, \tag{A.16}$$

where

$$\hat{u} \equiv \begin{pmatrix} \vec{u}_1^1 & \cdots & \vec{u}_1^N \\ \vec{u}_2^2 & \cdots & \vec{u}_2^N \end{pmatrix}, \quad \hat{v} \equiv \begin{pmatrix} \vec{v}_1^1 & \cdots & \vec{v}_1^N \\ \vec{v}_2^2 & \cdots & \vec{v}_2^N \end{pmatrix}. \tag{A.17}$$

So,

$$\mathcal{H} = \frac{1}{2}\Psi^\dagger \hat{U} \begin{pmatrix} \hat{E} & 0 \\ 0 & -\hat{E} \end{pmatrix} \hat{U}^\dagger \Psi \tag{A.18}$$

$$= \frac{1}{2}\sum_i (E_i \gamma_i^\dagger \gamma_i - E_i \gamma_i \gamma_i^\dagger), \tag{A.19}$$

where

$$\begin{pmatrix} \vec{\gamma} \\ \vec{\gamma^\dagger} \end{pmatrix} = \hat{U}^\dagger \begin{pmatrix} \vec{c} \\ \vec{c^\dagger} \end{pmatrix}, \tag{A.20}$$

or

$$\gamma_i = \sum_l \left[[\hat{u}]^*_{li} c_l + [\hat{v}]^*_{li} c_l^\dagger \right], \tag{A.21}$$

$$\gamma_i^\dagger = \sum_l \left[[\hat{u}]_{li} c_l^\dagger + [\hat{v}]_{li} c_l \right]. \tag{A.22}$$

It is obvious that $\gamma_i^\dagger \neq \gamma_i$. However, we have two special conditions for only zero-eigenvalues which is Eq. (A.15). Using them we will have,

$$\gamma_i^\dagger = \sum_l \left[[\hat{v}]^*_{li} c_l^\dagger + [\hat{u}]^*_{li} c_l \right] = \gamma_i. \tag{A.23}$$

Therefore, the zero-energy eigenstates are all Majorana.

Appendix B

Effective Realization of Odd-Parity Superconductivity

For generality, here we further include an out-of-plane Zeeman field. Accordingly, the normal state Hamiltonian is

$$H_0 = \sum_{\boldsymbol{k}} (c^\dagger_{\boldsymbol{k},\uparrow},\ c^\dagger_{\boldsymbol{k},\downarrow}) \begin{pmatrix} \xi_{\boldsymbol{k}} + h_z & l_x - il_y \\ l_x + il_y & \xi_{\boldsymbol{k}} - h_z \end{pmatrix} \begin{pmatrix} c_{\boldsymbol{k},\uparrow} \\ c_{\boldsymbol{k},\downarrow} \end{pmatrix}, \tag{B.1}$$

The spin singlet-pairing superconductivity is described by

$$H_{\rm SC} = \sum_{\boldsymbol{k}} (\Delta_s(\boldsymbol{k}) + i\Delta_d(\boldsymbol{k})) c^\dagger_{\boldsymbol{k},\uparrow} c^\dagger_{-\boldsymbol{k},\downarrow} + h.c., \tag{B.2}$$

where $\Delta_s(\boldsymbol{k}) = \Delta_0 + \Delta_s \eta_s(\boldsymbol{k})$ and $\Delta_d(\boldsymbol{k}) = \Delta_d \eta_d(\boldsymbol{k})$. We first follow Ref. [125] and do the following transformation

$$c_{\boldsymbol{k},\uparrow} = (\cos\frac{\theta_{\boldsymbol{k}}}{2} c_{\boldsymbol{k},+} + e^{-i\phi_{\boldsymbol{k}}} \sin\frac{\theta_{\boldsymbol{k}}}{2} c_{\boldsymbol{k},-}), \tag{B.3}$$

$$c_{\boldsymbol{k},\downarrow} = (e^{i\phi_{\boldsymbol{k}}} \sin\frac{\theta_{\boldsymbol{k}}}{2} c_{\boldsymbol{k},+} - \cos\frac{\theta_{\boldsymbol{k}}}{2} c_{\boldsymbol{k},-}), \tag{B.4}$$

where $\theta_{\boldsymbol{k}}$ satisfies $\cos\theta_{\boldsymbol{k}} = h_z/\Lambda_{\boldsymbol{k}}$ with $\Lambda_{\boldsymbol{k}} = \sqrt{h_z^2 + l_x^2 + l_y^2}$, and $\phi_{\boldsymbol{k}}$ satisfy

$$e^{i\phi_{\boldsymbol{k}}} = \frac{l_x + il_y}{\sqrt{l_x^2 + l_y^2}}. \tag{B.5}$$

Substituting Eq. (B.3) and Eq. (B.4) into Eq. (B.1), we have

$$H_0 = \sum_{\boldsymbol{k}} (\xi_{\boldsymbol{k}} + \Lambda_{\boldsymbol{k}}) c^\dagger_{\boldsymbol{k},+} c_{\boldsymbol{k},+} + (\xi_{\boldsymbol{k}} - \Lambda_{\boldsymbol{k}}) c^\dagger_{\boldsymbol{k},-} c_{\boldsymbol{k},-}. \tag{B.6}$$

For the superconducting part,

$$\begin{aligned} H_{\mathrm{SC}} &= \sum_{\boldsymbol{k}}\left(-\frac{h_z(\Delta_s(\boldsymbol{k})+i\Delta_d(\boldsymbol{k}))}{\Lambda_{\boldsymbol{k}}}c^{\dagger}_{\boldsymbol{k},+}c^{\dagger}_{-\boldsymbol{k},-}+h.c.\right) \\ &+\frac{1}{2}\sum_{\boldsymbol{k}}\left(\frac{-(\Delta_s(\boldsymbol{k})+i\Delta_d(\boldsymbol{k}))(l_x-il_y)}{\Lambda_{\boldsymbol{k}}}c^{\dagger}_{\boldsymbol{k},+}c^{\dagger}_{-\boldsymbol{k},+}+h.c.\right) \\ &+\frac{1}{2}\sum_{\boldsymbol{k}}\left(\frac{-(\Delta_s(\boldsymbol{k})+i\Delta_d(\boldsymbol{k}))(l_x+il_y)}{\Lambda_{\boldsymbol{k}}}c^{\dagger}_{\boldsymbol{k},-}c^{\dagger}_{-\boldsymbol{k},-}+h.c.\right) \end{aligned} \tag{B.7}$$

Below we go beyond Ref. [125] and do a band-dependent gauge transformation, $c_{\boldsymbol{k},+} = -\bar{c}_{\boldsymbol{k},+}e^{i\varphi_{\boldsymbol{k}}}$, $c_{\boldsymbol{k},-} = \bar{c}_{\boldsymbol{k},-}$, with

$$e^{i\varphi_{\boldsymbol{k}}} = \frac{\Delta_s(\boldsymbol{k})+i\Delta_d(\boldsymbol{k})}{\sqrt{\Delta_s^2(\boldsymbol{k})+\Delta_d^2(\boldsymbol{k})}}. \tag{B.8}$$

Accordingly, we have

$$H_0 = \sum_{\boldsymbol{k}}(\xi_{\boldsymbol{k}}+\Lambda_{\boldsymbol{k}})\bar{c}^{\dagger}_{\boldsymbol{k},+}\bar{c}_{\boldsymbol{k},+}+(\xi_{\boldsymbol{k}}-\Lambda_{\boldsymbol{k}})\bar{c}^{\dagger}_{\boldsymbol{k},-}\bar{c}_{\boldsymbol{k},-}, \tag{B.9}$$

$$\begin{aligned} H_{\mathrm{SC}} = &\sum_{\boldsymbol{k}}\left(\frac{h_z\sqrt{\Delta_s^2(\boldsymbol{k})+\Delta_d^2(\boldsymbol{k})}}{\Lambda_{\boldsymbol{k}}}\bar{c}^{\dagger}_{\boldsymbol{k},+}\bar{c}^{\dagger}_{-\boldsymbol{k},-}+h.c.\right) \\ &+\frac{1}{2}\sum_{\boldsymbol{k}}\left(\frac{-(\Delta_s(\boldsymbol{k})-i\Delta_d(\boldsymbol{k}))(l_x-il_y)}{\Lambda_{\boldsymbol{k}}}\bar{c}^{\dagger}_{\boldsymbol{k},+}\bar{c}^{\dagger}_{-\boldsymbol{k},+}+h.c.\right) \\ &+\frac{1}{2}\sum_{\boldsymbol{k}}\left(\frac{-(\Delta_s(\boldsymbol{k})+i\Delta_d(\boldsymbol{k}))(l_x+il_y)}{\Lambda_{\boldsymbol{k}}}\bar{c}^{\dagger}_{\boldsymbol{k},-}\bar{c}^{\dagger}_{-\boldsymbol{k},-}+h.c.\right). \end{aligned} \tag{B.10}$$

By further doing the following transformation

$$\bar{c}_{\boldsymbol{k},+} = \cos\frac{\gamma_{\boldsymbol{k}}}{2}\tilde{c}_{\boldsymbol{k},+}+\sin\frac{\gamma_{\boldsymbol{k}}}{2}c^{\dagger}_{-\boldsymbol{k},-}, \tag{B.11}$$

$$\bar{c}^{\dagger}_{-\boldsymbol{k},-} = \sin\frac{\gamma_{\boldsymbol{k}}}{2}\tilde{c}_{\boldsymbol{k},+}-\cos\frac{\gamma_{\boldsymbol{k}}}{2}\tilde{c}^{\dagger}_{-\boldsymbol{k},-}, \tag{B.12}$$

where

$$\gamma_{\boldsymbol{k}} = \arctan\frac{h_z\sqrt{\Delta_s^2(\boldsymbol{k})+\Delta_d^2(\boldsymbol{k})}}{\Lambda_{\boldsymbol{k}}\xi_{\boldsymbol{k}}}, \tag{B.13}$$

the Hamiltonian can be further transformed into the below form

$$H = \sum_{k\alpha}\epsilon_{\boldsymbol{k},\alpha}\tilde{c}^{\dagger}_{\boldsymbol{k},\alpha}\tilde{c}_{\boldsymbol{k},\alpha}-\frac{1}{2}\left(\frac{(\Delta_s(\boldsymbol{k})-i\alpha\Delta_d(\boldsymbol{k}))(l_x-i\alpha l_y)}{\Lambda_{\boldsymbol{k}}}\tilde{c}^{\dagger}_{\boldsymbol{k},\alpha}\tilde{c}^{\dagger}_{-\boldsymbol{k},\alpha}+h.c.\right), \tag{B.14}$$

where

$$\epsilon_{\boldsymbol{k},\pm} = \sqrt{\xi_{\boldsymbol{k}}^2 + \frac{(\Delta_s^2(\boldsymbol{k}) + \Delta_d^2(\boldsymbol{k}))h_z^2}{\Lambda_{\boldsymbol{k}}^2}} \pm \Lambda_{\boldsymbol{k}}. \tag{B.15}$$

It is readily seen that the Hamiltonian can be decoupled into two independent parts, *i.e.*, $H = H_+ \oplus H_-$, with

$$H_+ = \sum_{\boldsymbol{k}} \epsilon_{\boldsymbol{k},+} \tilde{c}_{\boldsymbol{k},+}^\dagger \tilde{c}_{\boldsymbol{k},+} - \frac{1}{2}\left(\frac{(\Delta_s(\boldsymbol{k}) - i\Delta_d(\boldsymbol{k}))(l_x - il_y)}{\Lambda_{\boldsymbol{k}}} \tilde{c}_{\boldsymbol{k},+}^\dagger \tilde{c}_{-\boldsymbol{k},+}^\dagger + h.c. \right), \tag{B.16}$$

$$H_- = \sum_{\boldsymbol{k}} \epsilon_{\boldsymbol{k},-} \tilde{c}_{\boldsymbol{k},-}^\dagger \tilde{c}_{\boldsymbol{k},-} - \frac{1}{2}\left(\frac{(\Delta_s(\boldsymbol{k}) + i\Delta_d(\boldsymbol{k}))(l_x + il_y)}{\Lambda_{\boldsymbol{k}}} \tilde{c}_{\boldsymbol{k},-}^\dagger \tilde{c}_{-\boldsymbol{k},-}^\dagger + h.c. \right). \tag{B.17}$$

It is obvious that both H_+ and H_- describe odd-parity superconductors. It is worthy pointing out the pairing forms in H_+ and H_- are similar to that in the toy model for second-order topological odd-party superconductors proposed in Ref. [191]. In the limit $h_z = 0$, we obtain Eq. 4.39 in Chapter 4.

Appendix C

Phase Boundaries in The $s + id$-Wave Pairing Regime

As shown in Fig. 4.1, the $s + id$-wave superconducting regime consists of three time-reversal symmetry breaking topologically distinct phases. The boundaries between these phases are two straight lines with the same slope but different intercepts. In this section, we are going to derive the equations of those two lines.

The nodes of $s + id$-wave pairing are located where both $\Delta_0 + \Delta_s \eta_s(\boldsymbol{k}) = 0$ and $\eta_d(\boldsymbol{k}) = 0$ are simultaneously satisfied in the first Brillouin zone while the Fermi surfaces of the normal state are determined by the equation $\varepsilon_\sigma(\boldsymbol{k}) = \xi(\boldsymbol{k}) + \sigma l(\boldsymbol{k}) = 0$. As explained in the main paper, a topological phase transition happens in the $s + id$-wave regime when the Fermi surface crosses these pairing nodes. It can be shown that the four pairing nodes in the first Brillouin zone satisfy,

$$\frac{4\Delta_0 t}{\Delta_s} + \sigma l(\boldsymbol{k}) = \mu, \tag{C.1}$$

or

$$\frac{4\Delta_0 t}{\Delta_s} \pm 2\sqrt{(\lambda_R \sin k_y + \lambda_D \sin k_x)^2 + (\lambda_R \sin k_x + \lambda_D \sin k_y)^2} = \mu. \tag{C.2}$$

Since $\eta_d(\boldsymbol{k}) = 0$ is satisfied on the two lines $k_x = \pm k_y$, using the fact that $\sin k_x = \pm \sin k_y$ on these two lines leads to

$$\sin^2 k_x (\lambda_R \pm \lambda_D)^2 = \frac{1}{2}(\frac{\mu}{2} - \frac{2\Delta_0 t}{\Delta_s})^2. \tag{C.3}$$

At the pairing nodes, we also have $\cos k_x = -\frac{\Delta_0}{\Delta_s}$, so,

$$\{1 - (\frac{\Delta_0}{\Delta_s})^2\}(\lambda_R \pm \lambda_D)^2 = \frac{1}{2}(\frac{\mu}{2} - \frac{2\Delta_0 t}{\Delta_s})^2. \tag{C.4}$$

For $\Delta_0 \ll \Delta_s$, we have

$$(\lambda_R \pm \lambda_D)^2 \simeq \frac{\mu^2}{8}. \tag{C.5}$$

If we restrict ourselves to the lines with positive slope in $\lambda_D - \mu$ plane, we will have

$$\lambda_D \simeq \frac{\sqrt{2}}{4}\mu \pm \lambda_R, \tag{C.6}$$

which are the equations of two lines with the slope $\sqrt{2}/4$ and intercept λ_R (the boundary between first- and second-order topological superconductivity phases) and intercept $-\lambda_R$ (the boundary between first-order topological phase and the topologically trivial phase).

Appendix D

The $\mathbb{Z}_2$ Topological Invariant

While the presence of a straight z-directional vortex line breaks translational symmetry in the x and y directions, the z direction still preserves translational symmetry and k_z is still a good quantum number. Therefore, the whole system can be taken as a quasi-1D superconductor. Since the presence of a vortex line also breaks the time-reversal symmetry, this quasi-1D superconductor thus falls into the D class of the Atland-Zirnbauer classification [273, 274]. As is known, when a superconductor in the D class is fully gapped, its band topology is characterized by a $\mathbb{Z}_2$ invariant of the form [114]

$$\nu = \mathrm{sgn}\{\mathrm{Pf}[H_{\mathrm{M}}(0)]\} \cdot \mathrm{sgn}\{\mathrm{Pf}[H_{\mathrm{M}}(\pi)]\}, \tag{D.1}$$

where $H_{\mathrm{M}}(k_z)$ represents the Hamiltonian in the Majorana representation, which is an anti-symmetric matrix forced by the intrinsic self-adjoint property of Majorana operators; "Pf" is a shorthand notation of Pfaffian. The formula (5.29) implies that a change of the $\mathbb{Z}_2$ invariant, or say a topological phase transition, can only occur at $k_z = 0$ or π, a consequence originating from the particle-hole symmetry. To obtain the explicit form of $H_{\mathrm{M}}(k_z)$, we introduce the following Majorana operators,

$$\gamma_{\alpha,s,\boldsymbol{r};1} = \frac{1}{\sqrt{2}}(c^{\dagger}_{\alpha,s,\boldsymbol{r}} + c_{\alpha,s,\boldsymbol{r}}) = \gamma^{\dagger}_{\alpha,s,\boldsymbol{r};1}, \tag{D.2}$$

$$\gamma_{\alpha,s,\boldsymbol{r};2} = \frac{i}{\sqrt{2}}(c^{\dagger}_{\alpha,s,\boldsymbol{r}} - c_{\alpha,s,\boldsymbol{r}}) = \gamma^{\dagger}_{\alpha,s,\boldsymbol{r};2}, \tag{D.3}$$

at orbital α, with spin s, and at site $\boldsymbol{r}$. Since only the two time-reversal invariant momenta are relevant for the determination of the underlying band topology, in the following we restrict ourselves to these two points. At $k_z = 0$, it is straightforward to find that the real space Hamiltonian is reduced as

$$H(k_z = 0) \quad = \quad \sum_{\bar{\boldsymbol{r}};\alpha\alpha';s,s'} \big\{ -\mu c^{\dagger}_{\alpha,s,\bar{\boldsymbol{r}}}\delta_{\alpha\alpha'}\delta_{ss'}c_{\alpha',s',\bar{\boldsymbol{r}}} + (m_0 - 2t)c^{\dagger}_{\alpha,s,\bar{\boldsymbol{r}}}[\sigma_z]_{\alpha\alpha'}\delta_{ss'}c_{\alpha',s',\bar{\boldsymbol{r}}}$$

$$
\begin{aligned}
&+h_z c^{\dagger}_{\alpha,s,\bar{\boldsymbol{r}}}\delta_{\alpha\alpha'}[s_z]_{ss'}c_{\alpha',s',\bar{\boldsymbol{r}}}\\
&-(tc^{\dagger}_{\alpha,s,\bar{\boldsymbol{r}}}[\sigma_z]_{\alpha\alpha'}\delta_{ss'}c_{\alpha',s',\bar{\boldsymbol{r}}+\hat{\boldsymbol{x}}}+tc^{\dagger}_{\alpha,s,\bar{\boldsymbol{r}}}[\sigma_z]_{\alpha\alpha'}\delta_{ss'}c_{\alpha',s',\bar{\boldsymbol{r}}+\hat{\boldsymbol{y}}}+h.c.)\\
&+(-i\lambda c^{\dagger}_{\alpha,s,\bar{\boldsymbol{r}}}[\sigma_x]_{\alpha\alpha'}[s_x]_{ss'}c_{\alpha',s',\bar{\boldsymbol{r}}+\hat{\boldsymbol{x}}}-i\lambda c^{\dagger}_{\alpha,s,\bar{\boldsymbol{r}}}[\sigma_x]_{\alpha\alpha'}[s_y]_{ss'}c_{\alpha',s',\bar{\boldsymbol{r}}+\hat{\boldsymbol{y}}}+h.c.)\\
&+(i\frac{\Delta_0(\bar{\boldsymbol{r}})}{2}c^{\dagger}_{\alpha,s,\bar{\boldsymbol{r}}}\delta_{\alpha\alpha'}[s_y]_{ss'}c^{\dagger}_{\alpha',s',\bar{\boldsymbol{r}}}+i(\frac{\Delta_s(\bar{\boldsymbol{r}}+\frac{\hat{\boldsymbol{x}}}{2})}{2}c^{\dagger}_{\alpha,s,\bar{\boldsymbol{r}}}\delta_{\alpha\alpha'}[s_y]_{ss'}c^{\dagger}_{\alpha',s',\bar{\boldsymbol{r}}+\hat{\boldsymbol{x}}}\\
&+\frac{\Delta_s(\bar{\boldsymbol{r}}+\frac{\hat{\boldsymbol{y}}}{2})}{2}c^{\dagger}_{\alpha,s,\bar{\boldsymbol{r}}}\delta_{\alpha\alpha'}[s_y]_{ss'}c^{\dagger}_{\alpha',s',\bar{\boldsymbol{r}}+\hat{\boldsymbol{y}}})+h.c.)\big\},
\end{aligned}
\tag{D.4}
$$

and at $k_z=\pi$, we have

$$
\begin{aligned}
H(k_z=\pi) \;=\; &\sum_{\bar{\boldsymbol{r}};\alpha\alpha';s,s'}\big\{-\mu c^{\dagger}_{\alpha,s,\bar{\boldsymbol{r}}}\delta_{\alpha\alpha'}\delta_{ss'}c_{\alpha',s',\bar{\boldsymbol{r}}}+(m_0+2t)c^{\dagger}_{\alpha,s,\bar{\boldsymbol{r}}}[\sigma_z]_{\alpha\alpha'}\delta_{ss'}c_{\alpha',s',\bar{\boldsymbol{r}}}\\
&+h_z c^{\dagger}_{\alpha,s,\bar{\boldsymbol{r}}}\delta_{\alpha\alpha'}[s_z]_{ss'}c_{\alpha',s',\bar{\boldsymbol{r}}}\\
&-(tc^{\dagger}_{\alpha,s,\bar{\boldsymbol{r}}}[\sigma_z]_{\alpha\alpha'}\delta_{ss'}c_{\alpha',s',\bar{\boldsymbol{r}}+\hat{\boldsymbol{x}}}+tc^{\dagger}_{\alpha,s,\bar{\boldsymbol{r}}}[\sigma_z]_{\alpha\alpha'}\delta_{ss'}c_{\alpha',s',\bar{\boldsymbol{r}}+\hat{\boldsymbol{y}}}+h.c.)\\
&+(-i\lambda c^{\dagger}_{\alpha,s,\bar{\boldsymbol{r}}}[\sigma_x]_{\alpha\alpha'}[s_x]_{ss'}c_{\alpha',s',\bar{\boldsymbol{r}}+\hat{\boldsymbol{x}}}-i\lambda c^{\dagger}_{\alpha,s,\bar{\boldsymbol{r}}}[\sigma_x]_{\alpha\alpha'}[s_y]_{ss'}c_{\alpha',s',\bar{\boldsymbol{r}}+\hat{\boldsymbol{y}}}+h.c.)\\
&+(i\frac{\Delta_0(\bar{\boldsymbol{r}})}{2}c^{\dagger}_{\alpha,s,\bar{\boldsymbol{r}}}\delta_{\alpha\alpha'}[s_y]_{ss'}c^{\dagger}_{\alpha',s',\bar{\boldsymbol{r}}}+i(\frac{\Delta_s(\bar{\boldsymbol{r}}+\frac{\hat{\boldsymbol{x}}}{2})}{2}c^{\dagger}_{\alpha,s,\bar{\boldsymbol{r}}}\delta_{\alpha\alpha'}[s_y]_{ss'}c^{\dagger}_{\alpha',s',\bar{\boldsymbol{r}}+\hat{\boldsymbol{x}}}\\
&+\frac{\Delta_s(\bar{\boldsymbol{r}}+\frac{\hat{\boldsymbol{y}}}{2})}{2}c^{\dagger}_{\alpha,s,\bar{\boldsymbol{r}}}\delta_{\alpha\alpha'}[s_y]_{ss'}c^{\dagger}_{\alpha',s',\bar{\boldsymbol{r}}+\hat{\boldsymbol{y}}})+h.c.)\big\},
\end{aligned}
\tag{D.5}
$$

where $\bar{\boldsymbol{r}}=(x,y)$ only involves the lattice sites because the kinetic terms in the z direction have been rewritten in wave vector space due to the preservation of translational symmetry in this direction. It is worth noting that because the vortex line is generated along the z direction, above we have accordingly taken $\boldsymbol{h}=(0,0,h_z)$. Substituting the Dirac fermion operators by Majorana operators, we get

$$
\begin{aligned}
H(k_z=0) \;=\; &\sum_{\bar{\boldsymbol{r}};\alpha\alpha';s,s'}\big\{-i\mu\gamma_{\alpha,s,\bar{\boldsymbol{r}};1}\delta_{\alpha\alpha'}\delta_{ss'}\gamma_{\alpha',s',\bar{\boldsymbol{r}};2}+i(m-2t)\gamma_{\alpha,s,\bar{\boldsymbol{r}};1}[\sigma_z]_{\alpha\alpha'}\delta_{ss'}\gamma_{\alpha',s',\bar{\boldsymbol{r}};2}\\
&+ih_z\gamma_{\alpha,s,\bar{\boldsymbol{r}};1}\delta_{\alpha\alpha'}[s_z]_{ss'}\gamma_{\alpha',s',\bar{\boldsymbol{r}};2}\\
&-it(\gamma_{\alpha,s,\bar{\boldsymbol{r}};1}[\sigma_z]_{\alpha\alpha'}\delta_{ss'}\gamma_{\alpha',s',\bar{\boldsymbol{r}}+\hat{\boldsymbol{x}};2}-\gamma_{\alpha,s,\bar{\boldsymbol{r}};2}[\sigma_z]_{\alpha\alpha'}\delta_{ss'}\gamma_{\alpha',s',\bar{\boldsymbol{r}}+\hat{\boldsymbol{x}};1})\\
&-it(\gamma_{\alpha,s,\bar{\boldsymbol{r}};1}[\sigma_z]_{\alpha\alpha'}\delta_{ss'}\gamma_{\alpha',s',\bar{\boldsymbol{r}}+\hat{\boldsymbol{y}};2}-\gamma_{\alpha,s,\bar{\boldsymbol{r}};2}[\sigma_z]_{\alpha\alpha'}\delta_{ss'}\gamma_{\alpha',s',\bar{\boldsymbol{r}}+\hat{\boldsymbol{y}};1})\\
&-i\lambda(\gamma_{\alpha,s,\bar{\boldsymbol{r}};1}[\sigma_x]_{\alpha\alpha'}[s_x]_{ss'}\gamma_{\alpha',s',\bar{\boldsymbol{r}}+\hat{\boldsymbol{x}};1}+\gamma_{\alpha,s,\bar{\boldsymbol{r}};2}[\sigma_x]_{\alpha\alpha'}[s_x]_{ss'}\gamma_{\alpha',s',\bar{\boldsymbol{r}}+\hat{\boldsymbol{x}};2})\\
&+\lambda(\gamma_{\alpha,s,\bar{\boldsymbol{r}};1}[\sigma_y]_{\alpha\alpha'}[s_y]_{ss'}\gamma_{\alpha',s',\bar{\boldsymbol{r}}+\hat{\boldsymbol{y}};2}-\gamma_{\alpha,s,\bar{\boldsymbol{r}};2}[\sigma_x]_{\alpha\alpha'}[s_x]_{ss'}\gamma_{\alpha',s',\bar{\boldsymbol{r}}+\hat{\boldsymbol{y}};1})\\
&+\frac{\mathrm{Re}\Delta_0(\bar{\boldsymbol{r}})}{2}(\gamma_{\alpha,s,\bar{\boldsymbol{r}};2}\delta_{\alpha\alpha'}[s_y]_{ss'}\gamma_{\alpha',s',\bar{\boldsymbol{r}};1}+\gamma_{\alpha,s,\boldsymbol{r};1}\delta_{\alpha\alpha'}[s_y]_{ss'}\gamma_{\alpha',s',\boldsymbol{r};2})\\
&-\frac{\mathrm{Im}\Delta_0(\bar{\boldsymbol{r}})}{2}(\gamma_{\alpha,s,\bar{\boldsymbol{r}};1}\delta_{\alpha\alpha'}[s_y]_{ss'}\gamma_{\alpha',s',\bar{\boldsymbol{r}};1}-\gamma_{\alpha,s,\bar{\boldsymbol{r}};2}\delta_{\alpha\alpha'}[s_y]_{ss'}\gamma_{\alpha',s',\bar{\boldsymbol{r}};2})
\end{aligned}
\tag{D.6}
$$

$$
\begin{aligned}
&+\frac{\mathrm{Re}\Delta_s(\bar{\boldsymbol{r}}+\frac{\hat{\boldsymbol{x}}}{2})}{2}(\gamma_{\alpha,s,\bar{\boldsymbol{r}};2}\delta_{\alpha\alpha'}[s_y]_{ss'}\gamma_{\alpha',s',\bar{\boldsymbol{r}}+\hat{\boldsymbol{x}};1}+\gamma_{\alpha,s,\bar{\boldsymbol{r}};1}\delta_{\alpha\alpha'}[s_y]_{ss'}\gamma_{\alpha',s',\bar{\boldsymbol{r}}+\hat{\boldsymbol{x}};2})\\
&-\frac{\mathrm{Im}\Delta_s(\bar{\boldsymbol{r}}+\frac{\hat{\boldsymbol{x}}}{2})}{2}(\gamma_{\alpha,s,\bar{\boldsymbol{r}};1}\delta_{\alpha\alpha'}[s_y]_{ss'}\gamma_{\alpha',s',\bar{\boldsymbol{r}}+\hat{\boldsymbol{x}};1}-\gamma_{\alpha,s,\bar{\boldsymbol{r}};2}\delta_{\alpha\alpha'}[s_y]_{ss'}\gamma_{\alpha',s',\bar{\boldsymbol{r}}+\hat{\boldsymbol{x}};2})\\
&+\frac{\mathrm{Re}\Delta_s(\bar{\boldsymbol{r}}+\frac{\hat{\boldsymbol{y}}}{2})}{2}(\gamma_{\alpha,s,\bar{\boldsymbol{r}};2}\delta_{\alpha\alpha'}[s_y]_{ss'}\gamma_{\alpha',s',\bar{\boldsymbol{r}}+\hat{\boldsymbol{y}};1}+\gamma_{\alpha,s,\boldsymbol{r};1}\delta_{\alpha\alpha'}[s_y]_{ss'}\gamma_{\alpha',s',\boldsymbol{r}+\hat{\boldsymbol{y}};2})\\
&-\frac{\mathrm{Im}\Delta_s(\bar{\boldsymbol{r}}+\frac{\hat{\boldsymbol{y}}}{2})}{2}(\gamma_{\alpha,s,\bar{\boldsymbol{r}};1}\delta_{\alpha\alpha'}[s_y]_{ss'}\gamma_{\alpha',s',\bar{\boldsymbol{r}}+\hat{\boldsymbol{y}};1}-\gamma_{\alpha,s,\bar{\boldsymbol{r}};2}\delta_{\alpha\alpha'}[s_y]_{ss'}\gamma_{\alpha',s',\bar{\boldsymbol{r}}+\hat{\boldsymbol{y}};2})\big\},
\end{aligned}
$$

and

$$
\begin{aligned}
H(k_z=\pi) \;=\; &\sum_{\bar{\boldsymbol{r}};\alpha\alpha';s,s'}\big\{-i\mu\gamma_{\alpha,s,\bar{\boldsymbol{r}};1}\delta_{\alpha\alpha'}\delta_{ss'}\gamma_{\alpha',s',\bar{\boldsymbol{r}};2}+i(m+2t)\gamma_{\alpha,s,\bar{\boldsymbol{r}};1}[\sigma_z]_{\alpha\alpha'}\delta_{ss'}\gamma_{\alpha',s',\bar{\boldsymbol{r}};2}\\
&+ih_z\gamma_{\alpha,s,\bar{\boldsymbol{r}};1}\delta_{\alpha\alpha'}[s_z]_{ss'}\gamma_{\alpha',s',\bar{\boldsymbol{r}};2}\\
&-it(\gamma_{\alpha,s,\bar{\boldsymbol{r}};1}[\sigma_z]_{\alpha\alpha'}\delta_{ss'}\gamma_{\alpha',s',\bar{\boldsymbol{r}}+\hat{\boldsymbol{x}};2}-\gamma_{\alpha,s,\bar{\boldsymbol{r}};2}[\sigma_z]_{\alpha\alpha'}\delta_{ss'}\gamma_{\alpha',s',\bar{\boldsymbol{r}}+\hat{\boldsymbol{x}};1})\\
&-it(\gamma_{\alpha,s,\bar{\boldsymbol{r}};1}[\sigma_z]_{\alpha\alpha'}\delta_{ss'}\gamma_{\alpha',s',\bar{\boldsymbol{r}}+\hat{\boldsymbol{y}};2}-\gamma_{\alpha,s,\bar{\boldsymbol{r}};2}[\sigma_z]_{\alpha\alpha'}\delta_{ss'}\gamma_{\alpha',s',\bar{\boldsymbol{r}}+\hat{\boldsymbol{y}};1})\\
&-i\lambda(\gamma_{\alpha,s,\bar{\boldsymbol{r}};1}[\sigma_x]_{\alpha\alpha'}[s_x]_{ss'}\gamma_{\alpha',s',\bar{\boldsymbol{r}}+\hat{\boldsymbol{x}};1}+\gamma_{\alpha,s,\bar{\boldsymbol{r}};2}[\sigma_x]_{\alpha\alpha'}[s_x]_{ss'}\gamma_{\alpha',s',\bar{\boldsymbol{r}}+\hat{\boldsymbol{x}};2})\\
&+\lambda(\gamma_{\alpha,s,\bar{\boldsymbol{r}};1}[\sigma_x]_{\alpha\alpha'}[s_y]_{ss'}\gamma_{\alpha',s',\bar{\boldsymbol{r}}+\hat{\boldsymbol{y}};2}-\gamma_{\alpha,s,\bar{\boldsymbol{r}};2}[\sigma_x]_{\alpha\alpha'}[s_y]_{ss'}\gamma_{\alpha',s',\bar{\boldsymbol{r}}+\hat{\boldsymbol{y}};1})\\
&+\frac{\mathrm{Re}\Delta_0(\bar{\boldsymbol{r}})}{2}(\gamma_{\alpha,s,\bar{\boldsymbol{r}};2}\delta_{\alpha\alpha'}[s_y]_{ss'}\gamma_{\alpha',s',\bar{\boldsymbol{r}};1}+\gamma_{\alpha,s,\boldsymbol{r};1}\delta_{\alpha\alpha'}[s_y]_{ss'}\gamma_{\alpha',s',\boldsymbol{r};2})\\
&-\frac{\mathrm{Im}\Delta_0(\bar{\boldsymbol{r}})}{2}(\gamma_{\alpha,s,\bar{\boldsymbol{r}};1}\delta_{\alpha\alpha'}[s_y]_{ss'}\gamma_{\alpha',s',\bar{\boldsymbol{r}};1}-\gamma_{\alpha,s,\bar{\boldsymbol{r}};2}\delta_{\alpha\alpha'}[s_y]_{ss'}\gamma_{\alpha',s',\bar{\boldsymbol{r}};2})\\
&+\frac{\mathrm{Re}\Delta_s(\bar{\boldsymbol{r}}+\frac{\hat{\boldsymbol{x}}}{2})}{2}(\gamma_{\alpha,s,\bar{\boldsymbol{r}};2}\delta_{\alpha\alpha'}[s_y]_{ss'}\gamma_{\alpha',s',\bar{\boldsymbol{r}}+\hat{\boldsymbol{x}};1}+\gamma_{\alpha,s,\bar{\boldsymbol{r}};1}\delta_{\alpha\alpha'}[s_y]_{ss'}\gamma_{\alpha',s',\bar{\boldsymbol{r}}+\hat{\boldsymbol{x}};2})\\
&-\frac{\mathrm{Im}\Delta_s(\bar{\boldsymbol{r}}+\frac{\hat{\boldsymbol{x}}}{2})}{2}(\gamma_{\alpha,s,\bar{\boldsymbol{r}};1}\delta_{\alpha\alpha'}[s_y]_{ss'}\gamma_{\alpha',s',\bar{\boldsymbol{r}}+\hat{\boldsymbol{x}};1}-\gamma_{\alpha,s,\bar{\boldsymbol{r}};2}\delta_{\alpha\alpha'}[s_y]_{ss'}\gamma_{\alpha',s',\bar{\boldsymbol{r}}+\hat{\boldsymbol{x}};2})\\
&+\frac{\mathrm{Re}\Delta_s(\bar{\boldsymbol{r}}+\frac{\hat{\boldsymbol{y}}}{2})}{2}(\gamma_{\alpha,s,\bar{\boldsymbol{r}};2}\delta_{\alpha\alpha'}[s_y]_{ss'}\gamma_{\alpha',s',\bar{\boldsymbol{r}}+\hat{\boldsymbol{y}};1}+\gamma_{\alpha,s,\boldsymbol{r};1}\delta_{\alpha\alpha'}[s_y]_{ss'}\gamma_{\alpha',s',\boldsymbol{r}+\hat{\boldsymbol{y}};2})\\
&-\frac{\mathrm{Im}\Delta_s(\bar{\boldsymbol{r}}+\frac{\hat{\boldsymbol{y}}}{2})}{2}(\gamma_{\alpha,s,\bar{\boldsymbol{r}};1}\delta_{\alpha\alpha'}[s_y]_{ss'}\gamma_{\alpha',s',\bar{\boldsymbol{r}}+\hat{\boldsymbol{y}};1}-\gamma_{\alpha,s,\bar{\boldsymbol{r}};2}\delta_{\alpha\alpha'}[s_y]_{ss'}\gamma_{\alpha',s',\bar{\boldsymbol{r}}+\hat{\boldsymbol{y}};2})\big\}.
\end{aligned}
\tag{D.7}
$$

Let us consider a system with open boundary conditions in both the x and y directions where the number of lattice sites is N_x in the x direction and N_y in the y direction. In terms of the Majorana representation

$$
\gamma_{k_z=0/\pi}=(\Gamma_{1,1},\Gamma_{2,1},...,\Gamma_{n,m},...,\Gamma_{N_x,N_y})^T,
\tag{D.8}
$$

with

$$
\begin{aligned}
\Gamma_{n,m}=(&\gamma_{a,\uparrow,n\hat{\boldsymbol{x}}+m\hat{\boldsymbol{y}};1},\gamma_{a,\uparrow,n\hat{\boldsymbol{x}}+m\hat{\boldsymbol{y}};2},\gamma_{b,\uparrow,n\hat{\boldsymbol{x}}+m\hat{\boldsymbol{y}};1},\gamma_{b,\uparrow,n\hat{\boldsymbol{x}}+m\hat{\boldsymbol{y}};2},\\
&\gamma_{a,\downarrow,n\hat{\boldsymbol{x}}+m\hat{\boldsymbol{y}};1},\gamma_{a,\downarrow,n\hat{\boldsymbol{x}}+m\hat{\boldsymbol{y}};2},\gamma_{b,\downarrow,n\hat{\boldsymbol{x}}+m\hat{\boldsymbol{y}};1},\gamma_{b,\downarrow,n\hat{\boldsymbol{x}}+m\hat{\boldsymbol{y}};2}),
\end{aligned}
\tag{D.9}
$$

the Hamiltonian can be written as

$$H(k_z = 0/\pi) = i\gamma^{\dagger}_{0/\pi} H_{\mathrm{M}}(k_z = 0/\pi)\gamma_{0/\pi}, \tag{D.10}$$

where H_{M} is an $8N_xN_y \times 8N_xN_y$ real antisymmetric matrix for which the Pfaffian is well defined. In this work, the Pfaffian has been calculated by using the code developed in Ref. [91].

Appendix E

Boundary Fermi Surface and Vortex Bound States

In the chapter 5, we have shown that the low-energy effective Hamiltonian on the bottom surface reads [see Eq.(5.24)]

$$\mathcal{H}_{\text{eff}}(k_x, k_y) = 2\lambda(k_y s_x - k_x s_y)\tau_z + M_{\text{Z}} s_z + M_{\text{S}}\tau_x, \tag{E.1}$$

where $M_{\text{S}} = \Delta_0 + 2\Delta_s$ and $M_{\text{Z}} = h_z$. Such a form is derived for the special case with $\mu = 0$. When $\mu \neq 0$, the low-energy effective Hamiltonian becomes

$$\mathcal{H}_{\text{eff}}(k_x, k_y) = 2\lambda(k_y s_x - k_x s_y)\tau_z - \mu\tau_z + M_{\text{Z}} s_z + M_{\text{S}}\tau_x. \tag{E.2}$$

Accordingly, the energy spectra are

$$E(k_x, k_y) = \pm\sqrt{4\lambda^2(k_x^2 + k_y^2) + \mu^2 + M_{\text{Z}}^2 + M_{\text{S}}^2 \pm 2\sqrt{\mu^2[4\lambda^2(k_x^2 + k_y^2) + M_{\text{Z}}^2] + M_{\text{Z}}^2 M_{\text{S}}^2}}, \tag{E.3}$$

whose gap gets closed at $k_x = k_y = 0$ only when $M_{\text{Z}}^2 = \mu^2 + M_{\text{S}}^2$. As long as $\mu < \sqrt{M_{\text{Z}}^2 - M_{\text{S}}^2}$ (since here only the absolute values of μ and h_z are relevant, we consider both of them to be positive in this section for the convenience of discussion), no matter whether the superconducting pairing is purely on-site ($\Delta_s = 0$) or extensive ($\Delta_s \neq 0$), the system corresponds to a second-order topological superconductor with chiral Majorana hinge states circling around the top and bottom surfaces because the nature of Dirac masses on these two surfaces is different from that of the side surfaces.

In Fig. 5.10, we have shown the absence of vortex-end Majorana zero modes when the superconductor falls in the chiral second-order superconducting phase. From a surface viewpoint, this result can be simply understood as a consequence of the absence of a boundary Fermi surface in the normal state. The underlying reason is that the vortex-core Majorana

zero modes must originate from certain low-energy modes, so the absence of a boundary Fermi surface naturally implies the absence of vortex-core Majorana zero modes. As the condition for the existence of a boundary Fermi surface before the introduction of superconductivity is $\mu > h_z$, whereas the chiral second-order topological superconducting phase requires $\mu < \sqrt{M_{\rm Z}^2 - M_{\rm S}^2} < h_z$, their incompatibility indicates that vortex-end Majorana zero modes will always be absent on the top and bottom surfaces when the system is in the chiral second-order topological superconducting phase.

Focusing on the normal state, in effect, the Zeeman term not only opens a gap of the size $2h_z$ on the top and bottom surfaces, but also reduces the bulk gap. This can be easily inferred from the normal-state Hamiltonian which reads

$$H_N(\boldsymbol{k}) = \quad (m_0 - 2t\sum_{i=x,y,z}\cos k_i)\sigma_z s_0 + 2\lambda\sum_{i=x,y,z}\sin k_i \sigma_x s_i + h_z\sigma_0 s_z, \tag{E.4}$$

whose energy spectra are given by

$$E(\boldsymbol{k}) = \pm\sqrt{4\lambda^2(\sin^2 k_x + \sin^2 k_y) + \left(h_z \pm \sqrt{4\lambda^2\sin^2 k_z + (m_0 - 2t\sum_{i=x,y,z} t\cos k_i)^2}\right)^2}. \tag{E.5}$$

According to the above equation, one can easily find that the bulk gap will reduce from E_g (the zero-field value) to $E_g - 2h_z$ when $h_z < E_g/2$. When $h_z > E_g/2$, the normal state will become a Weyl semimetal. Importantly, the increase of surface gap and the decrease of bulk gap imply that bulk and boundary Fermi surfaces will coexist when $h_z > E_g/4$ and $h_z < \mu < E_u$, where E_u denotes the upper limit beyond which the surface states do not exist on the top and bottom surfaces. Therefore, in the regime $h_z > E_g/4$, the low-energy surface Hamiltonian only cannot fully describe the low-energy physics. In the following, we restrict to the regime $h_z < E_g/4$, so that the low-energy surface Hamiltonian can faithfully describe the low-energy physics when the chemical potential only crosses the surface bands.

We first consider that the superconducting pair contains both on-site and extended s-wave components, and the configuration of the band inversion surface and the pairing node surface realizes a helical (time-reversal invariant) second-order topological superconductor at $h_z = 0$ and $\mu = 0$. Next, we consider $h_z > |\Delta_0 + 2\Delta_s|$, so that the system realizes a chiral second-order topological superconductor at $\mu = 0$. In Fig. E.1(a), the numerical result shows that increasing μ will induce a gap closure on the top and bottom surfaces when $\mu = \sqrt{h_z^2 - (\Delta_0 + 2\Delta_s)^2}$ (see the dashed purple line). The gap closure signals a change of the topological property on the boundary. When $\mu < \sqrt{h_z^2 - (\Delta_0 + 2\Delta_s)^2}$, robust chiral Majorana modes exist on the hinges, as shown in Fig. E.1(b). When $\mu > \sqrt{h_z^2 - (\Delta_0 + 2\Delta_s)^2}$, we find that the hinges previously harboring one chiral Majorana modes now harbor two counter-propagating Majorana modes, as shown in Fig. E.1(c). The existence of two counter-propagating Majorana hinge modes in this regime is similar to the helical case at the limit $h_z = 0$. However, because the

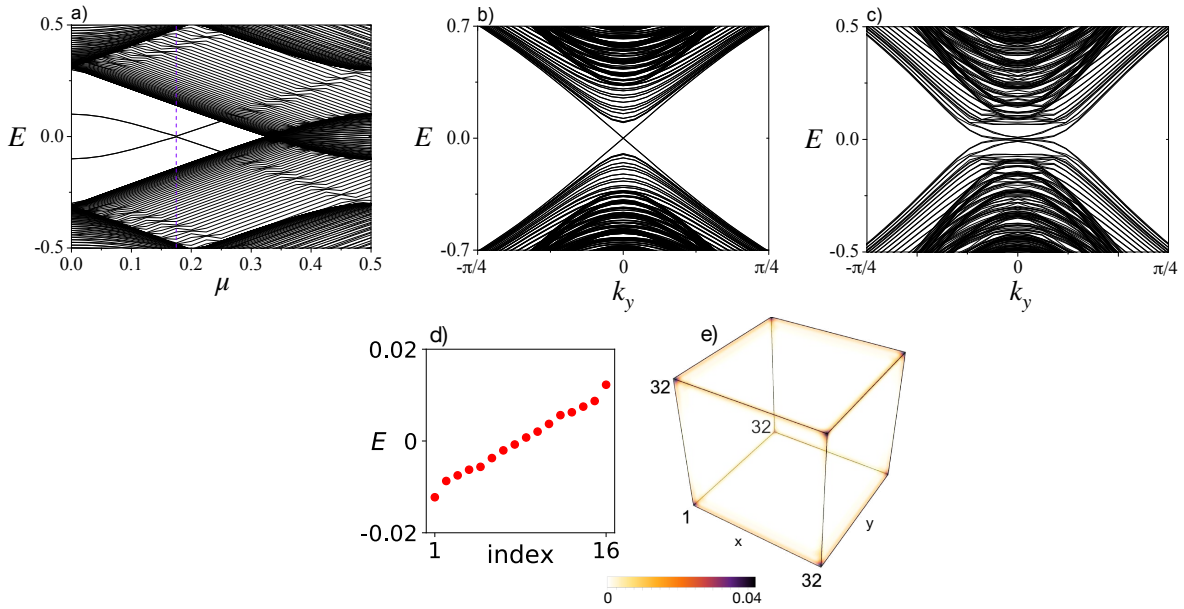

Figure E.1: (Color online) Common parameters are $t = 1$, $m_0 = 2.5$, $\lambda = 0.5$, $\Delta_0 = -\Delta_s = 0.1$, and $\boldsymbol{h} = (h_x, h_y, h_z) = (0, 0, 0.2)$. (a) Energy spectra for a geometry with open boundary directions in the z direction ($L_z = 200$) and periodic boundary conditions in the x and y directions. Only the energy spectra at $(k_x, k_y) = (0, 0)$ are shown. The mid-gap spectra correspond to surface states on the z-normal surfaces, which show a gap closure at $\mu_c = \sqrt{h_z^2 - (\Delta_0 + 2\Delta_s)^2} = 0.173$. (b)(c) Energy spectra for a geometry with open boundary conditions in the x and z directions ($L_x = L_z = 30$) and periodic boundary conditions in the y direction. $\mu = 0$ for (b) and $\mu = 0.25$ for (c). In (b), the mid-gap spectra have two-fold degeneracy, which indicates that each of the y-directional hinges harbors one chiral Majorana mode. In (c), there are eight mid-gap spectra, which indicates that each of the y-directional hinges harbors two counter-propagating gapless Majorana modes. (d) The lowest 16 eigen-energies for a geometry with open boundary conditions in all directions. The z-directional vortex line is located at the center of the xy plane. (e) The total probability density profiles of the lowest 16 eigen-states shown in (d). There is no signature for the existence of vortex bound states in the given energy window. In (d)(e), $\mu = 0.25$, $\xi = 4$ and $L_x = L_y = L_z = 32$.

time-reversal symmetry is broken by a finite h_z, the counter-propagating Majorana modes on each hinge are no longer protected by time-reversal symmetry but by certain additional symmetry on the hinge. After inserting a π-flux vortex line along the z direction, we diagonalize the Hamiltonian under the cubic geometry with lattice sizes $L_x = L_y = L_z = 32$. The numerical results presented in Figs. E.1(d)(e) suggest that the lowest-energy modes are located at the hinges. Within the energy window shown in Fig. E.1(d), we do not find the signature of vortex bound states. There are two possible reasons for this result. The first possibility is that the vortex line itself is trivial so there is no Majorana zero mode at the vortex-line ends. The second possibility is that the vortex line is topological and harbors Majorana zero modes at its ends, but the hybridization between the vortex-end Majorana zero modes and

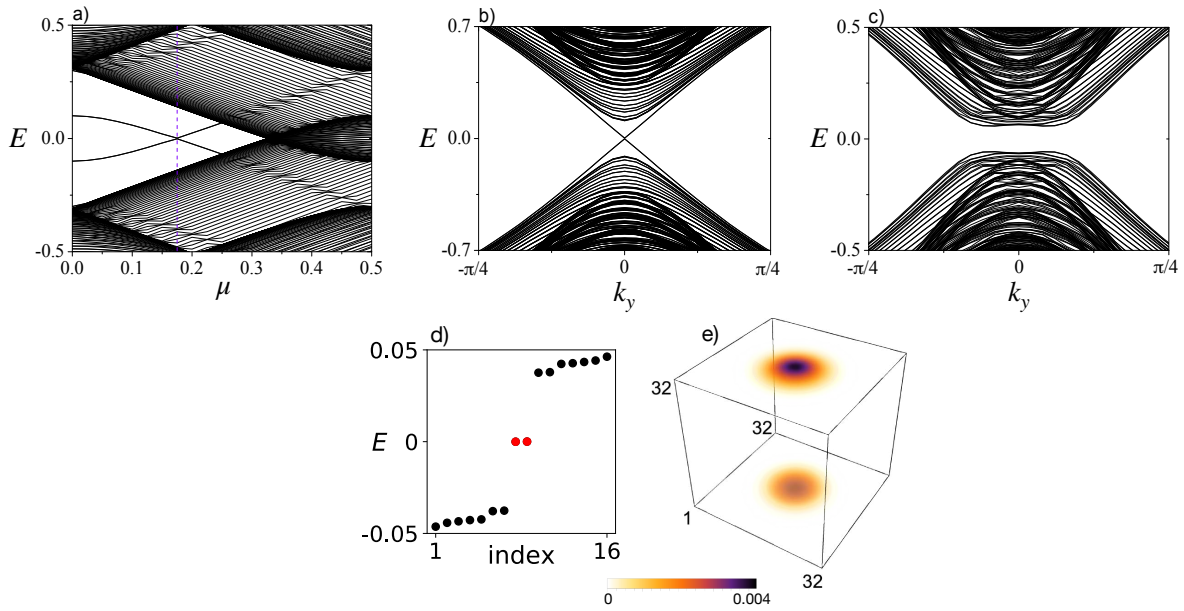

Figure E.2: (Color online) Common parameters are $t = 1$, $m_0 = 2.5$, $\lambda = 0.5$, $\Delta_0 = 0.1$, $\Delta_s = 0$, and $\boldsymbol{h} = (h_x, h_y, h_z) = (0, 0, 0.2)$. (a) Energy spectra for a geometry with open boundary directions in the z direction ($L_z = 200$) and periodic boundary conditions in the x and y directions. Only the energy spectra at $(k_x, k_y) = (0, 0)$ are shown. The mid-gap spectra correspond to surface states on the z-normal surfaces, which show a gap closure at $\mu_c = \sqrt{h_z^2 - (\Delta_0 + 2\Delta_s)^2} = 0.173$. (b)(c) Energy spectra for a geometry with open boundary conditions in the x and z directions ($L_x = L_z = 30$) and periodic boundary conditions in the y direction. $\mu = 0$ for (b) and $\mu = 0.25$ for (c). In (b), the mid-gap spectra have two-fold degeneracy, which suggests that each of the y-directional hinges harbors one chiral Majorana mode. The result in (c) shows the absence of gapless Majorana modes. (d) The lowest 16 eigen-energies for a geometry with open boundary conditions in all directions. The z-directional vortex line is located at the center of the xy plane. (e) The probability density profiles of the lowest two eigen-states shown in (d) (labeled by red dots). The results in (d) and (e) indicate the existence of Majorana zero modes at the vortex ends. In (d)(e), $\mu = 0.25$, $\xi = 4$ and $L_x = L_y = L_z = 32$.

the low-energy modes on the hinge shift the energies of the vortex-end Majorana zero modes to finite values, similar to the helical case. In order to distinguish them, we further consider the case with pure on-site s-wave pairing for comparison.

In order to have a direct comparison, we consider that the value of Δ_0 for the case with pure on-site s-wave pairing is equal to the value of $|\Delta_0 + 2\Delta_s|$ for the case with both on-site and extended s-wave pairings, so that the superconductivity-induced Dirac masses for these two cases are equivalent. Because of this equivalence, one can find that the results shown in Figs. E.2(a)(b) are almost the same as those in Figs. E.1(a)(b). However, when $\mu > \sqrt{h_z^2 - \Delta_0^2}$, the difference emerges. In Fig. E.2(c), we show the numerical result for $\mu > h_z$. One can see that there are no gapless Majorana modes on the hinges. Because of

the absence of low-energy Majorana modes on the hinges, the hybridization between low-energy vortex bound states and low-energy Majorana hinge modes can be avoided. After the insertion of a π-flux vortex line, we also diagonalize the Hamiltonian under the cubic geometry with lattice sizes $L_x = L_y = L_z = 32$. The results shown in Figs. E.2(d)(e) now clearly demonstrate the appearance of vortex-end Majorana zero modes. As here the only difference is the absence of gapless Majorana hinge modes, we reach the conclusion that the absence of low-energy vortex bound states within the given energy window in Fig. E.1(d) originates from the hybridization between the vortex bound states and the gapless Majorana hinge modes.

Now we can establish a complete picture for the interplay of second-order topology and vortex-line topology from a surface perspective. For the low-energy surface Hamiltonian given in Eq. (E.2), it is known that it can be mapped to a form describing a chiral p-wave superconductor by some basis transformations. When $\mu < h_z$, the boundary Fermi surface is absent and the effective chiral p-wave superconductor falls into the so-called strong-pairing phase [200]. According to the physics in chiral p-wave superconductors, it is known that the vortex core does not harbor any Majorana zero mode in the strong-pairing regime [200]. As here the chiral second-order topological superconducting phase always has $\mu < h_z$, it indicates that vortex-end Majorana zero modes are always absent when the system is in the the chiral second-order topological superconducting phase. In the regime $h_z < E_g/4$ and $\mu > h_z$, the low-energy surface Hamiltonian description is valid, and the effective surface chiral p-wave superconductor falls into the weak-pairing regime [200]. Accordingly, the vortex will bind one robust Majorana zero modes at its core. However, if there exist gapless Majorana modes on the hinges and the vortex is generated to be close to the hinges, then the hybridization between the vortex-core Majorana zero modes and the gapless Majorana hinge modes will split the vortex-core Majorana zero modes and lead to the absence of robust Majorana zero modes at the vortex core.